Anti-fouling surfaces based on polymer-infiltrated ZnO nanowires via capillary rise infiltration

Hong Huy Tran

To cite this version:

Hong Huy Tran. Anti-fouling surfaces based on polymer-infiltrated ZnO nanowires via capillary rise infiltration. Material chemistry. Université Grenoble Alpes [2020-..], 2022. English. NNT : 2022GRALI029 . tel-03685281

HAL Id: tel-03685281
https://theses.hal.science/tel-03685281v1

Submitted on 2 Jun 2022

THÈSE

Pour obtenir le grade de

DOCTEUR DE L'UNIVERSITÉ GRENOBLE ALPES

Spécialité : 2MGE : Matériaux, Mécanique, Génie civil, Electrochimie

Arrêté ministériel : 25 mai 2016

Présentée par

Hong Huy TRAN

Thèse dirigée par **David RIASSETTO**
et codirigée par **Daeyeon LEE**

préparée au sein du **Laboratoire Laboratoire des matériaux et du génie physique**
dans **l'École Doctorale I-MEP2 - Ingénierie - Matériaux, Mécanique, Environnement, Energétique, Procédés, Production**

Surfaces antisalissures à base de nanofils de ZnO infiltrés de polymère par remontée capillaire

Anti-fouling surfaces based on polymer-infiltrated ZnO nanowires via capillary rise infiltration

Thèse soutenue publiquement le **8 mars 2022**,
devant le jury composé de :

M. Lionel FLANDIN
Professeur, Université de Savoie, (Président)

M. Frédéric GUITTARD
Professeur, Université Côte d'Azur, (Rapporteur)

Mme. Doris VOLLMER
Professeur Associée, Max Planck Institute for Polymer Research, (Rapporteure)

Mme. Lydie PLOUX
Directrice de Recherche CNRS, Université de Strasbourg, (Examinatrice)

Mme. Céline TERNON
Maitresse de Conference, Grenoble INP, (Examinatrice)

Mme. Sigolène LECUYER
Chargée de Recherche CNRS, ENS de Lyon, (Invitée)

Acknowledgments

I consider this part the most challenging to write as I reflect on all the exciting and worrying experiences during the last three years of my PhD study at once. But then, at this moment, I feel grateful for having this PhD opportunity and having those experiences.

First and foremost, I would like to express my sincerest gratitude to my two wonderful advisors, Prof. David Riassetto and Prof. Daeyeon Lee. They taught and provided me with enthusiastic guidance, unlimited patience, care, and constant support. My PhD research could not have become a reality without the grace of my advisors. Thank both of you for taking the risk and facing many administrative barriers to accepting me as your PhD student. My honor and thankfulness from that time are still with me at the very moment, and I will never forget it. That event taught me that there is not a barrier that we cannot climb through. Thank you for providing me with an excellent working experience and always being available and supportive when I am stuck with experiments or writing. Your wisdom and generosity about time made me feel like I would not ever be alone and pushed me forwards. Working with both of you has been a great pleasure, and I am sure that I am fortunate to have had the chance to be part of this awesome collaboration. This collaboration allowed me to visit and perform experiments in several great places and learn from many great researchers. I am immensely grateful for those valuable and inspiring experiences as they taught me to think like a scientist and trained me for the next steps in my career.

I would like to thank Prof. Frédéric Guittard and Prof. Doris Vollmer for their generosity in accepting to evaluate my PhD thesis. It is my great honor to have the chance to get feedback from notable scientists whose works have tremendously inspired me throughout my PhD research. I would also like to thank Prof. Lionel Flandin, Dr. Lydie Ploux, Dr. Sigolène Lecuyer, and Dr. Céline Ternon for agreeing to be the members of my PhD committee. In addition, I wish to thank two great members of my CSI committee, Dr. Cyril Picard and Dr. Marianne Weidenhaupt. You provided me with many valuable suggestions, exciting ideas and directions for improvement, and encouragement.

This work would not have been achievable without generous financial support. I wish to acknowledge the Chair of Excellence Program's support from the Nanosciences Foundation for funding my PhD and research expenses. In particular, I would like to thank Prof. Alain

Fontaine for creating such an exciting research program and for your support of my PhD admission. Although the program has been discontinued, I firmly believe that the science produced by the program will continue to make a huge impact. I would also like to thank the Initiative D'EXcellence for awarding me a fellowship that supported my stay in the US. I also acknowledge the support from Agence Nationale de Recherche and National Science Foundation.

I have been fortunate to work with many wonderful colleagues who helped me throughout my PhD. Thank you, Dr. Youngjin Kim, for your guidance and help at the initial stage of my PhD. I learned a lot from you, and it was enjoyable working with you. Thank you, Bharath Venkatesh, for your generosity in sharing your expertise in polymer infiltration with me and your help during my time at the Lee lab. I am also grateful to Dr. Céline Ternon for offering her expertise in synthesizing ZnO nanowires to help me with technical issues and for carefully proofread my paper. I wish to express a special thanks to Dr. Sigolène Lecuyer for her generous help and excellent guidance with antibacterial studies. On the first day working in a new field, I expected struggles that could happen. Fortunately, with your help and enthusiastic support, those things seem to mitigate. I could not thank you enough for your help with proofing my thesis manuscript and discussing the result whenever it was midnight or on the weekend. It has been beneficial for me to learn new skills, extend my vision, and even open an exciting opportunity for the next step in my career. Also, I wish to thank Prof. Franz Bruckert for his enthusiasm and stimulating discussions. You gave me two excellent books and encouraged me to study more about biology. You thought knowing about biology would open my horizons, which turns out to be very true. Thank you for always being generous with your time, and I enjoyed the drinks we had together. Moreover, I wish to express my gratitude to Prof. Robert Baptist for his kindness, support, and encouragement. He was so supportive and greatly encouraged me to pursue my PhD in Grenoble. I would also thank Dr. Pham Van Viet for his excellent guidance in my undergraduate studies, which provided excellent preparation for my PhD. Besides, I am grateful to Prof. Cao Minh Thi for his generous support in funding my undergraduate lab.

I would also like to thank Dr. Viet Huong Nguyen and Dr. Nguyen Thi Thu Thuy for their generous help at the beginning of my PhD and for spending an enjoyable time with me outside work. I wish to express my thankfulness to other colleagues for their help with technical and administrative work, including but not limited to Drs. Carmen Jiménez, Odette Chaix, David Muñoz-Rojas, Valérie Stambouli, Isabelle Gélard, Serge Quessada, Matthieu Jouvert, Laurent Marichal, Paul Machillot, Hervé Roussel, Mikhail Anikin, Antoine Maze, Valentine Bolcato, Laetitia Rapenne, Etienne Pernot, Annie Ducher, Michèle San Martin, Josiane Viboud, Virginie Charrière…

Doing a PhD allows me to interact with many people I have absolutely enjoyed the interaction with and from whom I have learned so much. My lovely friends filled a great part of my PhD, who made my journey memorable. I could not list all of you, but I believe you know that I am grateful for your time with me. I would recognize the invaluable help of Ibtihel and the joyful time to be working together with you. Thanks for making my journey unforgettable: Anh Chiêu, Khánh, Linh, Thư, Phát, Abdou, Tabassom & Danial, Shruti, Petros, Maxime, Lorenzo, Chiara, Guislain, Carlos, Adeel, Morgane, Dorina, Guillaume, Monica, Clement, Fanny, Joe, Arthur, Neha, and many more. I am proud to have been part of such a great community. Their sense of humor and sharing in research and personal life made my PhD journey more joyful.

I save this important position to express my sincerest gratitude to my family, who have given me complete trust, support, and encouragement. This milestone would not have been possible without the invaluable support of my family back in Vietnam.

Now, I am looking forward to discovering what the future holds for me!

Abstract

Liquid-repellent surfaces provide useful functionality for many coating applications. However, maintaining the stability of such liquid repellency over a long time remains an unresolved challenge. Moreover, despite remarkable progress, conventional methods for fabricating these surfaces require multiple steps and are only suitable for lab-scale fabrication. This thesis focuses on fabricating anti-fouling nanocomposite surfaces that maintain their liquid repellency under challenging conditions. Specifically, we fabricate these nanocomposite surfaces by inducing the infiltration of polymers into the interstices of surface-grown ZnO nanowires. Two capillary-based techniques are developed: 1) leaching-enabled capillary rise infiltration of uncross-linked and mobile oligomer chains from a poly(dimethylsiloxane) (PDMS) elastomer and 2) wicking of silicone oil into the space between ZnO nanowires. Our methods enable a cost-effective and large-scale fabrication of ZnO nanowires-based liquid-repellent surfaces. By changing the infiltrated species (PDMS or silicone oil), two types of liquid repellency- superhydrophobic or slippery - can be achieved. Our liquid-repellent surfaces present several useful features: self-cleaning, anti-icing, solvent and chemical resistance, high transparency, self-healing, and anti-biofouling properties. The key findings of this thesis are: 1) a straightforward and scalable approach for fabricating liquid-repellent nanocomposite surfaces that precisely retain the original morphology of ZnO nanowires; 2) retaining lubricant within the nanostructures, which is a key for producing stable slippery liquid infused surfaces. The approaches developed in this study are straightforward, efficient, and potentially scalable. The fundamental understanding from this work can enable others to design long-lasting liquid-repellent surfaces. In addition, we also describe the applicability of these ZnO nanowires-based liquid-repellent surfaces to preventing bacterial biofilm formation, in which we have found some encouraging preliminary results. Furthermore, we show the ability to grow ZnO nanowires on commercial membranes (glass fiber and stainless-steel mesh) to extend the applicability of our findings for separation applications.

Résumé

Les surfaces hydrofuges offrent des fonctionnalités utiles pour diverses applications de revêtements. Cependant, le maintien de la stabilité d'une telle répulsion des liquides sur une longue période reste un défi non résolu. De plus, malgré des progrès remarquables, les méthodes conventionnelles de fabrication de ces surfaces nécessitent plusieurs étapes et ne conviennent qu'à une fabrication à l'échelle du laboratoire. Cette thèse se concentre sur la fabrication de surfaces nanocomposites anti-fouling qui maintiennent leur stabilité dans des conditions difficiles. Plus précisément, nous avons préparés des surfaces nanocomposites via l'infiltration de polymères dans les interstices entre des nanofils de ZnO que nous avons fait croitre à la surface de nos échantillons. Deux techniques utilisant la capillarité ont été développées : 1) infiltration par remontée capillaire activée par lixiviation de chaînes d'oligomères mobiles et non réticulées à partir d'un élastomère poly(diméthylsiloxane) (PDMS) et 2) infiltration capillaire d'huile de silicone dans l'espace entre les nanofils de ZnO. Les méthodes dévelloppées au cours de cette thèse permettent d’envisager une fabrication à grande échelle et rentable de surfaces hydrofuges à base de nanofils de ZnO. Suivant les espèces infiltrées (PDMS ou huile de silicone), deux types de répulsion des liquides peuvent être obtenus : superhydrophobe ou glissant sur un liquide infusé (SLIPS). Nos surfaces hydrofuges présentent plusieurs caractéristiques utiles : autonettoyage, antigivrage, résistance aux solvants et aux produits chimiques, haute transparence, propriétés d'auto-cicatrisation et anti-biofouling. Les principaux résultats de cette thèse sont : 1) une approche simple et compatible avec une production à grande échelle pour la fabrication de surfaces nanocomposites hydrofuges qui conservent précisément la morphologie originale des nanofils de ZnO ; 2) retenir le lubrifiant dans les nanostructures glissantes ce qui est une clé pour produire des surfaces stables de ce type. Les approches développées dans cette thèse sont simples, efficaces et potentiellement utilisables à grande échelle. La compréhension fondamentale des mécanismes de non-mouillabilité mise en avant dans ce travail peut permettre à d'autres de concevoir des surfaces hydrofuges durables. En outre, nous décrivons également l'applicabilité de ces surfaces hydrofuges à base de nanofils de ZnO à la prévention de la formation de biofilms bactériens, en nous appuyant sur des résultats préliminaires encourageants. De plus, nous montrons la capacité de faire croître des nanofils de ZnO sur des membranes commerciales (fibre de verre ou mailles en acier inoxydable) pour étendre l'applicabilité de nos matériaux au domaine de la séparation de fluides.

Table of Content

List of Figures

Chapter 1. Introduction and Backgrounds

Content

1.1 General context

Repellent surfaces, which can prevent fouling by liquids, solids, and other biological species, represent an important class of advanced technologies in human society.[1-5] Two notable natural examples are self-cleaning superhydrophobic leaves and slippery surfaces on pitcher plants.

As societal demands have grown, the applications of repellent surfaces have advanced considerably from earlier benefits that were placed on protection from the natural environment. Surfaces that can control solid, liquid, or vapor accumulation hold great potential. Since the first synthesis of superhydrophobic surfaces in 1996,[6] the world has observed a remarkable deployment of repellent surfaces, which have represented a key player in tackling pressing challenges, such as environmental disasters,[7, 8] sustainable energy,[2, 9] medical safety,[10, 11] and water production and utilization.[12-14] For instance, superhydrophobic surfaces are being studied to maintain the cleanness of the photovoltaic panel surfaces from dirt,[15, 16] reducing the formation of ice on airplanes,[3] prevent bacterial biofilms on medical implant coatings (**Figure 1.1**).[17, 18] Notably, this topic won a spot in the Top Ten Emerging Technologies in Chemistry in 2021 by the International Union of Pure and Applied Chemistry (IUPAC) for its contribution to the well-being of society and the sustainability of Planet Earth.[19] Thus, with the rapid and continuous developments of scientific discoveries and technological advances, repellent surfaces promise to open new opportunities in addressing current fouling problems and beyond.

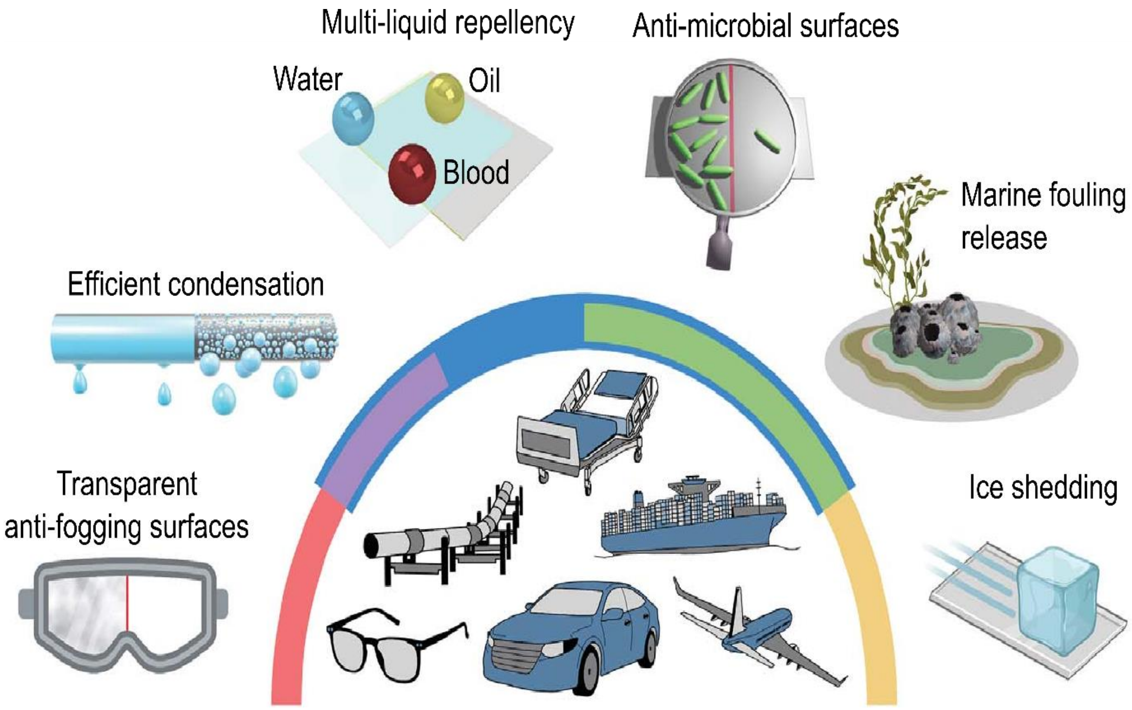

Figure 1. 1 : Diverse applications of anti-fouling surfaces that control different states of matter accumulations.

The figure is adapted from Ref [20].

There are several strategies for producing repellent surfaces. Although not universal, the main groups of repellent surfaces include air-trapped and lubricant-infused surfaces.[21] Details on the fundamental mechanisms and properties of these repellent surfaces will be provided in the next section. Realizing repellent surfaces typically requires a combination of topographical features and low surface energy chemistry. The critical factors to repellency are a trapped air layer in the case of nano/microstructured superhydrophobic or superoleophobic surfaces or an infused lubricant layer in the case of slippery lubricant-infused porous surfaces. However, the Cassie state (described below and the Wenzel state) is only metastable.[22, 23] It can easily collapse under external influences, leading to a Cassie-to-Wenzel transition on nano/microstructured superhydrophobic or superoleophobic surfaces.[24, 25] Also, the surface textures are usually fragile, and the frequent use of perfluorinated compounds to reach low surface energy causes significant concerns about health and environmental impact.[26] Meanwhile, the lubricant layer depletes over time, leading to the degradation and failure of slippery lubricant-infused porous surfaces.[27, 28] Ensuring the long-term robustness of such repellent surfaces remains challenging.

Nanocomposite coatings have promised to enhance the stability of repellent surfaces.[29, 30] However, a key drawback associated with nanocomposite films is their mechanical vulnerabilities and highly sophisticated fabrications. The development of repellent nanocomposite films from a low-cost, multifunctional nanomaterial with high mechanical robustness and potential for large-scale manufacturing holds enormous promise. Zinc oxide nanowires (ZnO NWs) are an exciting class of nanostructured materials that could promote repellency stability because of their unique morphology. However, it remains challenging to retain the original morphology of NWs during nanocomposite fabrication. To overcome the processing challenges of conventional methods, a new approach to fabricating nanocomposite films in a scalable fashion has been developed by taking advantage of the capillarity-based phenomena, uniquely representing it as a practical approach for fabricating anti-fouling nanocomposite films with ZnO NWs.[31-35]

In the following sections, we will describe the fundamental concepts of repellent surfaces, highlighting notable works throughout the development of the field. Key challenges to the stability of the repellent surfaces will be identified. Emerging solutions by creating anti-fouling nanocomposite films with ZnO NWs will also be described. The introduction section will end by stating the goals and the outline of the thesis.

1.2 Repellent surfaces

1.2.1 The development of repellent surfaces

In 1805, Thomas Young was the first to explain the behaviors of a water droplet on an assumed ideally smooth and chemically homogenous solid surface at an equilibrium state.[36] His pioneering study described the fundamental concepts of solid-liquid interactions, including wetting and non-wetting phenomena. The wetting property of a solid surface is characterized by the contact angle of a liquid droplet on the solid surface, depending on the interfacial tension between the solid-vapor, solid-liquid, and liquid-vapor interfaces at the three-phase contact line (**Figure 1.2**).[36-38]

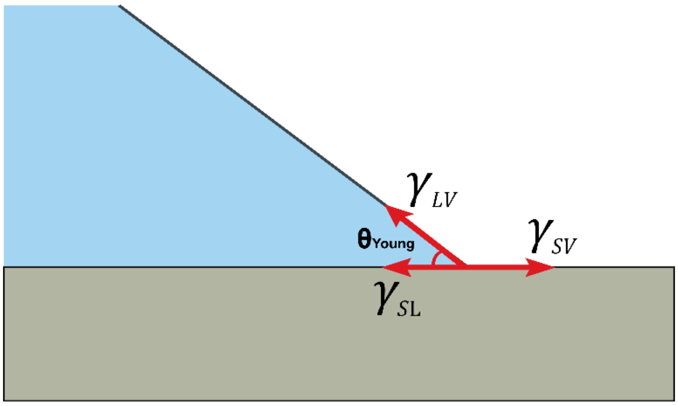

Figure 1. 2 : Schematic illustration showing Young's contact angle of a liquid droplet on an ideally smooth and chemically homogenous solid surface at the equilibrium state.

The figure is adapted from Ref [3].

The equilibrium contact angle (θ_{Young}) for a liquid droplet on a flat, chemically homogeneous, and rigid surface, is presented by Young equation (**Eqn. 1.1**) as follows:

$$cos(\theta_{Young}) = \frac{\gamma_{SV} - \gamma_{SL}}{\gamma_{LV}} \tag{1.1}$$

where γ_{SV}, γ_{SL}, and γ_{LV} are the interfacial tensions at the solid-vapor, solid-liquid, and liquid-vapor interfaces, respectively. Accordingly, a surface can be classified as superhydrophilic, hydrophilic, hydrophobic, or superhydrophobic when it has a water contact angle of ~0°, <90°, 90°–150°, or >150°, respectively.[37, 38] Likewise, a surface can be classified as superoleophilic, oleophilic, oleophobic, or superoleophobic by determining its oil contact angle.[39] As the surface tension of oils is typically lower than that of water, a surface with oil repellency will also exhibit water repellency.[37, 39] The contact angle value of a droplet on a solid surface also describes the adhesion and mobility of the liquid droplet to the solid surface.[37]

However, most solid surfaces present a certain level of roughness, which Young did not consider. The effect of surface roughness is critical in understanding the pinning of a liquid droplet on a solid surface. Wenzel and Cassie–Baxter developed models that account for the effect of surface roughness on the contact angle of the liquid on the surface. In the Wenzel state, the liquid droplet fills up the surface texture, creating a "fully wetted" interface (**Figure 1.3**a).[40] The apparent contact angle (θ*) in this state can be described through the Wenzel equation (**Eqn. 1.2**) as follows:

$$cos(\theta^*) = rcos(\theta_{Young}) \qquad (1.2)$$

where r is the roughness factor, showing the ratio of the actual surface area to the projected surface area of the solid surface.

Since the Young and Wenzel equations are derived using semi-empirical assumptions, the contact angle obtained from these two equations does not present a unique value on an actual surface. The contact angle generally varies within their receding and advancing contact angle values. The difference between the receding and advancing contact angles is called contact angle hysteresis.[41] Surface roughness can magnify the wetting properties of both hydrophilic and hydrophobic surfaces.

Unlike the assumption in Young and Wenzel's equations about a homogenous solid surface, Cassie's equation considers a chemically heterogeneous surface. In the Cassie–Baxter state, the liquid droplet does not fill in the textured repellent surface but rests on an air-solid composite interface (**Figure 1.3**b).[42] The θ*, in this case, can be described through the Cassie–Baxter equation (**Eqn. 1.3**) as follows:

$$cos(\theta^*) = -1 + \emptyset_S\left[cos(\theta_{Young}) + 1\right] \qquad (1.3)$$

where $\emptyset_S$ is the solid area fraction of the substrate interacting with the liquid droplet.

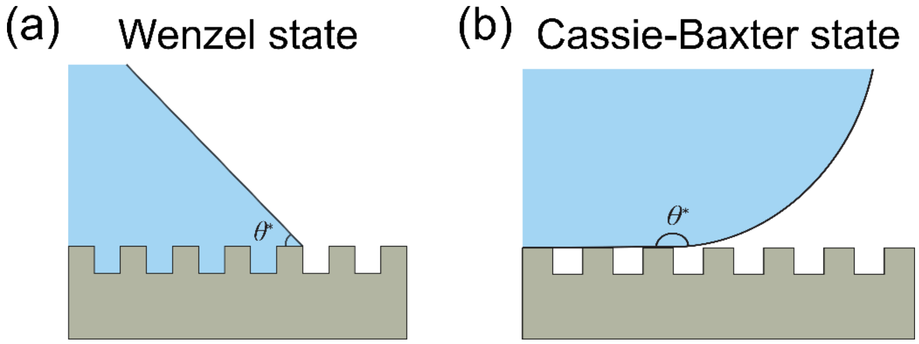

Figure 1. 3: Schematic illustration of (a) Wenzel state and (b) Cassie–Baxter state for describing the apparent contact angle of a liquid droplet on a rough surface.

The figure is adapted from Ref [3].

These concepts primarily established the essential requirements for creating repellent surfaces. Another critical factor in the development of repellent surfaces is the discovery of hydrophobic polymers. Polydimethylsiloxane (PDMS) and polytetrafluoroethylene (PTFE or Teflon) are two notable polymers in developing repellent surfaces.[3] PTFE and PDMS were synthesized in 1938 and 1940, respectively.[43] Many superhydrophobic surfaces have been fabricated, taking advantage of the low surface tension of these hydrophobic polymers. Also, the innovations of electron microscopies have unveiled the structure of naturally repellent surfaces, consequently uncovering the underlying mechanisms of those naturally repellent surfaces. One of the most important findings was the study of Barthlott and Neinhuis in 1997, explaining the superhydrophobicity mechanism of lotus leaves by observing their microstructure via a scanning electron microscope.[44]

In 2007, a new type of repellent surface was introduced to improve the stability of superhydrophobic surfaces and address the high demand for resisting low surface tension liquids, known as superomniphobic surfaces.[45] Typically, surfaces with contact angles >90° or >150° with liquid droplets of oils, solvents, alcohols, acids, and bases, are categorized as omniphobic or superomniphobic, respectively.[46] One of the most important structures of this type of repellent surface is the re-entrant or double re-entrant structure because of its highly stable superoleophobicity.[45, 47, 48] Despite the remarkable enhancement of stability demonstrated by these re-entrant or double re-entrant structures, the spaces between the surface features are potentially susceptible to failure under harsh conditions. To address this problem, a new class of repellent surface, slippery liquid-infused porous surfaces (SLIPS), was introduced in 2011.[49] SLIPS comprises a porous scaffold and a lubricant layer stabilized within and above the surface of the porous scaffold. The remarkable liquid repellency of SLIPS originates from the lubricant layer above the porous scaffold. This infused lubricant with low surface energy fills the air pockets in the space of the porous scaffold, providing a mobile liquid surface with no contact line pinning and excellent pressure stability. In summary, a timeline of the developments of repellent surfaces is shown in **Figure 1.4**. The following sections will thoroughly describe further details on these repellent surfaces.

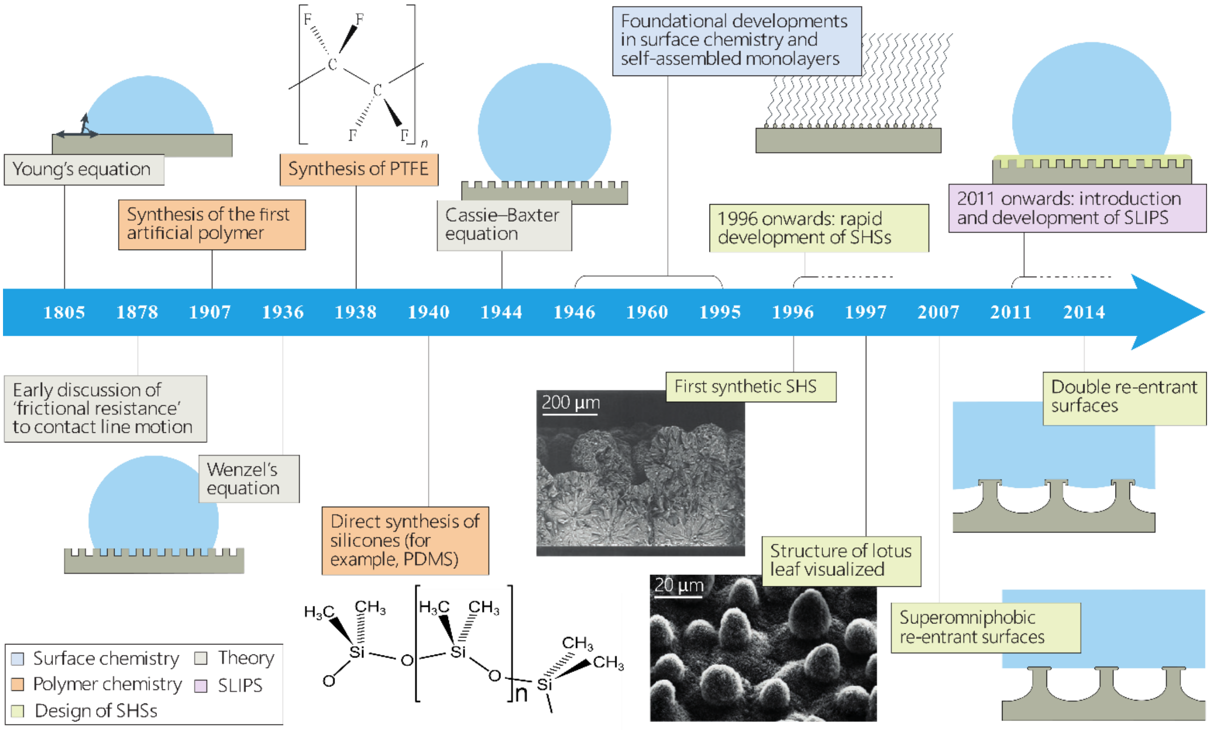

Figure 1. 4: Timeline of significant developments of repellency surfaces. The timeline highlights notable advances, including theoretical concepts, the discovery of hydrophobic polymers, and the development of superhydrophobic surfaces (SHSs), superomniphobic surfaces, and slippery liquid-infused porous surfaces (SLIPS).

The figure is adapted from Ref [3].

1.2.2 State-of-the-art repellent surfaces

Proposed strategies for fabricating repellent surfaces can be divided into three main approaches (**Figure 1.5**). The first approach involves the fabrication of hydrophobic micro- or nanostructures to trap an air layer, minimizing the contact area between the liquid and the solid surface, including superhydrophobic and superomniphobic surfaces (**Figure 1.5**a).[50, 51] In the second approach, a liquid-like monolayer is covalently attached to the solid surface to form a surface known as slippery omniphobic covalently attached liquid (**Figure 1.5**b).[52-54] The third approach involves lubricating porous structures with a suitable lubricant to produce a mobile and slippery surface (**Figure 1.5**c).[3, 49, 55] An illustration based on the contact angle hysteresis versus the apparent contact angle of the three state-of-the-art liquid-repellent surfaces is shown in **Figure 1.5**d. This section will provide additional details regarding the design and application of each type of the three state-of-the-art repellent surfaces.

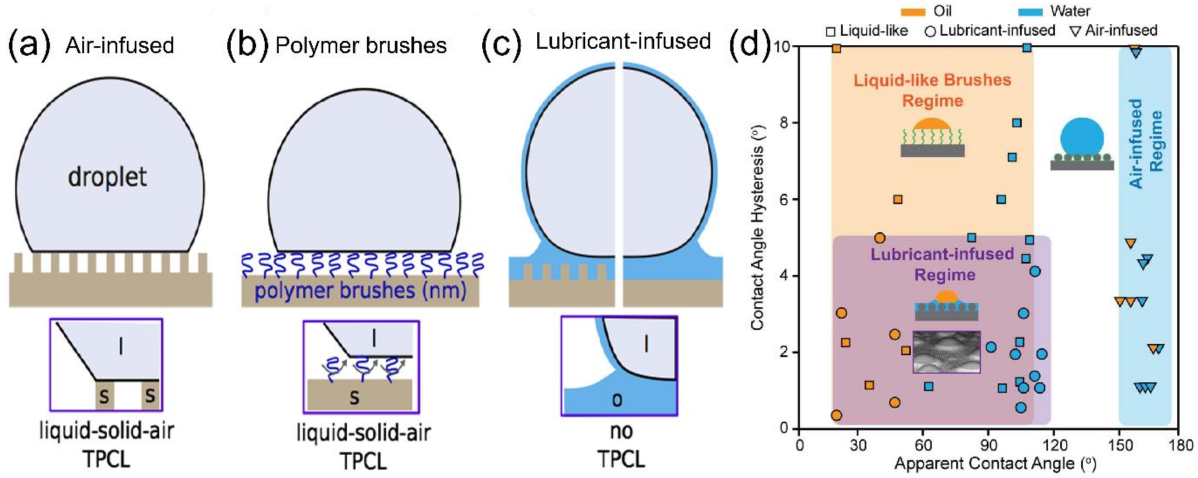

Figure 1. 5: Schematic illustration of three main approaches in designing repellent surfaces. (a) Air-infused structures. (b) Surfaces grafted with polymer brushes. (c) Lubricant-infused porous surfaces. (d) The contact angle hysteresis versus the apparent contact angle for three different state-of-the-art liquid-repellent surfaces.

The figure is adapted from Refs [20, 21].

1.2.2.1 Superhydrophobic and Superoleophobic Surfaces

A surface is classified as superhydrophobic if it presents a water contact angle >150°.[38] Designing superhydrophobic surfaces depend on two key components, including the roughness and chemistry of the surface.[6, 56-58] Interestingly, these fundamental understandings were only known after discovering the self-cleaning mechanism of lotus leaves (**Figure 1.6**a).[44, 59] Lotus leaves leverage the self-cleaning properties to remove dust on their surface when exposed to water (**Figure 1.6**b,c). This property comes from a hierarchical structure with micro and nanoscale features (**Figure 1.6**d). The leaf comprises a convex cell papilla at the microscale (**Figure 1.6**e), while epicuticular wax crystals are observed at the nanoscale (**Figure 1.6**f). Later, researchers explored many other living creatures to learn and mimic their superhydrophobicity. We refer readers to some dedicated reviews for a detailed description of these naturally repellent surfaces.[59-69]

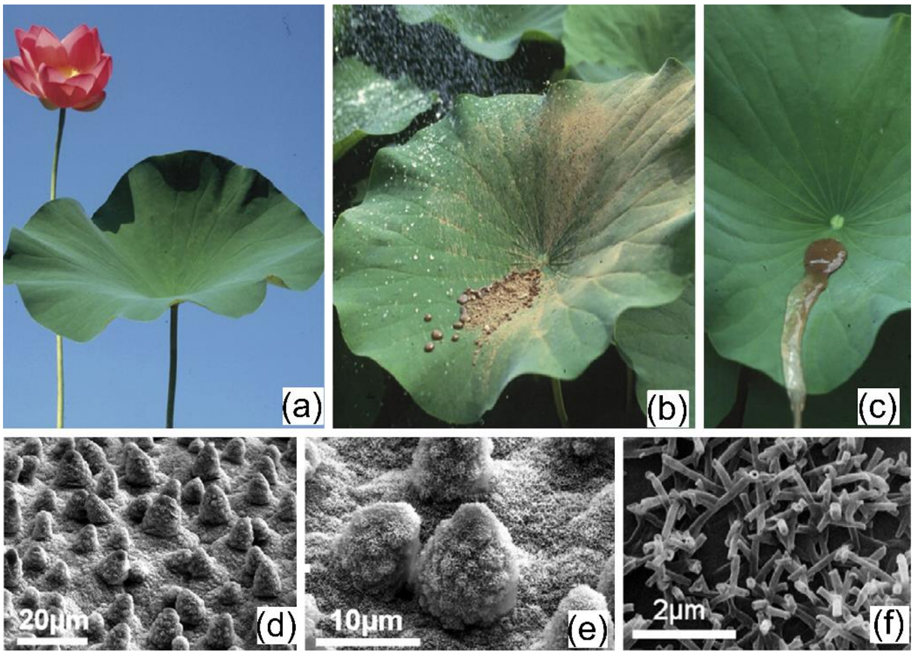

Figure 1. 6: Images of superhydrophobic lotus leaves with self-cleaning properties at different magnifications.

The figure is adapted from Ref [44].

In 2011, to address the need for repelling low surface tension liquids, a new and scalable approach was introduced for fabricating robust repellent surfaces by taking advantage of the self-assembly of micro and nano SiO_2 beads (**Figure 1.7**).[70] In this approach, candle soot templated SiO_2 nano-shells were deposited on a glass substrate (**Figure 1.7**a,b). After fluorination, the as-obtained coating demonstrated an outstanding repellency against both water and organic solvents (**Figure 1.7**c). Having such a chain-like structure, the coating can potentially retain its repellency if the structure is presented. This approach has been extended to fabricating several hierarchical structures of other materials, such as TiO_2 and PTFE beads.[7, 71, 72] Even though the strength of this type of repellent surface is greater than silicon-based superhydrophobic surfaces, these surfaces remain vulnerable to extreme working environments, such as strong mechanical abrasion, high hydrostatic pressure, and marine biofouling.[73-75]

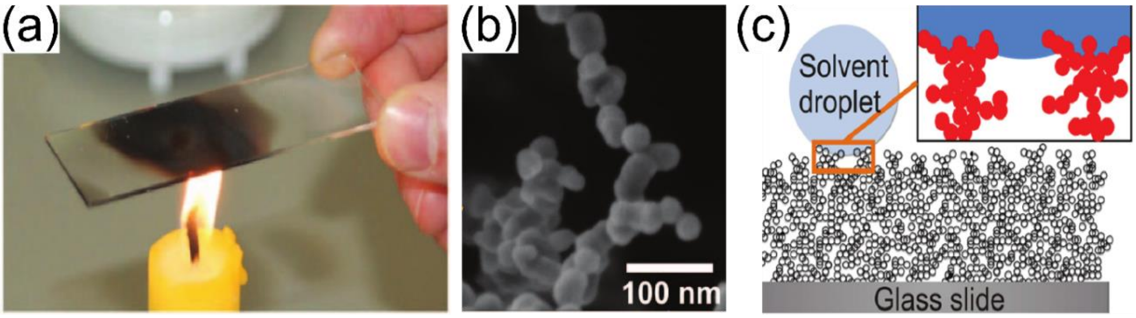

Figure 1. 7: (a) Photograph describing the candle soot coating preparation. (b) High-resolution scanning electron microscope (SEM) image of the soot deposit with a single particle chain made up of almost spherical carbon beads. (c) Schematic illustration of a liquid droplet rested on the super repellent coating.

The figure is adapted from Ref [70].

Superhydrophobic surfaces have exhibited tremendous benefits in many applications, including self-cleaning,[64, 76] anti-icing,[77-79] anti-bacterial,[80-82] drag reduction,[83-85] enhanced heat transfer,[86-88] water harvesting surfaces,[89-91] and many more. These valuable properties come from the thin air layer trapped by the micro-/nano structures. Furthermore, superhydrophobic surfaces have been commercialized, such as NeverWet®. Some notable achievements of these repellent surfaces are highlighted in **Figure 1.8**. Several boiling and condensing-based applications suffer substantial energy loss during liquid-vapor phase change processes. When the heat flux grows to reach the critical heat flux, the rate of droplets nucleation also raises and causes droplets to coalesce, consequently forming a continuous liquid film on the surface of the device, particularly on surfaces with high surface tensions (**Figure 1.8**a).[86] The formation of such a liquid film is not desired because of its high resistance to heat transfer.[86] In contrast, if the surface is covered with a low-energy non-wetting material, the vapor forms discrete liquid droplets, known as dropwise condensation (**Figure 1.8**b).[92, 93] The progressive removal of these condensing droplets by gravity facilitates refreshing the surface for re-nucleation. Dropwise condensation has been shown to enhance 5–7 times heat transfer performance compared to the filmwise mode.[94-96]

Another critical application is water/oil separation (**Figure 1.8**c-f). Oil-water mixtures can come from several sources, such as petroleum mining, textile, and leather processing. Because of the complexity, cost, and energy needs associated with conventional separation approaches, membrane-based approaches for oil-water separation have shown great potential for addressing the oil pollution problem.[97-100] Membranes with engineered surface wettability, such as hydrophobic-oleophilic membranes, can let lower surface tension oils go through while blocking water (**Figure 1.8**c).[45] However, this type of membrane is unsuitable for the gravity-driven oil-water separation process because the water phase typically contacts the membrane surface first due to its higher density. Also, hydrophobic membranes are prone to fouling by the oil phase or surfactants.[101-103] Membranes that are simultaneously hydrophilic and oleophobic can overcome these limitations (**Figure 1.8**d,e).[97, 104-107] The developed membranes separated a wide range of oil-water mixtures with >99.9% separation efficiency.[97] The hygro-responsive membranes could be coupled with hydrophobic and oleophilic membranes to accelerate continuous oil-water emulsion separation (**Figure 1.8**f). Given the currently pressing state of the environment, this research direction holds great potential.

Notably, advancing from the conventional surfaces, by coupling with the state-of-the-art 3D printing techniques, a wide range of 3D bulk superhydrophobic objects have been created (**Figure 1.8**g).[108] Such advances may further expand the application of superhydrophobic surfaces to new fields, such as cell arrays/aggregations construction and blood-repellent medical devices. Despite the huge potential of the superhydrophobic and superoleophobic surfaces, stability, production cost, and scalability remain significant challenges.

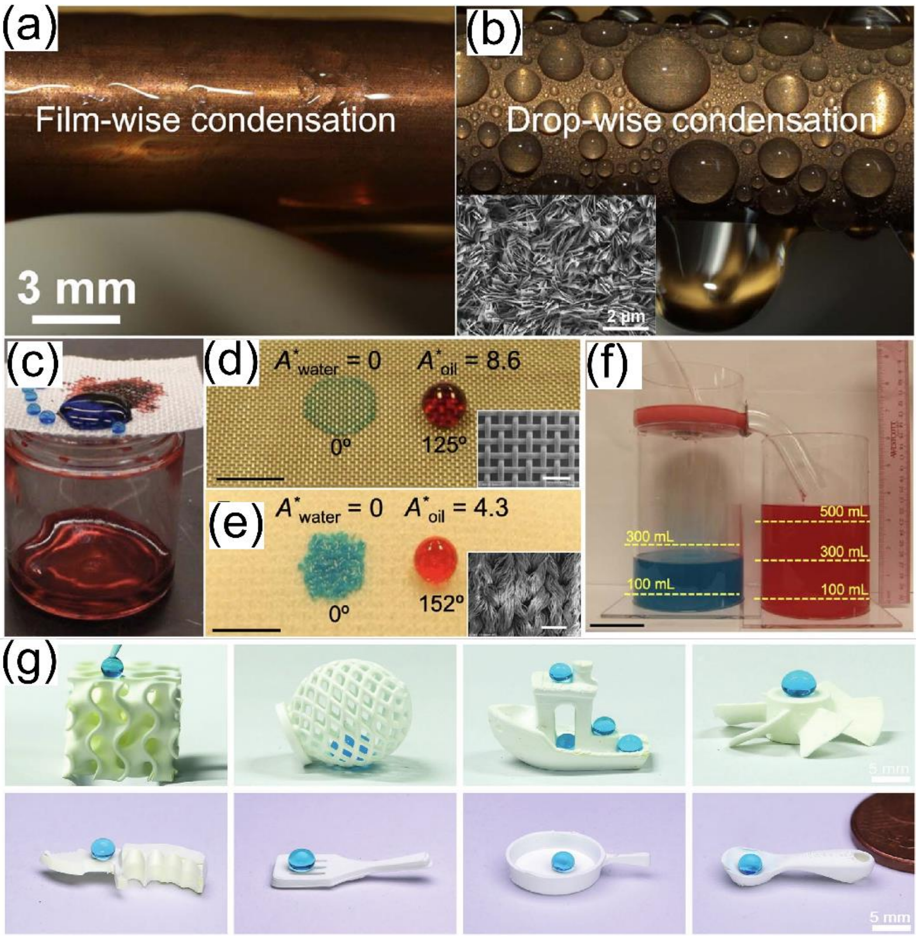

Figure 1. 8: Applications of superhydrophobic and superoleophobic surfaces. a) Filmwise condensation on a hydrophilic Cu tube. (b) Dropwise condensation on a superhydrophobic Cu tube. The inset displays a superhydrophobic CuO nanostructured surface that improves dropwise condensation. (c) A steel mesh coated with fibers containing fluorodecyl POSS used for oil-water separation. Octane droplets (red) go through the membrane, while water droplets (blue) bead up on the surface. (d and e) Droplets of water (dyed blue) and oil (dyed red) on stainless-steel mesh (top) and polyester fabric (bottom). (f) A photograph showing the continuous separation of a water-in-hexadecane emulsion using a wettability-engineered membrane. (g) 3D superhydrophobic objects printed, showing the design flexibility.

The figure is adapted from Refs [45, 97, 108, 109].

1.2.2.2 Liquid-like repellent surfaces

Smooth surfaces are fundamentally disadvantage of liquid repellency because of a maximum contact angle of ca. 130°, a high contact angle hysteresis, and liquid pinning. [110, 111] Interestingly, an innovative method has been proposed for improving repellency on smooth surfaces by grafting long and flexible polymer chains to the smooth surface.[112, 113] Such an approach is commonly called a "liquid-like" surface, indicating a polymer chain attached to a surface and presenting liquid characteristics.[52, 114-116] A typical grafting process to a surface is shown in **Figure 1.9**a. The polymer chains in polymer brushes arrange themselves in a soft polymeric layer. The high mobility of the PDMS chains on the obtained surface enables an excellent repellency to water, olive oil, and hexadecane (**Figure 1.9**b).[117] Surface grafting with PDMS has shown promise, particularly in liquid repellency and anti-icing.[52, 113, 117] In addition, such an approach can be coupled with photocatalytic materials to achieve repellency and photocatalytic activities simultaneously.[118] Thus, this surface type could be promising for anti-fouling applications such as anti-icing and marine fouling. However, there are several drawbacks to how readily grafting chemistry can be employed to all the existing substrates, the behavior of the liquid-like layer, and further details on stability remain to be studied.

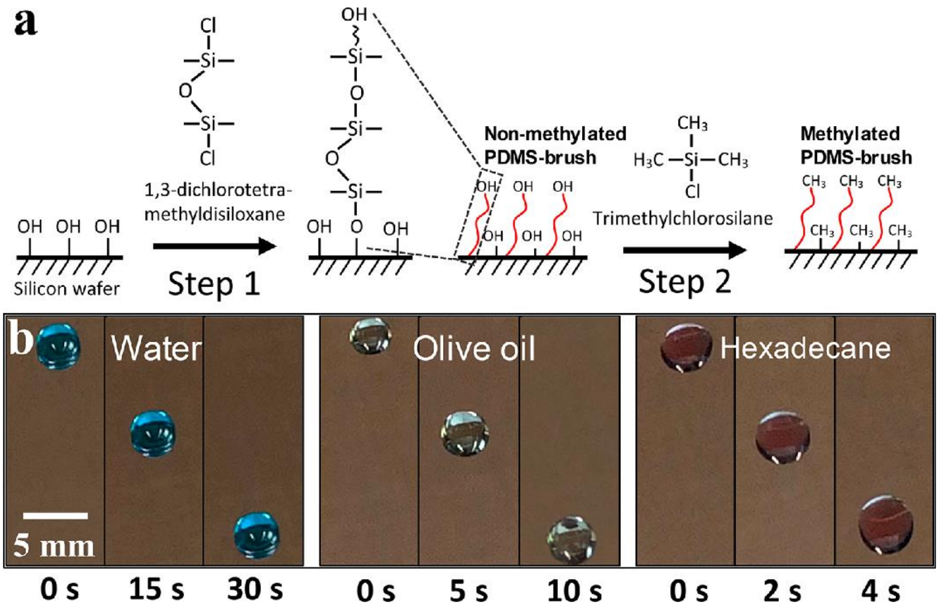

Figure 1. 9: (a) Schematics of the PDMS brush grafting to silicon substrates via hydrolysis and polycondensation. (b) Photographs showing the sliding of 15 µL droplets of water, olive oil, and hexadecane on the obtained PDMS brush substrates, tilted angle of 3°.

The figure is adapted from Ref [117].

1.2.2.3 Slippery Liquid-infused Porous Surfaces

To overcome the poor pressure stability on air-infused surfaces, a new repellent surface was created by altering the air cushion with a lubricant layer, slippery liquid-infused porous surfaces (SLIPS).[49] This lubricant layer plays a primary role in inhibiting the attachment of foreign immiscible liquids, which has shown incredible effectiveness in preventing surface fouling.[18, 21, 49]

The two critical components for creating SLIPS include a porous solid underlying scaffold and an infiltrating lubricant combined to produce a mobile and repellent liquid overlayer.[49] The solid scaffold can be smooth or rough, but requisitely matches the chemistry of the infiltrating lubricant.[3] The lubricant is blocked within the solid scaffold by van der Waals and capillary forces.[49] Typically, SLIPS designs are governed by thermodynamic criteria.[49, 119] The interfacial energy at different wetting states is shown in **Figure 1.10**. The solid must be wetted by the infiltrating lubricant (Liquid B) rather than the foreign liquid (Liquid A). This criterion ensures that Liquid A remains on top of Liquid B. In **Figure 1.10**, liquid A on the substrate (E_A), liquid B on the substrate (E_2), and liquid B on the substrate with liquid A (E_1). When E_A is greater than E_1 and E_2, the substrate is more favorable to be wetted by liquid B.[49] Later, spreading parameter and disjoining pressure were added to ensure the design criteria of SLIPS further.[119, 120]

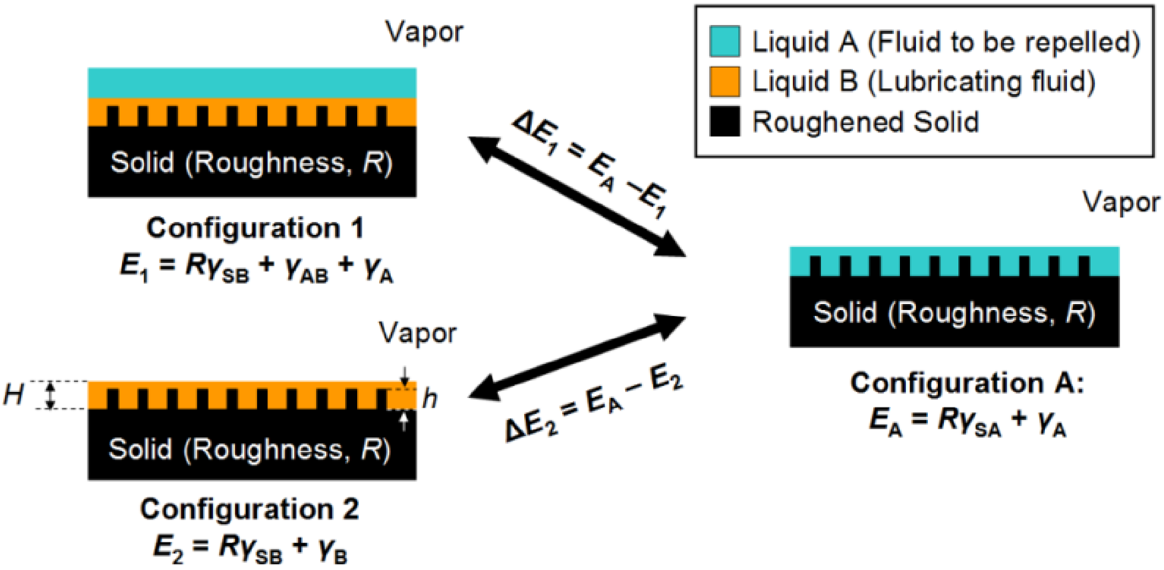

Figure 1. 10: Schematic drawings illustrating the interfacial energy at different wetting statuses. The figure is adapted from Ref [49].

The first SLIPS was fabricated by drop-casting of perfluorinated lubricants to the surface of Teflon nanofibrous membranes to create SLIPS (**Figure 1.11**a).[49] Since then, several approaches have been adopted for infiltrating lubricants. The infiltration of lubricants can be performed using typical methods such as immersion, spin coating, spray coating, or dip coating (**Figure 1.11**b).[120] However, these approaches likely present challenges in precisely controlling the thickness of the infiltrating lubricant. With the tremendous expansion in fabrication techniques, several types of SLIPS have been fabricated (**Figure 1.12**). Based on the structure of the solid scaffold, there are three classes of SLIPS: 1- dimensional, 2- dimensional, and 3- dimensional.[3]

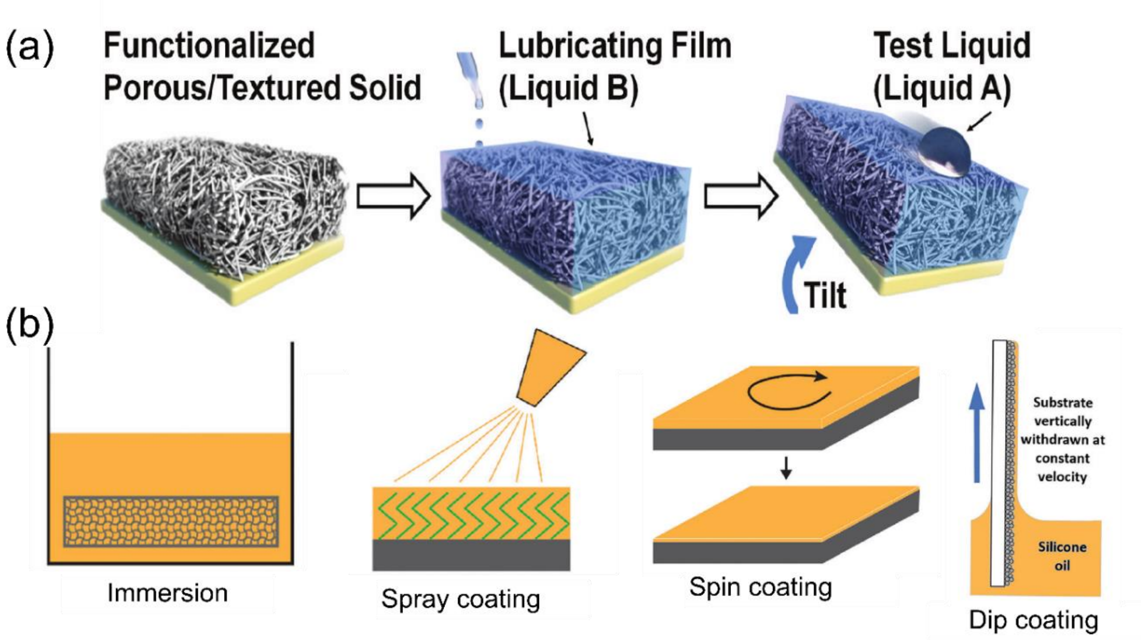

Figure 1. 11: (a) The first fabrication of SLIPS by drop-casting. (b) Common methods for making SLIPS.

The figure is adapted from Refs [49, 120].

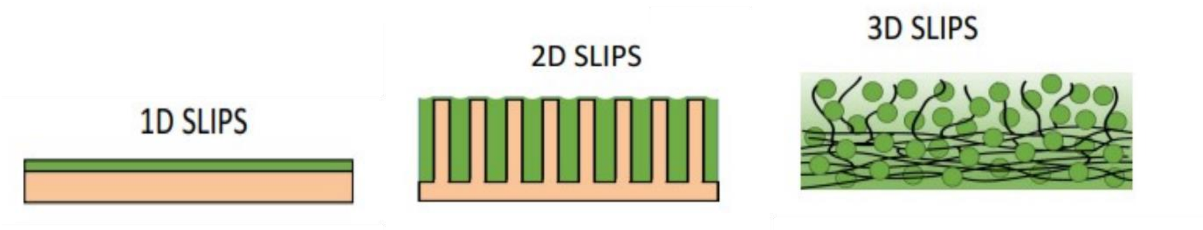

Figure 1. 12: Diversity in SLIPS structures.

The figure is adapted from Ref [3].

SLIPS offer useful functions for various key applications, including self-cleaning,[121, 122] anti-icing,[123-125] anti-fouling,[55, 126-130] corrosion-resistant,[131, 132] food packaging,[133, 134] wave guiding,[135] separations,[136] heat transfer enhancing,[137-140] drag-reducing,[141-143] and water harvesting coatings.[13, 144-147] Some notable applications of SLIPS are shown in **Figure 1.13**. One of the transformative properties of SLIPS is the anti-icing ability. SLIPS have demonstrated a remarkable reduction in ice adhesion strength, from ~100 kPa (superhydrophobic surfaces) to ~10 kPa (liquid-infused gel),[148] even down to 2 Pa (magnetic fluids) (**Figure 1.13**a).[149] In addition, SLIPS have demonstrated superior anti-bacterial properties, interestingly surpassing superhydrophobic surfaces over extended exposure to bacteria (**Figure 1.13**b).[55] SLIPS also significantly repels repelling mussel adhesion (**Figure 1.13**c).[126] Furthermore, SLIPS have been demonstrated to repel various biological fluids, leading to many biomedical applications (**Figure 1.13**d), such as tubing and catheters,[18] endoscopies,[150] dental care.[151] Recently, SLIPS have also shown their potential as a detection platform for surface-enhanced Raman scattering as droplets would shrink and eventually evaporate into a tiny dot without contact line pinning. This behavior markedly increases the concentration of the targeting chemicals, consequently identified through the surface-enhanced Raman scattering (**Figure 1.13**e).[152]

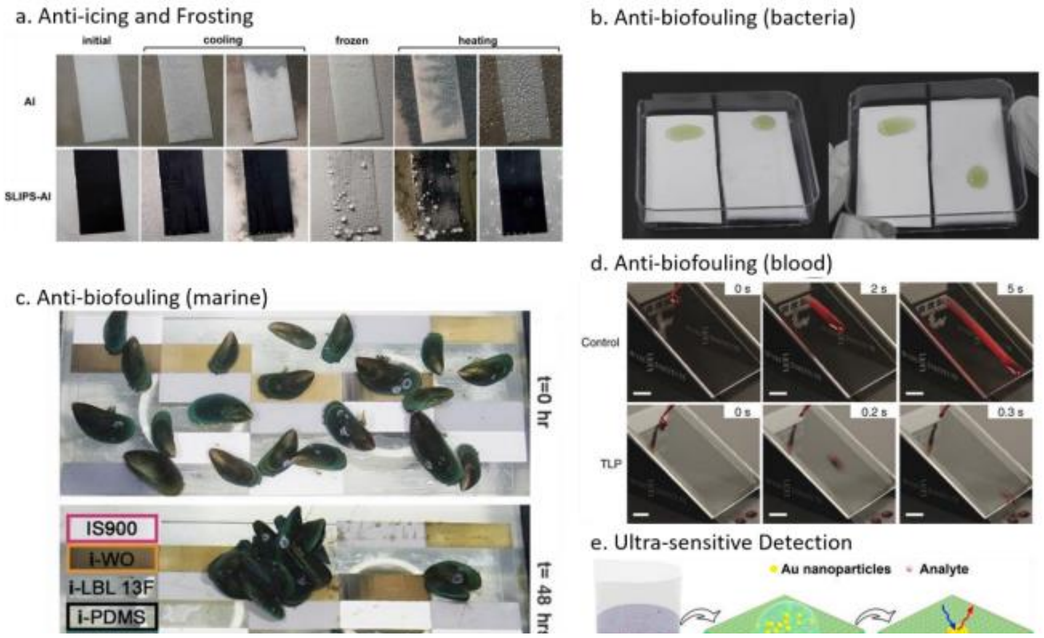

Figure 1. 13: Notable applications of SLIPS. (a) Anti-icing properties. (b) Anti-bacterial properties. (c) Anti-marine fouling. (d) Anti-blood fouling. (e) Detection platform for surface-enhanced Raman scattering.

The figure is adapted from Refs [11, 55, 123, 126, 152].

1.2.3 Challenges of the state-of-the-art repellent surfaces

This section discusses the pressing challenges of the current repellent surfaces, including the Cassie-to-Wenzel wetting transition on air-infused surfaces and the lubricant depletion on SLIPS.

1.2.3.1 Metastable state of the Cassie state

Section **1.2.2.1** described several applications of superhydrophobic surfaces. These applications come from an air pocket trapped by the micro- or nanostructured surfaces. This air layer induces the Cassie state, minimizing the contact area between the surface and the water droplet (**Figure 1.14**a).[24, 42, 153] However, superhydrophobicity based on the Cassie state is fragile and can be damaged easily under harsh conditions, such as high pressures, droplet impact, surface vibration, and prolonged immersion time.[154-156] The Cassie state is metastable, transiting to a more stable Wenzel state after receiving sufficiently external energy, such as vibration, evaporation, impact, and electric field (**Figure 1.14**b).[157-159] Theoretically, the droplet in the Cassie state presents higher surface energy than in the Wenzel state.[160] Consequently, a transition from the Cassie state to the Wenzel state is typically observed. In contrast, the opposite transition takes place only under scarce situations since it is an experimentally irreversible process because of considerable energetic barriers to the reverse transition, although it is possible in a simulation study.[24] The Cassie-Wenzel wetting transition indicates the failure of surface repellency. Typically, this wetting transition or superhydrophobicity failure can be observed via the disappearance of the plastron phenomenon on the surface when immersed underwater. This wetting transition remains the biggest challenge for repellent surfaces that use air pockets as the protective layer.

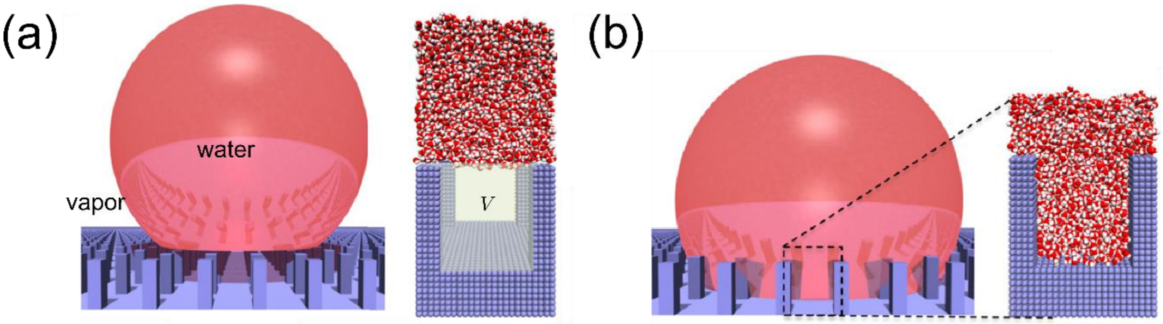

Figure 1. 14: (a) A water droplet on a superhydrophobic surface in the Cassie state. (b) After the Cassie state transited into the Wenzel state.

This figure is adapted from Ref [24].

To enhance the stability of the air-cushion layer, a new type of structure has been developed, which is called re-entrant structures. The re-entrant structures have demonstrated the most effective design for creating robust superhydrophobic surfaces among numerous explored surface structures.[45, 46, 161, 162] With such a re-entrant structure, liquid fronts are locally trapped to generate upward-supporting capillary force, amplifying the breakthrough pressure and maintaining a Cassie state (**Figure 1.15**).[20, 161, 162] Such re-entrant structures mimic the surface structure of springtails (**Figure 1.15**a-c). Also, the robustness of the re-entrant structure can be significantly improved using the doubly re-entrant[48, 163, 164] and triply re-entrant structures,[165] which present the repellency against very low surface tension liquids (**Figure 1.15**d-f). Notably, surface chemistry modification is unnecessary for the double re-entrant and triply re-entrant structures to achieve superoleophobicity. Recently, advancing from these re-entrant structures, a state-of-the-art springtail cuticle-inspired surface has been developed, having multilayered, doubly re-entrant posts with increasing diameter from top to bottom (**Figure 1.15**g).[166] Such a new type of structure possesses both a high contact angle and a superior breakthrough pressure gradient. However, springtail-inspired repellent surfaces are fabricated through the silicon etching method, which is costly and challenging for scalable manufacturing.

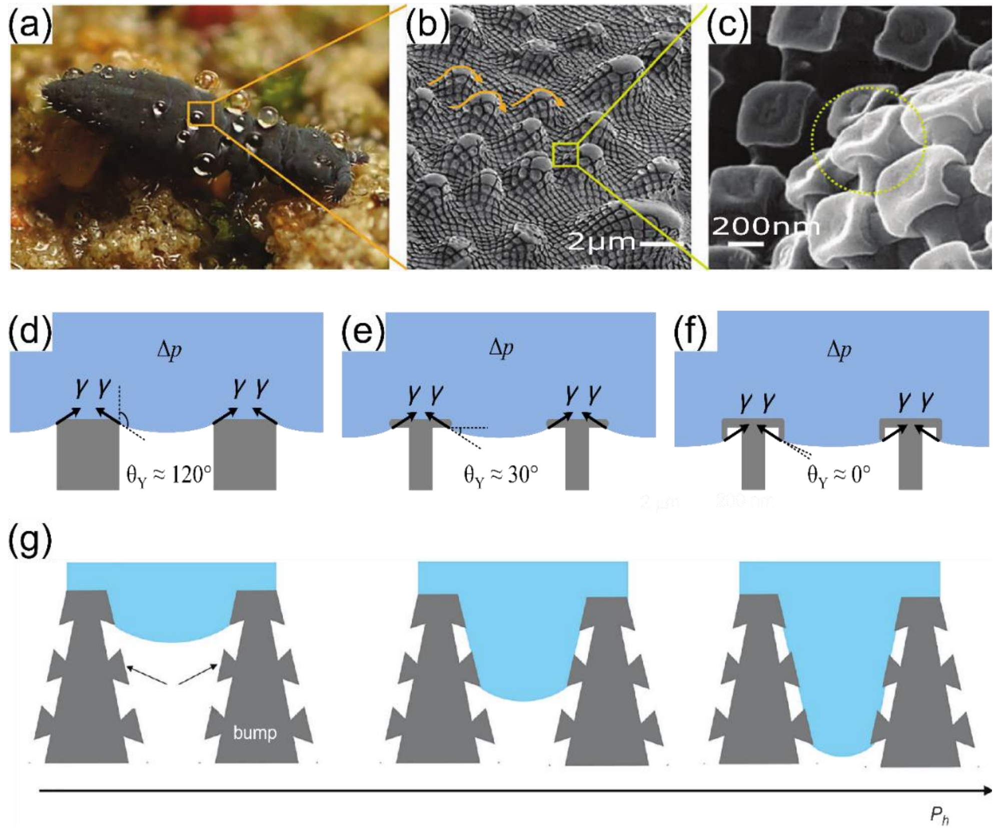

Figure 1. 15: (a) Photograph of a springtail showing liquid repellency and resistance to high-pressure raindrops. SEM images show a springtail cuticle's hierarchical primary (b) and secondary granules (c). Liquid suspension on surface structures of three different topologies. (d) Simple structures require θ_{Young} *> 90° to stop the water. (e) Re-entrant structures allow* θ_{Young} *< 90° to stop oil or solvents. They would fail if* θ_{Young} *~ 0°. (f) Doubly re-entrant structures allow* θ_{Young} *~ 0° to stop any liquids, (g) Schematics of the wetting dynamics through the overhang-decorated tapered bumps.*

This figure is adapted from Refs [48, 166, 167].

1.2.3.2 Lubricant depletion

Different from air-infused surfaces, the remarkable liquid repellency of SLIPS originates from the lubricant layer above the porous scaffold.[21, 168] The infused lubricant with low surface energy fills the voids of the porous scaffold, providing a mobile surface with no contact line pinning and excellent pressure stability.[49] Also, the surface properties of the lubricant layer are highly tunable because of the vast choice of lubricants that are available with a wide range of properties (viscosity, solubility, and surface tension).[169] However, the lubricant layer depletes over time, leading to the degradation and failure of SLIPS. For example, the ability to induce dropwise condensation of low surface tension fluids makes SLIPS a unique solution for enhancing the heat transfer efficiency in various industrial processes, such as refineries, biomass combustion, and natural gas manufacture;[170, 171] the depletion of lubricant from such a SLIPS surface, however, decreases heat transfer by 80%, severely impeding the condensation of toluene.[172] Another notable property of SLIPS is their excellent anti-fouling ability that originates from the fluid-like feature of the lubricant layer, effectively inhibiting the adhesion of biological species (e.g., individual bacteria, bacterial biofilm, and mussel).[55, 126, 127] Such an anti-fouling property, however, can be lost due to lubricant depletion under various conditions. For example, silicone oil-infused porous polydimethylsiloxane substrates with a lubricant thickness of ~26 μm have been shown to experience complete lubricant loss under flow in 7 days (shear stress of 0.007 Pa), increasing the contact angle hysteresis substantially and degrading the repellency of these SLIPS.[173] Furthermore, the lubricant from the wetting ridge has been shown to contaminate and alter the surface tension of the contacting water droplets,[174, 175] potentially contaminating collected water in fog harvesting applications.

Lubricant can deplete through several mechanisms. Mechanisms that cause lubricant depletion include evaporation of lubricant,[176, 177] physical force (shear force/frost/gravity)-induced lubricant loss,[124, 178-181] and moving liquid droplet-induced loss.[27, 28, 172, 182, 183] Several lubricant depletion paths can be prevented by changing the structure and composition of SLIPS. For example, the problem of lubricant evaporation can be overcome by using non-volatile liquids as lubricants.[184, 185] Perfluorinated lubricants and colloidal nanoparticles, for example, have been shown to form self-suspended nanoparticle fluids that could significantly reduce evaporative lubricant loss at 50 °C for three months.[186] The frost-induced lubricant depletion has been suppressed by making the pore of the infused surface smaller than the pore size of frost dendrites, thereby offering a much stronger capillary force for retaining the lubricant during frosting and icing processes.[124]

Lubricant depletion resulting from the movement of liquid droplets on the infused surface remains a significant problem in maintaining the liquid repellency of SLIPS. The physical origin of this lubricant depletion path comes from the formation of a wetting ridge or a cloaking layer surrounding the moving liquid droplet.[27] The formation of the wetting ridge directly contributes to lubricant depletion. Lubricant taken along with moving droplets leads to progressive loss of lubricant from the infused surface, and an additional shear flow could rapidly accelerate the lubricant depletion.[187] The formation of a wetting ridge on SLIPS is arguably unavoidable and limits the long-term durability and applicability of this type of repellent surface.

Despite the enormous progress in the development and application of SLIPS since the first report at the beginning of the 2010s, lubricant depletion over time has been largely overlooked. Most of the existing literature on SLIPS describes its fabrication methods and applications.[3, 18, 20, 188-193] Only a very small number of studies have reported on the suppression of wetting ridges despite its critical role in lubricant depletion.[120, 168, 169] The main focus of these reports, however, is the choice of porous scaffold and lubricant types or strategies to replenish lubricant upon depletion. Thus, understanding the physics of lubricant depletion through the formation of a wetting ridge is essential to developing strategies to overcome the current limitations of SLIPS. Suppression of wetting ridge formation holds great potential for producing stable SLIPS. Here, we describe the fundamental physics and phenomena behind the formation of wetting ridges and highlight the recent findings on the suppression of wetting ridge-induced lubricant depletion in SLIPS. Such understanding will aid in the design of stable SLIPS that can be used in a wide array of applications.

The principle of wetting ridge formation

The formation of wetting ridges was initially recognized in the wetting phenomena on soft solids, long before the invention of SLIPS.[194, 195] It has been shown that when a wetting droplet meets a soft surface such as gels, creams, foams, and polymers, there is a local deformation of the soft surface, leading to the formation of wetting ridges, as shown in **Figure 1.16**.[195-200] Interfacial forces primarily govern the formation of wetting ridges among the involved phases. Accordingly, a droplet placed on a lubricant-infused surface forms a complex 4-phase system that comprises the porous surface, the lubricant layer, the liquid droplet, and the surrounding vapor. A wetting ridge is a meniscus of lubricant drawn up around the liquid droplet through capillarity.[27, 201] Each interface has an associated characteristic interfacial tension, originating from the difference between the cohesive forces of molecules from two different phases.[27, 37, 168] The wetting ridge forms a region with negative Laplace pressure because of its negative curvature, which draws more lubricant into it until the pressure in the lubricant layer is identical to the pressure within the wetting ridge.[27, 202, 203]

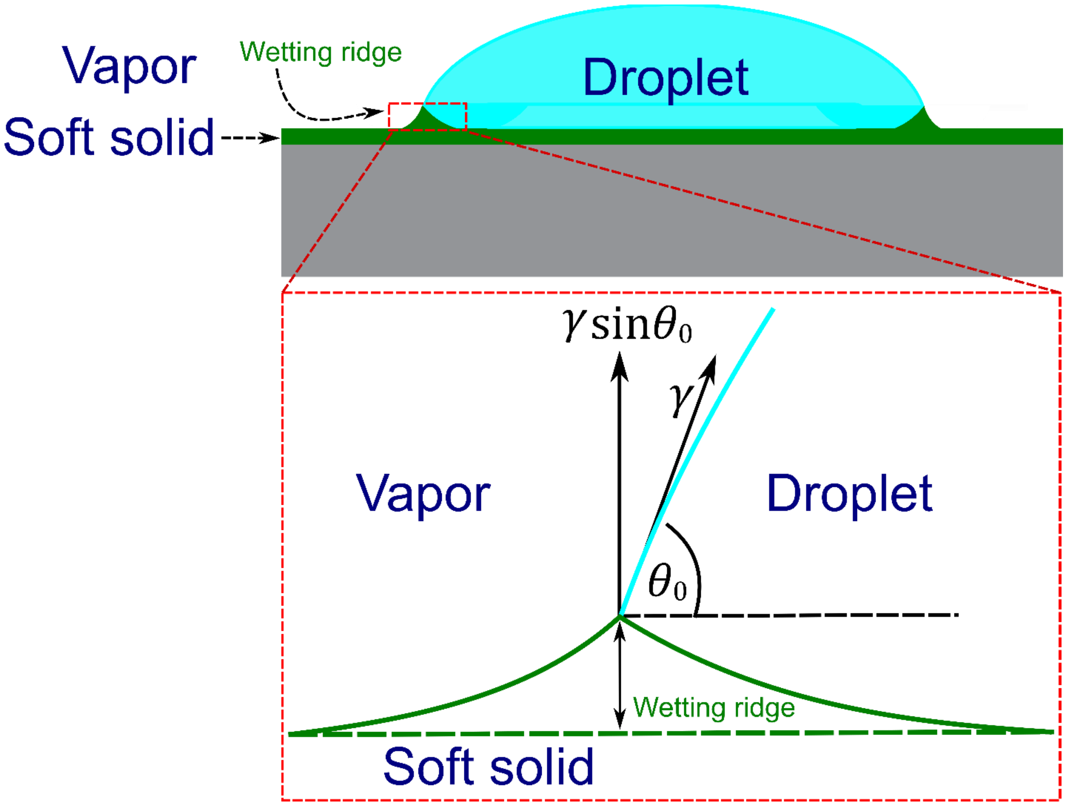

Figure 1. 16: Schematic illustration of a liquid droplet sitting on a soft solid surface, leading to the formation of wetting ridges. The Zoom-in part shows the wetting ridge at the triple line. The green line represents the growth of a wetting ridge caused by the deformation of the vertical component from the soft solid surface.

The static equilibrium shape of a wetting ridge

A wetting ridge can exist in two configurations depending on the spreading coefficient (S) of the lubricant on the surface of the droplet. The spreading coefficient can be calculated using **Eq. (1.3)**:[119]

$$S_{LD} = \gamma_{DV} - \gamma_{DL} - \gamma_{LV} \tag{1.3}$$

where γ is the interfacial tension between the two phases, and the subscripts D, V, and L stand for droplet, vapor, and lubricant, respectively.

When $S_{LD} < 0$, the wetting ridge presents a meniscus surrounding the droplet, as shown in **Figure 1.17**a. In contrast, the wetting ridge can cloak the droplet as a wrapping layer when $S_{LD} > 0$, as shown in **Figure 1.17**b.[119, 120, 169] These proposed situations capture the formation of the wetting ridge under the assumption that the wetting ridge forms on a smooth, homogenous lubricant layer and neglects the critical role of the porous surface in the formation of the wetting ridge. Indeed, the porous surfaces with different pore sizes have been shown to affect the height of the wetting ridge by confining lubricant within their pore structures through capillarity. Thus, a more comprehensive theoretical understanding of wetting ridge on SLIPS with the introduction of the porous surface will be needed.

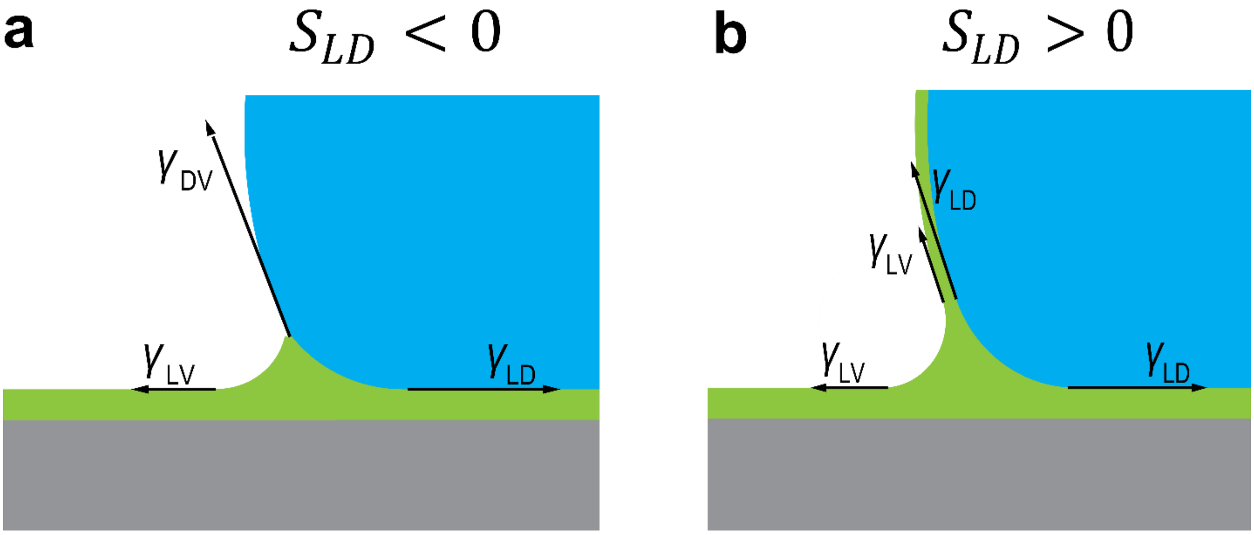

Figure 1. 17: Effect of spreading coefficient on the configuration of the wetting ridge. (a) a water droplet with a meniscus wetting ridge, and (b) a water droplet with a lubricant wrapping layer. The growth of the wetting ridge through an interfacial force balance between the liquid droplet, the lubricant layer, and the air.

This figure is adapted from Ref [27].

At equilibrium, the pressure inside and outside the wetting ridge is the same as the meniscus; the Laplace pressure is equivalent at all meniscus positions.[204, 205] By applying the Young-Laplace equation across the interfaces, the pressure in the droplet (P_D) can be determined.[27, 37] When $S_{LD} < 0$ (**Figure 1.18**a), the pressure in the droplet can be calculated through the pressure difference of the droplet-vapor interface, as described by **Eqs. (1.4)** and **(1.5)**:

$$\Delta P_{DV} = P_D - P_V = \frac{2\gamma_{DV}}{R} \tag{1.4}$$

$$P_D = P_V + \frac{2\gamma_{DV}}{R} \tag{1.5}$$

When $S_{LD} > 0$ (**Figure 1.18**b), the droplet is covered by a wrapping layer of lubricant. Thus, the pressure differences between the wrapping layer and the vapor and between the wrapping layer and the droplet should be considered, as described in **Eqs. (1.6)** – **(1.7):**

$$\Delta P_{LV} = P_L - P_V = \frac{2\gamma_{LV}}{R} \tag{1.6}$$

$$\Delta P_{DL} = P_D - P_L = \frac{2\gamma_{DL}}{R} \tag{1.7}$$

$$P_D = P_L + \frac{2\gamma_{DL}}{R} \tag{1.8}$$

$$P_D = P_V + \frac{2(\gamma_{LV} + \gamma_{DL})}{R} \tag{1.9}$$

where P_V, P_L and P_D are the atmospheric pressure, the pressure of the lubricant layer, and the droplet pressure, respectively. R is the radius of the droplet. Because the thickness of the lubricant wrapping layer is negligible, R is used as the radius of the droplet in the calculation for both cases with and without the wrapping layer of lubricant.

Generally, the pressure in the wetting ridge can be determined from the Laplace pressure across the meniscus interfaces through **Eq. (1.10)**.[27, 200, 204]

$$\Delta P_{AB} = P_A - P_B = \gamma_{AB}(\frac{1}{R_1} + \frac{1}{R_2}) \tag{1.10}$$

where ΔP_{AB} presents the pressure difference across the interface of phase A and phase B. γ_{AB} is the interfacial tension between the two phases. R_1 presents the radius of the curvature from the wetting ridge, and R_2 is the radius of the curvature formed by the droplet (air bubble or liquid).

The pressure in the wetting ridge can be calculated either through the wetting ridge-vapor interface or the wetting ridge-droplet interface. Accordingly, R_1 can be presented as r_{ext} when the wetting ridge-vapor interface is considered and r_{int} when the wetting ridge-droplet interface is used (**Figure 1.18**). For a water droplet sitting on SLIPS, the radius of the curvature formed by the water droplet (R_2) is equal to the base radius of the droplet (a). Depending on which interface (wetting ridge-vapor or wetting ridge-droplet) is considered, a can be positive or negative. A positive value of a implies the curvature is concaved-in relative to phase A. Thus, when the wetting ridge-vapor interface is considered, a represents a convex curvature and has a negative value. In contrast, when the wetting ridge-droplet interface is considered, a represents a concave curvature and has a positive value. By using appropriate parameters in **Eq. (1.10)**, the pressure in the wetting ridge can be calculated through the Laplace pressure across either the wetting ridge-vapor interface or the wetting ridge-droplet interface as presented in **Eq. (1.11)**:

$$\begin{aligned} P_{ridge} &= P_V - \gamma_{LV}(\frac{1}{r_{ext}} - \frac{1}{R}) \\ &= P_D - \gamma_{LD}(\frac{1}{r_{int}} + \frac{1}{R}) \end{aligned} \qquad (1.11)$$

where r_{ext} and r_{int} is the external and internal radii of the wetting ridge, respectively. γ_{LV} and γ_{LD} is the interfacial tension between the lubricant-vapor phases and lubricant-droplet phases, respectively. a represents the base radius of the droplet.

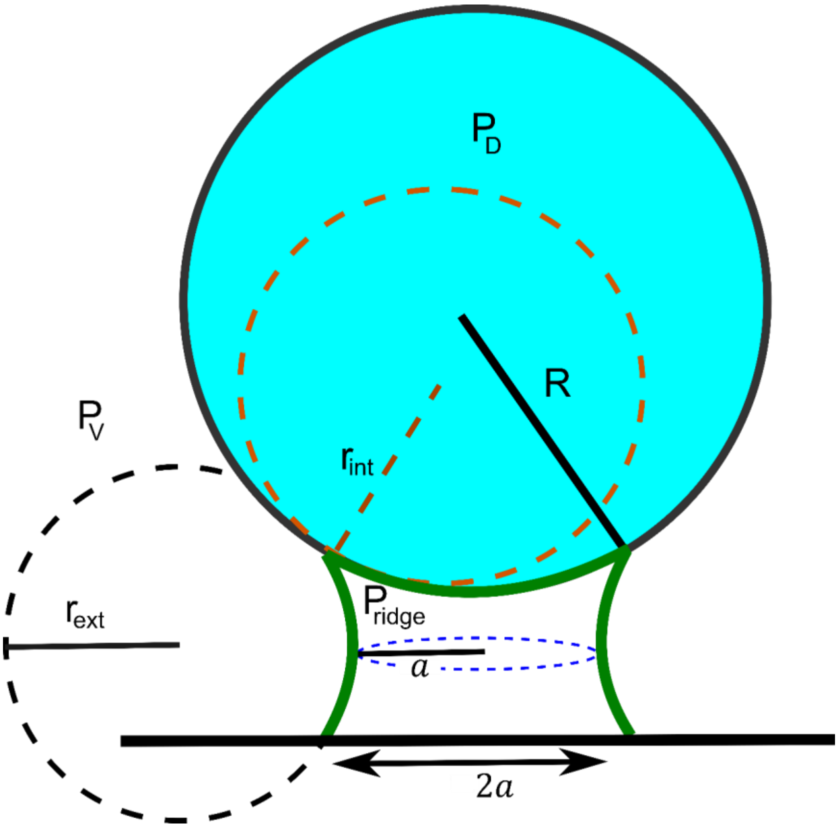

Figure 1. 18: The schematic illustration demonstrates a wetting ridge profile on SLIPS caused by a water droplet with its accompanying curvatures.

In addition to the effect of the interfacial tensions, the initial thickness of the lubricant layer can also affect the configuration of the wetting ridge. For example, recent computational studies have shown that a wetting ridge surrounding a droplet can transform into a lubricant layer wrapping the droplet when the thickness of the lubricant layer is comparable to the size of the droplet, as shown in **Figure 1.19**.[206, 207] Such a transformation is shown to affect the sliding velocity of the droplet.

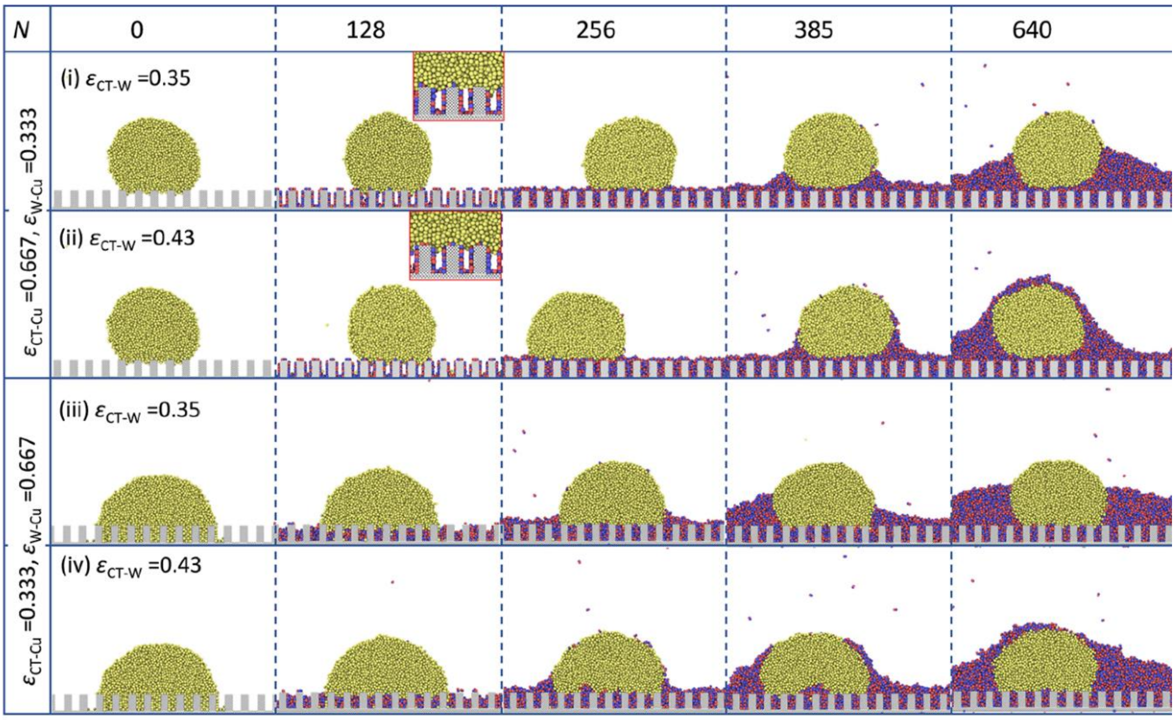

Figure 1. 19: Computational prediction of possible configurations of a wetting ridge surrounding a liquid droplet on SLIPS under different lubricant numbers.

This figure is adapted from Ref [206].

Wetting ridge around a moving droplet

The volume of a wetting ridge can considerably increase around a moving droplet compared to a static droplet (**Figure 1.20**a) because such a moving droplet can draw more lubricant into its wetting ridge due to capillarity, which will be discussed more in detail later.[27] Such a wetting ridge moves along with the droplet and leads to the loss of lubricant from the porous surface when the droplet slides off the surface.[201] This section will highlight the effect of droplet movement on lubricant depletion.

The changes in the lubricant height beneath and behind a moving droplet with velocity on SLIPS have been shown to follow the entrainment of liquid film during a dip-coating process as described by the Landau–Levich–Derjaguin model.[27, 208, 209] Indeed, it has been explicitly shown that the volume of a wetting ridge (V_{ridge}), as determined by **Eq. (1.12)**, is equivalent to the volume of lubricant being depleted (V_{lost}):

$$V_{ridge} = \alpha 2\pi a r_{ext}^2 \tag{1.12}$$

where α is a geometric factor to account for the shape of the ridge, and it can change because the wetting ridge grows and depend on capillary number (Ca), which accounts for the ratio of the drag force to the surface tension force; α generally stays at about 0.5 because the wetting ridge can be estimated as a triangle.

Through reflection interference contrast microscopy and white-light interferometry measurements, the thickness profile of the lubricant trail behind the moving droplet can be determined. From these thickness profiles, the amount of lost lubricant (V_{lost}) can be calculated by **Eq. (1.13)**.

$$V_{lost}(L) = \int_0^L 2(a + w r_{ext}) \Delta h dL + V_0 \tag{1.13}$$

where Δh presents the change in the thickness of the lubricant layer, L is the distance traveled by the droplet, w represents the geometric factor showing the expanded width of the wetting ridge, and $V_0 = \alpha 2\pi R r_{ext,0}^2$ represents the volume of the wetting ridge when the droplet initially meets the surface.

The loss of lubricant due to a droplet moving with different Ca is shown in **Figure 1.20**b. The droplets with higher capillary numbers deplete much less lubricant than slower-moving droplets on less viscous lubricants, and V_{lost} plateaus to a maximum value at high velocities for the highest Ca. Other studies also showed that slowly moving droplets induce a more significant loss of lubricant because they can draw more lubricant into their wetting ridge.[27, 206] Importantly, the volume of the wetting ridge V_{ridge} follows that of V_{lost} (**Figure 1.20**c).

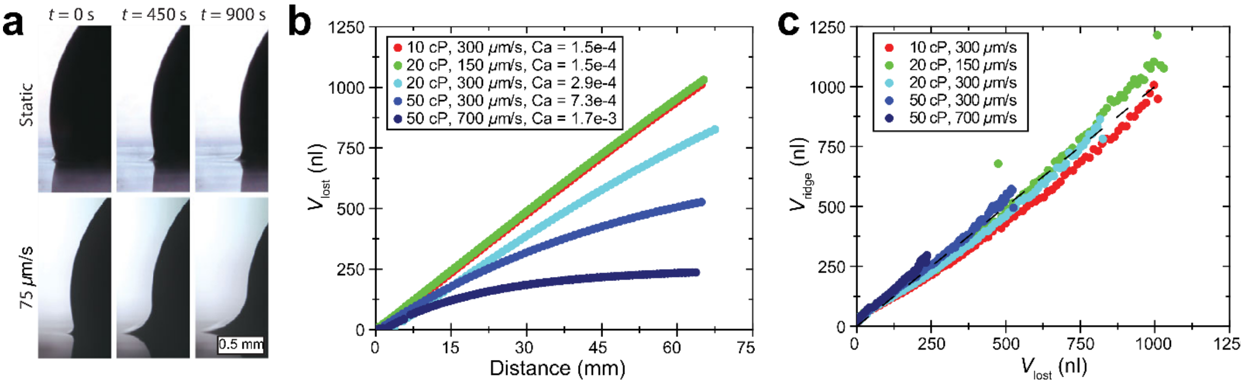

Figure 1. 20: (a) Study of wetting ridge growth on SLIPS under static and dynamic conditions over time using goniometer technique. (b) V_{lost} *vs distance for droplets moving with different capillary numbers on a lubricant layer of silicone oil with* h_i *= 4 μm. (c)* V_{ridge} *vs* V_{lost} *for experiments on silicone oil with various capillary numbers. The sole fitting parameter* $\alpha = 0.52$*.*

Adapted from Ref [27].

There are two competing dissipation mechanisms for moving droplets on SLIPS: droplet and wetting ridge-dominated dissipation.[210] These two dissipation regimes can be explained through the interaction between contact line pinning and viscous friction in terms of wetting ridge size, consequently affecting the dynamic of moving droplets on SLIPS.[201] The droplet-dominated dissipation regime involves a droplet with high viscosity. In this regime, viscous dissipation mainly remains inside the droplet. Accordingly, the velocity of the droplet increases as the viscosity of the droplet is lowered until it plateaus. The wetting ridge-dominated regime involves a droplet with viscosity below a critical value under which the velocity of the droplet remains unchanged. In this regime, viscous dissipation in the wetting ridge becomes predominant compared to dissipation in the droplet. Thus, the velocity of the droplet is dependent on the viscosity of the lubricant. This wetting ridge-dominated dissipation regime is of great interest in SLIPS studies because water has lower viscosity than typical lubricants used for SLIPS fabrication.

In addition, the wettability of the lubricant can affect the mobility of a droplet on SLIPS, which has been shown through the interplay between viscous friction and contact line pinning at the wetting ridge-droplet interface.[201] Specifically, there are two regimes (for lower θ_{app} (<90°) and higher θ_{app} (>90°)) affecting the dynamic of droplets on SLIPS. For larger θ_{app} (i.e., close to 110°), it has been shown that liquid droplets with smaller wetting angles (i.e., close to 30°) on the lubricant move faster than those with larger wetting angles (i.e., close to

60°) on the lubricant. In contrast, for lower θ_{app} (i.e., close to 45°) droplets with smaller wetting angles move slower than those with larger wetting angles. It is hypothesized that such inversion originates from a change in the importance of viscous dissipation and contact line pinning at the wetting ridge-droplet interface. In particular, it has been shown that, for a large θ_{app}, contact line pinning dictates droplet movements, and droplets with pronounce wetting ridges move faster. In contrast, for a small θ_{app}, viscous friction in the wetting ridge dominates. Viscous dissipation depends strongly on the shape of the wetting ridge; moving droplets with tiny wetting ridge thus move faster. These discussions are illustrated in **Figure 1.21**.

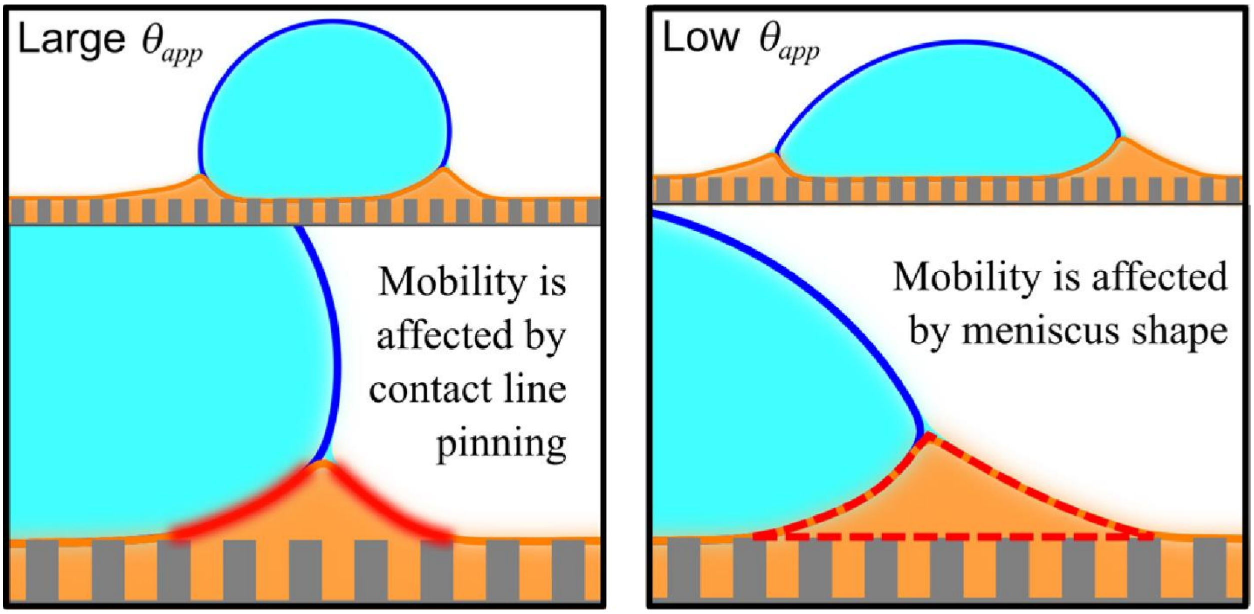

Figure 1. 21: Droplet mobility on SLIPS is affected by the wettability of lubricant through a change in the dominance between viscous dissipation and contact line pinning at the wetting ridge-droplet interface. This figure is adapted from Ref [201].

Strategies to suppress wetting ridges

The growth of wetting ridges directly leads to lubricant depletion and degradation of surface functionality of lubricant-infused surfaces. Although wetting ridges seem unavoidable, recent studies show potential strategies to suppress their growth, enhancing the stability and durability of SLIPS. Typically, the fundamental principle is to fabricate rough and porous SLIPS where the lubricant is held within the porous structure by capillary forces or is stabilized at the surface of a rough topography without any excessive lubricant. We highlight these recent notable developments in this section, which could inspire future discoveries.

Having a thick and smooth lubricant layer is unnecessary because any lubricant not held by capillary forces is prone to deplete rapidly. Thus, a nanoscale thin lubricant layer stabilized around a rough topography by capillarity forces is the most stable configuration, showing excellent water harvesting and anti-biofouling properties. Notably, slippery Wenzel surfaces have been developed by optimizing the thickness of the lubricant on infused-hierarchical nano- and microscale textures to make a highly slippery rough surface (**Figure 1.22**a).[211] Optimization of the spin coating process is used to achieve the desired lubricant layer (**Figure 1.22**b). The interaction of a water droplet and the slippery Wenzel state is different from a typical SLIPS, in which the water droplet does not rest on a smooth lubricant layer and is surrounded by wetting ridges (**Figure 1.22**c). Despite such a cavity filling behavior, liquid droplets can still slide on the lubricated surface (**Figure 1.22**d), which shows great potential in water harvesting applications. Similarly, a rough SLIPS based on silicone oil and well-ordered nanoporous anodic alumina plates have been prepared, showing that the sliding behavior of a water droplet on the lubricated surface is sensitive to the porosity (i.e., pore diameters and interpore spaces) of the geometry texture of the nanoporous anodic alumina plates (**Figure 1.22**e).[212] In particular, the sliding angle of a water droplet on these lubricated surfaces linearly increases with decreasing porosity of the substrate texture (**Figure 1.22**f).

Atomic force microscopy (AFM) meniscus force measurement studies have shown that SLIPS surfaces with roughness are very stable against lubricant depletion.[213, 214] Such a stable topography of a rough SLIPS is illustrated in **Figure 1.22**g. AFM meniscus force measurements enable mapping lubricant thickness with nanoscale resolution directly. The working principle of this technique is illustrated in **Figure 1.22**h. Briefly, the surface is mapped using force−distance curves to obtain the thickness of the lubricant layer. When the tip contacts the top of the lubricant layer, a meniscus forms and pulls the tip downward because of capillarity. When the tip makes hard contact with the solid surface, the tip deflects in the opposite direction. The distance between these two points indicates the thickness of the lubricant layer. One advantage of mapping the lubricant layer is the ability to reconstruct the three-dimensional structure of the lubricant-infused surface (**Figure 1.22**i). Overall, prior studies emphasize the importance of having a rough lubricant layer that conforms around the surface structures. This understanding is a key to preventing wetting ridge-induced lubricant depletion because such a macroscopically rough, slippery surface can reduce the interaction between the liquid droplet and the lubricant layer. Spin coating-based fabrication techniques, however, pose a challenge to scalable production of SLIPS due to the restriction in the sample size and time-consuming optimization necessary for the desired lubricant layer.

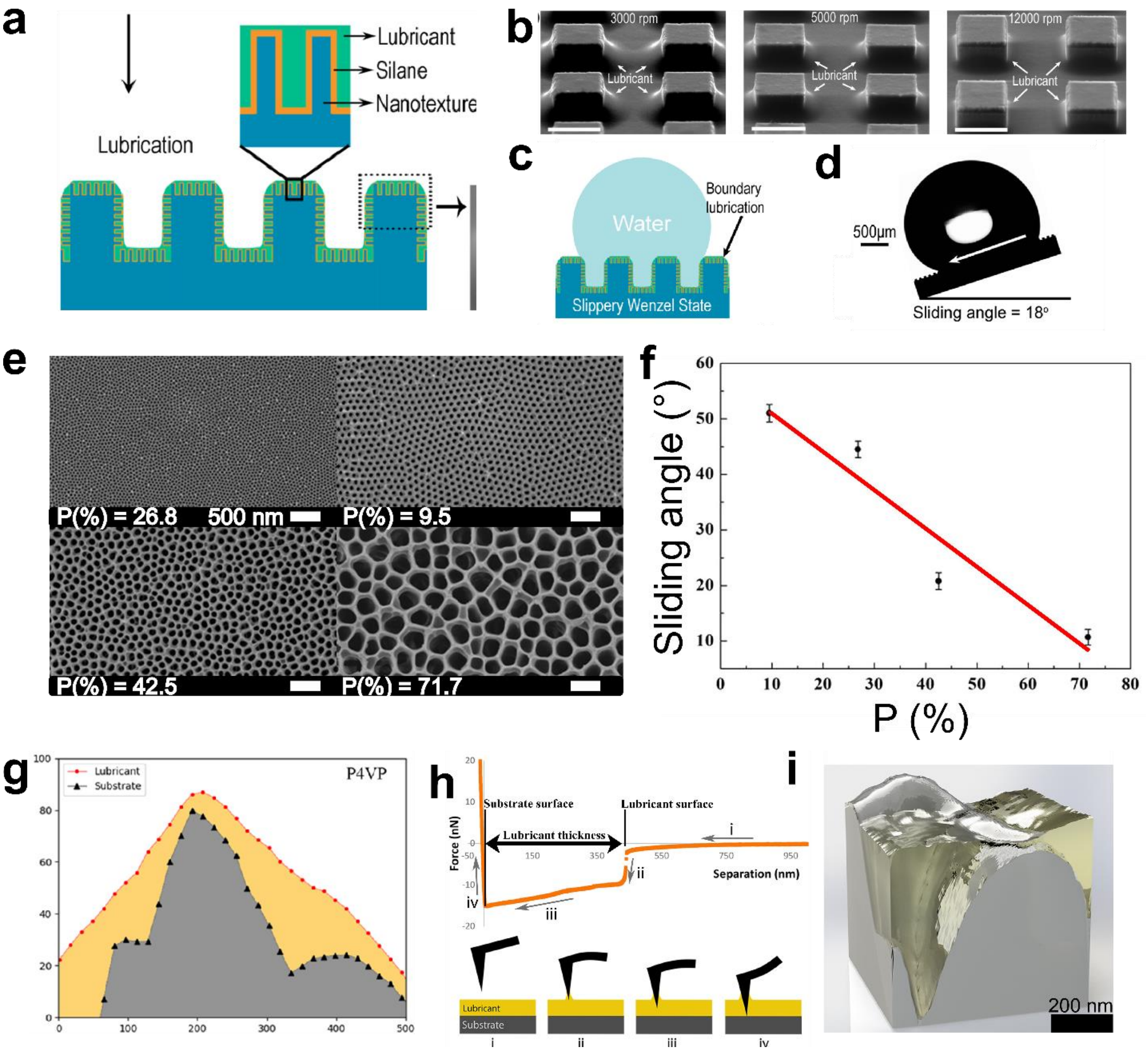

Figure 1. 22: (a) Schematic illustration for fabricating a rough SLIPS. (b) Morphology of rough SLIPSs during the optimization via a spinning process. (c) Schematic illustration of a water droplet placed on the surface of rough SLIPS where the substrate's root is filled with water from the droplet. (d) The moving of the water droplet on the rough SLIPS at a tilted angle. (e) SEM images of well-ordered nanoporous anodic alumina plates with different porosity and (f) their associated sliding behavior upon lubrication. (g) Schematic illustration of a stable lubricant-infused configuration. (h) Schematic of the AFM meniscus force measurement for determining the thickness and mapping the distribution of the lubricant layer. (i) 3D reconstruction of a SLIPS from the AFM meniscus force measurements.

This figure is adapted from Refs [211] [212] [213] [214].

The application of nanostructures as a porous template effectively prevents lubricant depletion because of the strong capillarity that retains the lubricant in place within the nanopores.[122, 215-219] For example, nanoscale roughness has been shown to be the key to retaining the lubricant film via capillary forces during water condensation processes.[182] The morphology of a nanostructure that provides high capillary force is shown in **Figure 1.23**a. Such a nanostructure provides a porous scaffold having a height equivalent to the roughness of the nanostructure, which can be imaged via AFM (**Figure 1.23**b). To quantitatively study the rate of lubricant depletion by droplets during the condensation process, falling droplets were collected over a 10 h long experiment. By measuring the loss of water and lubricant via thermogravimetric analysis, a considerable decrease in the lubricant layer thickness was detected over 10 h (**Figure 1.23**c). Interestingly, the height of the remaining lubricant layer is equal to that of the nanostructure, indicating that the high capillarity can resist lubricant depletion. Also, the lubricant layer thickness depletes faster at the beginning of the process (0 − 4 h), which is likely due to a lubricant overlayer that accelerates lubricant depletion.

In another example, the concept of "capillary balancing" has been proposed to address frost-induced lubricant depletion (**Figure 1.23**d). Lubricant depletion in SLIPS during frosting and icing could be avoided by introducing nanoscale fillers with smaller pore sizes than that between frost dendrites, which provides strong capillarity forces to retain the lubricant during the freezing of the liquid droplet. Using such an approach, lubricant retention was achieved under harsh frost growth conditions, whereas the lubricant infused into a surface with micrometer scale structures underwent freezing and depletion (**Figure 1.23**e).

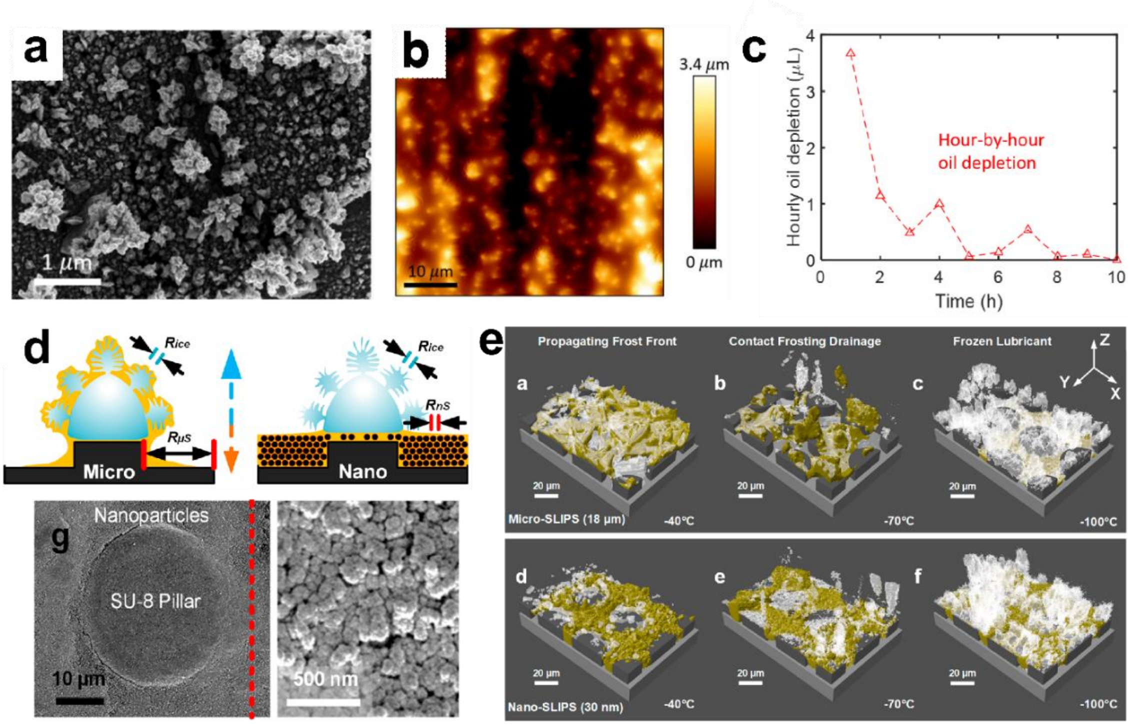

Figure 1. 23: (a) SEM image of the nanostructured surface showing closely spaced nanoflorets. (b) AFM image for observing the surface topography. (c) Cumulative and hour-by-hour lubricant loss as a function of time. (d) Schematic and SEM images of the capillary balancing structure for suppressing frosting-induced lubricant depletion. (e) Effective lubricant retention of the capillary balancing structure compared with the microstructure under harsh frosting conditions.

This figure is adapted from Refs [124, 182].

1.3 Nanocomposite films via capillary rise infiltration methods

With the remarkable development of nanostructured materials, polymer nanocomposite films have represented a unique class of materials for advanced applications.[220-224] Polymer nanocomposite films blend the unique properties of nanostructured materials and the processability and flexibility of polymers, generating many fascinating opportunities.[225-229] Polymer nanocomposite films are beneficial for numerous applications, such as electronic displays,[230] environmental remediation,[231] sensing technologies,[232] tissue regeneration,[233] protective coatings,[234] membrane separation,[235, 236] solar cells.[237] Notably, polymer nanocomposite films have also represented applications as self-cleaning,[238] anti-corrosion,[239] anti-fouling coatings.[240-243] Having synergistic properties, repellent polymer nanocomposite surfaces are currently the most promising approach to address contamination and fouling challenges (**Figure 1.24**).

These exciting functionalities typically come from nanostructured material fillers. Previous studies have revealed that increasing the fraction of nanostructured material fillers (e.g., >50%) could enable the nanocomposite films to exhibit unique or multi functionalities, promising huge potential for advanced applications.[224, 228, 244-250] However, the fabrication of nanocomposite films with a high filler fraction using conventional methods remains challenging. Nanomaterials have a high aggregation tendency during nanocomposite fabrication because of their high interparticle attraction and large effective surface area, thus making traditional mixing or compounding processes extremely difficult. Melt-based approaches usually have a relatively low optimized filler fraction (~10 vol%).[251-254] Layer-by-layer assembly has been successfully employed to generate nanocomposites with high filler fractions.[255, 256] However, this approach involves multiple steps and a limited set of water-soluble species of opposite charge and is thus time-consuming and only appropriate for lab-scale fabrication. To overcome these barriers, a new approach to fabricating nanocomposite films with a high filler fraction in a scalable fashion has been developed by taking advantage of the capillarity-based phenomena.[31-35] This section will briefly describe the working principles and applications of such an approach in generating nanocomposite films.

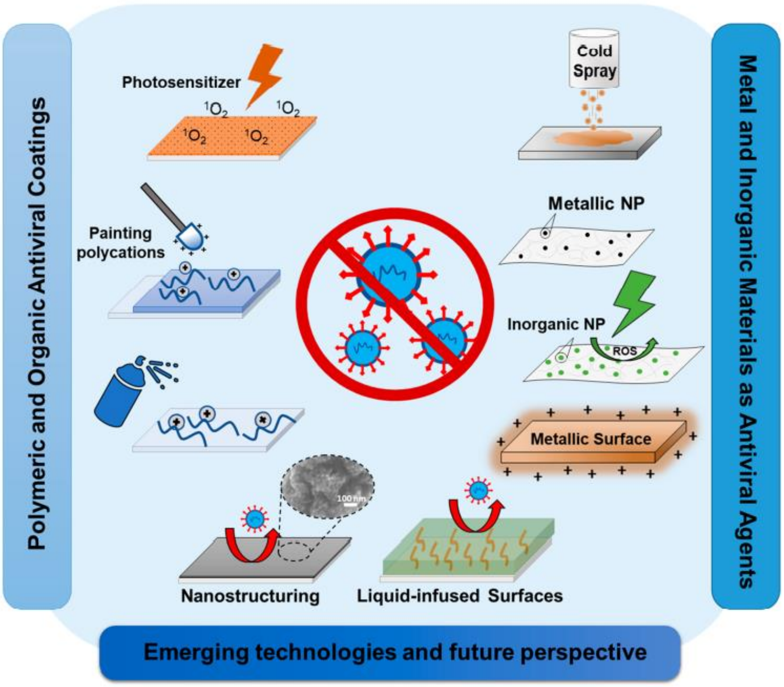

Figure 1. 24: Schematic demonstration of the current research and emerging anti-fouling coatings, showing the potential of repellent nanocomposite coatings by synergizing the advantages from polymeric and inorganic materials.

This figure is adapted from Ref [243].

1.3.1 Capillary action

Nanotechnology is at the core of most advanced technologies,[257] capillarity and wetting phenomena thus have found new importance due to their dominant effect at the nanoscale. In principle, capillarity-based phenomena arise from the action of deformable interfaces between two phases, and the mechanics at the surface of the interface are governed by surface tension, γ (N/m). Surface tension is attributed to unbalanced forces from the interaction of molecules at the surface and is also expressed as the energy required to create an additional unit area of the interface. Surface tension values vary from substance to substance and temperature and pressure. When two dissimilar materials come into contact, the interfacial tension between them depends on the relative strength of intermolecular interactions between the constituent atoms/molecules of one substance (cohesion) and their interaction with the atoms/molecules of the other substance. When a small volume of a liquid is placed on top of a solid, the liquid may spread out and cover as much of the surface as possible or form a droplet subtending an angle at the triple-phase contact line.[37] This angle is called the equilibrium contact angle and measures the wetting of the solid by the liquid. By a minimization of free energy at equilibrium, the equilibrium contact angle can be estimated as **Eqn (1.14)**:

$$Cos\theta = \frac{\gamma_{SV} - \gamma_{SL}}{\gamma_{LV}} \qquad (1.14)$$

where γ_{LV} is the surface tension at the liquid-air interface, γ_{SV} and γ_{SL} are the surface tension at the solid-air and solid-liquid interfaces, respectively. Contact angle values close to 0 indicate complete wetting of the solid by the liquid, and higher contact angles(< 90°) indicate partial wetting.[37] Thus, the contact angle describes the shape of the interface between a liquid and solid surrounded by air.

When a capillary tube is kept at the surface of a liquid, the liquid will form a meniscus inside the tube such that the equilibrium contact angle is obeyed, and the curved interface generates a Laplace pressure at the meniscus given by **Eqn (1.15)**:

$$\Delta P = \frac{2\gamma cos\theta}{R} \qquad (1.15)$$

This capillary pressure is responsible for the rise of liquids inside capillary tubes if the radius of the tube (R) is small enough such that the P_{cap} is higher than the atmospheric pressure.

1.3.2 Capillary rise infiltration-based nanocomposite fabrication methods

Capillary rise infiltration (CaRI) represents a powerful strategy for creating unique nanocomposite films with an extremely high fraction of nanostructured fillers that can be easily adapted for manufacturing at an industrial scale. CaRI-based fabrications have been demonstrated over a bilayer consisting of a nanoparticles film and a polymer film.[32, 33, 258] Typically, a polymer film is deposited on a substrate, and then a nanoparticles film is deposited on the top of the polymer film; however, an inverted bilayer is also possible. Nanoparticle films are a porous structure, having interconnected nanopores with a typical porosity of ~0.35 regardless of the size of the nanoparticle.[32] To facilitate the polymer infiltration in CaRI, this bilayer is subjected to a higher temperature than the T_g of the polymer (**Figure 1.25**a,b). One of the unique advantages of CaRI is that it can heal structural defects in the nanoparticles film effectively (**Figure 1.25**c). The dynamics of polymer infiltration in CaRI have been shown to follow the Lucas-Washburn equation (**Figure 1.25**d).

Interestingly, by controlling the original thickness of the polymer film and the heating time, nanocomposite films with uniform or graded porosity with tunable refractive indices can be fabricated (**Figure 1.25**e), showing great potential in generating antireflection coatings.[31] An additional unique advantage of CaRI is that it can potentially be used for fabricating nanocomposite films with many materials. Also, besides heating, CaRI process can be induced by solvents.[33] Although previous studies primarily focused on making nanocomposite films with a packing of nanoparticles, the extension of such an approach to anisotropic nanomaterials promises to bring several fascinating opportunities.

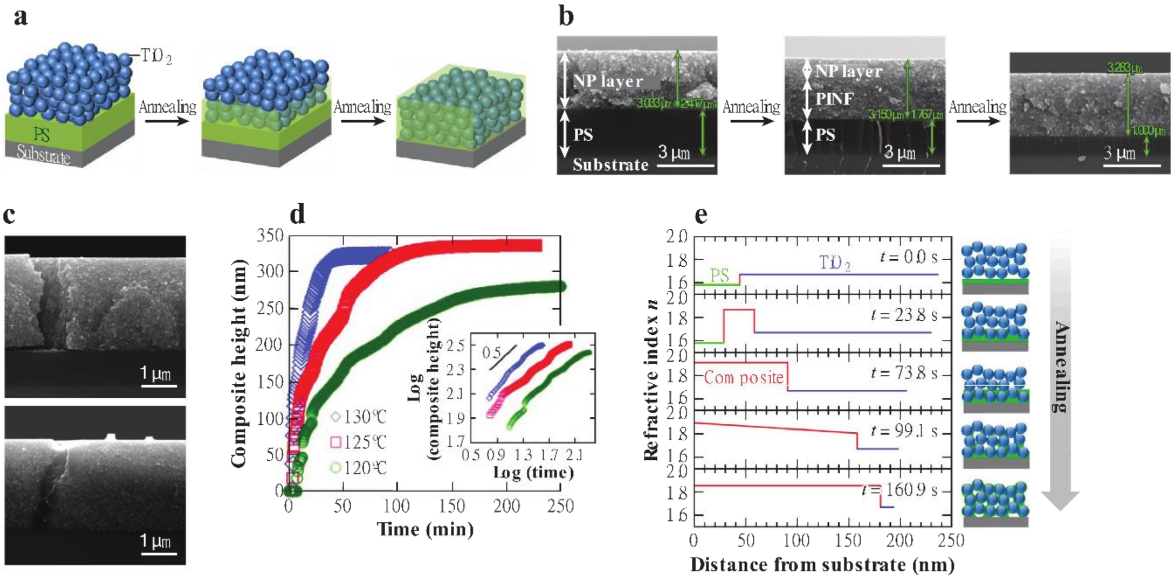

Figure 1. 25: (a) Schematic illustration of CaRI of polymer into a nanoparticles film. (b) SEM images showing shifts of polymer thickness upon infiltration. (c) Initial cracks in a nanoparticle film are healed after CaRI. (d) The dynamic of polymer infiltration in CaRI follows the Lucas–Washburn equation. (e) Refractive index profiles at different stages in the unsaturated CaRI process. The schematic on the right illustrates the same.

This figure is adapted from Refs [31, 32].

1.4 Functional nanocomposite films based on ZnO nanowires

With these previous backgrounds, enhancing the stability of repellent surfaces represents a unique opportunity for potentially addressing the fouling problem. Nanostructured coatings have presented great promise in improving the robustness of repellent surfaces. However, surfaces with nanostructures still exhibit two main drawbacks: mechanical vulnerabilities and highly sophisticated fabrications. The development of repellent surfaces from a low-cost, multifunctional, mechanically robust nanomaterial and has potential for large-scale manufacturing holds enormous promise. Zinc oxide nanowires (ZnO NW) are an exciting class of nanostructured materials that could promote repellency stability because of their unique morphology. The outstanding use of ZnO NWs also comes from their ease of synthesizing and integrating several types of applications. ZnO NWs present several remarkable functionalities and have been actively explored during the last 20 years. This section briefly highlights the significant advantages of ZnO NW-based advanced coatings, particularly in anti-fouling applications.

1.4.1 Fundamental properties of ZnO nanowires

ZnO is a semiconductor material with a direct and wide bandgap (~3.37 eV) and presents several exciting properties, which are highly valuable for many advanced technologies.[259-268] Clearly, ZnO has been a vital component of the current industrial systems, broadly presented in paints, ceramics, textiles, cosmetics, and medical products.[269, 270] At the nanoscale, because of its hexagonal-wurtzite crystal structure, ZnO can grow effortlessly in one-dimensional nano- or microstructures.[260] Having a high surface-to-volume ratio (**Figure 1.26**), ZnO NWs show many fascinating opportunities.[265, 271-276] In particular, because of the quantum confinement, ZnO NWs can efficiently transport electrons and holes within the structure, which is highly beneficial for energy harvesting and converting applications. [277-279] Notably, the alignment of ZnO NWs have shown a vast potential given its superior mechanical robustness, such as an excellent additive for improving the mechanical properties of advanced composites.[244, 267, 280] In addition to the mechanical robustness, the morphology and alignment of ZnO NWs are highly tunable, making them an excellent platform for fabricating repellent surfaces that require a high surface roughness and capillarity from the nanostructure are incredibly favorable. Indeed, ZnO NWs have successfully addressed fouling over several applications, such as self-cleaning,[281] superhydrophobic,[271] air-purification,[282] solar cells,[277] anti-bacterial,[273, 274, 283] anti-infection on medical implants.[284, 285] ZnO NWs have been extensively studied. Thus, the properties and fabrication methods of ZnO NWs are well-studied, optimized, and matured, which provide significant advantages for research using ZnO NWs can be immediately manufactured in a scalable fashion and applied in a broad range of situations. Many approaches for fabricating ZnO NWs include sol-gel,[286] hydrothermal,[287] chemical bath deposition,[288] solvothermal,[289] MOCVD,[290] and electrochemical deposition approaches.[291] For in-depth details about the fabrication methods and properties of ZnO NWs, readers are referred to some dedicated reviews.[262, 270, 291-296]

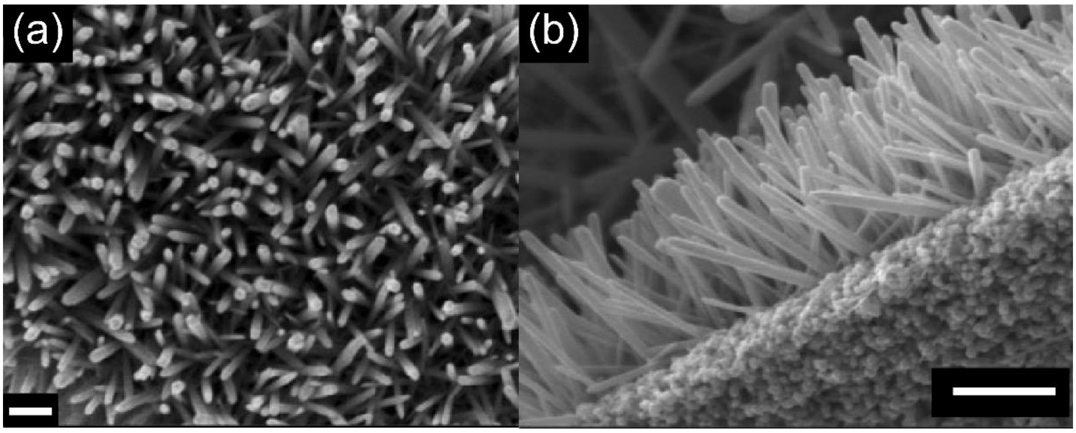

Figure 1. 26: Morphology of ZnO NWs observed by (a) top-view and (b) cross-section SEM images. Scale bars are 1 µm and 2 µm for (a) and (b), respectively.

This figure is adapted from Ref [297].

1.4.2 Current ZnO NW-based repellent surfaces

The unique morphology and fascinating properties of ZnO NWs have driven tremendous success in anti-fouling applications. For example, having excellent mechanical robustness, ZnO NWs can resist failure due to mechanical forces, potentially achieving a long-term repellent surface.[267] The tunable morphology of ZnO NWs also enables great ability to regulate the adhesion and viability of bacteria and other biological species.[298-303]

Previous studies have shown several notable performances of ZnO NW-based coatings for preventing fouling (**Figure 1.27**). A schematic illustration of a liquid droplet that cannot spread due to the repellency of a ZnO NW-based coating is shown in **Figure 1.27**a.[304] Such a phenomenon has been applied to make anti-fouling wearable clothes. A hybrid structure between ZnO NWs and $Ti_3C_2T_x$ MXene has demonstrated an outstanding repellency against several liquids (**Figure 1.27**b).[305] Hierarchical structures based on ZnO NWs are also a great way to enhance the stability of superhydrophobicity underwater because of the unique ability to capture and retain a stable gas layer of ZnO NWs (**Figure 1.27**c-e).[306] Even in a much more challenging condition, ZnO NW-based coatings have shown impressive prevention of marine algae fouling compared to a surface without ZnO NWs over 22 days (**Figure 1.27**g,h).[307] A recent study has also shown that surfaces with ZnO NWs can rapidly kill bacteria through their unique morphology to reduce the risk of infection (**Figure 1.27**i).[308]

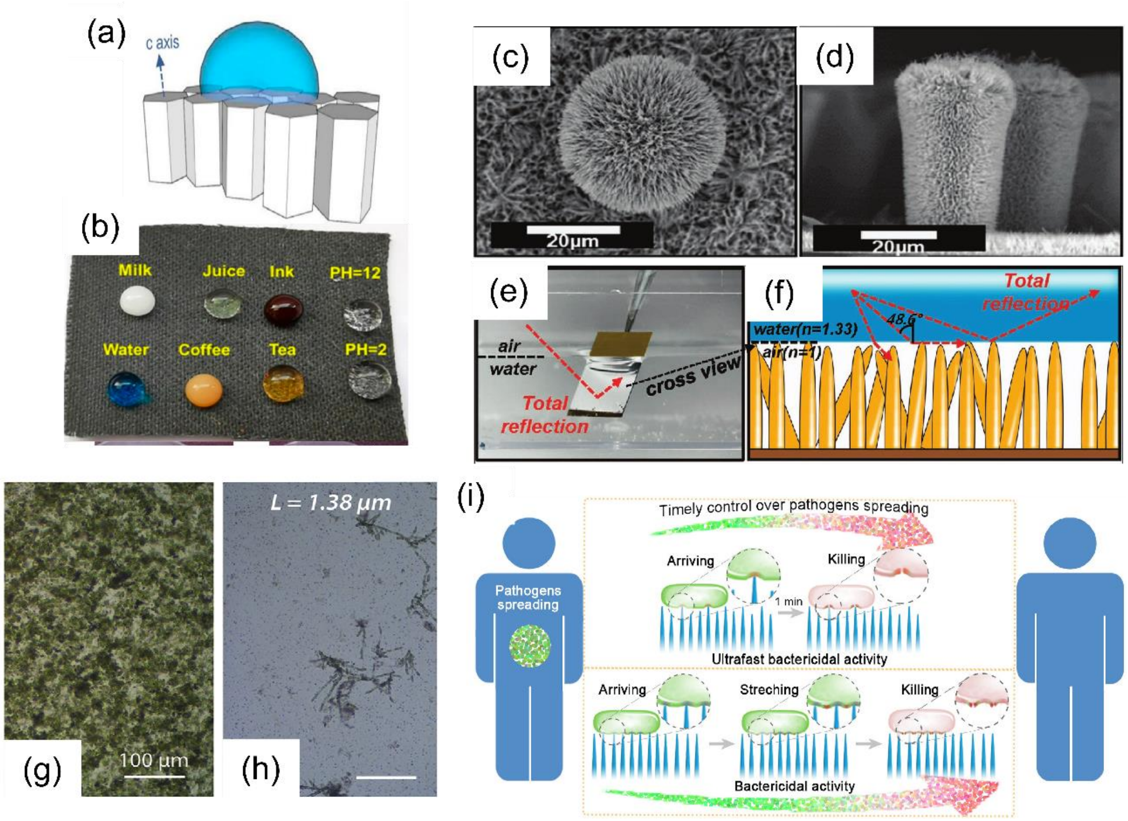

Figure 1. 27: Anti-fouling applications of ZnO NW-based coatings. (a) Schematic illustration of a liquid droplet repelled by the surface of ZnO NWs. (b) A ZnO NW-based hierarchical coating shows repellency against several liquids. (c) top-view and (d) cross-section SEM images of a hierarchical structure for stable underwater superhydrophobicity. (e) Reflection phenomenon of the superhydrophobic surface underwater and (f) its mechanism illustration. Optical image showing marine algae fouling coverage on (g) control and (h) superhydrophobic ZnO NWs surfaces after 20 days of algae fouling. (i) Rapid bacterial killing behavior on ZnO NW surfaces.

The figure is adapted from Refs [304-308].

1. 5 Goals and structure of the thesis

As described in the previous sections, anti-fouling surfaces are key for various coating applications. However, it remains a major challenge to maintain the stability of such repellency over time. Also, despite remarkable progress, the conventional methods for making these surfaces involve multiple steps and are only suitable for lab-scale fabrication. The goal of this thesis is thus to develop anti-fouling nanocomposite surfaces with high stability under challenging conditions. To achieve this goal, two new capillarity-based methods are developed for fabricating two types of repellent surfaces: multifunctional superhydrophobic nanocomposite coatings and lubricant depletion-resistant slippery lubricant-infused porous surfaces. Capillarity-based techniques present a tremendous simplification in manufacturing anti-fouling nanocomposite films. The approaches developed during this thesis are straightforward, efficient, and potentially scalable strategies to produce multifunctional nanocomposite films with a wide range of properties and applications, which also has an excellent capability for scalable manufacturing. These works are presented in this thesis as follows:

Chapter 2 describes experimental details on the growth and optimization of ZnO NWs by a chemical bath deposition method and preparation of polydimethylsiloxane elastomers by a typical cross-linking reaction. Characterization techniques used to study the properties of the obtained materials will also be described in this chapter.

Chapter 3 presents a new method for fabricating a nanocomposite film with vertically aligned ZnO NWs, leveraging leaching-enabled capillary rise infiltration of uncross-linked and mobile oligomers from a poly(dimethylsiloxane) (PDMS) slab into the space between NWs. Several essential properties are demonstrated, including superhydrophobicity, self-cleaning, solvent resistance, anti-icing, high transparency, and anti-reflection properties.

Chapter 4 depicts a robust method for producing stable SLIPS that resist lubricant depletion by wetting ridge formation. We thought controlling the pore features of NWs could be an effective way to improve the stability of the infiltrated lubricant. One way to do this would be to change the orientation of NWs. The orientation of nanowires strongly affects lubricant infiltration and the stability of SLIPS properties. The strong lubricant retention ability provided by the nanoporous structure of the random NWs array suppresses the growth of a wetting ridge around a water droplet and can even resist lubricant depletion under strong external forces.

Chapter 5 presents our preliminary studies in some exciting directions to which the findings from our works could further contribute. For example, some preliminary results on the effectiveness of our nanocomposite films based on ZnO NW against biofilm formation or removing established biofilms are shown. The extension of our materials to membrane substrates for potential separation applications is also discussed with some promising preliminary results.

Chapter 2.

Materials preparation and characterization techniques

Contents

This chapter provides experimental details on the growth of ZnO nanowire arrays by a chemical bath deposition method and the preparation of polydimethylsiloxane elastomer via a cross-linking reaction. Optimization of ZnO nanowire morphology is also discussed. Subsequently, characterization techniques used to analyze the properties of the obtained materials are described.

2.1 Fabrication of ZnO nanowire arrays

2.1.1 Overview of chemical deposition method

Given the extensive application of ZnO nanowires (NWs), many techniques have been implemented to produce ZnO NWs.[291, 309-315] The chemical bath deposition (CBD) represents a low-cost and scalable approach because it does not require high temperature or low vacuum conditions.[292, 316-318] In addition, this approach readily allows excellent control of the morphology and orientation of ZnO nanomaterials over a wide range of structures, as shown in **Figure 2.1**.[295, 297, 319-322]

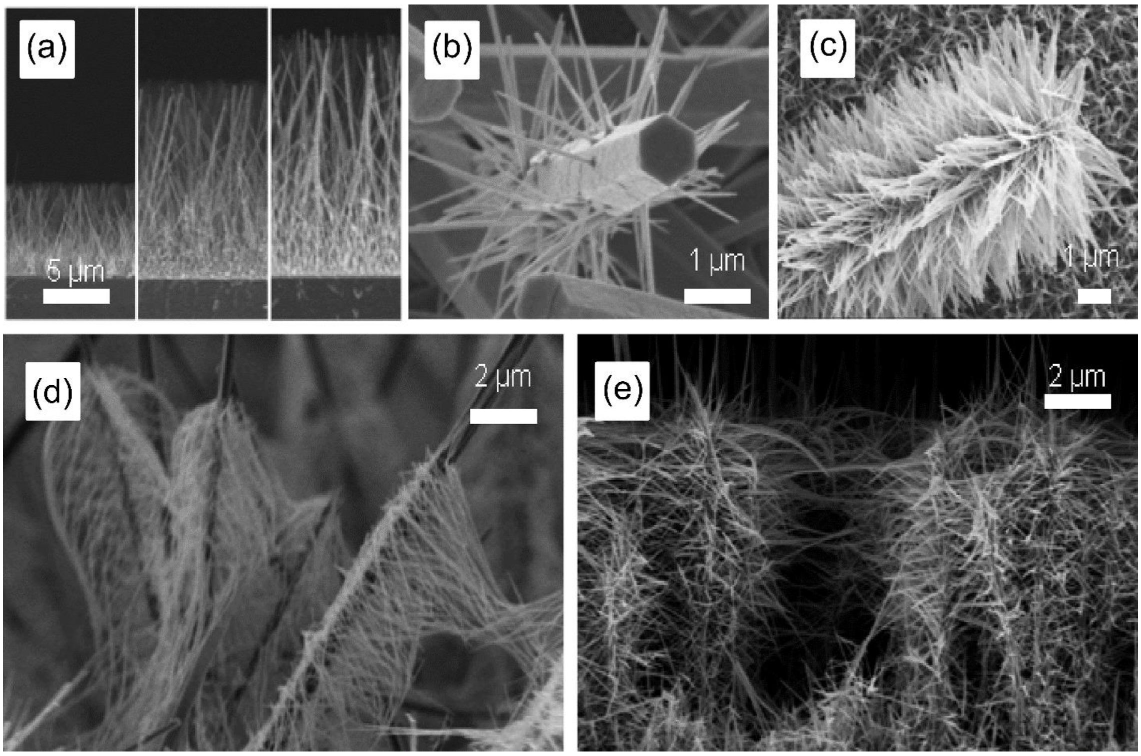

Figure 2. 1 : Diversity in the morphology of ZnO NWs prepared by the CBD method. SEM images of ZnO NWs. (a) Vertical NWs, (b) branded NWs, (c) NWs trees, (d) and (e) a NWs forest.

This figure is adapted with permission from Ref [323].

In principle, this CBD process takes advantage of the heterogeneous growth of ZnO NWs on a nucleation surface, submerged in a bath of zinc and hydroxide ions source at a moderate temperature varied between 60 – 90 °C.[324-328] The growth of ZnO NWs through the CBD method necessarily entails three main components, which include a zinc ions source and a hydroxide ions source (e.g., hexamethylenetetramine (HMTA)), and a nucleation surface (e.g., seed layer).[329] One of the unique advantages of the CBD method is its ability to tune the morphology of NW arrays. In particular, the concentration and pH of the two chemical precursors (zinc and hydroxide ions) are shown to govern the growth of ZnO NWs.[326, 327, 330-332] For example, it has been extensively shown that besides its role as a pH buffer, HMTA can be adsorbed by the sidewalls of ZnO NWs, consequently reducing the growth of those directions.[330, 331]

Importantly, the growth of ZnO NWs is regulated by the surface reactions on the polar c-planes and the diffusive transport of the zinc and hydroxide ions from the bulk solution to the nucleation surface. Therefore, it is shown that one of the critical factors for manipulating the morphology of ZnO NWs is by controlling the nucleation surface.[333-335] Previous studies have presented several strategies for effectively tuning the ZnO seed layer by changing the input concentration of ZnO sol solution or the grain size.[325, 335-339] Furthermore, one of the critical concerns in growing ZnO NWs by the CBD method is to prevent homogeneous growth of ZnO inside the solution, which leads to NWs with micrometer sizes uncontrolled morphology.[331, 340] In general, the process is more controllable if homogeneous nucleation is avoided because the concentration of species (metal ions, dopants, ligands) does not vary a lot during the deposition. In addition, if much homogeneous nucleation happens in the solution, the solution gets depleted of the metal ions very quickly, slowing down the growth of the desired material.

2.1.2 Experimental details

Chemicals and materials

All chemicals and materials used in this thesis are listed in this subsection. The two main types of substrates used as supports of the ZnO seed layer are microscope glass slides and (100) silicon wafer substrates. Zinc acetate dehydrate (ZAD, $Zn(CH_3COO)_2{\cdot}2H_2O$, 99.99%), zinc nitrate hexahydrate ($Zn(NO_3)_2{\cdot}6H_2O$, >99.00%), monoethanolamine (MEA, C_2H_7NO, >99.00%), and hexamethylenetetramine (HMTA, $C_6H_{12}N_4$, >99.00%), are purchased from Sigma Aldrich. Poly(dimethylsiloxane) (PDMS), Sylgard 184, are purchased from Sigma-Aldrich in the form of a silicone elastomer kit composed of siloxane oligomers base and a curing agent to be mixed in a 10 (base): 1 (curing agent) ratio by weight. Silicone oil ($M_n \approx 550$ g mol^{-1}) with a viscosity of 20 cSt at 25 °C is also purchased from Sigma Aldrich. The surface energy of the silicone oil was 24 mJ m^{-2} at 20 °C. The DI water system at LMGP provides deionized (DI) water.

Substrate preparation

Glass and silicon wafer substrates are annealed at 500 °C for 3h to remove organic contaminants and promote the adsorption of hydroxyl groups that will facilitate the deposition of sol solution. The substrates are cut into 2.5 cm × 2.5 cm slices and thoroughly cleaned with ethanol. The substrates are then stored in DI water.

Preparation of ZnO sol solution

Our group previously developed a protocol for preparing the ZnO sol solution.[288, 336, 337] Briefly, the sol is made by mixing ZAD and MEA in 1-butanol with an optimized (1:1) molar ratio. This method forms Zn-oxoacetate particles in the solution through sol-gel reactions.[341] The obtained sol is then aged under a strong stirring condition for 3h at room temperature. It has been shown that this obtained sol solution is chemically stable, allowing reproducible deposition of ZnO seed layers for several weeks, and more prolonged use can be achieved for lower concentrations. Based on our previous experimental parameters, the concentration of the sol solution used in this thesis is 0.37 M.

Deposition of ZnO seed layer films

We use the spin coating method for depositing ZnO seed layer films on planar substrates (glass or silicon wafer). Before depositing the ZnO seed layer, the substrate is vigorously washed with ethanol. Nitrogen gas is then flowed to dry the surface. Next, a seed layer is prepared by depositing 300 μL of 0.37 M ZAD sol on the substrate at 3000 rpm for 10 s. In case of multiple seed layer depositions, the coated substrate is placed in an oven at 300 °C for 10 min, stabilizing the film and promoting the initial crystallization. This substrate is cooled down before the subsequent layer deposition. After the last deposit with the desired number of seed layers, the seed layer-coated substrate is then placed in an oven at 540 °C for 1h, promoting the complete crystallization of the seed layer. The resulting seed layer is stored in a plastic container under ambient conditions. The effect of seed layers on the orientation of ZnO NW arrays will be presented later in this chapter.

The growth of ZnO NWs through the CBD method

Briefly, the seed layer coated substrate is first treated with oxygen plasma (at a vacuum level of 0.4 torrs, with a power of 12.0 W, for 2 min) to enhance its hydrophilicity and remove organic contaminants. Subsequently, the seed layer substrate is fixed, coated side facing down to prevent the deposition of large homogenously grown NWs in the solution, on a Teflon holder with a 45° tilt angle. Meanwhile, a mixture of 100 mL of zinc nitrate hexahydrate and 100 mL of hexamethylenetetramine is preheated at 90 °C on a hot plate. The substrate is then immersed in the bath maintained at 90 °C for a duration varying from 30 min to 5 h, depending on the desired length. The effect of growth time will be presented later in this chapter. After the growth, the sample is carefully rinsed with DI water, dried with a nitrogen stream, and then stored in a plastic container. Note that the above procedure produces vertical or tilted NWs with an average aspect ratio (ratio between the length and the diameter from 14.5 to 37.8 depending on the number of seed layer depositions).

Growth of random ZnO NWs

The growth of random ZnO NWs is adapted from a previously developed protocol from our group.[336] Briefly, to prepare random ZnO NW arrays, the seed layer-coated substrate is treated with oxygen plasma for 2 min and preheated on a hotplate at 135 °C for 15 min before the CBD step. The growth solution was prepared by mixing 400 μL of zinc nitrate hexahydrate in 199.2 mL of DI water, and then heating the solution to 90 °C. At 90 °C, 400 μL of hexamethylenetetramine is added; the mixture is then stirred for 2 min. The preheated seed layer is then immersed in the growth solution for several hours (between 3 to 24 hours) depending on the desired length to produce high aspect ratio random NW arrays. **Figure 2.2** shows the representative morphology of random ZnO NWs, which grew for 3h. The SEM images show that when NWs are grown with a high aspect ratio (i.e., the ratio between the length and diameter), they undergo aggregation to form bundles upon drying.

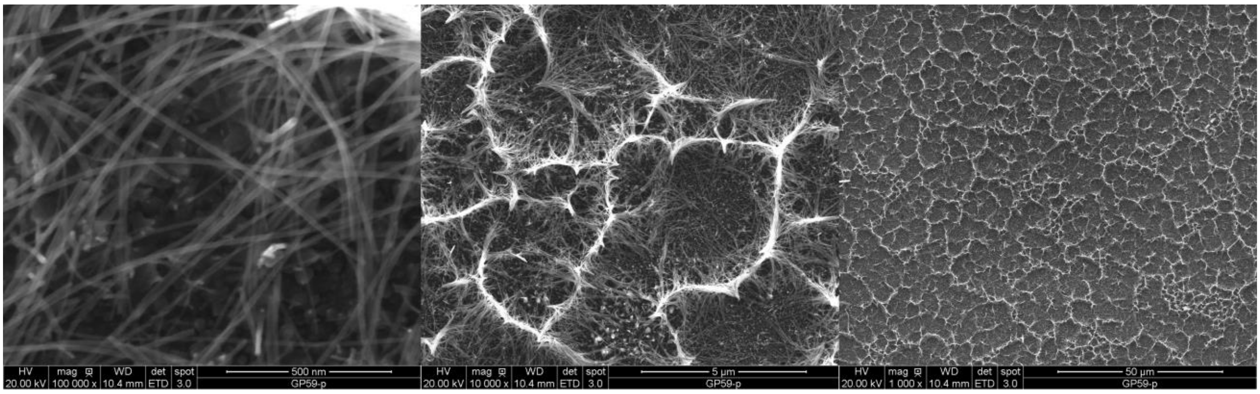

Figure 2. 2: The morphology of random ZnO NWs by SEM images. These ZnO NWs are grown for 3h.

2.1.3 Optimization of ZnO NWs

Effect of precursors concentration

As aforementioned, the concentration of the two chemical precursors (zinc nitrate hexahydrate and hexamethylenetetramine) plays an essential role in the growth of ZnO NWs. The effects of each of the two chemical precursors during the growth of ZnO NWs by the CBD method have been extensively reported.[326, 327, 330-332] Therefore, this subsection mainly describes the procedure for determining the optimal experimental parameters for our system. The optimal concentration of zinc nitrate hexahydrate and hexamethylenetetramine and growth time effects are presented. These preliminary experiments were performed with a single seed layer-coated silicon substrate. We have varied the concentration of zinc nitrate hexahydrate and hexamethylenetetramine (2, 25, 50 mM) and the growth time (0.5, 2, 5h). Our results suggest that the concentration of 2 mM does not allow a robust growth of ZnO NWs, showing no growth of ZnO NWs for a short growth time (0.5h) and a formation of short ZnO NWs with a tapered structure for a long growth time (5h). At the concentration of 25 mM, a robust growth of ZnO NWs is obtained even for a short time of growth (0.5h) and a significant growth after 2h. A longer growth time (5h) or an increased concentration (50 mM) does not present a significant difference, as shown in **Figure 2.3**. Thus, an optimized concentration of 25 mM and a growth time of 2h is used for later experiments; otherwise, changes will be specified.

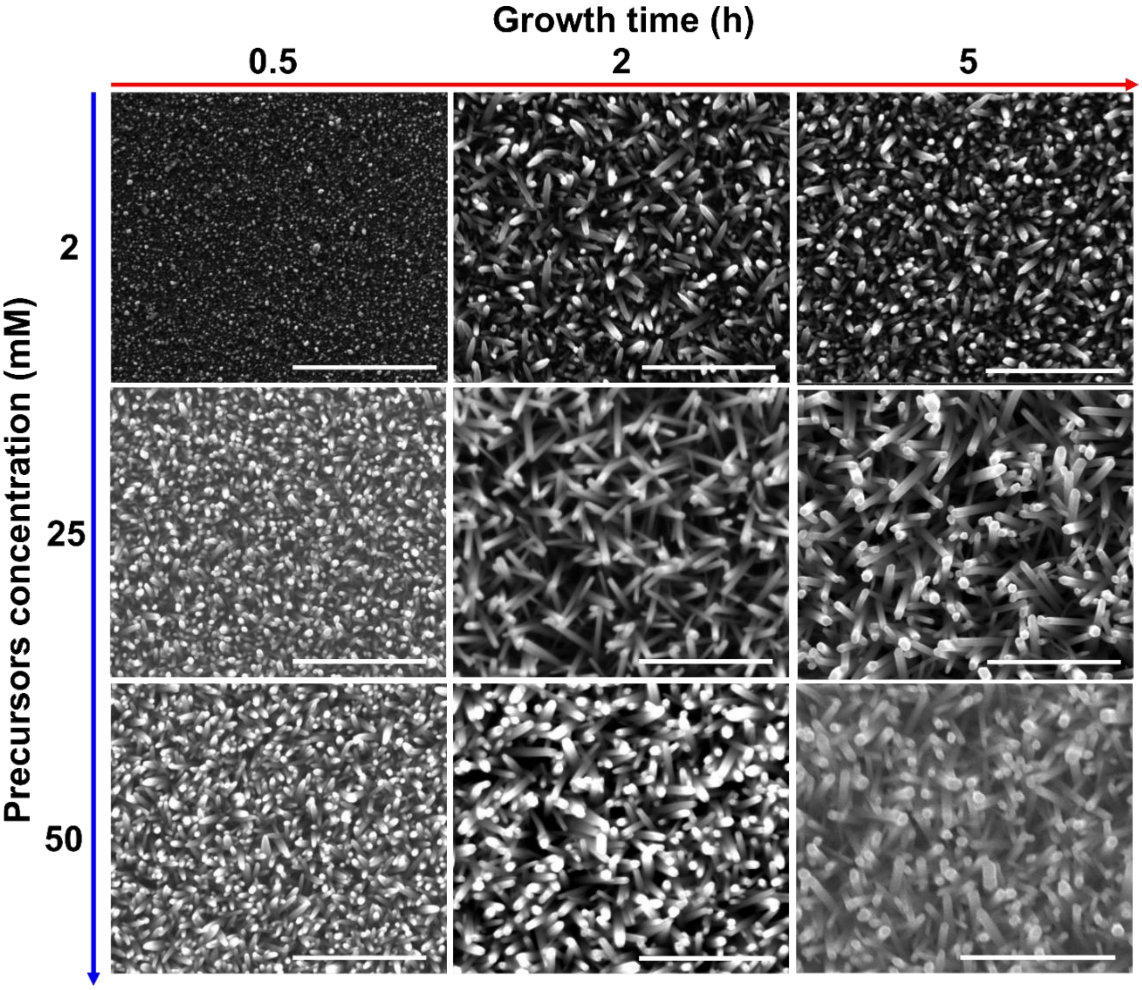

Figure 2. 3: Effect of precursors concentration and growth time on ZnO NWs in the CBD process. Scale bars: 1 µm

Effect of seed layer number

A previous study from our group has comprehensively shown how the morphology of ZnO NW arrays can be precisely tuned by changing the number of seed layer numbers.[337] In particular, a higher number of seed layer deposition gives rise to a larger grain size of ZnO on the nucleation surface, consequently promoting the vertical growth of NWs. Accordingly, we adopt those preliminary results to our experimental system and optimize our protocol for controlling the orientation of ZnO NWs via controlling the number of seed layer depositions. Our results show that a higher number of seed layer deposition, indeed, leads to a noticeable improvement in the verticality of NW's orientation, as shown in **Figure 2.4**. Also, the NWs grew on the substrate with a thicker seed layer due to the higher number of seed layer deposition, presenting a larger diameter of NW and higher surface coverage, which is in good agreement with our previous study.

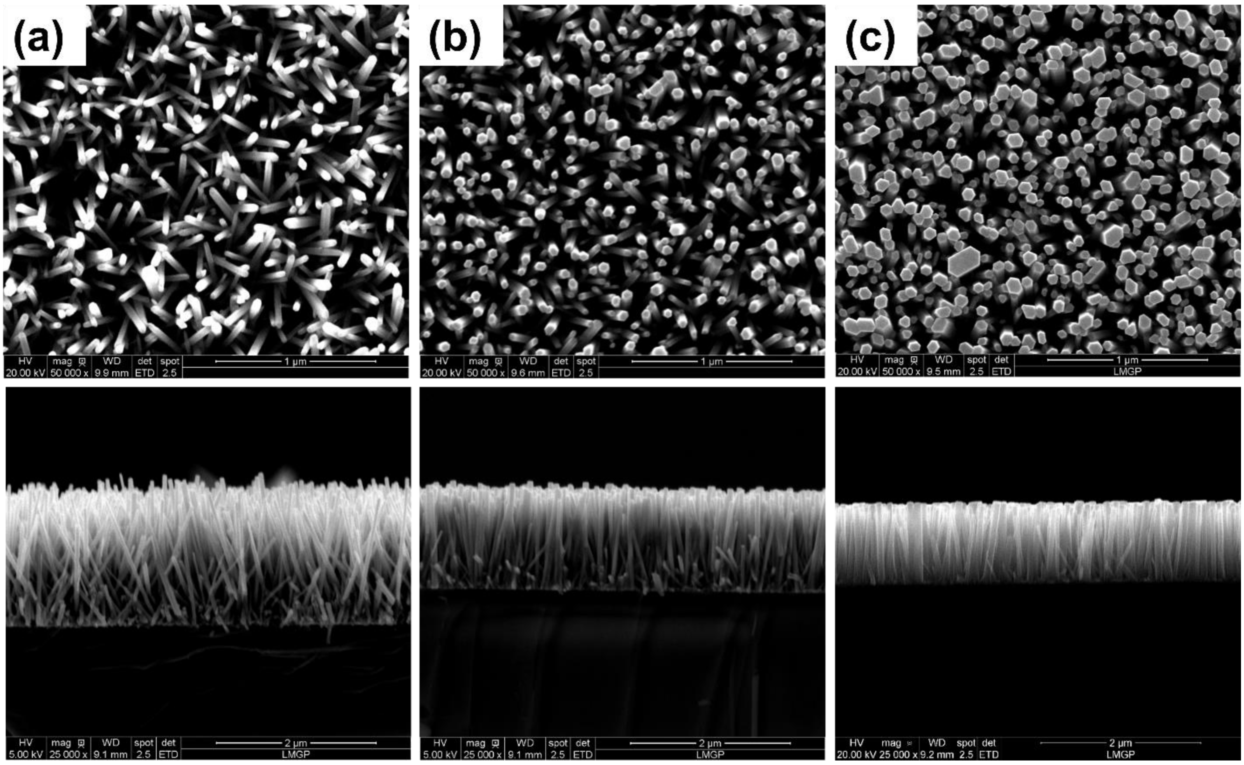

Figure 2. 4: The effect of seed layer deposition number on the verticality of ZnO NWs. SEM images of ZnO NWs grown by the CBD method for 2h on a silicon wafer substrate with (a) one, (b) two, and (c) three seed layer depositions.

2.2 Preparation of poly(dimethylsiloxane) elastomer

This study uses Sylgard 184 as a poly(dimethylsiloxane) (PDMS) source. Sylgard 184 comes as a two-component kit, a siloxane oligomers base (vinyl-terminated PDMS), and a curing agent (methylhydrosiloxane-co-dimethylsiloxane). Polymer chains go through a chemical reaction known as cross-linking or curing, which covalently connects polymer chains through crosslinkers. This process generates a 3D net-like structure known as a polymer network. An illustration of this cross-linking process is shown in **Figure 2.5**.

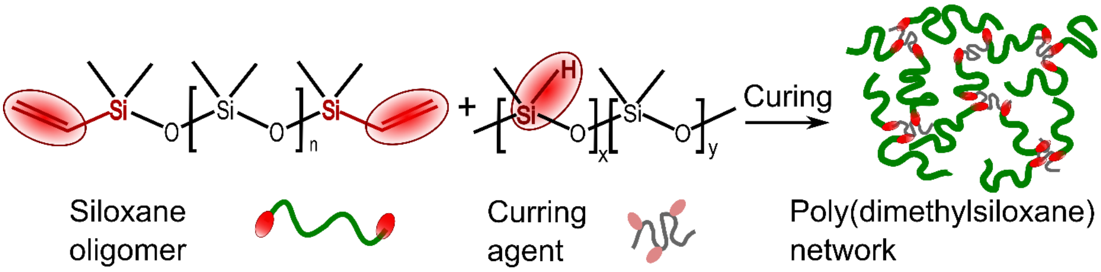

Figure 2. 5: Schematic illustration of the cross-linking process of Sylgard 184 PDMS

Experimentally, before cross-linking, PDMS is a viscous liquid. The two components, siloxane oligomers base and a curing agent, are mixed according to the manufacturer's recommendation with a 10:1 base to curing mass agent ratio. This mixture is then poured into a glass petri dish. The recommended heating temperature for curing Sylgard 184 PDMS is 80 °C for at least 2h.

2.3 Characterization techniques and properties tests

2.3.1 Scanning electron microscopy

Scanning electron microscopy (SEM) images are taken on a FEI QUANTA 250 to observe the morphology of the materials. SEM images are captured at an accelerating voltage of 20 kV for ZnO NW samples and 5 kV for polymer-contained samples, and a working distance of 10 mm. Energy-dispersive X-ray (EDX) is used to acquire the EDX composition spectra. Also, SEM images of silicone oil-lubricated samples were captured in a low-vacuum mode; liquid nitrogen can be used to cool down and stabilize infused samples.

2.3.2 UV-Vis

Optical transmittance is measured in the 350 to 900 nm wavelength range using a PerkinElmer UV-Vis-Near IR Lambda 950 spectrophotometer.

2.3.3 Raman

Raman scattering spectra are obtained using a Jobin Yvon/Horiba Labram spectrophotometer equipped with a liquid nitrogen-cooled CCD detector. A He–Ne laser is used to induce a 632.8 nm excitation line. The excitation laser beam is focused on an area smaller than 1 μm^2 using a 50× long working distance objective. Raman scattering spectra are calibrated using a silicon (100) reference sample with a theoretical peak value of 520.7 cm^{-1} at room temperature.

2.3.4 Water contact angle measurement

A macroscopic configuration of a liquid droplet can be readily captured using standard digital single-lens reflex cameras or portable capturing devices. The camera settings used in this thesis are AF-P NIKKOR 70-300 mm 1:4.5-6.3 G ED lens on a Nikon D5600. The cross-section of a typical liquid droplet can be observed using a water contact angle goniometer (**Figure 2.6**), which enables direct observation of the contour of the sessile droplet, typically using a macro zoom lens. This method is frequently used to determine the apparent contact angle of a sessile droplet on a surface. It is performed by capturing an image of a water droplet placed on a surface and observing its shape. However, care should be taken in the observation process to avoid dynamic or scaling effects.[27] Besides, this technique is highly susceptible to operating conditions, including disruption due to external vibrations, organic vapors, and dust.[38] The static water contact angle (CA) values are measured using a Krüss, DSA10-MK2 goniometer connected to a video camera. Five water droplets of 5 μL volume are dropped on different areas of the sample surface using a microsyringe, and water contact angle values are measured. The CA values are calculated and collected using the drop shape analysis software (DSA4).

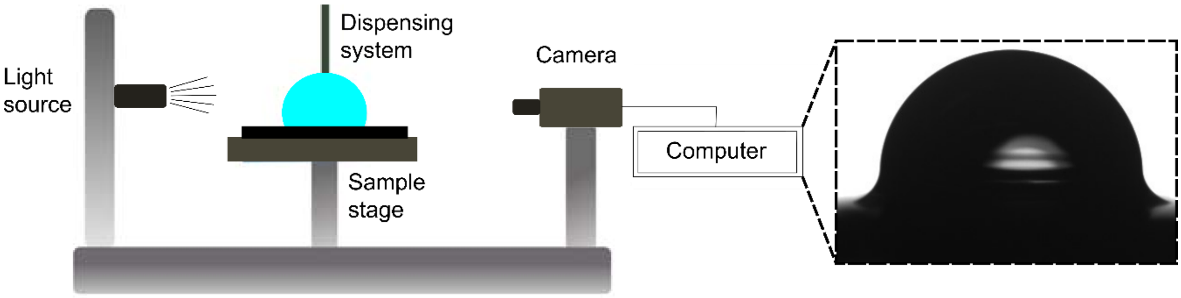

Figure 2. 6: A basic goniometer setup for observing a water droplet placed on a surface.

This figure is adapted with permission from Ref [38].

2.3.5 UV exposure

During this test, the samples are illuminated by three UVA lamps (PLS 11 W Philips), essentially emitting at a 365 nm wavelength (negligible UVB and UVC emission). The samples are placed 1 cm under the UV lamps for 3h. The process is conducted at 20 °C and 40% relative humidity in a humidity chamber.

2.3.6 Oxygen plasma treatment

The plasma treatment experiments are conducted using an oxygen plasma instrument (Evactron Decontaminator RF Plasma cleaner, XEI Scientific) at 12 W for 5 min. The oxygen plasma instrument setup is shown in **Figure 2.7**.

Figure 2. 7: The oxygen plasma instrument setup for cleaning the surface of the sample.

This chapter provided all experimental details on the growth and optimization of ZnO NW arrays by a chemical bath deposition method. In principle, this chemical bath deposition process leverages the heterogeneous growth of ZnO NW arrays on a nucleation surface (e.g., glass, silicon wafer), submerged in a bath of zinc and hydroxide ions source at a moderate temperature of 90 °C. We optimized the zinc nitrate hexahydrate and hexamethylenetetramine concentrations, and the growth time is at 25 mM and 2h, respectively. Notably, we regulated the orientation of ZnO NW arrays by controlling the number of ZnO seed layer depositions. Our results showed that a higher number of seed layer deposition leads to an improvement of verticality of NW orientation due to a larger grain size of ZnO. All details about the preparation of infiltrating polymers and lubricants used in this thesis were also described in this chapter. For example, the preparation of a poly(dimethylsiloxane) (PDMS) elastomer through a cross-linking process was described. Information about the characterization techniques, such as SEM, EDS, Raman, and water contact angle measurement and devices for sample preparation and testing (i.e., UV lamps, oxygen plasma system, thermal copper substrate) were fully provided. We will use these materials and techniques for our studies in the following chapters.

Chapter 3.

Multifunctional Composite Films with Vertically Aligned ZnO Nanowires by Leaching-enabled Capillary Rise Infiltration

Reproduced from Ref [342] with permission from the Royal Society of Chemistry.

Contents

Nanocomposite films (NCFs), having vertically aligned ZnO nanowires (NWs), exhibit several beneficial properties owing to the unique morphology of ZnO NWs. One of the critical challenges in fabricating such a NCF is retaining the original alignment of NWs throughout NCF fabrication. Conventional methods require multiple steps and are thus time-consuming and only suitable for lab-scale fabrication, limiting their widespread applicability. This chapter describes a new method for generating a NCF with vertically aligned ZnO NWs, leveraging leaching-enabled capillary rise infiltration of uncross-linked and mobile oligomers from a poly(dimethylsiloxane) (PDMS) slab into the space between NWs. PDMS-infiltrated ZnO NW NCFs present several essential properties, including superhydrophobicity, self-cleaning, solvent resistance, anti-icing, high transparency, and anti-reflection properties. The NCF can also recover its superhydrophobicity after being compromised through plasma treatments or exposure to intense UV irradiation. Our method represents a straightforward, efficient, and potentially scalable strategy to create multifunctional NCFs while maintaining precise control over the original nanoscale structure of vertically aligned ZnO NW arrays for a wide range of critical applications. The results shown in this chapter were published in the following paper: H. Tran, B. Venkatesh, Y. Kim, D. Lee, D. Riassetto, *Nanoscale* **2019**, 11, 22099 – 22107.

3.1 Introduction

Nanocomposite films (NCFs), consisting of inorganic nanomaterials and polymers, represent an important class of functional structures with synergistic properties.[31, 32, 35, 343-349] Unique functionality and emergent properties such as exceptionally high strength and toughness can be achieved by extremely high loadings of nanoparticles (> 50 vol%) as well as the inclusion of anisotropic nanomaterials such as high aspect ratio nanowires (NWs) and their alignment.[31, 244, 344, 346, 350, 351] In particular, vertical alignment of high aspect ratio NWs provides a powerful approach to fabricating NCFs with a wide range of useful functionalities owing to its unique morphology.[244, 351-358] Amongst NW materials, zinc oxide (ZnO) NWs, which can be prepared using a simple method such as chemical bath deposition described in Chapter 2, offer a wide range of valuable features such as high strength, photocatalytic, electronic, optical, and antibacterial properties.[122, 308, 359-361] NCFs incorporating vertically aligned ZnO NWs have demonstrated useful properties owing to their morphology.[244, 277, 354, 361-367] For example, Kim *et al*.[354] designed antireflective layers consisting of vertically aligned ZnO NWs and a polymeric matrix. A polymer precursor was cast onto the surface of the ZnO NWs, followed by a curing step. The cured polymer layer containing ZnO NWs at the outermost surface was then mechanically peeled off the substrate for applications. More recently, Yeom *et al*.[244] reported the fabrication of a tooth enamel-inspired nanocomposite by filling the interstitial space between vertically oriented ZnO NWs using layer-by-layer (LbL) assembly. By repeating the growth of ZnO NWs and LbL assembly, light-weight multilayer nanocomposites that exhibit ultra-high stiffness and vibrational damping were fabricated.

One of the key features that give rise to such useful functionalities to these NCFs is the vertical alignment of the NWs; it is, however, challenging to retain vertical alignment during nanocomposite fabrication. Solution-based processes such as mixing/dispersing NWs are not suitable as the alignment is difficult to achieve without applying an external field such as a magnetic or electric field.[352, 368-370] Given that several methods can directly produce vertically aligned NW arrays on solid surfaces, producing NCFs without detaching the vertically grown NWs from the substrate provides the most straightforward approach to retaining the vertical alignment of NWs. As described above, polymer casting followed by curing as well as LbL assembly has been successfully used to produce NCFs based on vertically aligned arrays of ZnO NWs.[244, 353, 371] However, these processes involve multiple steps, thus being time-consuming and only suitable for lab-scale production, consequently limiting their widespread applicability.

This chapter describes the fabrication of multifunctional NCFs with vertically aligned ZnO NWs via leaching-enabled capillary rise infiltration (LeCaRI) of uncross-linked and mobile oligomers in an elastomer network. The polymer infiltration-based method overcomes the challenges of traditional methods of making NCFs. LeCaRI can be performed while retaining the original morphology of the nanomaterials; thus, by implementing LeCaRI, it is possible to fabricate NCFs with vertically aligned ZnO NWs in a straightforward manner, making it a potentially scalable manufacturing method. We show that NCFs with vertically aligned ZnO NWs fabricated via LeCaRI have multiple useful properties, including superhydrophobicity, self-cleaning, solvent resistance, anti-icing properties, high transparency, and anti-reflection property. Successful fabrication of multifunctional NCFs with vertically aligned ZnO NWs demonstrates that LeCaRI is a powerful method to produce NCFs with well-controlled arrangements of functional and anisotropic nanomaterials and can potentially enable scalable manufacturing of multifunctional NCFs with various types of polymers and nanomaterials.

3.2 Poly(dimethylsiloxane) elastomer with uncross-linked oligomers

3.2.1 Leaching of uncross-linked oligomers

PDMS has been used in many applications because of its ease of use and several useful properties, such as high transparency, excellent mechanical properties, flexibility, and hydrophobicity.[372, 373] It is readily accessible as a commercial product. PDMS -based devices are prepared through the cross-linking process, as described in **Chapter 2**. However, PDMS -based devices designed using Sylgard 184 exhibit two significant drawbacks despite their tremendous applicability: leaching uncross-linked oligomers from the network and being fouled quickly by hydrophobic molecules from the surrounding medium.[374-377] Previous studies showed that in a PDMS elastomer there are nearly 5% by weight of oligomers stay uncross-linked and mobile even after an extensive curing process.[174, 374, 378] A schematic illustration of PDMS oligomers that are not incorporated in the polymer network is shown in **Figure 3.1**. These uncross-linked and mobile oligomers are low molecular weight species that can diffuse to the surface and alter the surface properties of the elastomer.[174, 379-381] Thus, the leaching of these uncross-linked and mobile oligomers has been identified as one of the critical challenges in using PDMS elastomers. For instance, they can contaminate the cell culture medium.[374, 382] The leaching of uncross-linked and mobile oligomers from the PDMS network was experimentally evidenced by their presence in the solution produced from a PDMS cell culture device using mass spectrometry.[374] In addition, the extraction of the uncross-linked oligomers from a PDMS network through capillarity at the water-air interface was successfully established, as shown in **Figure 3.2**.[174, 175] Generally, the leaching of uncross-linked and mobile chains from a PDMS network is considered a problem. Consequently, several approaches are employed to remove these uncross-linked oligomers, such as Soxhlet extraction,[379] extensive extractions in organic solvents,[174] and extended baking in an oven to reach a complete cross-linking.[380]

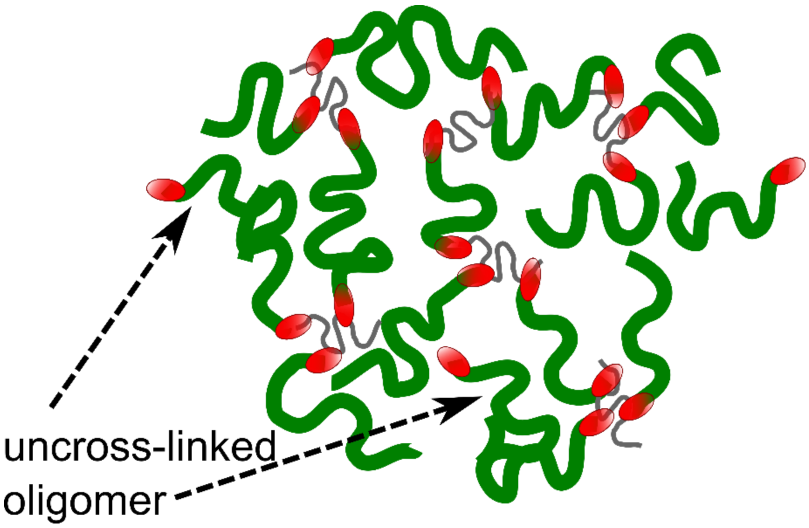

Figure 3. 1 : Schematic illustration of uncross-linked and mobile oligomers in a PDMS elastomer.

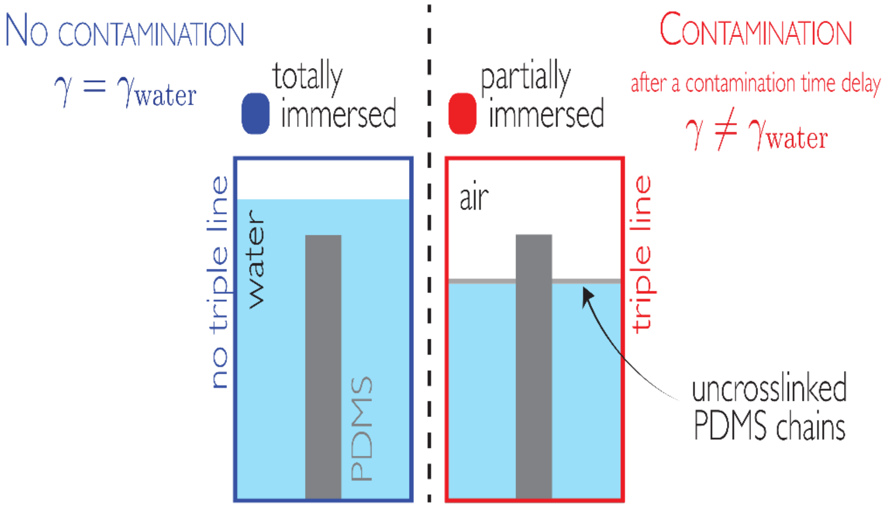

Figure 3. 2: Schematic illustration of the extraction of uncross-linked oligomers from a PDMS elastomer at PDMS-water (left side) and PDMS-water-air interfaces (right side).

This figure is adapted with permission from Ref [175].

However, the leaching of uncross-linked and mobile oligomers has also led to several remarkable observations. For example, the extraction of uncross-linked oligomers from a PDMS elastomer at water-air interfaces by capillarity represents a remarkable strategy for manipulating the dynamics of droplets on the surface of the elastomer.[174] As shown in **Figure 3.3**a,b, a water droplet placed on a tilted PDMS elastomer presents two-speed regimes.

The uncross-linked oligomers at the PDMS elastomer and the water droplet interface have been identified as the critical attributes for this phenomenon. These migrated uncross-linked oligomers are shown to contaminate and consequently lower the surface tension of the water droplet, resulting in the speed transition when a critical amount of migrated oligomers is accumulated, as shown in **Figure 3.3**c. Such a speed transition is indeed attributed to the uncross-linked oligomers. Such a phenomenon is not present when these uncross-linked oligomers are removed beforehand and reemerges when re-filling the elastomer with silicone oil. Overall, several useful properties have been achieved by taking advantage of the leaching of uncross-linked oligomers, including adhesion of a silica microbead at a four-phase contact line,[383] osmocapillary phase-separation,[384] drag reduction on a superhydrophobic surface,[385] shaping of composite structures,[386] and manipulation of droplet dynamics.[174] These findings thus suggest a huge potential resulting from the leaching of uncross-linked and mobile oligomers from a PDMS network.

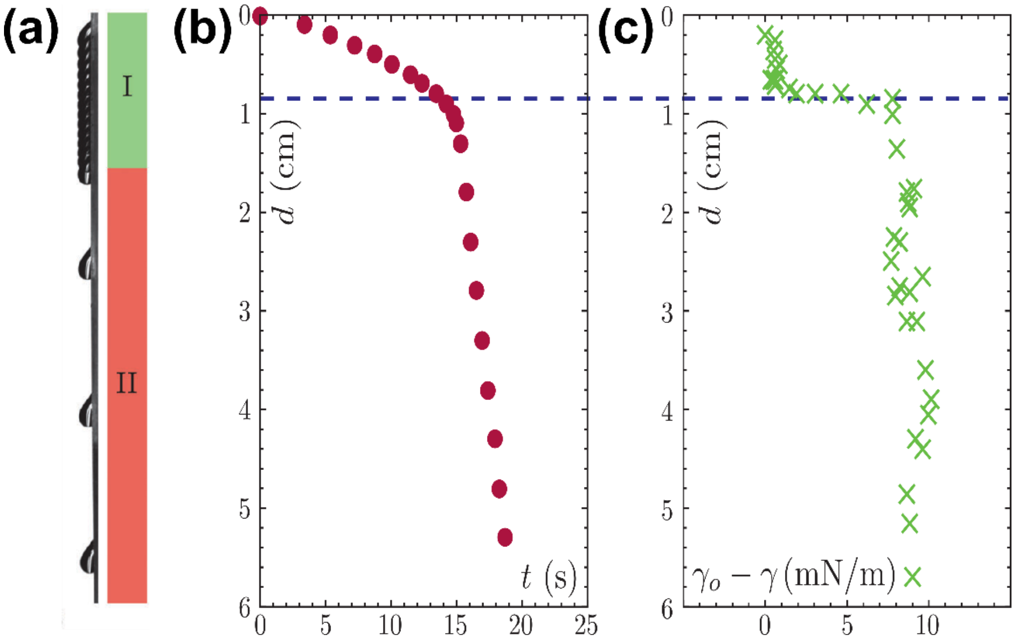

Figure 3. 3: The change in droplet dynamic due to the presence of uncross-linked oligomers. (a) Two-speed regimes (I and II) of a water droplet on a tilted PDMS elastomer. Snapshots are captured every 1.28 s. (b) Distance vs. time diagram: d is the distance traveled by the water droplet, and t is time. (c) Distance vs. surface tension diagram: ($\gamma_0 - \gamma$) is the change between the surface tension of pure water and the observed surface tension of the droplet that has traveled a distance d.

This figure is adapted with permission from Refs [174] [175].

3.2.2 Transfer of uncross-linked oligomers

Notably, the leaching of uncross-linked oligomers represents an innovative approach for selectively transferring PDMS to other surfaces, which holds great potential for various applications. For example, by bringing a PDMS micro stamp into close contact with a silicon surface, the uncross-linked and mobile oligomers from the PDMS network move out to the contact areas and form a PDMS oligomer layer on the silicon surface, as shown in **Figure 3.4**a.[387] After contacting the PDMS stamp, the silicon substrate presents uniform arrays of patterns. The patterns on the surface of the silicon substrate present an identical shape to the PDMS stamp, as shown in **Figure 3.4**b. These results thus suggest the potential for purposeful transfer of uncross-linked and mobile oligomers from a PDMS elastomer to another surface in a straightforward fashion and with precise control.

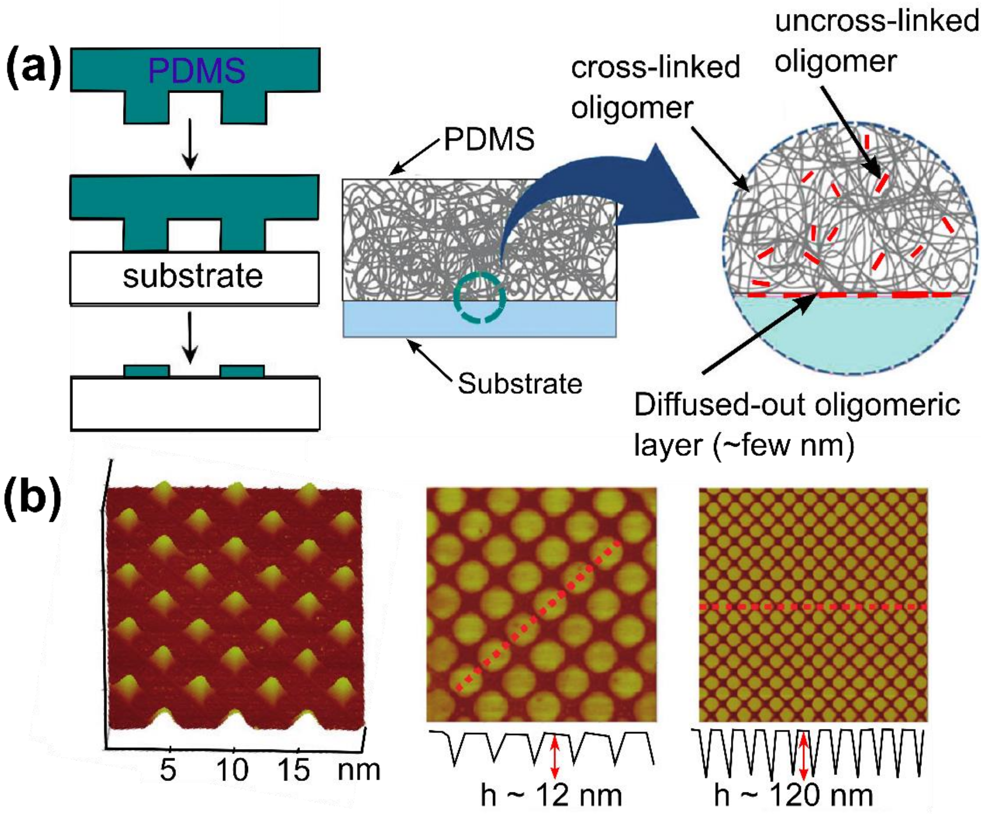

Figure 3. 4: Pattern transfer by taking advantage of the leaching ability of the uncross-linked and mobile oligomers from a PDMS stamp. (a) A schematic illustration of the pattern transfer process shows the diffusion of uncross-linked and mobile oligomers from the PDMS network to the contact areas between the PDMS stamp and the substrate. (b) Surface profiles of the patterned locations on the substrate after the pattern transfer via AFM images.

Adapted with minor modifications from Ref [387].

In NCF fabrication, the ability to induce leaching of these uncross-linked and mobile oligomers from the elastomer network and their infiltration into interstitial pores between nanomaterials makes it an ideal platform to produce NCFs. Indeed, a recent report has shown that mobile oligomeric species can be induced to undergo infiltration into densely packed nanoparticle films from the PDMS network to produce NCFs with extremely high filler fractions (> 50 vol%).[388] As shown in **Figure 3.5**, the uncross-linked and mobile oligomers from the PDMS network are successfully infiltrated into the porous structure of the nanoparticle film. Furthermore, a patterned nanocomposite film can be fabricated using a PDMS stamp with precise control. Thus, the leaching of uncross-linked and mobile oligomers from a PDMS elastomer has shown a significant advantage in patterning surfaces, creating polymer-infiltrated nanoparticle films, and accelerating the moving velocity of droplets. However, the thickness of transferred oligomeric layers is relatively low, generally from a few nanometers to around 250 nm. Despite its tremendous potential, the application of such leaching of uncross-linked and mobile oligomers from a PDMS elastomer to systems having anisotropic features and a much greater thickness, such as ZnO NWs film (> 1 µm), has not been already reported.

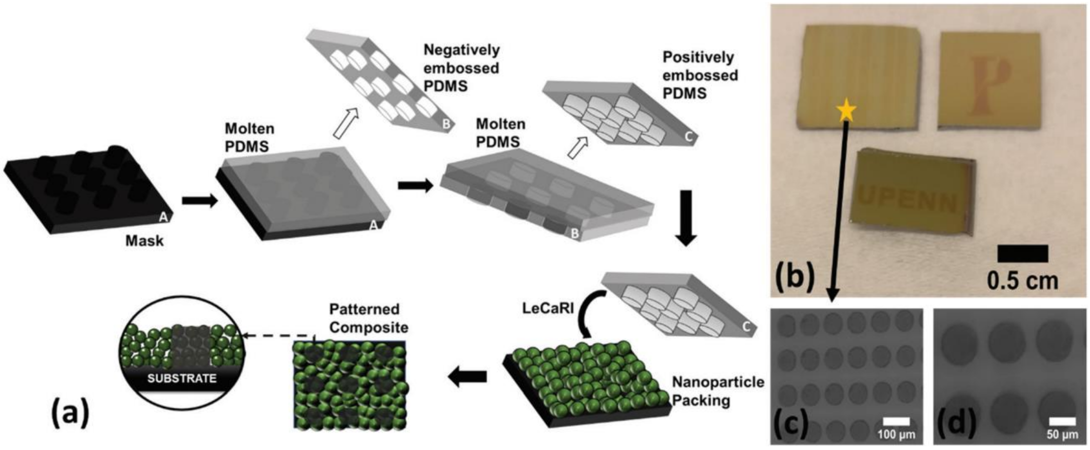

Figure 3. 5: Patterning nanoparticle films using the leaching of uncross-linked oligomers from a PDMS stamp into the pore structure of the nanoparticle film.

This figure is adapted with permission from Ref [388].

3.3 Leaching-enabled capillary rise infiltration with ZnO NWs

3.3.1 Fabrication of nanocomposite films

Our method takes advantage of the growth of vertically aligned ZnO NWs on a solid substrate and the infiltration of oligomers from an elastomer network. As aforementioned, leaching uncross-linked and mobile oligomers from an elastomer network are generally considered a drawback. However, the ability to induce leaching of these uncross-linked and mobile oligomers from the elastomer network and induce their infiltration into interstitial pores between nanomaterials makes it an ideal platform for producing NCFs that retain the original alignment of ZnO NW arrays. The detailed procedures for making ZnO NW arrays and PDMS elastomers are described in **Chapter 2**. Briefly, ZnO NWs are prepared by the ZnO-seeded chemical bath deposition growth,[288, 336, 337] having a diameter, a length, and a horizontal angle of 73±16 nm, 1.2±0.17 µm, and 89±12°, respectively, on glass slides (2.5 cm × 2.5 cm). Before Leaching-Enabled Capillary Rise Infiltration (LeCaRI), ZnO NW arrays on glass slides are placed in the oven at 540 °C for 5 min to remove organic contaminants and water vapor, which exists between adjacent nanowires. Elastomer samples are made as described in **Chapter 2**. These PDMS elastomers contain a significant amount of uncross-linked PDMS oligomer chains for the LeCaRI experiment. The uncross-linked PDMS oligomers can leach out the PDMS elastomer into the surface and the interstices between ZnO NWs film at room temperature. However, because the thickness of the ZnO NWs film (1.2 ± 0.17 µm) is much greater than that of the SiO_2 nanoparticle films (250 nm) in the previous work,[388] we increase the processing temperature to accelerate the infiltration, resulting in increasing amounts of PDMS oligomers transferred from the PDMS elastomer to the ZnO NWs.

The process of fabricating a NCF with vertically aligned ZnO NWs via LeCaRI is schematically presented in **Figure 3.6**. ZnO NW arrays are brought into conformal contact with a slab of PDMS elastomer (2.5 cm × 2.5 cm × 0.25 cm) to induce the transfer of uncross-linked and mobile oligomers from the elastomer into the crevices of the ZnO NW arrays. To maximize the number of transferred oligomers, the sample with PDMS elastomer atop ZnO NW arrays should be placed in an oven maintained at 150 °C. Although the top of the ZnO NW array does not present a very smooth surface, PDMS can be induced to form conformal contact with the ZnO NW array due to its compliance and flexibility. Subsequently, the oligomer infiltrated ZnO NW arrays are heated at a maintained temperature of 80 °C for 1h to cure the unreacted chains transferred into the interstices of ZnO NW arrays. Note that the sample with 10 s contact with PDMS elastomer at room temperature is hereafter referred to as NCF-10s@RT, while the sample subjected to LeCaRI for a long time at a higher temperature (24h at 150 °C), is hereafter referred to as NCF-24h@150 °C.

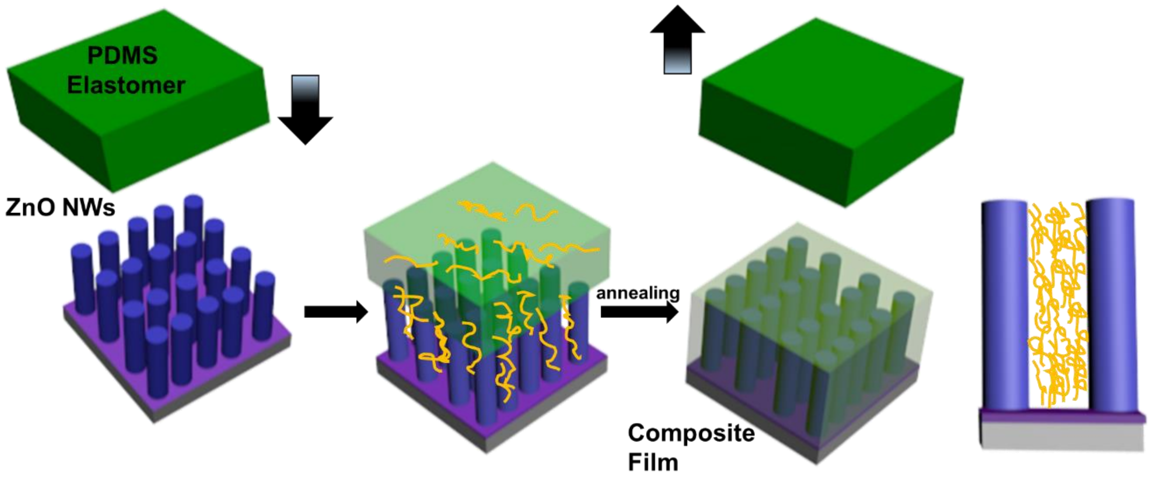

Figure 3. 6: Schematic illustration showing the LeCaRI process for fabricating nanocomposite films with vertically aligned ZnO NWs. For clarity, schematic illustrations are not drawn to scale.

3.3.2 Morphology of materials

Optical microscope observation

The surface of ZnO NW arrays before and after infiltration is captured using a Leica DM LM microscope with a modular design connected with a high-quality video camera (Olympus SC30). Images are taken using a 50× long working distance objective. The photos were taken and collected by using the Stream Start software. The optical microscope images show that after infiltrating, the surface of the ZnO NW array becomes more homogenous after infiltration, likely due to the filling of the crevices between NWs by oligomer chains, as shown in **Figure 3.7**.

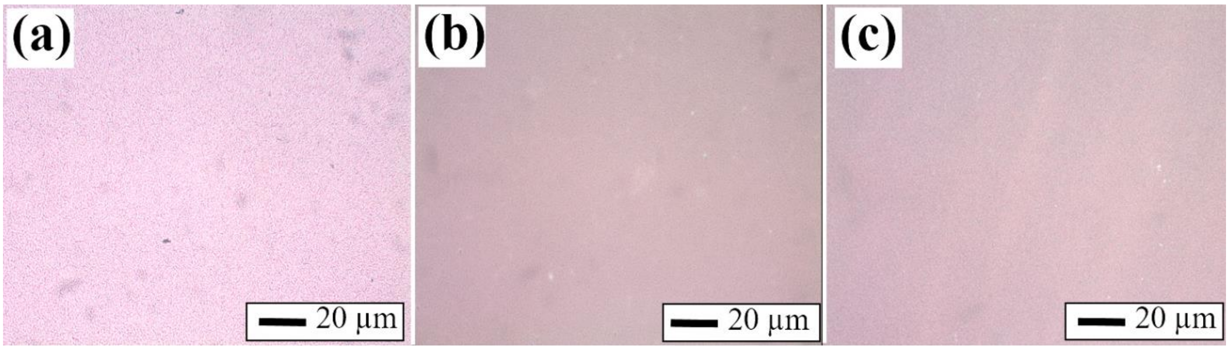

Figure 3. 7: Optical microscope of ZnO NWs, PDMS-ZnO NWs-10s, and PDMS-ZnO NWs-150 °C-24h

Scanning electron microscopy

The morphology of the ZnO NW arrays before and after infiltration for different duration are observed through scanning electron microscopy (SEM), as shown in **Figure 3.8**. The SEM images confirm the presence of PDMS oligomers in the ZnO NW array after LeCaRI. Even after a very short infiltration duration (NCF-10s@RT), the oligomers have partially filled the interstices and surfaces between NWs, as shown in **Figure 3.8**b, e. For the sample subjected to LeCaRI for a long time at a higher temperature (NCF-24h@150 °C), the crevices in the ZnO NW arrays are almost filled, forming a uniform NCF, as shown in **Figure 3.8**c, f. EDS profiles are provided to confirm the presence of PDMS oligomer chains in the crevices of the ZnO NW arrays, as evidenced by an increase in the amount of silicon in the NCFs after LeCaRI, as shown in **Figure 3.8**g-i and **Figure 3.9**.

Most importantly, ZnO NWs retain their vertical alignment after the LeCaRI process. Despite the filling of the space between ZnO NWs, the top surface of the NW array is not fully covered with a visible and smooth layer of PDMS (**Figure 3.8**f) and thus retains the nanoscale surface roughness of the ZnO NW array. As we will show later, such surface roughness could play an important role in determining the wetting properties of these NCFs.

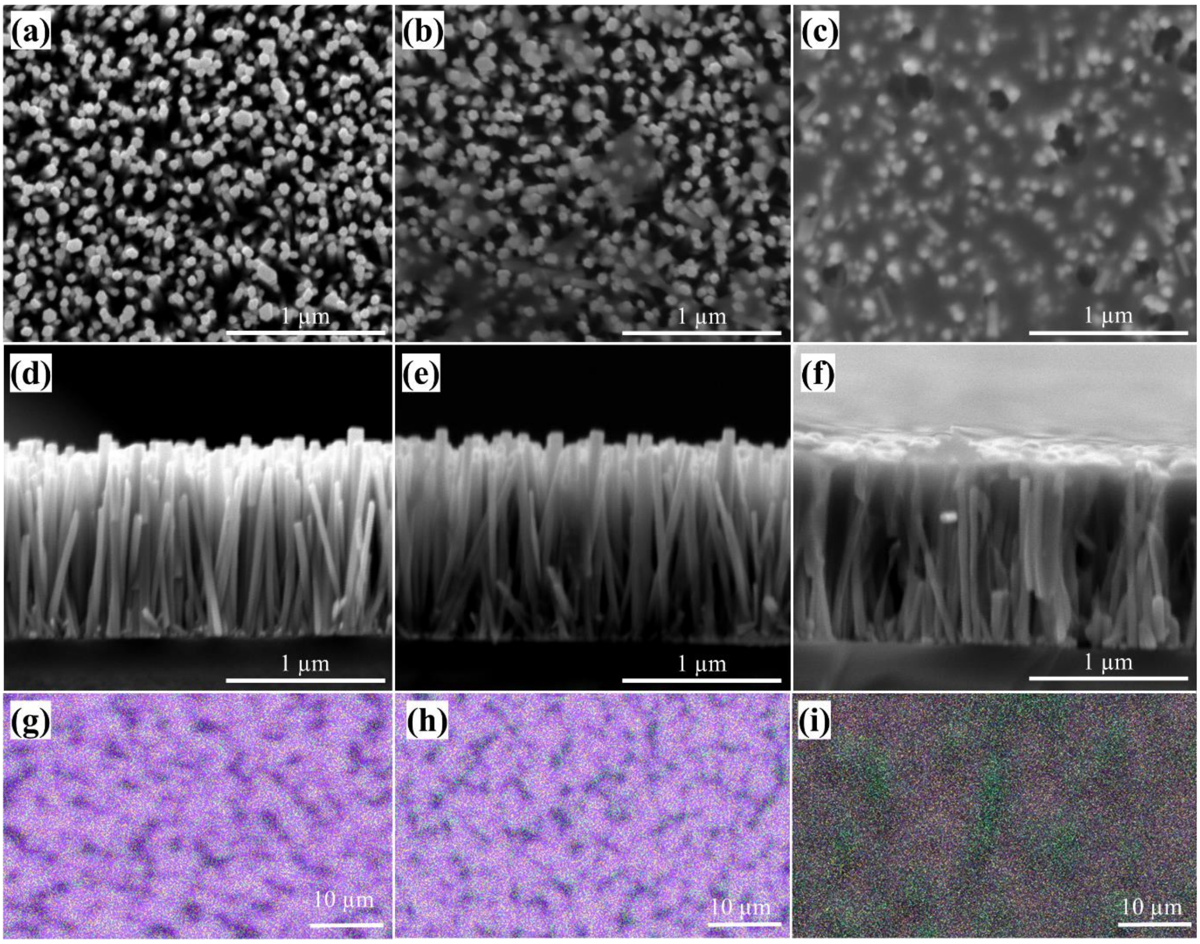

Figure 3. 8: (a, b, c) Top-view, (d, e, f) cross-section SEM images, and (g, h, i) EDS mapping profiles of ZnO NWs, NCF-10s@RT, and NCF-24h@150 °C, respectively. Green and violet dots represent the presence of Si and Zn, respectively.

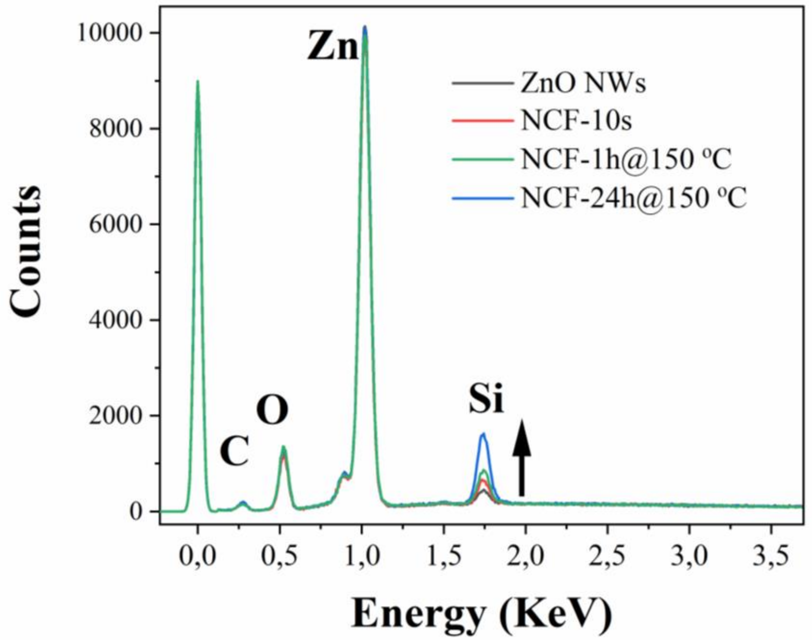

Figure 3. 9: EDS profile of ZnO NWs and nanocomposite films.

3.3.3 Characterization by Raman spectroscopy

Raman scattering spectroscopy is used to confirm the presence of PDMS oligomers in the NCFs. The Raman spectra are taken in the range of 50-3700 cm^{-1}. **Figure 3.10** shows that besides the typical Raman peaks for ZnO NWs, there are peaks associated with Si-O-Si symmetric stretching (488 cm^{-1}), Si-CH_3 symmetric rocking (687 cm^{-1}), CH_3 symmetric stretching (2907 cm^{-1}), and CH_3 asymmetric stretching (2965 cm^{-1}) of PDMS.[389, 390] The right side is the spectra taken between 50-750 cm^{-1} for more detailed analysis. This result again confirms the presence of PDMS oligomer chains in the NCFs upon the LeCaRI transfer mechanism and the increase of PDMS loading with LeCaRI duration.

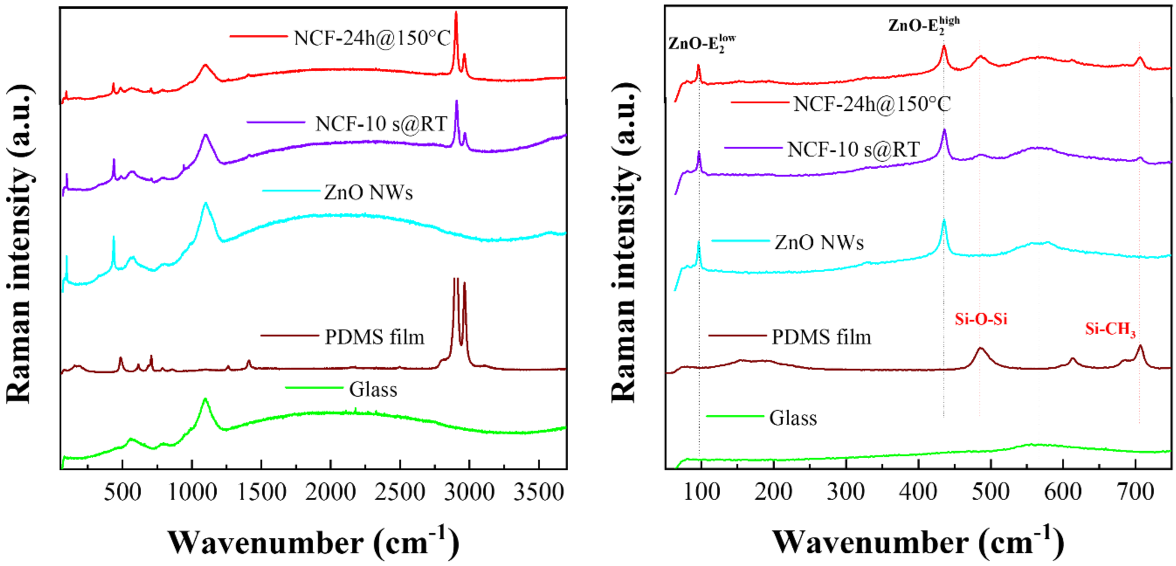

Figure 3. 10: Raman spectra of glass, ZnO NWs, PDMS film, NCF-10s@RT, and NCF-24h@150 °C (a) in the range of 50-3700 cm^{-1} and (b) in the range of 50-750 cm^{-1}.

3.3.4 Inverse process of infiltration via LeCaRI

To confirm that oligomers infiltrate the interstices between NWs via capillarity, we conducted an inverted infiltration experiment to eliminate the effect of gravity. The substrate containing ZnO NW arrays is placed on top of a PDMS elastomer in which the ZnO NW arrays were brought into conformal contact with the PDMS elastomer for 10 seconds to induce the transfer of uncross-linked and mobile chains from the elastomer network into the interstices of the ZnO NW arrays. Finally, the infiltrated ZnO NW arrays were heated to 80 °C for 1h to cure the unreacted chains transferred into the interstices of ZnO NW arrays. The schematic illustration and SEM images showing the inverse LeCaRI process to fabricate nanocomposite films with vertically aligned ZnO NWs via inverse LeCaRI are shown in **Figure 3.11**. With the results obtained with both configurations (normal and inverse) being precisely the same, we can conclude that the infiltration of PDMS is not induced by gravity but mainly by capillary effects confirming the LeCaRI transfer mechanism of PDMS.

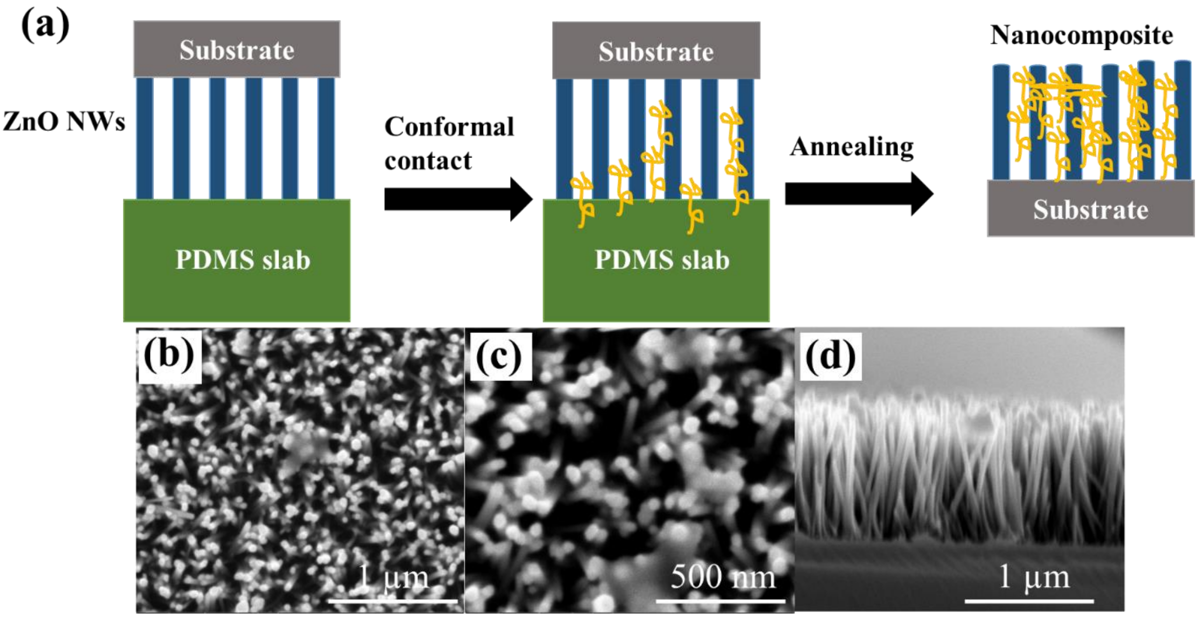

Figure 3. 11: (a) Schematic illustration showing the inverted LeCaRI process to fabricate nanocomposite films with vertically aligned ZnO NWs. For clarity, schematic illustrations are not drawn to scale. (b) and (c) Top-view SEM images at different magnifications, and (d) side-view SEM images of NCF-10s@RT produced via inverted LeCaRI.

3.3.5 Optical properties

One of the disadvantages of using ZnO NW arrays on a solid surface is that they scatter light and thus make it difficult to use them in applications that require high transparency, such as coatings on windows and solar cells. With a refractive index of 2.0 for bulk ZnO and a non-continuous morphology, the significant refraction and scattering of incident light at the air−ZnO interface leads to a significant transmittance loss through ZnO NW arrays.[391] Infiltration of PDMS oligomers into the interstices can significantly reduce light scattering by reducing the difference in the refractive index between the NW phase and the continuous phase of the NCF. We test this idea by characterizing the transmittance of the ZnO NW arrays before and after LeCaRI via UV-Vis spectroscopy (**Figure 3.12**). A bare glass slide and a PDMS film on glass are also characterized as references. **Figure 3.12**a clearly shows that infiltration of PDMS oligomers into the ZnO NW arrays significantly enhances the transmission of the NCFs. The enhancement of the transparency upon LeCaRI also can be observed on macroscopic photos of the samples, as shown in **Figure 3.12**b. Remarkably, the transmission of the NCF-24h@150 °C sample shows that this sample is more transmissive than a bare glass slide in most of the visible range, suggesting that the NCF is acting as an anti-reflection coating, as shown in **Figure 3.12**c. We believe such anti-reflection property is due to the graded transition of refractive index $n_{PDMS} < n_{ZnO}$ across the nanocomposite films.[363, 392] Digital photograph images of NCFs under light illumination showing the suppression of reflection compared to the glass side demonstrate the anti-reflection property of the NCFs (**Figure 3.12**d).

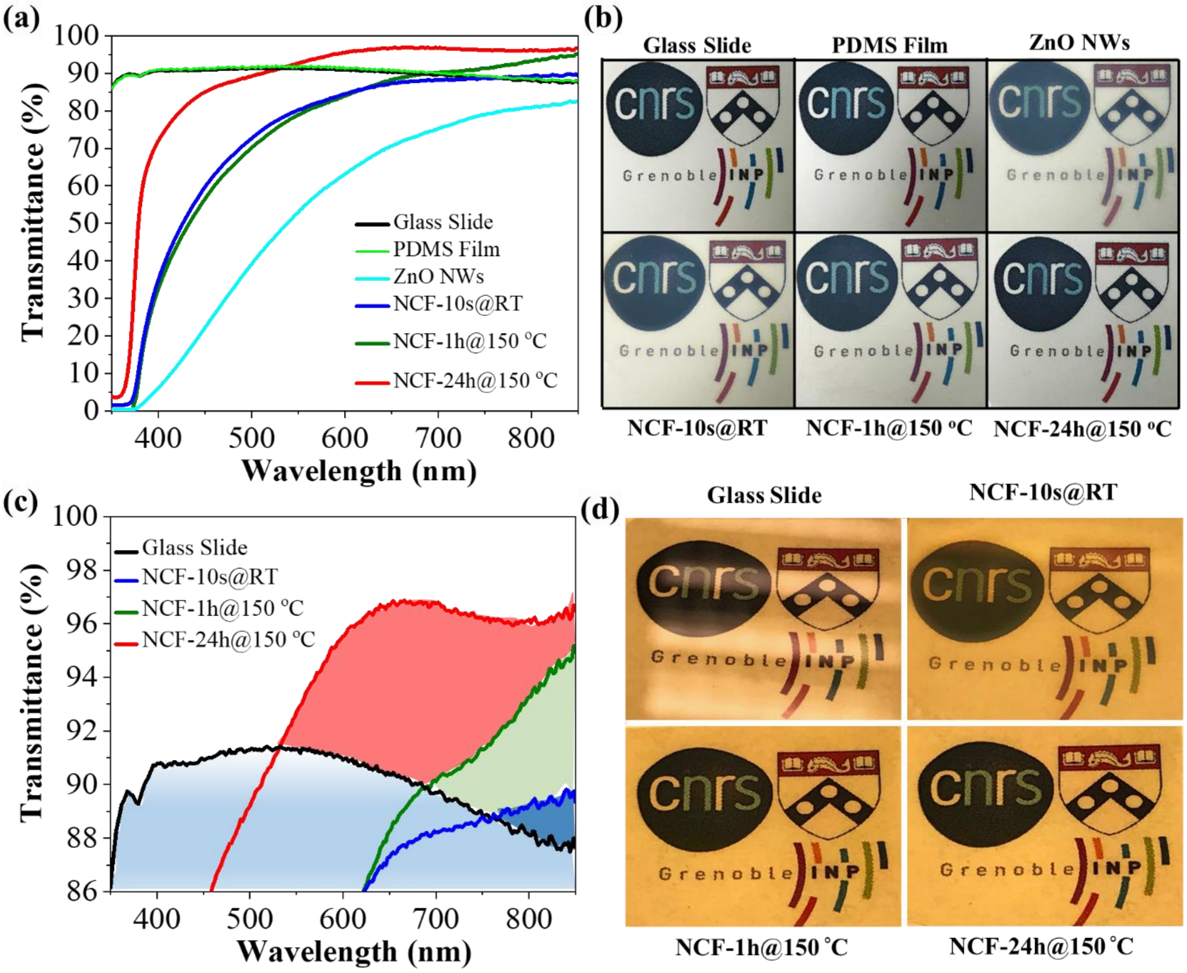

Figure 3. 12: (a) Transmittance spectra of glass side, PDMS film, ZnO NWs, and PDMS-infiltrated ZnO NWs, (b) corresponding digital photos of the samples showing their transparency, (c) enlarged transmittance spectra of glass side, NCF-10s@RT, NCF-1h@150 °C, and NCF-24h@150 °C, and (d) digital photograph images of NCFs under light illumination showing the suppression of reflection compared to the glass slide.

3.3.6 Surface wettability

The uncross-linked and mobile oligomers leached from a PDMS elastomer have been found to drastically change the wettability on the surface of the PDMS elastomer.[174, 175] We thus envision unique wetting properties derived from these PDMS/ZnO NW NCFs. The surface of ZnO NW arrays is highly hydrophilic, whereas the surface of planar PDMS is hydrophobic. Upon infiltration of PDMS via LeCaRI, the surface of the ZnO NW arrays becomes superhydrophobic even after 10 seconds of infiltration at room temperature, as shown in **Figure 3.13**a. Regardless of the infiltration time**,** the surface of the NCFs maintains its superhydrophobicity over one year of storage in the ambient air. When a droplet of water is brought into dynamic contact with the NCF surface, the droplet does not stick to the surface even if it is pressed onto the surface.

In contrast, a water droplet sticks readily to the smooth PDMS film, as shown in **Figure 3.13**b. These results strongly suggest that LeCaRI of PDMS oligomers into the ZnO NW arrays have rendered these surfaces superhydrophobic, likely owing to the combination of surface roughness of the NW array and the hydrophobicity of PDMS, resulting in the so-called Cassie-Baxter state.[393] Even after partial infiltration due to a very short contact time (e.g., 10 sec) at room temperature, the surface of NWs is rendered superhydrophobic thanks to the transfer of oligomeric PDMS into the interstices between ZnO NWs. We believe even a small amount of PDMS in the interstices facilitates air trapping, thus making the surface superhydrophobic. Given the simplicity of the LeCaRI method, superhydrophobic materials can be quickly prepared at room temperature without the use of any extra surface modifiers (e.g., fluorine-containing reagents).

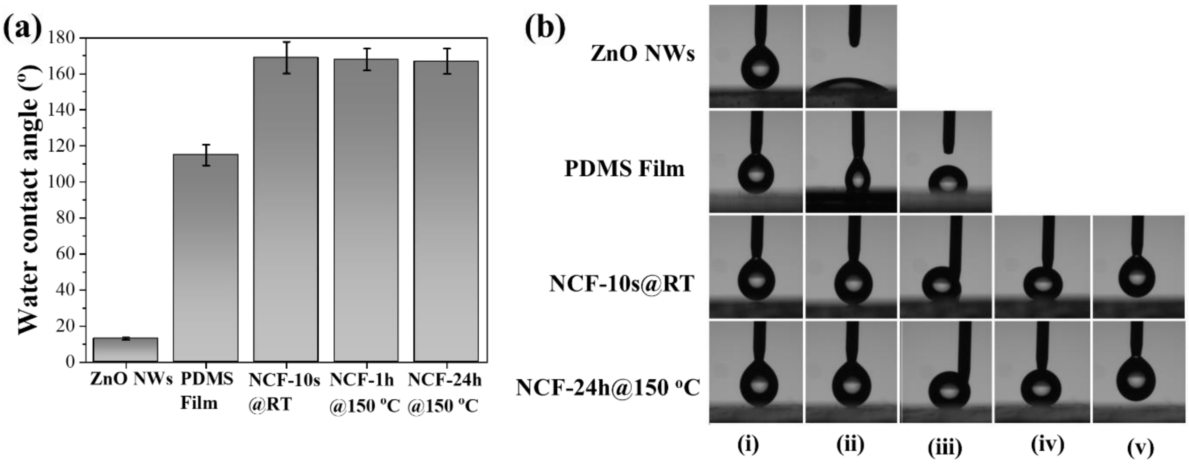

Figure 3. 13: (a) Static water contact angles on ZnO NWs, PDMS film, and ZnO/PDMS LeCaRI NCFs and (b) time-lapse photos showing the wetting properties of the ZnO NWs, PDMS film, and PDMS/ZnO NW NCFs under dynamic contact with a water droplet. A water droplet is brought in contact with the surface of the sample and then pressed onto the surface. Subsequently, the droplet is retracted from the surface. i-v steps represent the initial state (not in contact), initial contact upon approach, pressed contact, right before detachment during retraction, and full retraction, respectively.

3.4 Multifunctionality of the PDMS-ZnO NW NCF

3.4.1 Self-cleaning

A superhydrophobic surface, exhibiting a water contact angle (WCA) larger than 150° and easy roll-off of water droplets, makes an excellent self-cleaning surface with a wide range of applications.[64, 76, 394] **Figure 3.14** shows self-cleaning behaviors of ZnO NWs film, PDMS film, and PDMS/ZnO NW NCF-10s@RT when their surfaces are contaminated by soil and placed horizontally in a plastic container, then subsequently exposed to droplets of Orange G solution (concentration of 5×10^{-5} M, added to facilitate visual inspection of self-cleaning behavior) from a syringe that is placed 5 cm above the sample surface. Droplets readily spread when they are in contact with the highly hydrophilic surface of the ZnO NW arrays (**Figure 3.14**a), whereas droplets stick to the hydrophobic surface of PDMS (**Figure 3.14**b). Due to its superhydrophobic surface, PDMS/ZnO NW NCF-10s@RT exhibits an excellent self-cleaning behavior by inducing roll-off of water droplets that pick up and remove the contaminants on the surface shown in **Figure 3.14**c.

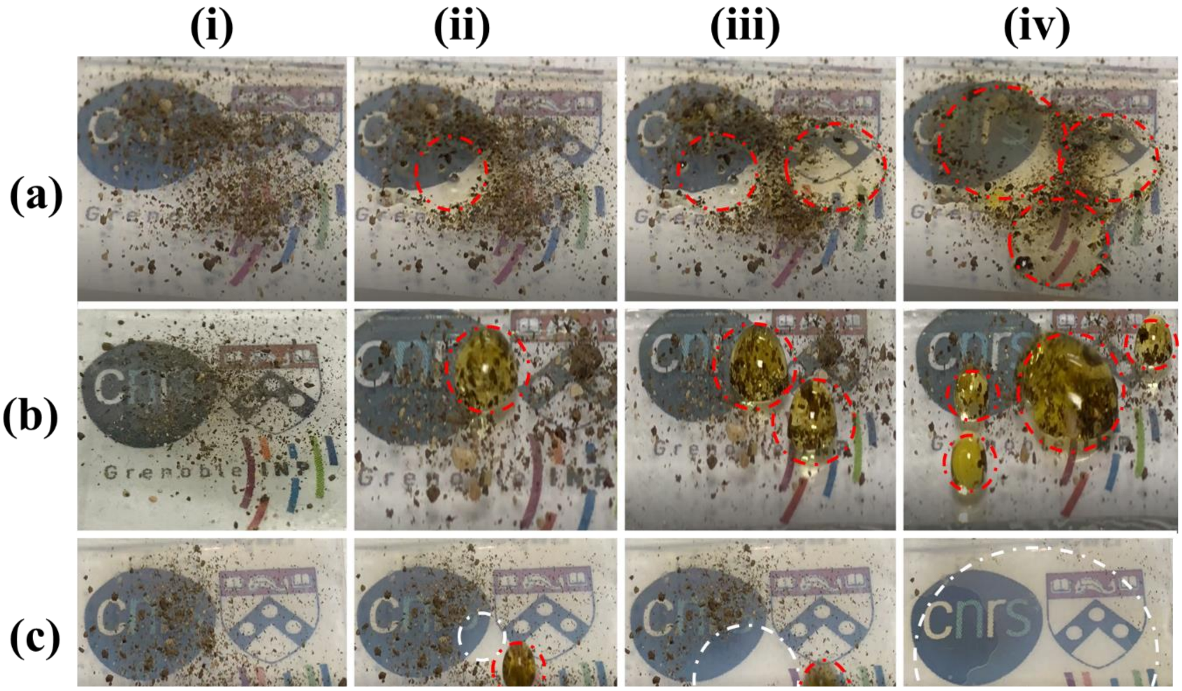

Figure 3. 14: (i-iv) Sequential photographs showing the removal of soil from the surface of (a) ZnO NWs, (b) PDMS-coated glass, and (c) PDMS/ZnO NW NCF-10s@RT by water droplets with Orange G. Red circles represent shapes and behavior of droplets when they are in contact with the surface of the sample, whereas white circles show the cleaned surface area after exposure to droplets.

3.4.2 Anti-icing

Ice accumulation on the solid surface can pose severe problems in many industrial applications. For example, ice formation on aircraft and electric transmission lines could cause significant complications. Moreover, accreted ice on surfaces can significantly decrease heat transfer efficiency in refrigerators/heat exchangers.[77, 395, 396] It is, thus, highly desirable to impart an anti-icing property to various solid surfaces. To show the potential of our nanocomposite films for anti-icing applications, we perform an anti-icing experiment to determine the time it takes for a water droplet to freeze on different surfaces. The freezing delay time is the time between the physical contact of a water droplet with a subcooled substrate and the onset of freezing.[395] The samples are placed on a thermally controlled copper substrate, and they are cooled down to −15 °C. After 10 min to ensure thermal equilibrium, water droplets are placed on the sample surface, and the freezing times of water droplets on different samples are recorded. Initially, the droplets are clear and transparent on the surface of the samples. However, white ice crystals appear in the droplet with time, which eventually turns into an opaque ice crystal. **Figure 3.15**a shows that the PDMS/ZnO NWs NCFs exhibit a superior anti-icing property than ZnO NWs and PDMS film, significantly delaying the formation of ice nuclei and reducing the growth rate of ice crystals. As shown in **Figure 3.15**b, the freezing times of PDMS/ZnO NWs NCFs are much longer than those of the ZnO NWs and PDMS film. The results demonstrate the excellent ability of ZnO/PDMS NCFs to suppress ice formation and accumulation.

This significant increase in the freezing time of NCFs compared to that of ZnO NWs and PDMS film is likely due to the superhydrophobicity, reducing the contact area between the water droplet and the surface and therefore dramatically reducing heat transfer between the NCFs at -15°C and the droplet that is surrounded by air at 20°C.[397, 398] In addition, the remarkable delayed-icing ability of the NCF-24h@150 °C compared to that of the NCF-10s@RT, we believe, is due to the different amounts of PDMS oligomers infiltrated into nanowires via the LeCaRI process. The infiltrated PDMS layer at the top surface of the NCF-10s@RT is thinner than the NCF-24h@150 °C, as clearly shown in the SEM images and especially in the EDS mapping image (**Figure 3.9**c, f, and i). Considering the thermal transport path in the ZnO NW arrays, heat transfer occurs through the vertically aligned ZnO NWs from the Peltier modulus to the substrate to the water droplet at the surface. Thus, the thicker the infiltrated PDMS layer at the top surface, the bigger the heat transfer resistance to the water droplet, resulting in enhanced delayed-icing. We believe this is the main reason for the efficient delay-icing ability of the NCF-24h@150 °C with complete infiltration compared to that of the NCF-10s@RT with partial infiltration. Significantly longer freezing times indicate that ZnO/PDMS NCFs could be highly advantageous in de-icing applications since water droplets can easily roll off with slight tilt angles or mild vibration before freezing.

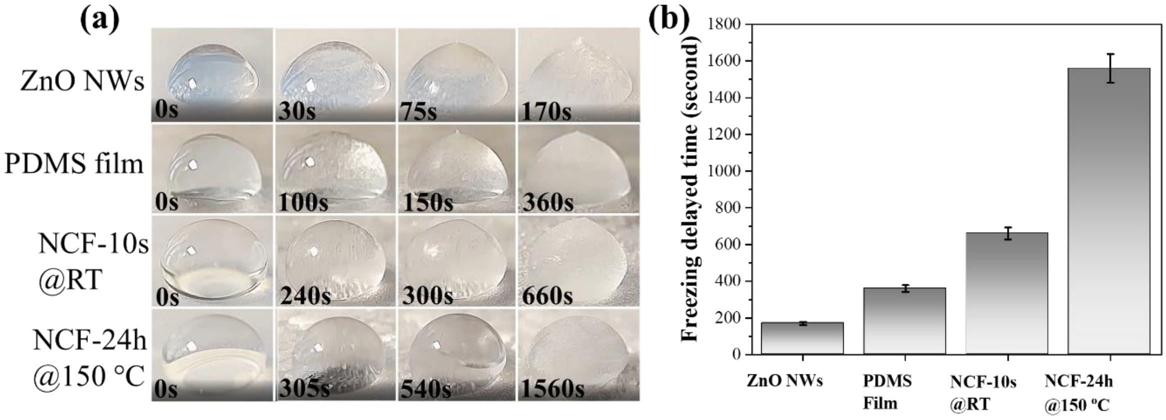

Figure 3. 15: (a) Ice accumulation on the surface of ZnO NWs, PDMS film, NCF-10s@RT, and NCF-24h@150 °C at −15 ± 1 °C environment with the delayed freezing time recorded by observing the non-transparency of the water droplets (b) Freezing time of ZnO NWs, PDMS film on glass, NCF-10s@RT, and NCF-24h@150 °C at -15 °C.

3.5 Stability of the PDMS-ZnO nanocomposite film

Nanocomposite materials must have high stability against several challenging conditions for practical applications. PDMS-based materials are highly soluble in nonpolar organic solvents, consequently leading to swelling of the polymer.[378] Also, polymer nanocomposite materials with photocatalytic fillers present a potential degradation of the polymer part upon activating the photocatalytic part by UV light. This section describes the stability of our PDMS/ZnO NW NCFs under some of the most critical conditions directly related to their inherent properties and their ability to recover hydrophobicity after being lost through plasma treatment.

3.5.1 Solvent resistance

One of the potential concerns for these NCFs is that PDMS oligomers can be removed when the NCFs are exposed to harsh conditions such as organic solvents. A cumulative series of experiments have been implemented on the same sample to test the anti-fouling to relatively low boiling point organic solvents in sequence with ethanol, acetone, toluene, and water at 37 °C. The sample is immersed in a solvent container for 10 min, and then placed in air for 2 min to evaporate the solvents. For the case of water, the samples that underwent solvents exposure were immersed in a water bath in a humidity chamber kept at 37 °C and 40 % relative humidity for 60 h. After each experiment, the wettability of the samples was evaluated according to the procedure described in the water contact angle measurement. **Figure 3.16** clearly shows that exposure to these solvents does not significantly change the wetting properties of the PDMS/ZnO NW NCFs. At the same time, such treatments induce significant changes in the surface wettability of the reference samples (bare glass slide and ZnO NWs). Upon complete evaporation of the solvents from the surface, the NCF surface still retains its superhydrophobic property. This result shows that the microstructure and composition of the NCFs likely do not experience significant changes even after these NCFs are brought in contact with these common organic solvents. It further indicates that the NCF could be used in later biological applications by retaining its superhydrophobicity in an aqueous environment at 37 °C for a long time.

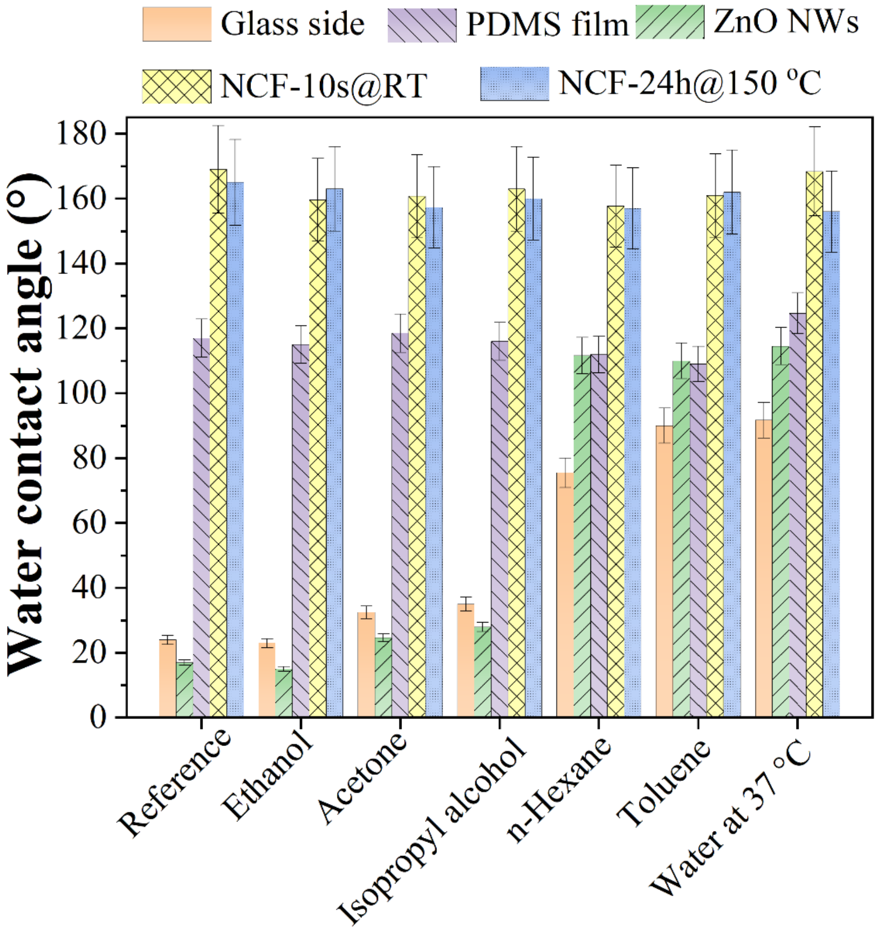

Figure 3. 16: WCA of samples before and after exposure to a series of organic solvents by sequentially exposing to ethanol, acetone, isopropyl alcohol, n-hexane, and toluene and water at 37 °C.

3.5.2 UV light resistance

Another potential concern associated with superhydrophobic materials incorporating photocatalytic materials such as ZnO NWs is the permanent loss of superhydrophobicity upon UV irradiation. We, therefore, test the stability of the superhydrophobic NCF against intense UV irradiation (see detailed irradiation protocol in **Chapter 2**). As shown in **Figure 3.17**, the NCF-24h@150 °C retains its stable water contact angle of 165° after UV irradiation for several hours. The NCF-10s@RT with an infiltrated smaller amount of PDMS shows a slight decrease in its water contact angle value with UV irradiation time; however, the initial superhydrophobic behavior can be recovered by thermal treatment at 80 °C for 1h. The results indicate the high stability of the PDMS/ZnO NW NCFs and the easy recovery of superhydrophobicity of the NCF-10s@RT.

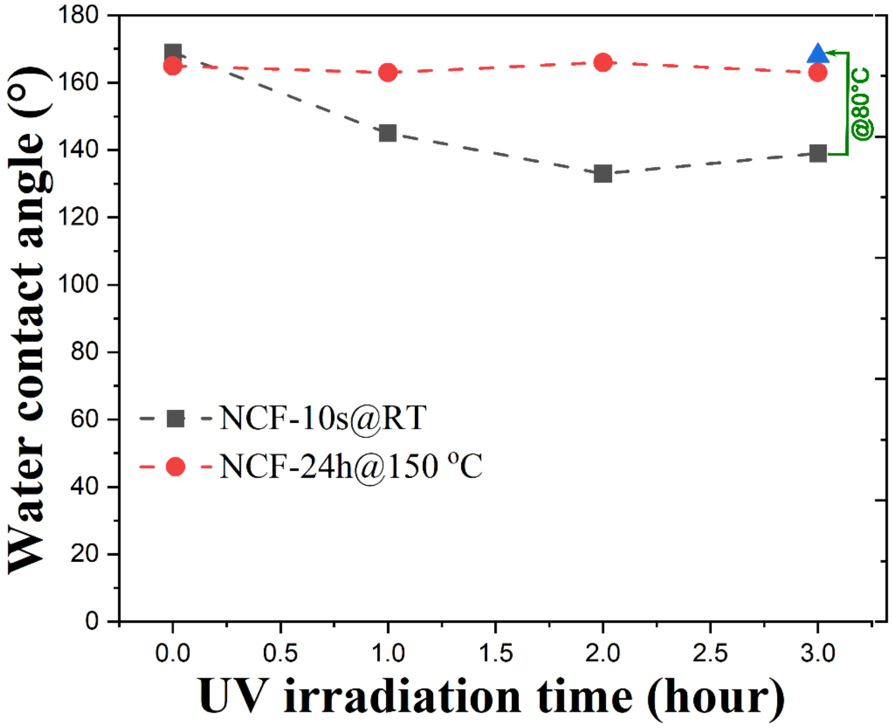

Figure 3. 17: Effect of UV irradiation on the static water contact angle on PDMS/ZnO NW NCFs.

3.5.3 Self-healing after plasma treatment

One of the most common surface treatments to eliminate and remove contaminants is oxygen plasma. Although this method is very effective in removing contaminants, its application on a superhydrophobic surface can potentially lead to a permanent loss of superhydrophobicity. Given the high mobility of PDMS species, we test whether the superhydrophobicity of PDMS/ZnO NW NCF can be recovered after an oxygen plasma treatment. As shown in **Figure 3.18**, the superhydrophobicity of the PDMS/ZnO NW NCFs is lost after oxygen plasma, and the surface becomes very hydrophilic with a water contact angle lower than 10°, likely due to the introduction of polar groups. However, the NCF surface quickly and easily recovers its superhydrophobicity after simple heat treatment at 80 °C for 30 min. Such recovery of superhydrophobicity can be repeated at least 9 times without reducing the initial water contact angle. According to previous reports on hydrophobicity recovery of PDMS,[349, 380, 381] this phenomenon is due to the out-diffusion of low molecular weight molecules of PDMS to the free surface.

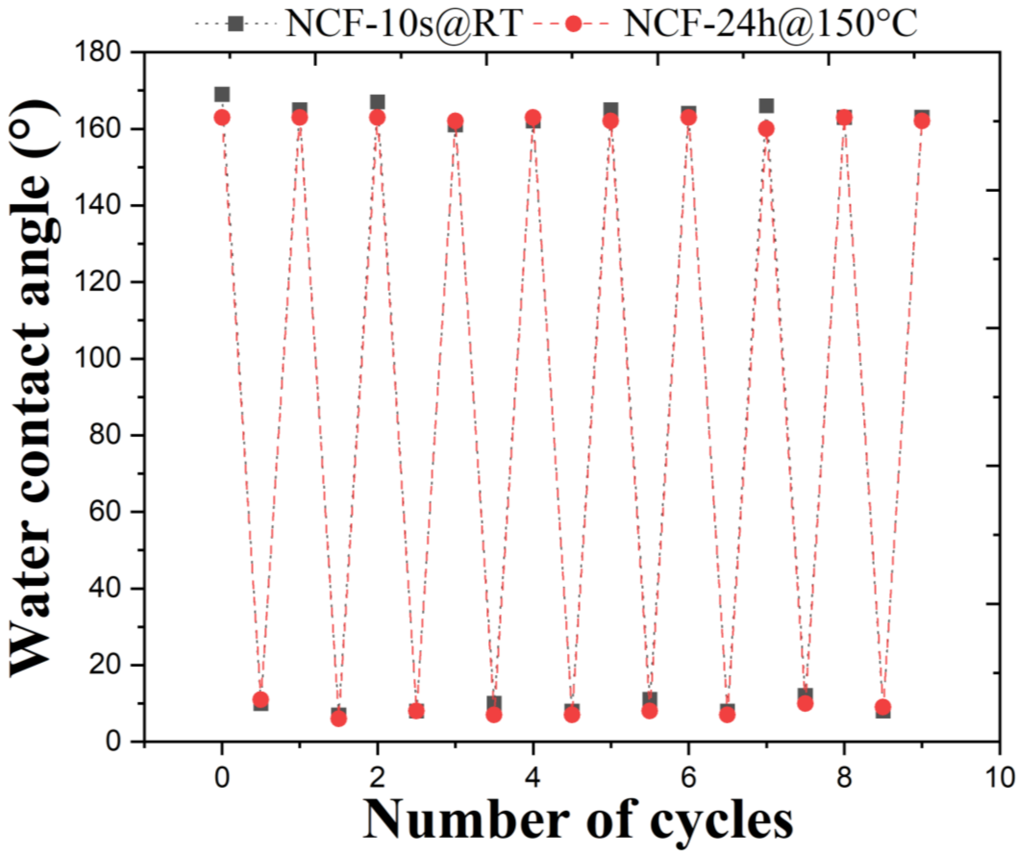

Figure 3. 18: Thermally induced healing of the PDMS/ZnO NW NCFs after repeated oxygen plasma treatment.

3.6 Conclusion

In conclusion, we report in this chapter a new method to fabricate nanocomposite films (NCFs) retaining the vertical alignment of ZnO NWs via leaching-enabled capillary rise infiltration (LeCaRI). PDMS-infiltrated vertically aligned ZnO NWs NCFs exhibit high transparency, anti-reflection, superhydrophobic, self-cleaning, and anti-icing properties. They can also retain their superhydrophobicity even after exposure to organic solvents or intense-UV irradiation and oxygen plasma treatment. Because the growth of ZnO NWs can be performed via solution-based methods and LeCaRI is a process that requires simple contact of PDMS with the ZnO NW arrays, we believe this process could potentially be scaled up to enable continuous fabrication of these versatile NCFs. Moreover, the process can produce NCFs with horizontally or randomly oriented NWs.

Despite the outstanding repellency of these PDMS/ZnO NW NCFs, their solid surface is not highly desirable for applications with more challenging conditions. For example, in situations where biological species (e.g., bacteria) are present, even if the surface of the PDMS/ZnO NW NCFs can prevent initial attachments of bacteria, with a permanent interaction in an extended time, the surface repellency will be lost, leading to surface fouling. Thus, we have further developed other surface functionalization to prevent such a problem potentially. These works will be described in **Chapter 4**.

Chapter 4.

Lubricant Depletion-Resistant Slippery Liquid-Infused Porous Surfaces via Capillary Rise Lubrication of Nanowire Array

Reproduced from Ref. [399] with permission from John Wiley and Sons.

Contents

Despite their promise in many applications, superhydrophobic PDMS/ZnO NW nanocomposite films have drawbacks that make their widespread applications challenging under harsh conditions, such as long-term immersion underwater or in contact with biological species. This is a fundamental limitation of superhydrophobic surfaces because of its repellency mechanism based on a solid-liquid interface and susceptibility of the air-cushion layer. We have adopted a new approach to using silicone oil as the infiltrating component to create a repellent surface with a mobile liquid-liquid interface to overcome these drawbacks. This method is inspired by the fabrication of slippery lubricant-infused porous surfaces (SLIPS). As mentioned in **Chapter 1**, one of the critical challenges in SLIPS is the lubricant depletion through the growth of a wetting ridge around a droplet of foreign liquid that removes the infused lubricant from the porous surface when the droplet slides off. Therefore, this chapter describes a method for producing stable SLIPS that resist lubricant depletion. Importantly, we will show that the orientation of nanowires strongly affects lubricant infiltration and the stability of SLIPS properties. The strong lubricant retention ability provided by the nanoporous structure of the random nanowire array suppresses the growth of a wetting ridge around a water droplet and can even resist lubricant depletion under a strong centrifugal force. This study provides a straightforward, robust, and potentially scalable approach for making stable SLIPS that suppresses lubricant depletion by taking advantage of the unique morphology of the random nanowire arrays and capillary rise lubrication. The results shown in this chapter were published in the following paper: H. Tran, Y. Kim, C. Ternon, M. Langlet, D. Riassetto, D. Lee, *Advanced Materials Interfaces* **2021**, 8, 2002058.

4.1 Introduction

Slippery lubricant-infused porous surfaces (SLIPS) show remarkable repellency against liquids, making them useful in various applications, from self-cleaning to water harvesting to anti-icing and anti-fouling.[11, 13, 49, 55, 121, 123, 124, 126, 400] The physical origin of the liquid repellency of SLIPS comes from a lubricant film within and above the surface of the porous template.[49, 401] In particular, this infused lubricant with low surface energy fills the air pockets in the space of the porous scaffold, providing a mobile liquid surface with no contact line pinning and excellent pressure stability. Additionally, the surface properties of the lubricant layer are highly tunable owing to the vast choice of lubricant properties (viscosity, solubility, and surface tension).[120, 169, 188] However, the lubricant layer depletes over time because of lubricant evaporation, shear force/frost-induced lubricant loss, and movement of liquid droplets on the infused surface.[27, 28, 141, 178-182, 214, 218]

The lubricant depletion leads to the degradation and failure of SLIPS performance, presenting a critical barrier to the widespread adoption of this powerful approach. For example, the ability to induce dropwise condensation of low surface tension fluids makes SLIPS a unique solution for enhancing the heat transfer efficiency in various industrial processes, such as refineries, biomass combustion, and natural gas manufacture.[170, 171] However, the depletion of the lubricant can decrease heat transfer by 80%, severely impeding the condensation of toluene.[172] A recent study proposed a new concept called "capillary balancing" for addressing frost-induced lubricant depletion to overcome lubricant depletion.[124] They showed that lubricant depletion in SLIPS during frosting and icing could be avoided by making the pore of the infused surface smaller than that between frost dendrites. In particular, the nanosize filler offered much stronger capillary forces, thus preventing lubricant depletion. However, in situations where SLIPS has to contact other liquids such as water, the formation of wetting ridges emerges as the primary mechanism of lubricant depletion because of the interaction between a water droplet and the lubricant film.[27] This interaction induces the rising of a thin lubricant film around the water droplet or even forms a lubricant film that entirely covers the water droplet.[209] These wetting ridges degrade the performance of lubricant film over time when the water droplet slides off the surface, resulting in permanent loss of the lubricant. Furthermore, the lubricant from the wetting ridge has been shown to contaminate and alter the surface tension of the contacting water droplets.[174, 175] Thus, the removed lubricant from SLIPS can lead to potential contamination of water in fog harvesting applications. It is thus critical to minimize or prevent the formation of wetting ridges, leading to stable SLIPS.

Despite its importance, suppression of wetting ridge on SLIPS has not been extensively addressed.[169] On the one hand, studies on SLIPS focus either on introducing new template/lubricant systems or exploring transformative applications.[18, 193, 402-404] On the other hand, some studies reported the effect of viscosity and thickness of lubricant film on the SLIPS properties.[183, 405-408] By carefully removing excess lubricant on a rough surface by rotating the infused surface for a specific time to reach the desired lubricant thickness, stable SLIPS have been produced.[211, 213, 409] However, current coating approaches fail to produce such a stable infused configuration without time-consuming optimization steps in which high shear force, causing the loss of repellency properties, is used.

Our work describes a robust method for fabricating stable SLIPS via capillary rise infiltration (CaRI) of silicone oil into interstitial nanovoids of ZnO nanowire arrays. We hypothesize that the growth of the wetting ridge and the subsequent loss of lubricant from SLIPS can be suppressed by eliminating extra lubricant outside the pores of the porous surface. To create such a structure, we infuse and confine silicone oil within the nanostructure of ZnO nanowire arrays via capillary forces. The silicone oil that resides in the interstitial pores between randomly aligned high aspect ratio ZnO nanowires can remarkably suppress the wetting ridge's growth. These structures also show excellent silicone oil retention against moving water droplets and shear force, leading to highly stable SLIPS. Capillary rise lubrication enables eliminating excess lubricant without any delicate optimization steps, making it a potentially scalable manufacturing approach.

4.2 Silicone oil-infused ZnO nanowire arrays via capillary rise lubrication

Capillarity at the nanoscale is a powerful force that enables the spontaneous transport of liquid into small pores.[32, 34] Capillary Rise Infiltration (CaRI) has been used recently to induce the imbibition of high molecular weight species such as polymers and oligomers into nanoporous media such as nanoparticle packings and assemblies.[31, 388] Here, we induce infusion and retention of silicone oil in the nanostructure of ZnO nanowire (NW) arrays via capillarity to produce stable SLIPS. The advantage of ZnO NW arrays is that the morphology of the porous structure can be varied by changing the orientation of NWs. For example, ZnO NW arrays can be produced from vertical to random alignments. These different alignments likely result in interstitial pores of different shapes and sizes. Here, we study how the orientation of ZnO NWs affects silicone oil infiltration and the stability of infiltrated surfaces against lubricant depletion.

4.2.1 Morphology of ZnO NW arrays before infiltration

ZnO NW arrays are grown on pre-seeded silicon wafer substrates via a chemical bath deposition method, as described in **Chapter 2**. The orientation of NWs is controlled by changing the seed layer morphology and the heat treatment step before immersion in the growth solution. We study three ZnO NW arrays with different orientations: vertical, tilted, and random geometry. The morphology of the three types of ZnO NW arrays before the infiltration of silicone oil is observed through scanning electron microscopy (SEM). The top-view SEM images (**Figure 4.1** a-c) indicate the presence of NW arrays with different orientation angles. Cross-section SEM images (**Figure 4.1** d and e) show that the vertical and tilted NW arrays have orientation angles against the vertical of 3.7° ± 3.2° and 19.3° ± 9.3°, respectively (**Figure 4.2** for statistical details). When NWs are grown with a high aspect ratio (i.e., the ratio between the length and diameter), they undergo aggregation to form bundles upon drying. We classify this structure as the random NW array (**Figure 4.1**f). These three types of ZnO NW arrays will be hereafter referred to as vertical NW array, tilted NW array, and random NW array, respectively.

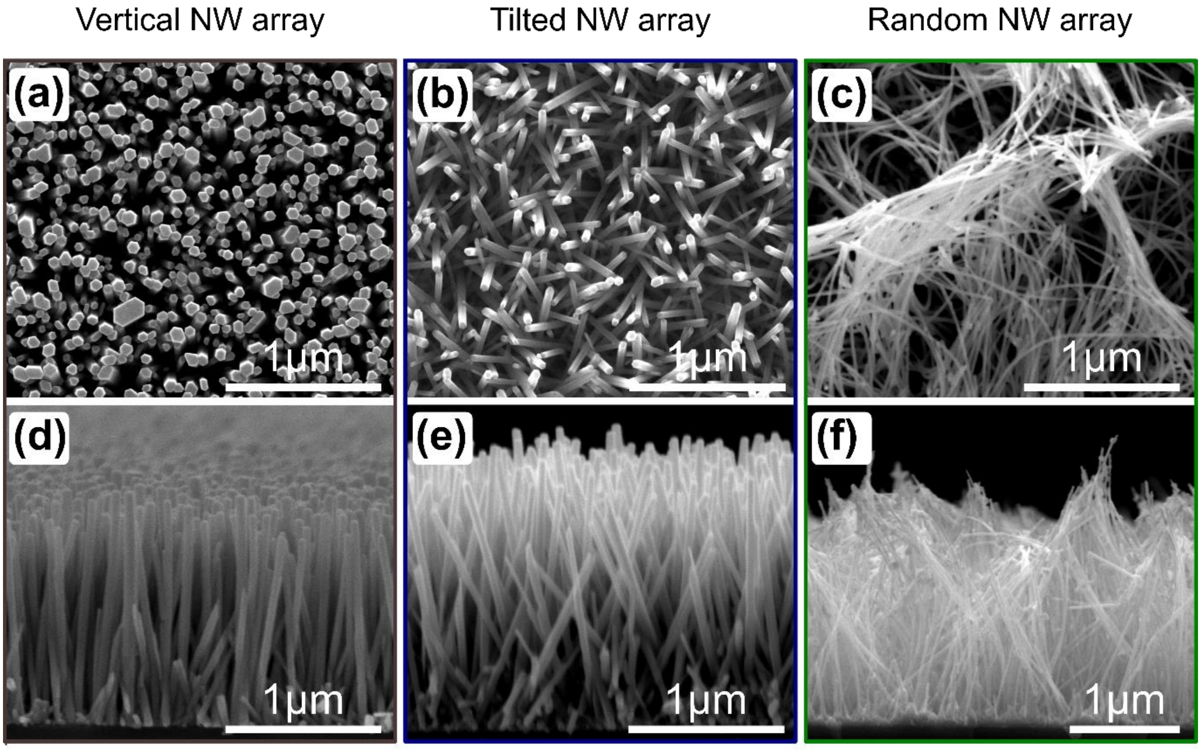

Figure 4. 1 : (a-c) Top-view and (d-f) cross-section SEM images of the ZnO NW arrays with three types of orientation.

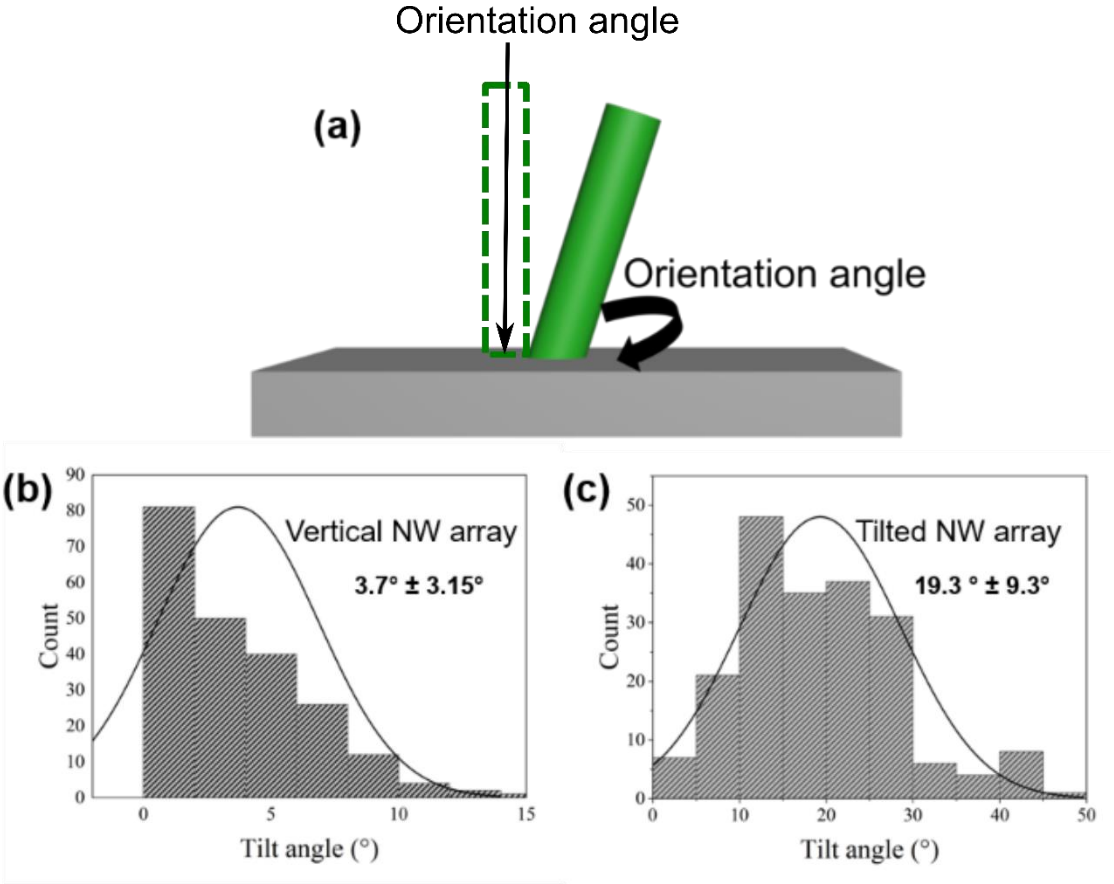

Figure 4. 2: (a) Definition of the orientation angle of NWs. Statistical analysis of the orientation angle of ZnO NW arrays, including (b) vertical NW array and (c) tilted NW array. At least 250 NWs are analyzed. The error bar is calculated based on the standard deviation.

4.2.2 Silicone oil lubrication via capillary rise infiltration

Preparation of silicone oil-infused ZnO NW arrays via capillary rise infiltration is described hereafter. Silicon substrates with ZnO NW arrays on the surface are thermally treated in an oven at 540 °C for 30 min to remove organic residues and water vapor before the wicking experiment. The substrates with ZnO NWs arrays are cut into 2 cm × 2 cm pieces and are held vertically in a silicone oil bath, as illustrated in **Figure 4.3**. We then induce CaRI of silicone oil into the interstitial nanogaps of ZnO NW arrays. We hypothesize that this approach will confine silicone oil within the interstitial voids between NWs and eliminate extra lubricant surfaces. The ZnO NW arrays could be subjected to a surface modification with C16 before wicking of silicone oil, which likely reduces the surface energy of ZnO NWs and significantly improves stability.

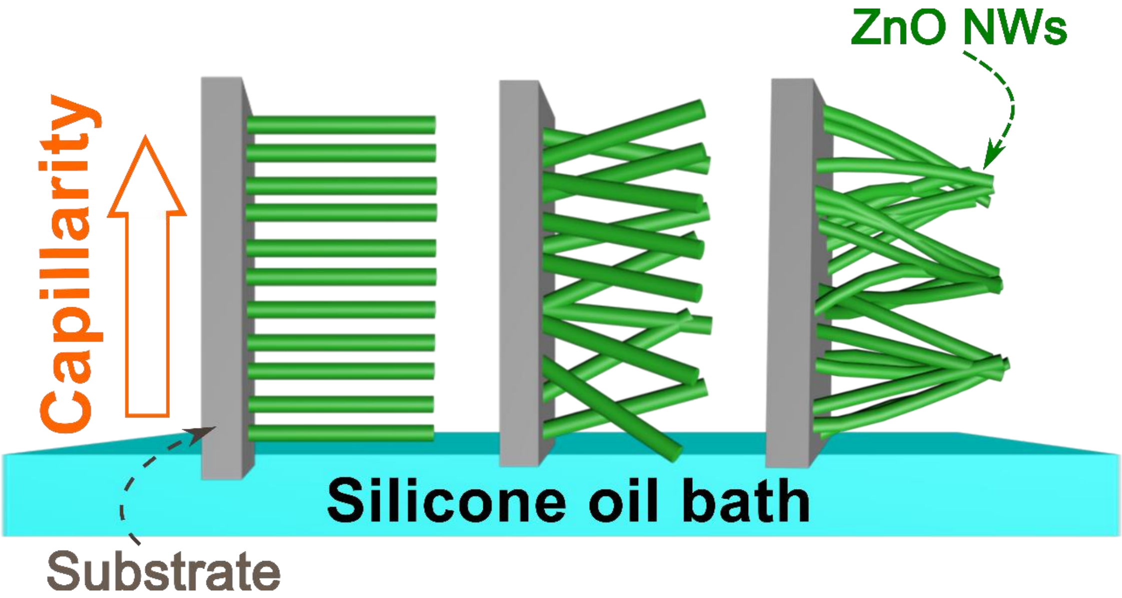

Figure 4. 3: Schematic illustration of the capillary rise infiltration (CaRI) lubrication of ZnO NW arrays with silicone oil. For clarity, objectives are not drawn to scale.

4.2.3 Wicking dynamics of silicone oil

The wicking dynamics are captured using a digital camera. In our experiments, we denote the starting time (i.e., $t = 0$) when the sample surface touches silicone oil and silicone oil starts to infuse vertically from the initial wicking front position. The three kinds of NW arrays differ in the rising silicone oil rates (**Figure 4.4**). The vertical ZnO NW array shows the slowest rate of silicone oil infiltration requiring 115 min to rise 1.8 cm. In comparison, the tilted ZnO NW array takes about 45 min to rise to the same height, while for the random ZnO NW array, composed of long and dense NWs, only about 18 min are needed to rise to the same height. As the liquid and material are the same between the three samples, we may consider that the dynamic viscosity, surface tension, and contact angle are constant for all the samples. Based on these assumptions and the dependence of the wicking rate on the pore size,[410, 411] these observations suggest that the capillary pressure in the random NW array sample is the largest among the three types of NW arrays. The random NW array likely presents a nanoscale porous structure within aggregated NW bundles, possibly explaining the robust wicking of this sample.

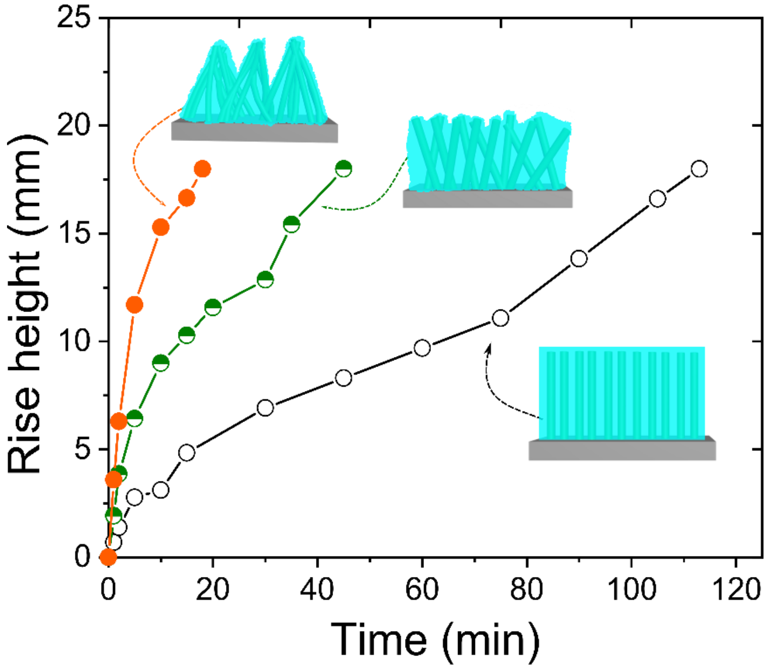

Figure 4. 4: Wicking rate of silicone oil in the structure of ZnO NW arrays with three types of orientation.

4.2.4 Morphology of infiltrated ZnO NW arrays

The morphology of ZnO NW arrays after CaRI imbibition of silicone oil can be observed using SEM images. Upon infiltration, the vertical and tilted ZnO NW arrays are densely covered by a micron size thick-silicone oil layer, as shown in **Figure 4.5**a,b. Although, the silicone oil on the surface of the tilted ZnO NW arrays is likely to present a thinner layer. Interestingly, the random NW array presents a rough lubricated structure where the silicone oil is confined within the NW bundles upon infiltration. Silicone oil conformally covers NWs following the morphology of the bundles, likely because the capillary force is considerably strong at the nanoscale (**Figure 4.5**c). It thus indicates that the formation of a structured lubricant layer where the lubricant is held within the structure of the porous template and presents a similar surface topography of the porous template is indeed plausible.

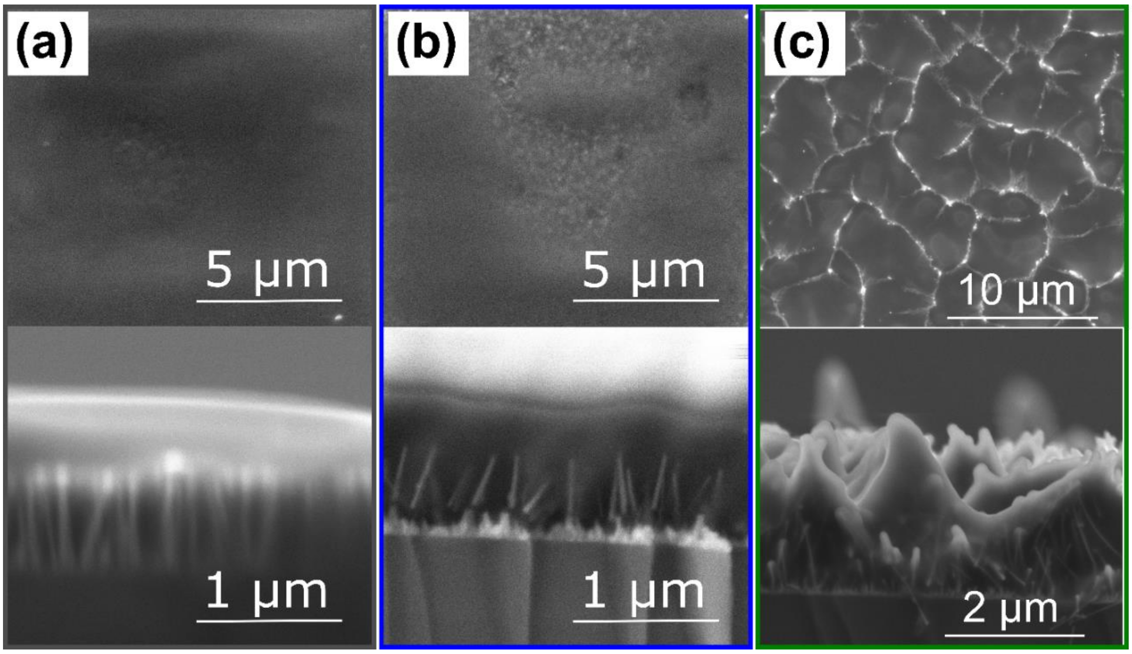

Figure 4. 5: SEM images of vertical NW array (a), tilted NW array (b), and random NW array (c) upon lubrication of silicone oil.

4.3 Wetting properties of the silicone oil-infused ZnO NW array surfaces

To understand the effect of extra lubricant on the wetting properties (i.e., the lubricant that is not confined in the interstices between NWs), we compare NW arrays lubricated by our capillary rise infiltration (CaRI) method with those lubricated using a standard top-down approach, i.e., lubrication by spin-coating of silicone oil directly onto the surface. Briefly, silicone oil is coated onto the surface of ZnO NW arrays using a spin coater (1000 rpm for 60 s).[14, 211] After the spin-coating step, the surface of ZnO NW arrays is infused and covered by a smooth silicone oil layer. We will then use these spin coating-lubricated samples as a reference compared to our CaRI-lubricated samples.

4.3.1 Water contact angle on silicone oil-infused surfaces

The cross-section of a typical wetting ridge surrounding a liquid droplet is a deformed triangle (see **Figure 1.16** and **Figure 4.6**a). Such a wetting ridge can be observed using a water contact angle goniometer (**Figure 2.6**) which enables direct observation of the contour of the sessile droplet, typically using a macro zoom lens. This method is frequently used to determine the apparent contact angle of a sessile droplet on a SLIPS. It is performed by capturing an image of a water droplet placed on a SLIPS and observing its shape. However, care should be taken in the observation process to avoid dynamic or scaling effects because of the dynamic nature of wetting ridge formation.[27] Besides, this technique is highly susceptible to operating conditions, including disruption due to external vibrations, organic vapors, and dust.[38] The illustration of a wetting ridge surrounding a water droplet on a lubricant-infused surface and the definition of the apparent contact angle is presented in **Figure 4.6**a. Water droplet contact angles on ZnO NW arrays spin-coated lubricant are between 80° and 90°. Water contact angles on the CaRI-lubricated NW arrays are larger than the corresponding values on spin-coated samples (**Figure 4.6**b). The random array has the highest contact angle compared to the two other kinds of the array for both spin-coating lubrication and CaRI lubrication.

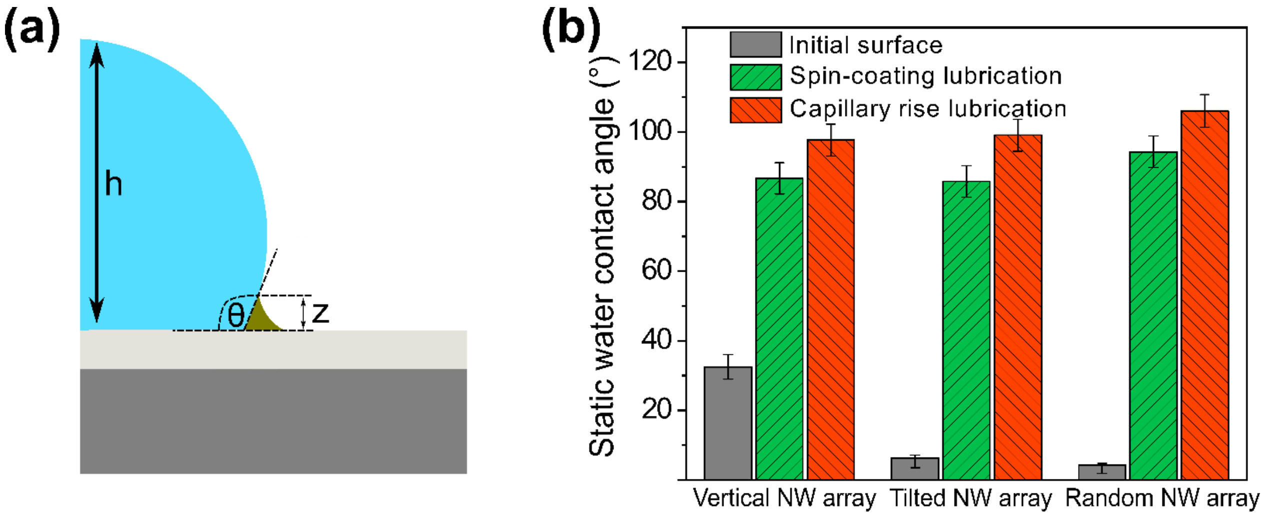

Figure 4. 6: (a) A schematic illustration of a water droplet on a lubricant-infused surface, showing a wetting ridge and definition of apparent contact angle. (b) Static water contact angle on ZnO NW arrays before and after silicone oil infusion via spin coating and CaRI.

4.3.2 Suppression in the growth of wetting ridges

Water droplets have prominent wetting ridges on all the spin-coated surfaces because of the rise of the lubricant film around the water droplet (**Figure 4.7**a, see the inset zoomed pictures for clarity). The appearance of a wetting ridge suggests that a thin layer of extra lubricant (i.e., the lubricant that is not confined in the interstitial void between NWs) exists above the height of the NWs. These wetting ridges are identified as the primary source of lubricant depletion on liquid-infused surfaces.[27, 182, 412] Remarkably, we observe a transition in the shape of the wetting ridge on CaRI-lubricated NW arrays as the orientation of the NWs is changed (see dashed blue insets in **Figure 4.7**b for clarity). A wetting ridge is observed around the water droplet on the vertical NW array; however, the wetting ridge's size is considerably reduced compared to the one observed on spin-coated samples. The formation of a wetting ridge is considerably suppressed for the tilted NW array and not visible for the random NW array.

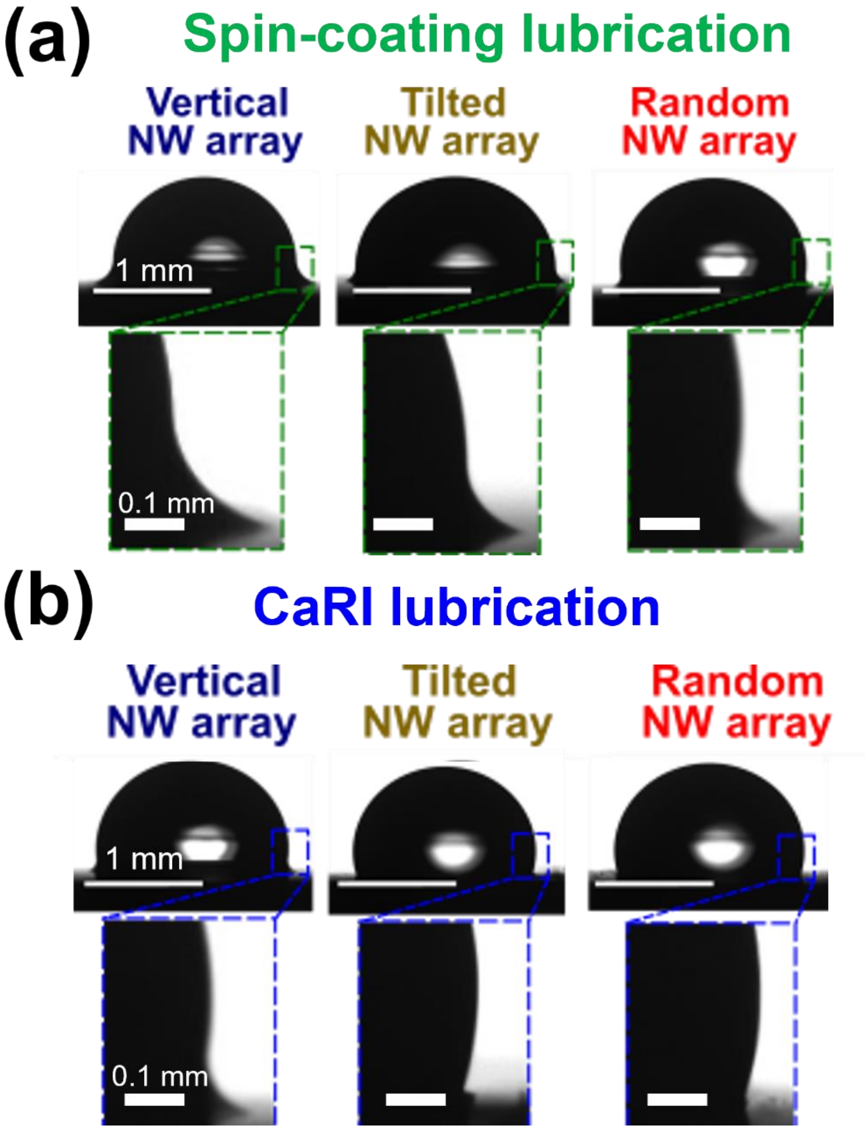

Figure 4. 7: (a) Micrographs of water droplets on the surface of ZnO NW arrays after infiltration of silicone oil via spin coating. b) Micrographs of water droplets on the surface of ZnO NW arrays after infusion of silicone oil by CaRI. The volume of water droplets is 10 µL.

For quantitative analysis, we evaluate the CaRI lubrication method's effectiveness in suppressing the growth of the wetting ridge as compared to the spin-coating method by calculating the ratio of lubricant ridge height (z) to the water droplet height (h), see **Figure 4.6**(a) for the definition and **Figure 4.8** for the results. The z/h ratios in NW arrays of spin-coated lubricant show high values because of a wetting ridge's prominent presence. However, the z/h ratio is lower for the tilted NW array than that of the vertical NW array and even lower for the random NW array (**Figure 4.8**). Using the CaRI lubrication approach, the z/h ratio is remarkably decreased for the vertical NW array and the tilted NW array compared to those observed on spin-coated samples. The wetting ridge is no longer visible on the lubricated random NW array surface, and it is impossible to calculate the z/h ratio. These results are consistent with the rates of capillary rise (**Figure 4.4**). Because of the nanoscale porous structure-induced high capillary pressure posed by tilted and random NW arrays, the infused lubricant stays trapped in the interstices among the NWs and does not form wetting ridges. As the morphology of NW varies from vertical to tilted and to random alignments, the pore structure of the NW array becomes more tortuous for the lubricant to escape. For instance, the vertical NW array has straight channel-like voids, providing a direct path for lubricant to go from the bottom surface to the top. In contrast, the random NW array's unique morphology of NW bundles likely provides a highly tortuous path. Thus the lubricant would have to move through a longer path to be depleted. Simultaneously, the random array of NWs has smaller pores, which would provide a stronger capillary force, a thermodynamic factor, that facilitates the retention of the lubricant. Our CaRI method thus represents an effective approach to suppressing the formation of wetting ridges compared to the standard coating approach, which will be further studied in the following sections.

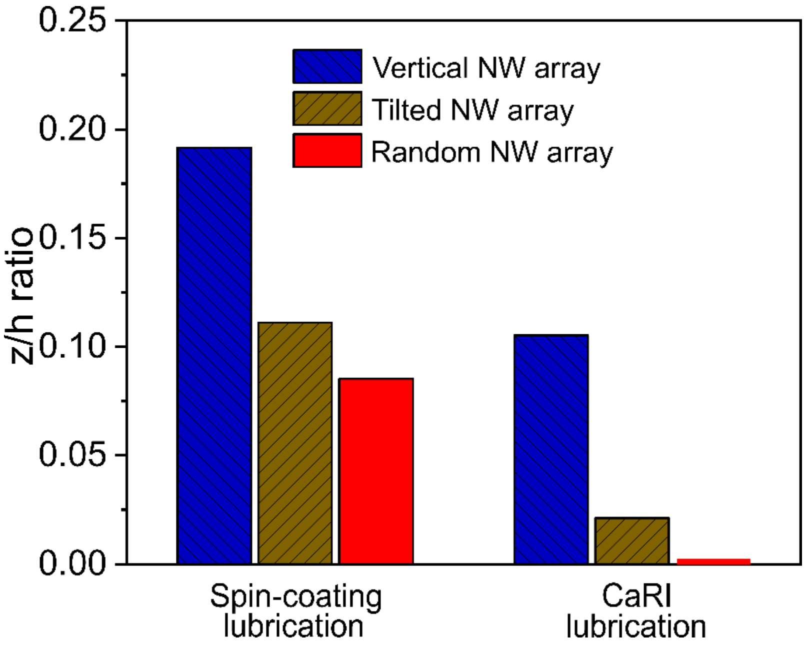

Figure 4. 8: Comparative analysis of z/h ratio of a water droplet on lubricant-infused surfaces using spin-coating and CaRI. h represents the height of the water droplet after sitting on the lubricant-infused surface, and z represents the height of the wetting ridge.

4.4 Stability of SLIPS

4.4.1 Stability against moving water droplets

Moving and shedding water droplets on lubricant-infused surfaces lead to lubricant loss if the water droplets are surrounded by wetting ridges. Thus, it is critical to make a stable lubricant-infused surface showing liquid repellency under dynamic (i.e., water-shedding) conditions. To gain more insights into the wetting ridge's effect on the lubricant depletion, we perform various experiments to observe NW morphology's impact on lubricant-infused NW arrays' stability. We first observe the traces left by water droplets sliding on lubricant-infused ZnO NW arrays. For these trail detection from moving water droplets experiments, the samples are tilted at an angle of 7°; a water droplet (~20 µL in volume) is dripped from a syringe held 2 cm above the sample surface. The water droplet is dripped from the syringe tip and slides on the infused surfaces. We observe these moving droplets using a digital camera. A trail is left by a sliding droplet on the vertical NW array (**Figure 4.9**a), dragging lubricant, presumably because of the wetting ridge's presence. The tilted NW array with lubricant also shows a slight trail left by a moving droplet, as shown in **Figure 4.9**b. In contrast, no visible track is seen on the lubricated random NW array surface after a droplet slid down the surface (**Figure 4.9**c). This observation agrees with the results shown in **Figure 4.8**; surfaces that suppress the ridge formation reduce lubricant loss from the surface.

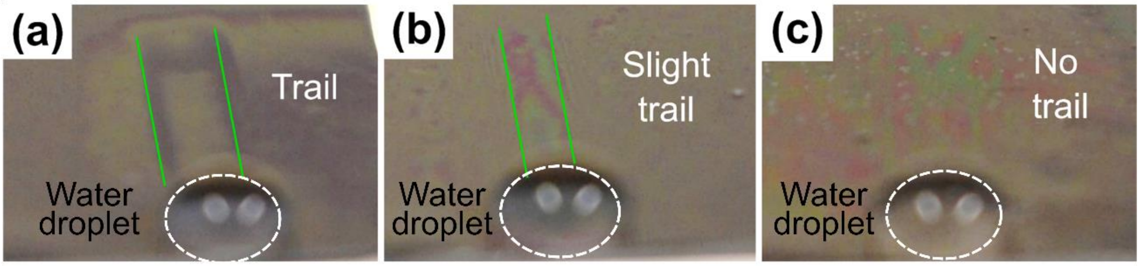

Figure 4. 9: Digital photographs of trails left by sliding water droplets on silicone oil-infused (a) vertical NW array, (b) tilted NW array, and (c) random NW array samples. The diameter of the water droplets is approximately 4 mm.

4.4.2 Water droplet impact and self-healing

We also studied the lubricant retention using a water droplet impact experiment in which water drops are dripped onto the surface of each sample (tilt angle of 7°) from a height of 2 cm. Each water droplet is approximately 20 µL in volume, and water droplets are dripped at roughly one droplet/sec. The number of water droplets striking and sliding off the surface of lubricant-infused NW arrays is counted until a water droplet stops sliding. Results indicate that the lubricant-infused random NW array can shed at least 23 water droplets from the same area (**Figure 4.10**). In contrast, lubricant-infused vertical and tilted NW arrays lose their liquid repellency after shedding only 6 and 13 water droplets, respectively.

To study the self-recovery of SLIPS properties, we leave our samples for five minutes in an ambient condition after they lose their repellency due to repeated droplet impact and re-perform the water impact test by dropping water droplets in the same area as previously. Just one or two droplets can slide on the surface of the vertical NW array during the second round of the water impact experiment. After the second round, this array completely loses its ability to shed water droplets with just 5 minutes of self-recovery time. The lubricant-infused tilted array shows some recovery of the SLIPS property: 9 and 2 water droplets shed off in the second and third rounds of water impact tests, respectively. Notably, the lubricant-infused random NW array retains its water repellency without reducing the number of water droplets shed after three cycles (**Figure 4.10**). Thus, the random NW array can recover its repellency rapidly without any external intervention after just five minutes. This self-healing effect indicates that silicone oil can spontaneously move within the NW array to fill depleted regions. Recent work done in our group has shown that low glass transition oligomers can spread from a filled region to an unfilled region of a nanoporous material via surface diffusion.[388] Thus, such a surface diffusion can be responsible for the observed self-healing behavior in our work.

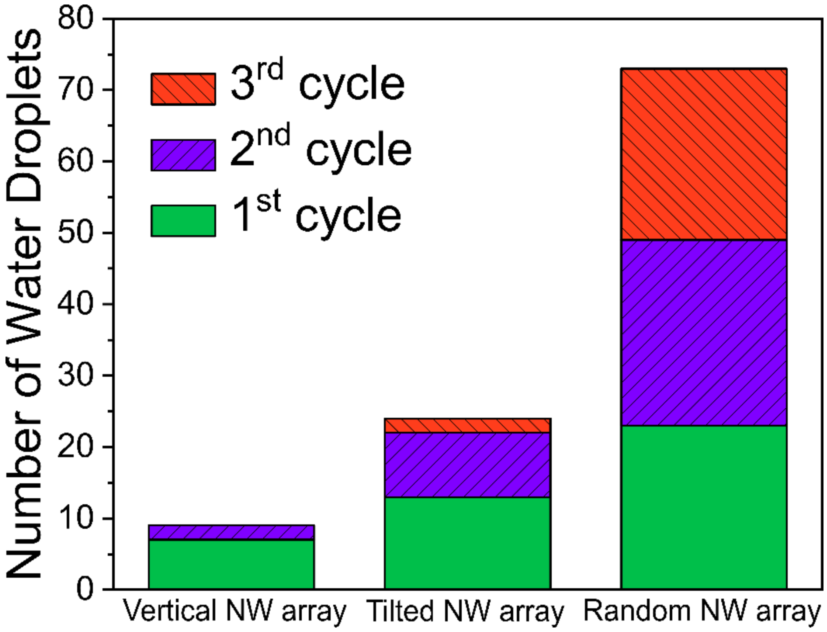

Figure 4. 10: Water droplet impact test, which shows the number of water droplets that shed from lubricated surfaces after one cycle (green-blank), two cycles (purple with right-to-left lines pattern), and three cycles (red with left-to-right lines pattern).

4.4.3 Stability against centrifugal force-induced failure

Loss of lubricant from SLIPS can also be induced by a mechanical force such as shear or centrifugal.[179] Few robust strategies against mechanical force-driven lubricant depletion have been presented.[28, 119, 400] We compare the stability of SLIPS properties against mechanical force-induced lubricant depletion by applying a strong centrifugal force to the samples by spinning them using a spin coater for 180 s at a speed of 4500 rpm and measuring the sliding velocity of a water droplet on the 7°-inclined surface before and after spinning (**Figure 4.11**). Previous studies have shown that the velocity of a water droplet sliding on lubricant-infused surfaces is proportional to the thickness of the lubricant film and conformality.[218] Consistent with this observation, a water droplet on the lubricated vertical NW array before applying centrifugal force has the fastest sliding velocity among the three NW arrays. For tilted and random NW arrays, the sliding velocity is slower as they have a thinner and non-conformal lubricant layer. The difference in lubricant thickness on the lubricated NW arrays' surface can also be inferred from the difference in the moving trail and their morphology (**Figure 4.9** and **Figure 4.5**).

After applying a strong centrifugal force, we observe a considerable decrease in the sliding speed of a water droplet (~23-fold decrease) on the vertical NW array. Remarkably, the lubricated random NW array does not show any reduction in the sliding velocity of a water droplet after it has been subjected to high centrifugal force. In contrast, a small decrease in the sliding speed is observed for the tilted array. These results suggest that the orientation of NW arrays indeed plays an important role in the retention of lubricant against a mechanical force, probably due to the combined effect of nanoscale pores that retain the lubricant thanks to their strong capillary pressure and tortuous paths that impinge lubricant flow.

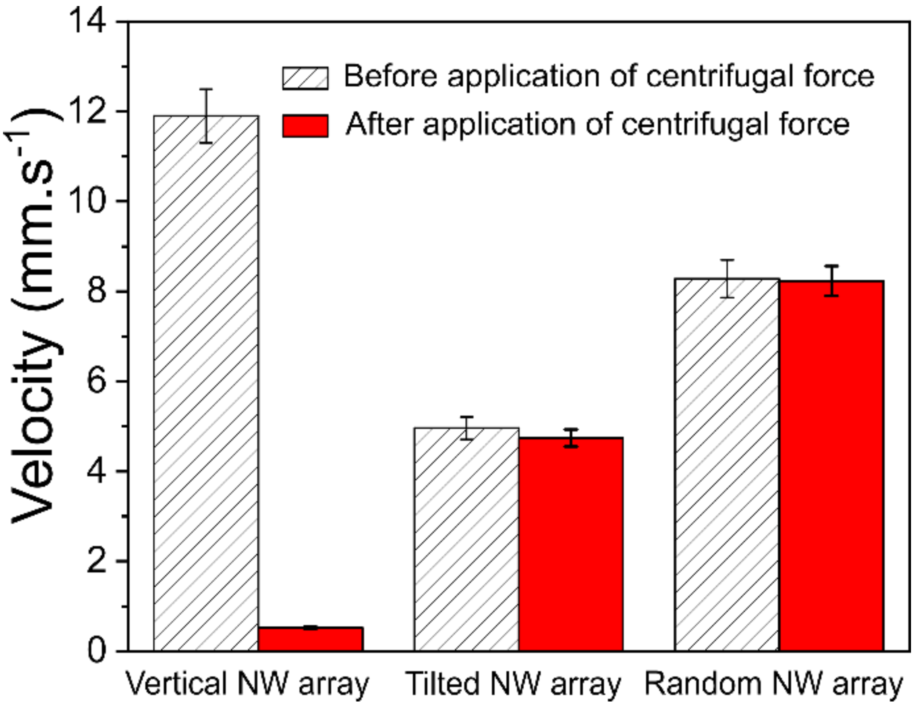

Figure 4. 11: The sliding velocity of water droplets on the 7°-inclined surface before and after applying a high-speed spinning test. The stability of the infused ZnO NW arrays against centrifugal force-induced failure is performed using a spin coater, rotating at a spin speed of 4500 rpm for 180 s.

4.4.4 Stability against acidic medium

One of the most detrimental factors that degrade the performance of coatings is prolonged contact with corrosive liquids.[413-417] Corrosion-resistant surfaces present a substantial advantage for marine and medical applications that involve challenging conditions. Notably, the most common origin for the failure of coatings in these applications comes from the lack of robustness against acidic media.[193, 418]

Given its remarkable liquid repellency, we study the stability of our obtained surfaces under an acidic environment. We first subject our surfaces to a liquid medium with a pH of 3.8 lower than a usual pH value produced from a marine and biofilm community;[419] the medium is vigorously stirred at 1000 rpm. At such a pH value, ZnO is prone to damage quickly due to the acidity, enabling our evaluation of the role of the coating in protecting the ZnO NWs surface. We exclusively use the random ZnO NW array sample for these additional tests since this sample presents the most promising liquid repellency. Results show that the random ZnO NW array is quickly removed upon immersion into the testing corrosive liquid, as shown in **Figure 4.12**a. The loss of the ZnO NW array coating can be observed by comparing the difference in the surface before and after the test using optical. Random ZnO NW-based SLIPS sample presents excellent protection against corrosion (**Figure 4.12**b). Specifically, after the test, the color of the coating can be seen clearly. Also, optical images show the nanowire patterns and the presence of silicone oil. This valuable property originates from the lubricant layer that prevents a permanent interaction between the surrounding corrosive liquid and the coating.

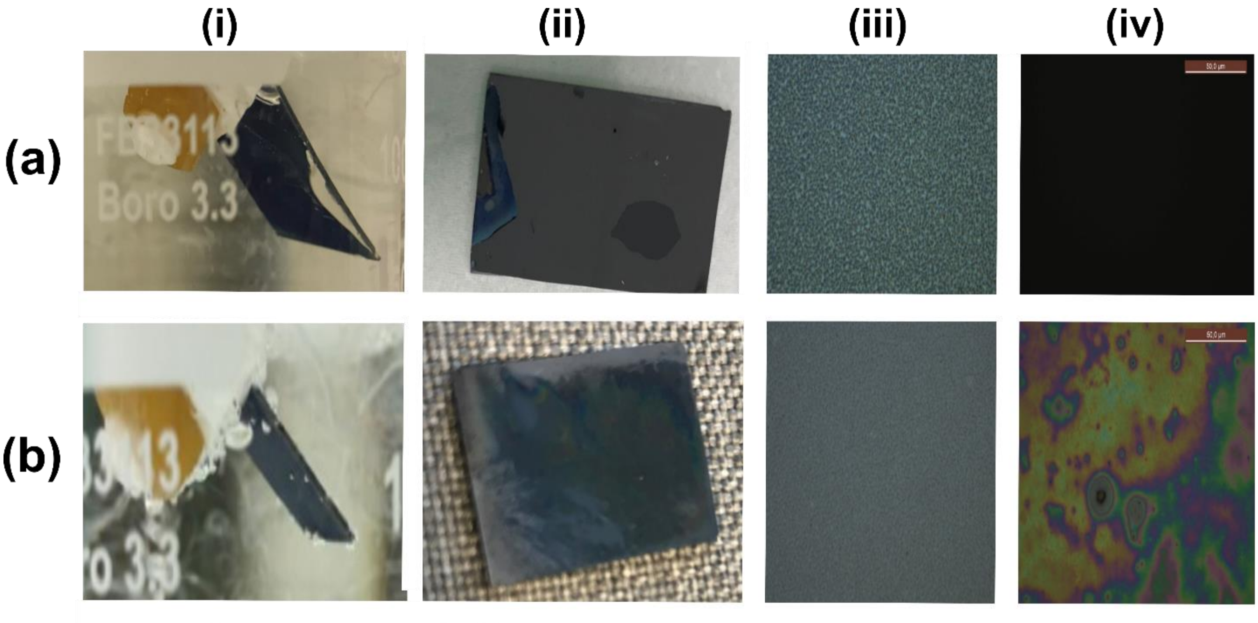

Figure 4. 12: Stability of the surfaces against acidic medium (pH of 3.8) and vigorous stirring (rotating speed of 1000 rpm). (a) Random ZnO NW: (i) upon immersion, (ii) after 30 min of exposure, (iii) and (iv) microscope image of the surface before and after immersion. (b) SLIPS based on random ZnO NW infiltrated with silicone oil: (i) upon immersion, (ii) after 30 min of exposure, (iii) and (iv) microscope image of the surface before and after immersion.

4.5 Conclusion

In conclusion, this chapter has described a robust approach for fabricating lubricant depletion-resistant slippery liquid-infused porous surfaces by inducing infiltration of silicone oil into interstitial nanogaps of ZnO nanowire (NW) arrays via capillary rise infiltration. By controlling the orientation of ZnO NW arrays, we show that random orientation and aggregation of long NWs are critical in suppressing the appearance of the wetting ridge. Such morphology likely gives nanoscale pores with significant capillary pressure and a highly tortuous path, leading to excellent silicone oil retention against moving water droplets and external forces. Our study provides a robust approach for making stable and self-healing SLIPS surfaces by circumventing the problem of lubricant depletion. While our work convincingly showed the importance of providing high capillary pressure to suppress lubricant depletion, the best performing surface also has a unique morphology compared to typical SLIPS surfaces; that is, the surface topography after lubricant infusion retains micro-scale roughness. The role of such roughness has not been extensively studied for SLIPS surfaces and warrants future investigation. Moreover, the precise shape of the interface and the wetting ridge could be visualized using X-ray tomography for an in-depth understanding of the properties of the wetting ridge.

With these encouraging results, we will study the anti-biofouling properties of these random ZnO NW-based SLIPS to extend their application domain further. Briefly, we will study the ability to prevent bacterial attachment and remove bacterial biofilms under shear on these ZnO NW-based SLIPS. These studies will be presented in **Chapter 5**.

Chapter 5. Extended Studies

Contents

This chapter presents some preliminary studies on exciting new directions advancing based on the findings described previously in this thesis. For example, preliminary results will be shown on the effectiveness of our ZnO NW-based nanocomposite surfaces against biofouling. The extension of our materials to membrane substrates will also be discussed with some promising preliminary results.

5.1 Bacterial biofilm prevention

5.1.1 The pressing problem of bacterial biofilm

The attachment and colonization of bacteria to surfaces facilitate the growth of bacterial biofilms, primarily responsible for several severe problems, such as fouling, infection, and corrosion.[420-424] Biofilms are organized bacterial communities attached to a surface, where bacteria produce extracellular polymeric substances.[420, 425] In a typical bacterial biofilm, bacteria access nutrients through a network of channels,[426] communicate through cell-cell interactions,[423] and show a diverse gene expression.[427, 428] This structured organization and the presence of a polymeric matrix protect bacteria under harsh environmental conditions. Also, bacteria can disperse from established biofilms to initiate a new cycle of biofilm formation somewhere else.[429] The typical process of forming biofilms is shown in **Figure 5.1**.

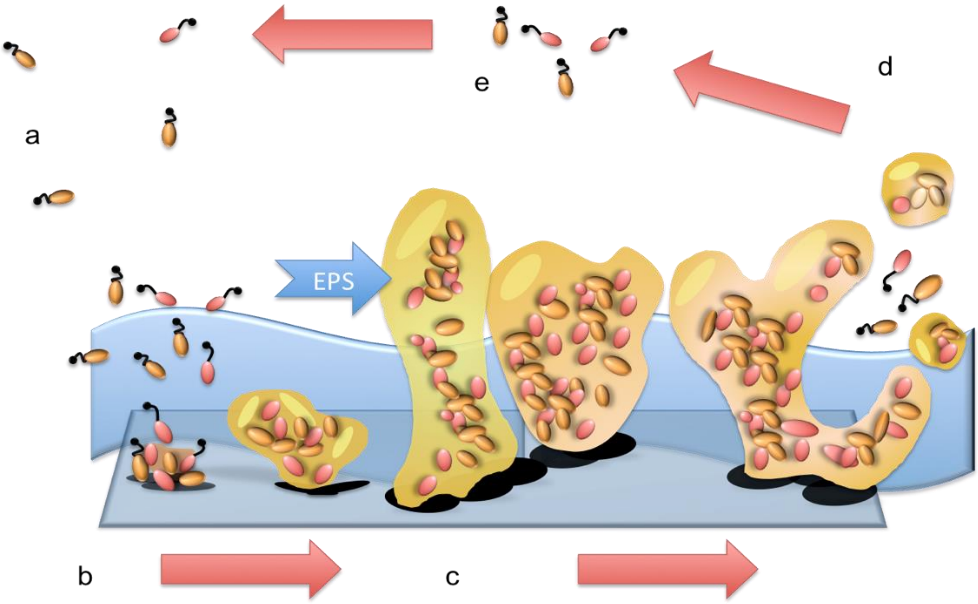

Figure 5. 1 : Typical stages of biofilm formation. (a) Planktonic bacteria. (b) Attachment of bacteria on a surface. (c) Formation of protective exopolymeric substances (EPS). (d) Quorum sensing and releasing microorganisms. (e) Returning to a planktonic state.

The figure is adapted with permission from Ref [430].

Bacterial biofilms represent one of the most pressing challenges in medical settings: attachment and colonization of bacteria to medical devices, orthopedic or dental implants, and catheters can cause severe infections and complications.[420, 423, 431, 432] In clinical settings, antibiotic therapy is one of the most conventional approaches for treating bacterial biofilms.[433-436] However, this treatment has several drawbacks. Antibiotic treatments suffer from low efficacy, cytotoxicity, side effects, and, most importantly, the emergence of bacterial drug resistance.[437-439] The structure of bacterial biofilms has been identified as one of the primary reasons for these challenges, as established bacterial biofilms can resist many antimicrobial treatments, potentially causing persistent pathogenic risks. It has been predicted that drug-resistant bacteria could cause ten million deaths globally by 2050.[420, 429, 440] Treatment of established bacterial biofilm is thus challenging, untraceable, risky, costly, and often impractical.

Several solutions have been developed to tackle bacterial biofilm development by reducing the initial attachment of bacteria.[429, 441-449] Recent advances in surface engineering present enormous potential for preventing the attachment of bacteria, thus reducing the risk of increasing bacterial-drug resistance (**Figure 5.2**).[441, 443] These approaches typically involve chemical or structural treatments. Chemical methods are based on zwitterionic, mixed-charge, low surface energy coatings, or hydrophilic coatings that significantly reduce bacterial adhesion.[450-454] Structural approaches are replied to creating surfaces with micro- or nanoscale features to limit the contact area between the surface and bacteria or even kill adhering bacteria through mechanical contact-killing mechanisms.[442, 443] Despite promising prevention of bacteria from attaching to surfaces, structural approaches are ineffective for long-term use since they are vulnerable to damage and liquid penetration.[455] Also, the mechanism of mechanical contact-killing is still debated, and the fundamental factor for the killing is unclear.[301] Importantly, bacteria can produce a conditioning matrix layer of exopolysaccharides that can accumulate on the surface and facilitate subsequent adhesion even though bacterial adhesion is suppressed initially.[456, 457]

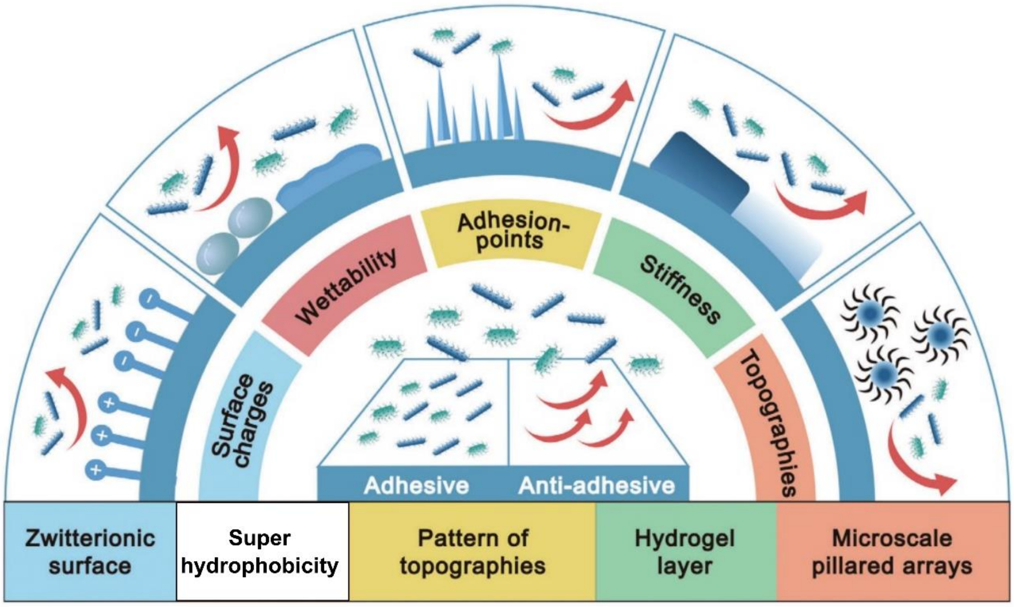

Figure 5. 2: Surface modifications for preventing bacterial adhesion.

This figure is adapted with permission from Ref [441].

As discussed in **Chapter 1**, repellent surfaces represent an outstanding solution for addressing fouling challenges.[458, 459] We have described the anti-fouling ability of our ZnO NW-based repellent surfaces to dust, ice, corrosion solutions, and organic solvents in **Chapters 3** and **4**. Given the excellent stability and self-healing ability of our newly proposed SLIPS (silicone-oil infiltrated random ZnO NW arrays), we will explore the potential anti-biofouling applications of this surface. Previous works have shown that surfaces with ZnO NWs present an excellent initial reduction of bacterial adhesion due to their unique structure.[298, 460-462] The dynamic interface between SLIPS and the liquid environment has demonstrated remarkable effectiveness in preventing bacterial adhesion.[11, 18, 55, 127, 150, 400, 463, 464] Thus, we anticipate that our SLIPS coating with silicone-oil infiltrated random ZnO NW arrays could provide remarkable anti-biofouling properties because of their unique structure where the morphology of random NWs is retained, and the dynamic lubricant layer is introduced.

5.1.2 Experimental details

Surface preparation

This study mainly focuses on random ZnO NWs as this structure provides the most promising anti-fouling properties and stability (**Chapter 4**). The general procedure for preparing surfaces with ZnO NWs and silicone oil-infiltrated ZnO NWs has been described in **Chapters 2** and **4**. The only change is using coverslips (thickness: 0.13 mm) as substrates for growing ZnO NWs to observe later bacteria with an optical microscope in transmission mode.

Growing a bacterial biofilm

We study the early biofilm formation of the model pathogen *Pseudomonas aeruginosa* on NWs-based surfaces.[465] Three different methods are used to evaluate the efficiency of NW-based surfaces to prevent biofilm formation: rolling-drop experiments, microtiter-dish formation assays, and flow cell experiments.

For each experiment, a culture of the model biofilm-former *Pseudomonas aeruginosa* (strain PAO1) is grown from freezer stock overnight in a rich medium (Luria-Bertani) at 37 °C. In the morning, the culture is diluted with fresh medium at a ratio of 1:100 and grown to the "mid-exponential" phase, as measured through the optical density of the solution at 600 nm (OD_{600}) between 0.4 and 0.6.

For rolling-drop experiments, the above solution is diluted in our standard medium (TB:PBS, 1 volume of tryptone broth, 10g/L, for 2 volumes of PBS without calcium and magnesium) to $OD_{600} = 0.01$. This diluted suspension is dripped onto the test surfaces, tilted to ~45°, so droplets can easily roll off the surface. The dripping speed is maintained at 1mL/hr using a syringe pump. The experimental setup is presented in **Figure 5.3**. The process is performed overnight, for a total of 12h. The surface is then rinsed with DI water, stained for 15 min using a 0.1 wt% crystal violet (CV) solution, then extensively rinsed with DI water, and dried before being observed with naked eyes and under a wide-field microscope.

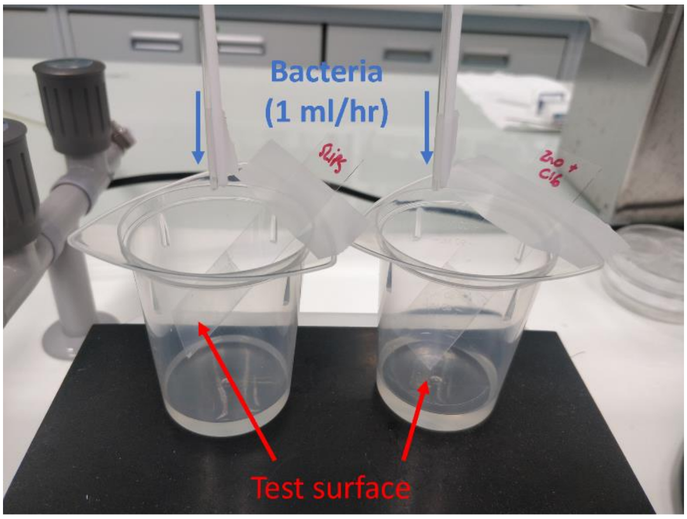

Figure 5. 3: Experimental setup of a rolling drop experiment to study the attachment of bacteria. Photo credit: Dr. Sigolène Lecuyer.

For microtiter dish biofilm formation experiments, the test surfaces are integrated into sterilized cell culture dishes (diameter of 34 mm). The NW surfaces are previously prepared on round glass coverslips and then glued to the bottom of the dishes, previously pierced with a 28-mm circular hole. This process allows direct observation of the bacteria in the dishes with high-resolution microscopy. Then, 2 mL of bacterial solution (obtained as described above, OD_{600}=0.01 in TB:PBS or M63 media [465]) are introduced into each dish. The culture dishes with bacterial solution are then incubated at 37 °C for bacterial growth, ranging from a few hours to several days (**Figure 5.4)**. After incubation, the solution is removed, and the surface is gently rinsed with 5 mL DI water two times. This step aims to remove unattached bacterial cells. The samples are then stained with CV before imaging with the microscope.

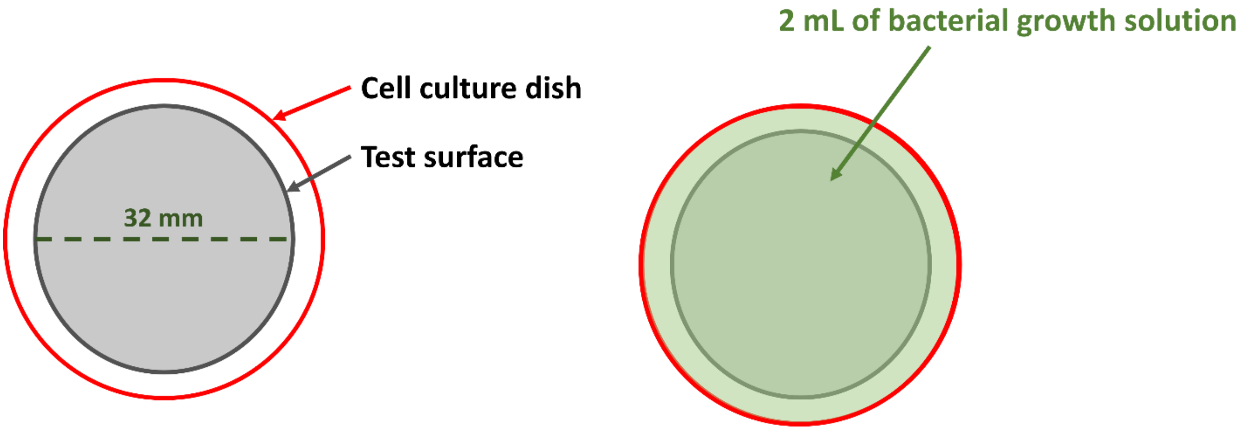

Figure 5. 4: Schematic illustration of microtiter dish biofilm formation assay.

The surface is cleaned and integrated into a lab-made microfluidic device for dynamic observations. The device is obtained by sealing together a test surface (NWs or silicone oil-infiltrated NWs on a glass coverslip) and a slab of PMMA bearing two holes for the inlet and outlet of the flow via double-sided sticky tape (Teraoka, Japan) of a calibrated thickness (170 µm) in which a 2 mm x 5 mm channel was previously cut. Channels are thus 2 mm x 5 mm x 170 µm (w x l x h). This device is heated at 90 °C for 10 min and subjected to a vacuum for 10 min to ensure tight bonding of the components. The device is then rinsed with PBS overnight to check for leaks and surface stability. After that, the bacterial suspension (OD_{600} = 0.01 in TB:PBS) is injected into the channel, and bacteria are left to attach without flow for 30 min. The syringe is then replaced by a sterile medium (TB:PBS supplemented with 4 mM glucose). Unadhered bacteria are flushed out with a medium at 100 µL/min for 5 min, then the flow rate is set to 7.22 µL/min, and the temperature is maintained at 37 °C. The device and observation set up on an optical microscope are presented in **Figure 5.5**.

Figure 5. 5: Experimental setup for the dynamic observation of bacterial adhesion under flow, showing a testing surface with an integrated channel and the observation system on an optical microscope.

5.1.3 Results

Bacterial adhesion with rolling droplets

The experimental details are described above in **section 5.1.2** and **Figure 5.3**. After 12 h of exposure to droplets of the bacterial solution, surfaces are stained with CV solution to allow visualization of attached biomass. We have observed very distinct results from different samples. In particular, control glass substrates show a clear attachment of bacteria at the location of impact of bacterial droplets (**Figure 5.6**a). The surface with ZnO NWs also shows a clear trace of bacterial attachment and biofilm formation, observed through naked eyes. This attachment can be attributed to its high hydrophilicity, allowing the bacterial droplets to spread and facilitate bacterial attachment (**Figure 5.6**b).

Interestingly, the silicone oil-infiltrated ZnO NW SLIPS sample remains clean after the test (**Figure 5.6**c). The surfaces are then observed on a microscope to image the possible formation of biofilms, and consistent results are obtained. Bacteria densely cover the contact area on the glass surface, showing the formation of bacterial biofilm (**Figure 5.6**d). In contrast, only a few bacteria are seen in the contact area on the silicone oil-infiltrated ZnO NW surface. Also, these bacteria are observed as individuals, not as clusters or communities (**Figure 5.6**e). Thus, they could likely be dead bacteria. These results indicate the excellent ability of our SLIPS surface to prevent bacterial proliferation, which seems to be due to the suppression of bacterial adhesion owing to the very low affinity between the media and the surface.

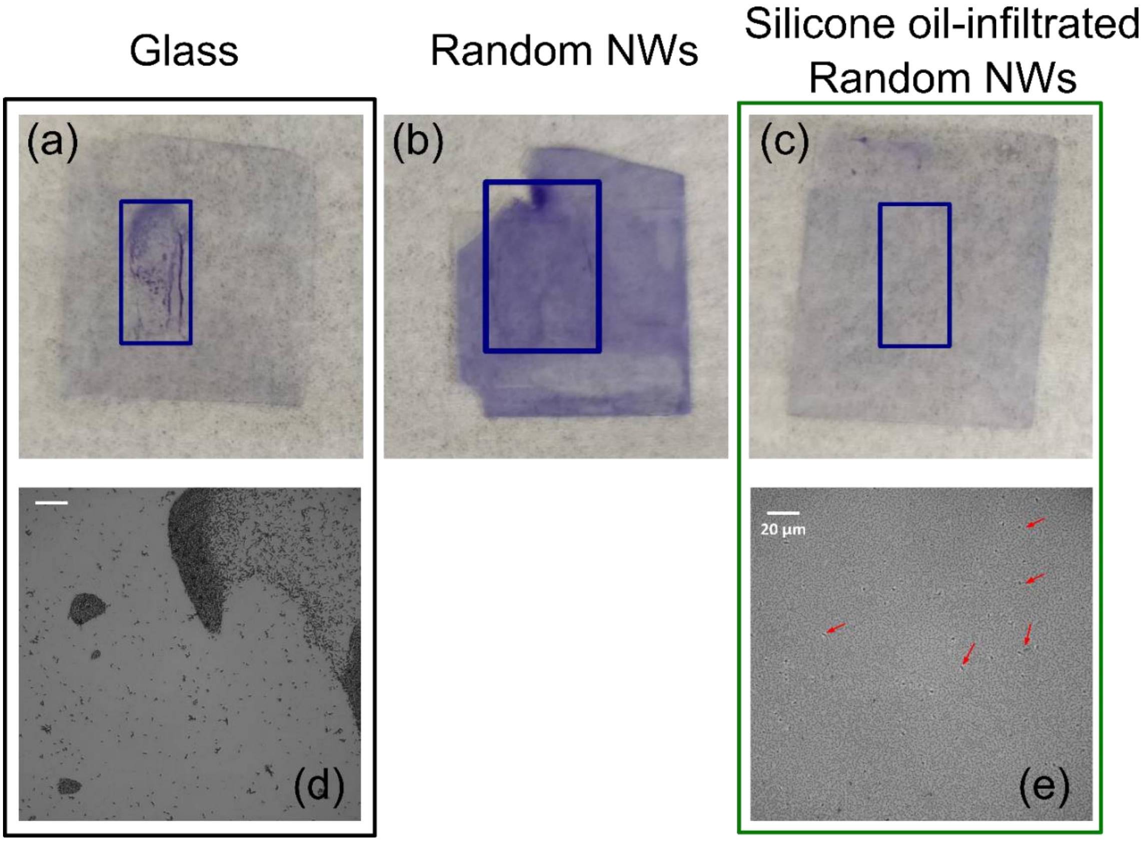

Figure 5. 6: Bacterial adhesion with rolling droplets. (a-c) Photographs of glass, random ZnO NWs, and silicone oil-infiltrated ZnO NW surfaces, respectively, after 12h of exposure to rolling bacterial droplets with CV staining. The highlighted areas represent the areas of contact with bacterial droplets. (d) and (e) show optical microscope images of glass and silicone oil-infiltrated ZnO NW surfaces, respectively. Red arrows point to individual bacteria that can be seen on the NW surface. Photo credit: Dr. Sigolène Lecuyer.

Microtiter dish biofilm formation assay

These experiments use static, batch-growth conditions that could facilitate bacterial biofilm formation. It has been shown that bacterial biofilms grown in microtiter dishes present properties similar to established biofilms, for example, antibiotic resistance.[465] Thus, results from this experiment can provide critical information about the growth of bacterial biofilms on the surfaces. After 46h of incubation with bacterial solution, the surfaces are rinsed carefully with DI water and imaged on an optical microscope. On the surface of the glass, most bacteria attach to the surface by their body, which shows a strong interaction between the bacterial body and the substrate, indicating the beginning of a bacterial biofilm formation, as shown in **Figure 5.7**a. The surface with ZnO NWs is also colonized by bacteria and even exhibits bacterial clusters called microcolonies (**Figure 5.7**b). These results suggest that the high hydrophilicity of these random NWs could facilitate the attachment of bacteria. The surface of the silicone oil-infiltrated ZnO NW sample presents much better prevention of bacterial attachment after 46h (**Figure 5.7**c). There are just a few bacteria on this SLIPS sample, and they seem to be vertically attached to the surface, probably just by their flagella (as we observed them spinning along the vertical axis during the experiment). The vertical position of bacteria suggests a weak interaction of the bacterial body with the surface. This result confirms the remarkable role of the dynamic lubricant layer in preventing bacterial attachment.

We have found that after 46 h a thick layer of bacterial biofilms develops in the culture dish containing our silicone oil-infiltrated ZnO NW SLIPS sample. However, this biofilm layer loosely attaches to the sample surface and can be detached easily (e.g., by vibrating, shaking, or strongly rinsing) to remove the biofilm from the surface (**Figure 5.8**). We anticipate that this biofilm likely comes from a self-organized arrangement of bacteria through their coaggregation in the liquid phase because there is no available area for their attachment. Typically, adherent bacterial biofilms are very difficult to treat, but our observations show that we can wash away bacterial biofilms from our SLIPS sample. Such an observation holds great potential in addressing the challenge of bacterial biofilms prevention by adapting our unique silicone oil-infiltrated ZnO NWs.

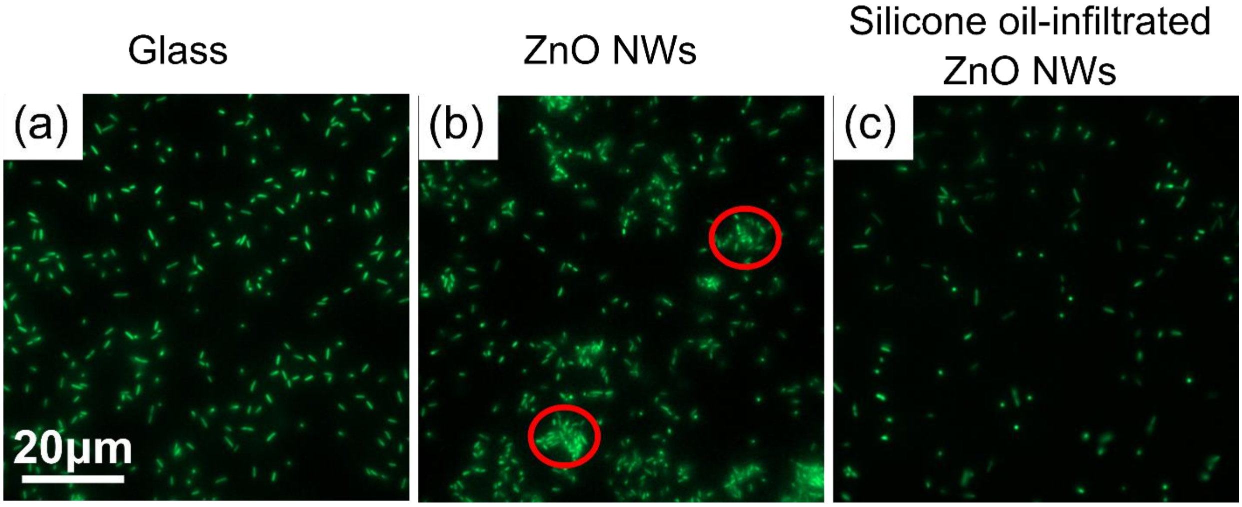

Figure 5. 7: Observation of the formation of bacterial biofilms developed on the surface of the glass (a), ZnO NWs (b), and the silicone oil-infiltrated ZnO NW sample (c) after 46h by optical microscope. Bacteria are constitutively fluorescent and modified to express GFP. Red circles indicate bacterial microcolonies.

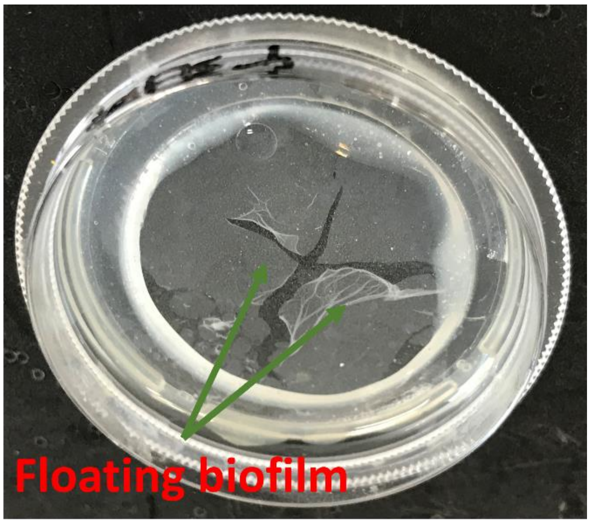

Figure 5. 8: A photograph shows a floating bacterial biofilm on the surface of the silicone oil-infiltrated ZnO NW sample, which can be removed easily.

The anti-fouling properties on these surfaces are also studied under dynamic conditions (flow velocity of 7.22 µL/min). A constant flow of medium renews nutrients and removes unattached bacteria so that firmly attached bacteria growing on the surface can be imaged in situ. In our case, we do time-lapse experiments, taking 1 frame every 30 seconds for several hours. By quantifying the surface coverage of bacteria on the surfaces (i.e., % of the surface covered by bacteria) over time, we can evaluate the prevention of bacterial adhesion on the surfaces (**Figure 5.9**). The glass surface is covered by bacteria rapidly. The results show that bacteria cover about 13.5% of the surface of the glass sample after 60 min, which agrees well with our previous experiments where bacteria easily cover the surface of the glass sample. Under these dynamic conditions, bacteria also adhere to the surface of ZnO NWs. Bacteria cover about 1.1% of the random ZnO NWs surface after 60 min, which is much lower than the glass. This result is surprisingly different from the microtiter dish biofilm formation assay. Such a suppressed bacterial adhesion on the surface of ZnO NWs could be due to a continuous fresh liquid film in contact with the highly hydrophilic surface because of the flow condition. Remarkably, the silicone oil-infiltrated random ZnO NW sample again presents promising prevention of bacteria adhesion. After 60 min, only about 0.6% of this surface is covered by bacteria, about 2 times smaller than on the random ZnO NWs surface and 20 times smaller than on the glass surface (**Figure 5.9**a). Furthermore, using Fiji for image processing, we observed that the average size of bacteria on the surface of the silicone oil-infiltrated random NWs sample varied in the range of 0.6 – 1.2 µm, which is about half compared to the other two samples (1.5 – 3.5 µm). These results support that bacteria stand on the surface of the silicone oil- infiltrated random NWs sample due to the weaker interaction between bacteria and the dynamic infiltrated silicone oil layer.

In addition, by plotting the %surface coverage vs. time curves using log-linear representation, the equivalent growth rate of bacteria on these surfaces can be evaluated. Accordingly, we have observed that the attachment of bacteria on the surface of the glass sample presents exponential growth. This is also the case for the random NWs sample, where the attachment of bacteria increases exponentially (**Figure 5.9**b). However, the equivalent growth rate on the surface of the random NWs sample is slower. These results likely suggest that the division rate of attaching bacteria is indeed slower or that there is a detachment of bacteria on the surface of the random NWs due to the continuous fresh liquid film.

Interestingly, the silicone oil-infiltrated random NWs surface exhibits no sign of bacterial attachment for ~ 30 min. As we described previously, bacteria have been found rotating around the vertical axis on the surface of silicone oil-infiltrated random NWs, which suggests that bacteria interact with the surface through the attachment of flagella. Previous work has reported that this attachment of flagella generally precedes bacterial detachment due to its weak interaction.[466, 467] After 30 min, the attachment of bacteria on this surface suddenly increases and is not precisely exponential (**Figure 5.9**b). We anticipate that this result does not indicate a sudden attachment of bacteria because the number of bacteria attaching to the surface is relatively low (~75 bacteria after 60 min). This result could indicate the transition of attaching behavior of bacteria that transit from a standing state to a typical flat state, consequently leading to higher surface coverage (**Figure 5.9**c).

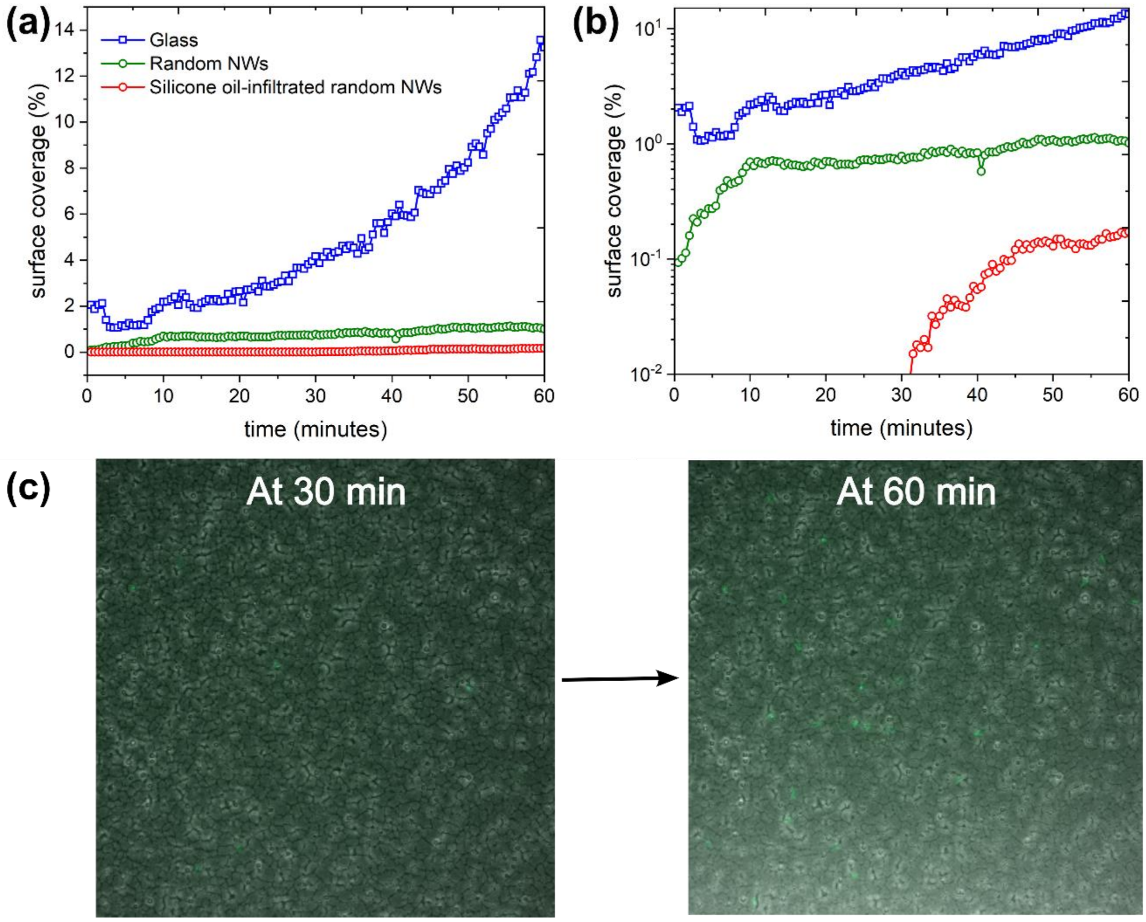

Figure 5. 9: Dynamic adhesion of bacteria on the surfaces. (a) Surface coverage by bacteria over time and (b) Log-Linear representation of the surface coverage. (c) Optical image of the silicone oil-infiltrated ZnO NWs surface after 30 min and 60 min, showing the transition in surface coverage. Bacteria are labeled in green.

Despite the excellent prevention of bacterial attachment, the silicone oil-infiltrated ZnO NW sample presents a surface loss at a later stage (under flow and bacteria presence). After 70 min, the surface of the silicone oil-infiltrated ZnO NW sample shows typical surface patterns due to its structured morphology and remains effective in preventing bacterial attachment, with few bacteria present and mostly standing on the surface (**Figure 5.10**a). However, after 90 min and 110 min, we have observed a removal phenomenon, where the surface pattern is gradually washed out, leaving a smooth surface (**Figure 5.10**b,c). Upon this removal of surface patterns, the surface of the sample is quickly colonized by bacteria that present typical dividing behaviors and microcolony formations (**Figure 5.10**d). Because the sample has been subjected to a rinsing step with the same experimental conditions (flow with the medium solution at a velocity of 7.22 µL/min) overnight and has not shown any stability issues, we anticipate the pattern removal to be linked to the presence of bacteria. Previous works have reported that bacteria can produce a small amount of organic acid and change the local pH value, damaging the coatings.[419, 444, 447] Bacteria also produce biosurfactants that could destabilize the oil layer. Although these studies are in progress, we envision one of the potential solutions for addressing this challenge to be the functionalization of ZnO NWs with low surface energy compounds to enhance the liquid repellency and enhance the bonding between ZnO NWs and silicone oil.

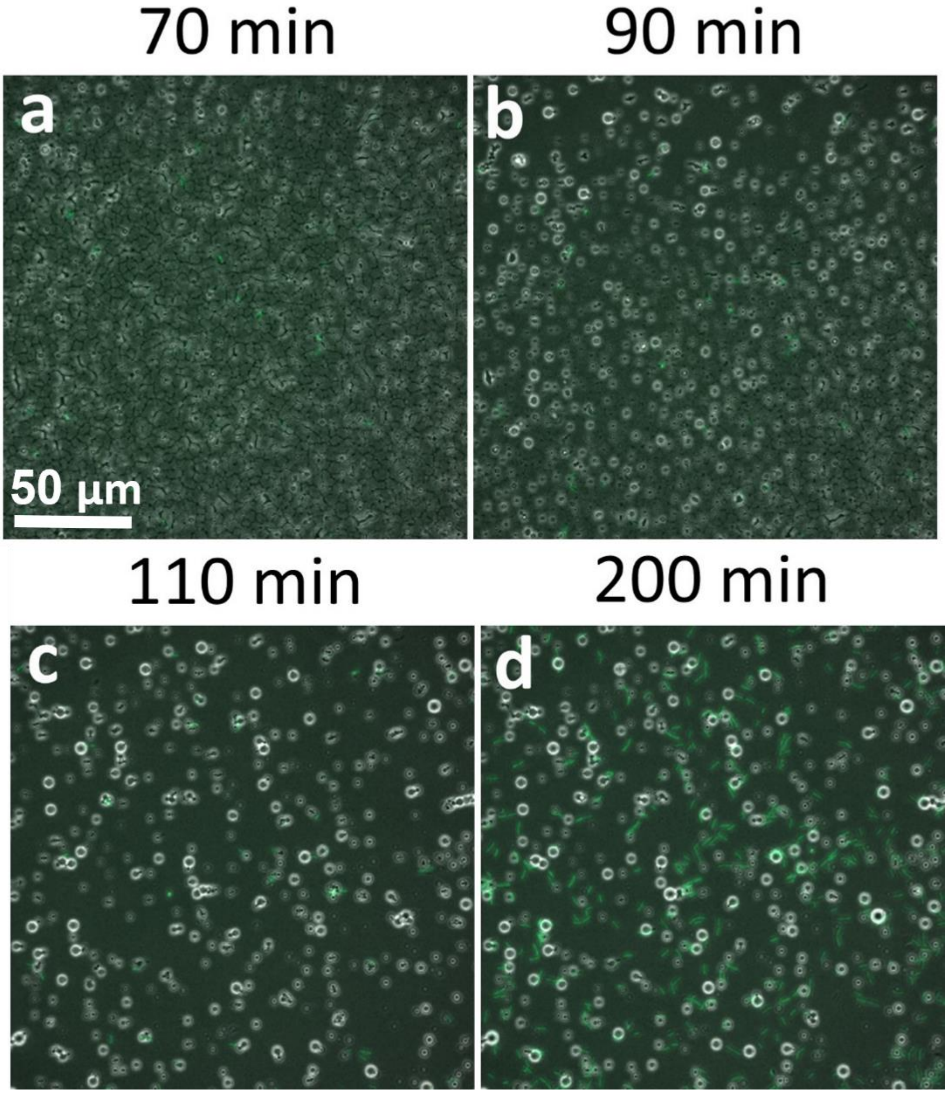

Figure 5. 10: Surface removal of the silicone oil-infiltrated ZnO NW samples under the flow cell experiments. (a) Surface with patterns before the removal. (b) The beginning of the surface removal. (c) The patterns on the surface are entirely removed. (d) Attachment and colonization of bacteria to the removed surface.

These preliminary studies suggest that the silicone oil-infiltrated ZnO NW samples exhibit an auspicious anti-biofouling property. Such excellent prevention against bacterial adhesion likely comes from the highly mobile and dynamic infiltrated silicone oil layer, forming liquid-liquid interfaces between this surface and the liquid environment. Such a mobile surface prevents contact points/areas between the surface and the liquid environment, which is not the case for other samples having a solid surface where the biological adhesives could make permanent interactions. Although works are still in progress to confirm the efficiency of our silicone oil-infiltrated ZnO NW samples, these very encouraging results indicate that our surface holds great potential as an effective anti-biofouling surface.

5.2 ZnO NW-based membranes

5.2.1 The need for membranes with anti-fouling properties

Water pollution represents one of the grand challenges that has been affecting humanity globally for decades.[468, 469] The sources of contamination are numerous, including thousands of chemical mixtures released from the industry or tons of oils spread because of disasters.[470-473] Pathogenic bacteria in the water are responsible for about 2 million deaths every year.[468, 474] These pollutants have stressed the world's access to clean water, which has already been threatened.[475, 476] Furthermore, access to clean water for drinking and sanitary during natural disasters becomes challenging as local water sources are typically polluted. Thus, it is critical to developing efficient and practical solutions to produce clean water from unconventional water sources (e.g., seawater or polluted water).

Membrane separation is a unique water treatment technology because of its simple use, low energy requirements, portable ability, and excellent tunability.[104, 477-484] With the significant development of polymer science and engineering, polymeric membranes have been most commonly used.[485-489] However, polymeric membranes exhibit several essential drawbacks.[478, 490] In particular, polymeric membranes are easily fouled and blocked by oils and bacterial biofilms.[491-496] Membrane fouling is challenging to treat, resulting in a continuous drop in flux and separation performance.[490, 497-499] Chemical cleaning is not suitable because such an approach generates secondary pollution and is costly. Polymeric membranes are also vulnerable and do not work well under harsh conditions because of their poor mechanical and chemical stability.[498, 499]

Membranes with nanostructured metal oxides have recently shown promising properties, such as improving membrane separation performance and mechanical properties imparting self-cleaning and chemical resistance.[500-507] Among them, ZnO NW-based membranes have demonstrated several exciting properties, such as improved permeability, self-cleaning, photocatalytic, and excellent oil/water separation.[501, 508-516] However, fabrication of these membranes requires expensive equipment and complicated procedures that seriously hinder large-scale manufacturing.[517-519] In addition, when ZnO NWs are prepared separately and then coated on the surface of membranes via conventional techniques (e.g., spray coating or spin coating), the resulting membranes usually present poor mechanical stability, low adhesion between the NWs and the membranes.[510, 520] Direct growth of ZnO NWs on the membranes can effectively address the above problem. However, it is challenging to directly grow ZnO

NWs on membranes as ZnO has low adhesion to most commercial membranes.[521, 522] Also, the poor diffusion of the precursors into the pore structure of membranes represents a considerable challenge for seeding and growing NWs.[523] Another challenge in growing ZnO NWs on membranes is the typical cylindrical or fiber-shaped membranes having large curvatures.[524]

Inspired by the results presented in this thesis, including a straightforward approach for fabricating ZnO NWs[288, 336] and scalable methods for producing stable anti-fouling surfaces,[342, 399] we envision that it is possible to adapt this knowledge and make membranes with remarkable anti-fouling properties in a scalable fashion. We aim to apply our membranes for oil/water separation where the surface wettability of ZnO NWs can be tuned to control which liquid can go through, while the excellent anti-fouling will ensure their long-term use. Typically, there are two types of oil/water mixtures based on the size of the droplets, including immiscible oil/water mixture (>20 µm) and emulsified oil/water mixtures (<20 µm).[525, 526] Thus, we have used stainless steel meshes (pore size: 50 µm) and glass fiber membranes (pore size: <10 µm) as substrates for growing ZnO NWs.

5.2.2 Stainless steel mesh-grown ZnO NWs

Membrane preparation

Stainless steel meshes (SSM) (pore size of 50 µm) are purchased from TWP Inc. SSMs are cut into 2.5 cm x 2.5 cm pieces. Next, these pieces are sonicated for 5 min in acetone, ethanol, and DI water, respectively. The meshes are dried with air and heated at 135 °C for 10 min. These SSMs are annealed at 500 °C for 1h and treated with oxygen plasma for 2 min before seed layer coating.

ZnO seed layer coating

ZnO sol solution is prepared according to the protocol described in **Chapter 2**. 300 µL of sol solution (0.37 M) is injected into the container of the spray coater. The distance from the membrane surface to the airbrush tip is 5 cm. After being coated with the sol solution, the membranes are placed into an oven at a temperature of 300 °C for 10 min, followed by 1h at 540 °C.

Growth of ZnO NWs

The procedure for growing ZnO NWs is similar to the protocol described in **Chapter 2**. Only one change is that the growth of ZnO NWs is implemented without stirring the precursor solution to reduce the attachment of microwires arising from the homogeneous growth in solution to the membrane surface.

Morphology of ZnO NWs-SSM membranes

The morphology of the as-prepared SSMs is observed using SEM images. The initial morphology of SSMs is shown in **Figure 5.11**a, showing a relatively smooth surface. After the seed layer deposition, the surface of fiber becomes rough with nanoparticle-like objects, indicating the successful coating of the ZnO seed layer (**Figure 5.11**b). Following the standard growth of ZnO NWs (**Chapter 2**), we have observed ZnO NWs uniformly grown on the surface of the SSM (**Figure 5.11**c,d). These results are strongly encouraging as by simply adapting our protocol, we can directly grow ZnO NWs on SSMs.

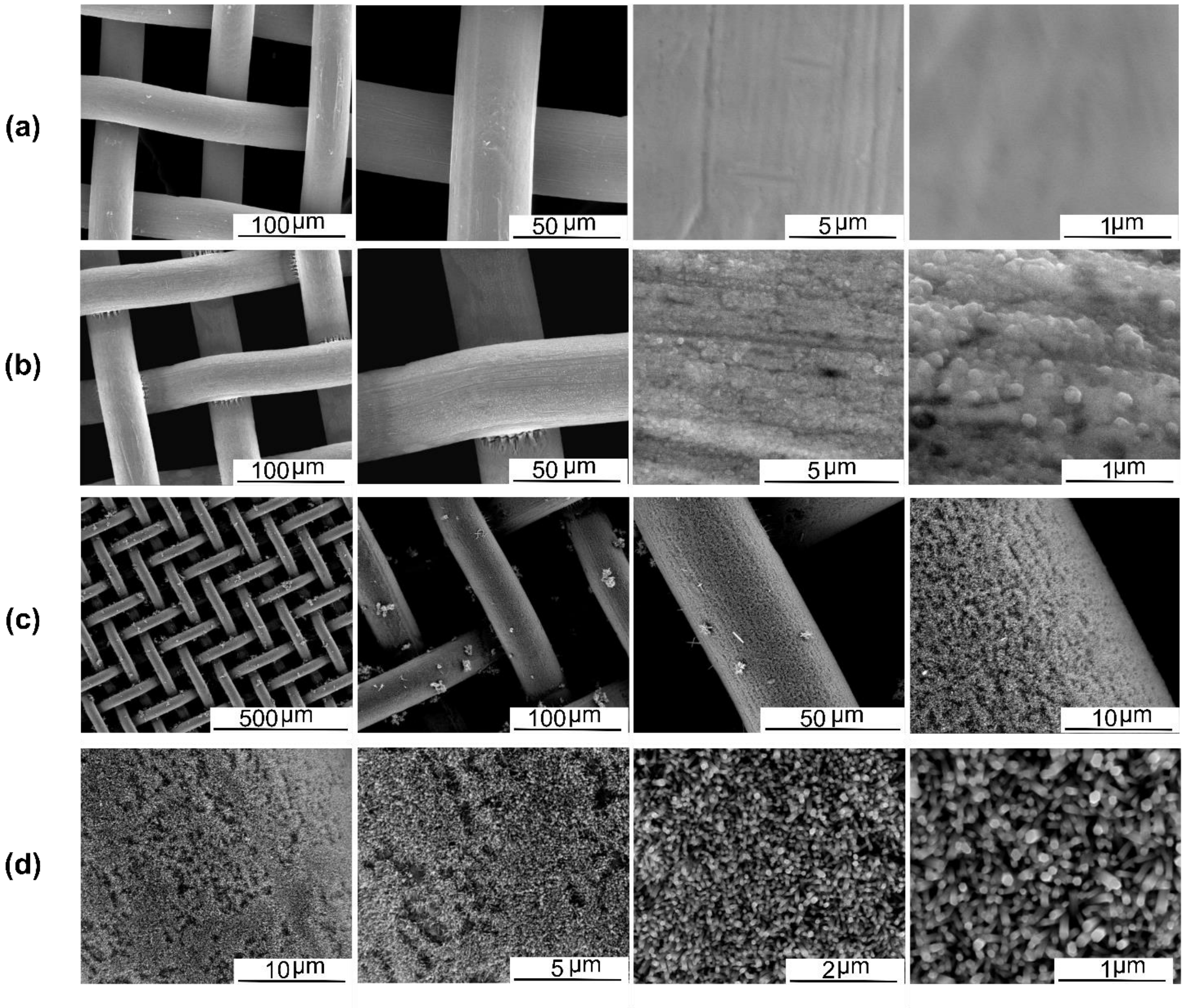

Figure 5. 11: Morphology of samples via SEM images. (a) Initial morphology of SSMs. (b) morphology of SSMs after seed layer deposition. (c) and (d) morphology of SSMs after ZnO NWs growth with different magnifications.

Besides this typical ZnO NW, we show that it is also possible to fabricate long and random ZnO NWs. By adopting the protocol for producing long and random ZnO NWs (**Chapter 2**), we have grown this type of NW on SSMs (**Figure 5.12**). Interestingly, these long and random NWs also present as aggregates and bundles as the ones seen on planar substrates. Furthermore, by increasing the growth time to a longer time (24h), we have obtained very long, thin NWs, closely covering the surface of the membrane, indicating a strong attachment of NWs.

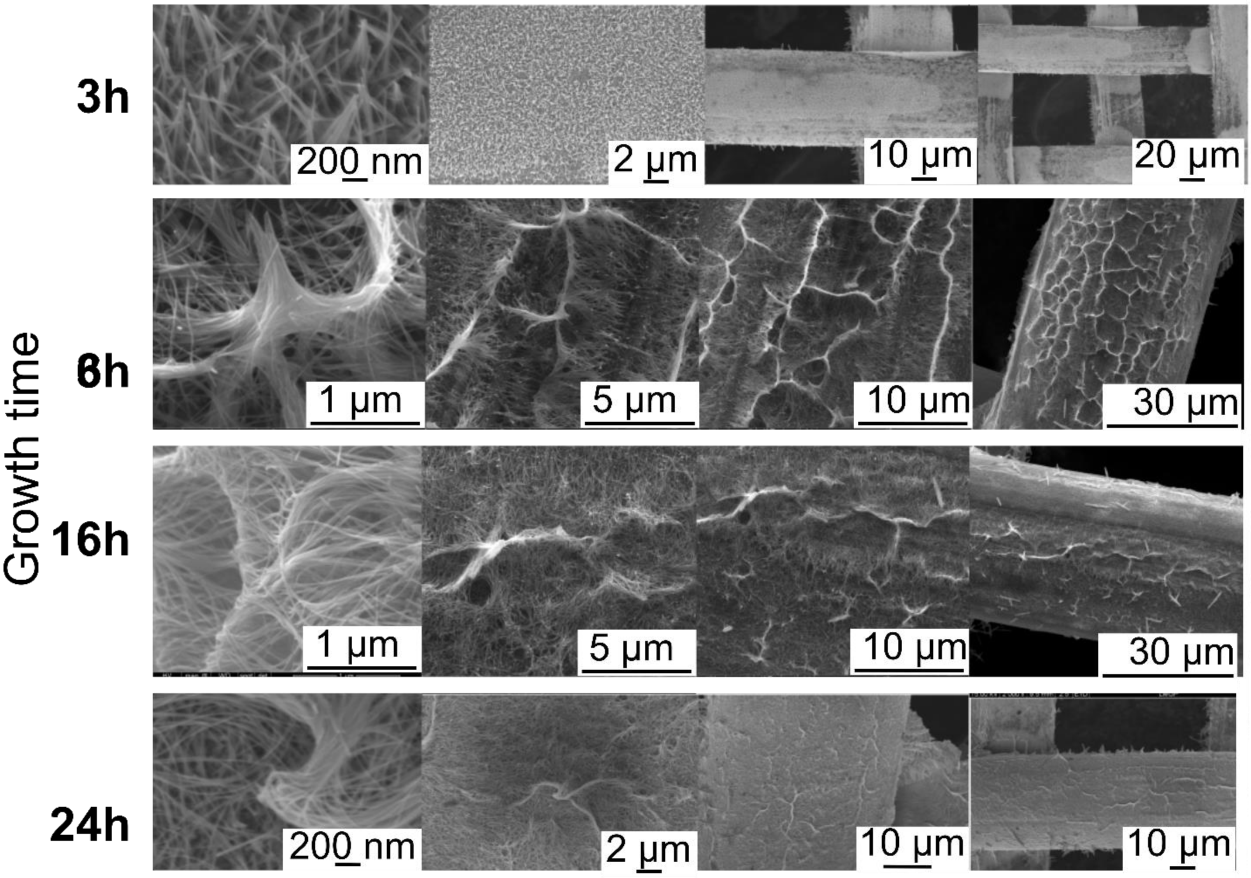

Figure 5. 12: SEM images showing the successful fabrication of long and random ZnO NWs on SSMs with different growth times (3h, 6h, 16h, and 24h respectively from top to bottom).

Furthermore, we have found that it is also possible to create hierarchical structures by combining the two above protocols. By using SSMs with standard ZnO NWs (**Figure 5.11**) as the substrate for the growth of long and random NWs, hierarchically structured membranes can be prepared (**Figure 5.13**). This new approach provides a more robust layer of long and random NWs. Such a structure with two different length scales likely has a strong capillarity for wicking and retaining properties. We envision that such a structure has a promising future, not only in membrane technology.

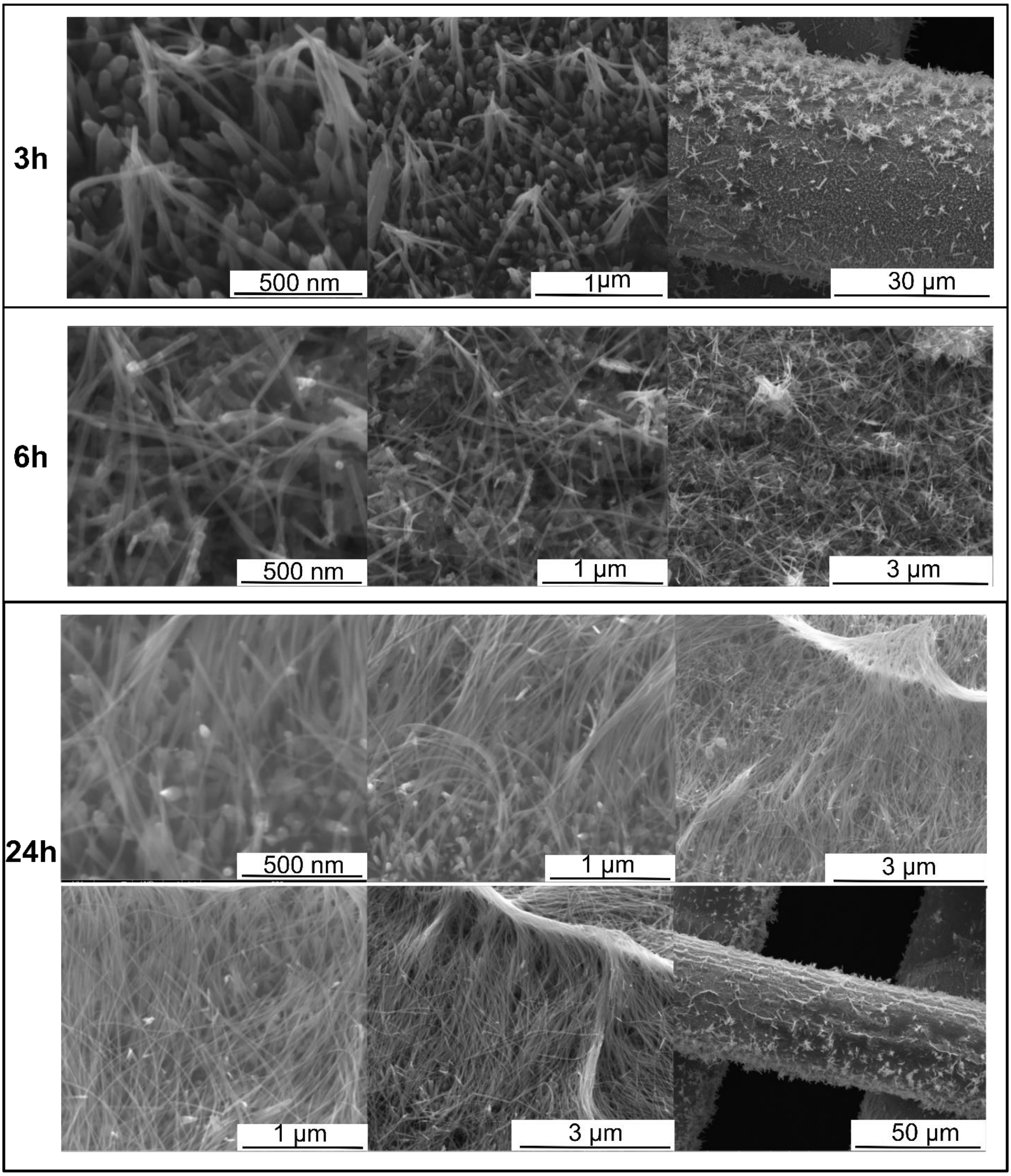

Figure 5. 13: SEM images showing the successful fabrication of hierarchically structured membranes SSMs with both standard and long, random ZnO NWs.

5.2.3 Glass fiber membrane-grown ZnO NWs

Membrane preparation

Glass fiber membranes (GFMs) (average pore size ranges from 0.7 to 2.7 μm) are purchased from Thermo Fisher Scientific. GFMs are cut into 2.5 cm x 2.5 cm pieces. Next, these pieces are sonicated for 5 min in acetone, ethanol, and DI water, respectively. The GFMs are dried with air and heated at 135 °C for 10 min. These GFMs are annealed at 500 °C for 1h. Before seed layer coating, the membranes are sonicated in 0.1 M NaOH/EtOH mixture for 5 min.

ZnO seed layer coating

ZnO sol solution is prepared according to the protocol described in **Chapter 2**. Spray coating is not suitable for coating GFMs as it is difficult to coat inner fibers uniformly. Also, as described in **section 5.2.1**, the sol solution suffers from a non-diffusion over membranes with extremely small pore size. Thus, we use dip coating for this study. The dip-coating process is performed on a lab-made dip coater. The clean GFMs are dipped into the sol solution (0.1M) and withdrawn at a very low speed (0.01 mm/s). After being coated with the sol solution, the membranes are placed into an oven at a temperature of 300 °C for 10 min, followed by 1h at 540 °C.

Growth of ZnO NWs

The procedure for growing ZnO NWs is similar to the protocol described in **Chapter 2**. Only one change is that the growth of ZnO NWs is implemented without stirring the precursor solution to reduce the attachment of microwires from the solution to the membrane surface.

Morphology of ZnO NWs-GFMs

The morphology of the as-prepared GFMs (average pore size of 2.7 μm) is observed using SEM images. The initial morphology of GFMs is shown in **Figure 5.14**a, showing a relatively smooth surface. After the seed layer deposition, the fiber surface has been covered by a uniform ZnO seed layer (**Figure 5.14**b). This result is strongly encouraging because coating the ZnO seed layer to GFMs is challenging, as discussed in section **5.2.2.1**.[521] With a relatively simple procedure, we have managed to nicely coat the surface of glass fibers with a ZnO seed layer.

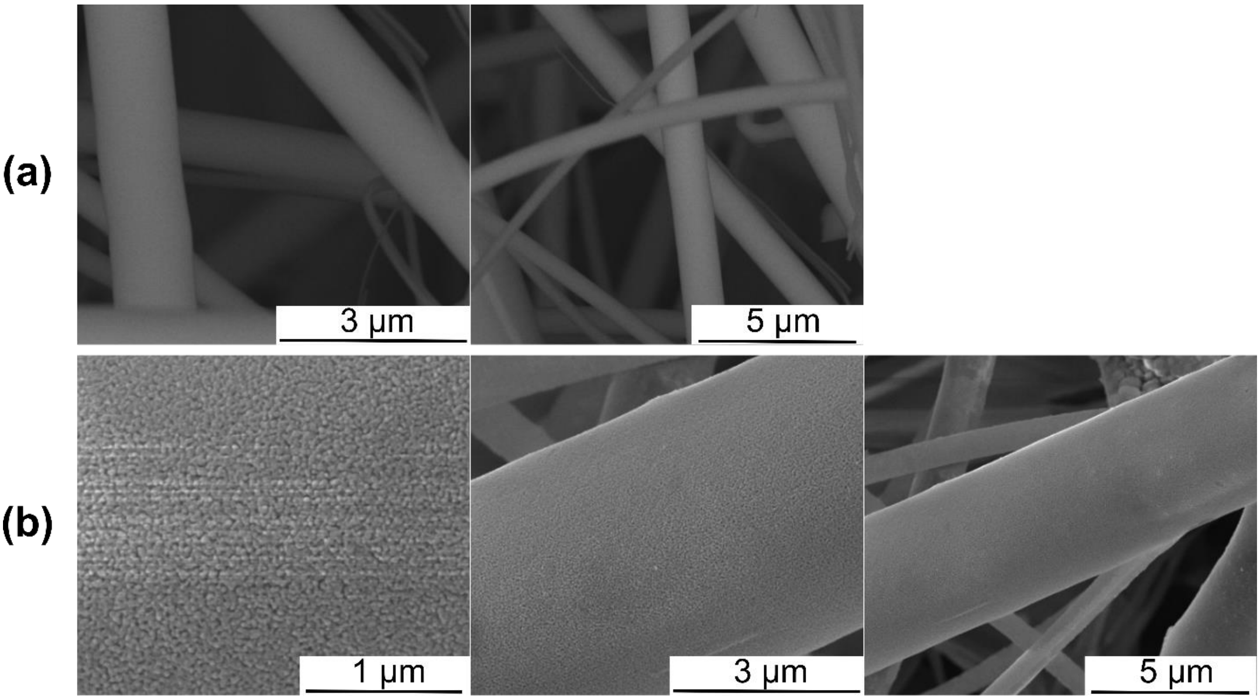

Figure 5. 14: Morphology of samples via SEM images. (a) Initial morphology of GFMs and (b) morphology of GFMs after seed layer deposition.

Having such a good seed layer, we have grown ZnO NWs from these seeded GFMs. Given the small membrane pore size, we also apply the growth of long, thin, and random ZnO NWs. Our results show that ZnO NWs have grown robustly on the seed layer, forming a spider network-like structure (**Figure 5.15**). Such a structure is highly needed to separate emulsified oil/water mixtures where the size of the oil droplets is tiny.

We have even applied our protocol to a smaller pore size GFM (0.7 μm), the smallest pore size of GFMs we could find. Although the poor diffusion of the precursors into the pore structure of membranes represents a considerable challenge for seeding and growing NWs over such a tiny pore size membrane.[523] We have successfully grown ZnO NWs on such a type of membrane. Thin and long ZnO NWs have been shown to cover the membrane surface fully (**Figure 5.16**). Thus, these results strongly suggest the success of our methods in fabricating ZnO NWs-based membranes via a scalable and straightforward approach, which holds great potential in the future.

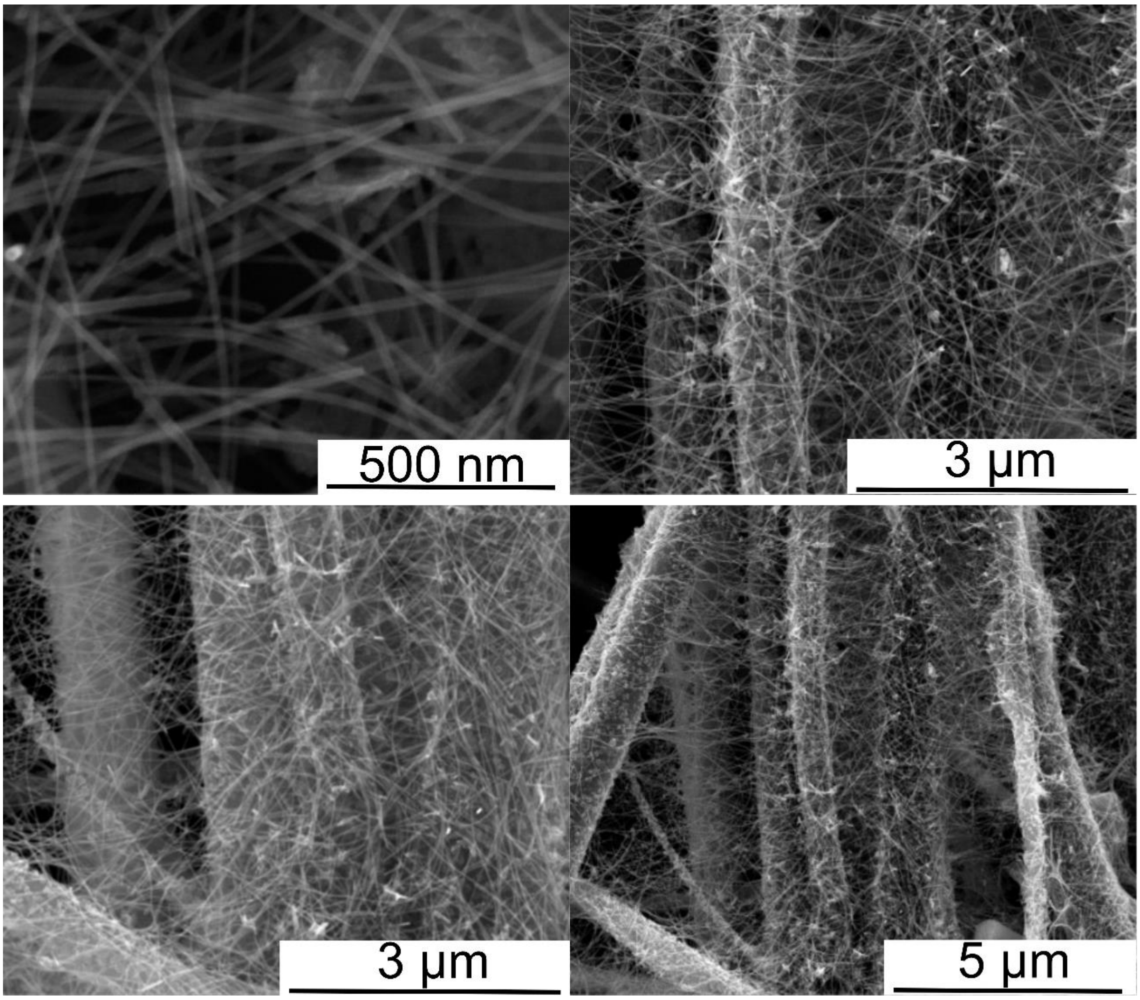

Figure 5. 15: SEM images showing the successful fabrication of long, random ZnO NWs on GFMs (pore size of 2.7 µm). Growth time: 16h.

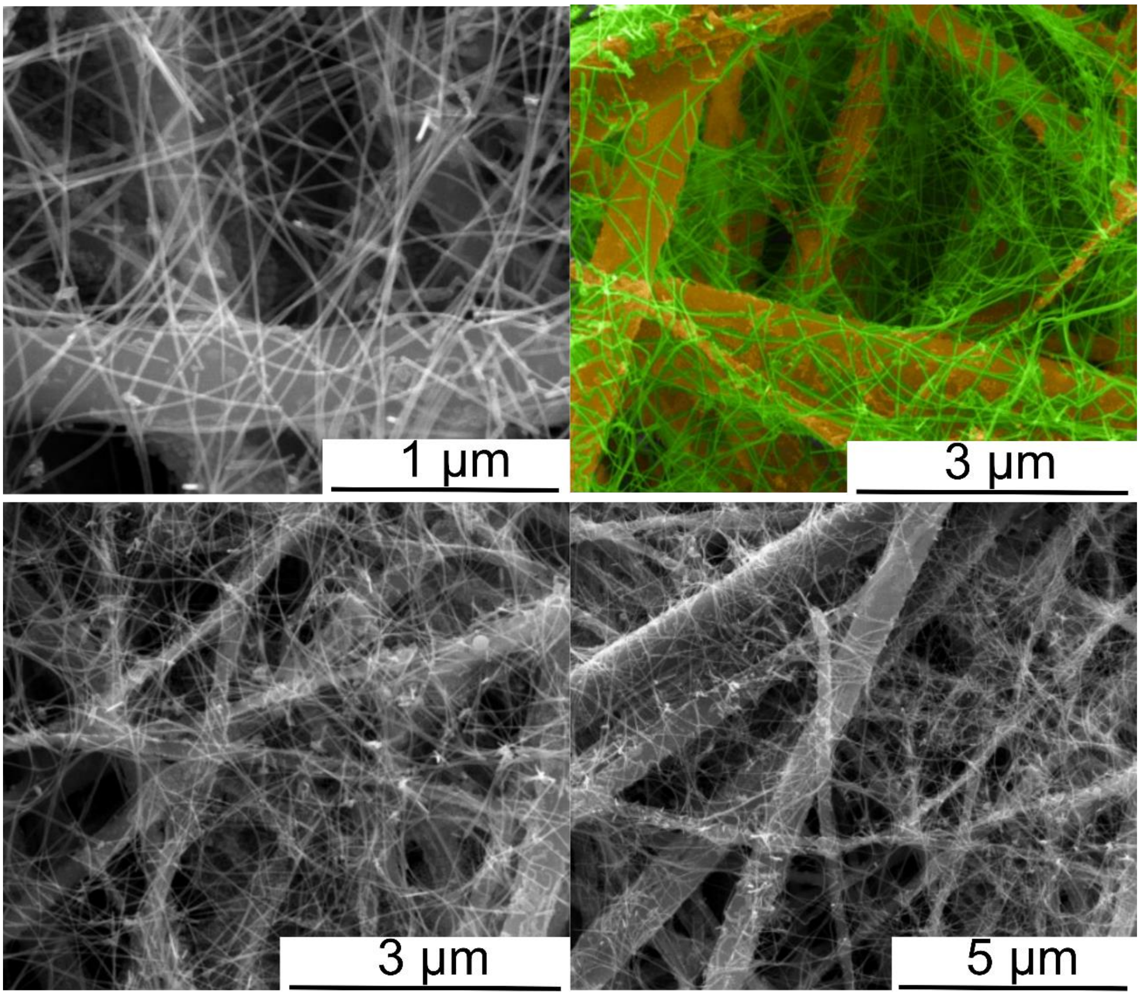

Figure 5. 16: SEM images showing the successful fabrication of long, random ZnO NWs on GFMs (pore size of 0.7 µm). Growth time: 16h. One image is colored for better distinction, where glass fibers are shown in brown and ZnO NWs are shown in green.

In summary, we explored the anti-biofouling property of our repellent surfaces. We studied the early biofilm formation of the model pathogen *Pseudomonas aeruginosa* on NWs-based surfaces through three experiments: rolling-drop experiments, microtiter-dish formation assays, and flow cell experiments. Our results suggested that the silicone oil-infiltrated random ZnO NW samples exhibited the most promising anti-biofouling property. Also, we studied the potential use of our ZnO NW materials for membrane separation applications. We described our first results on developing ZnO NWs-based membranes, using stainless steel mesh and glass fiber membrane as the substrates. We successfully grew arrays of vertical ZnO NWs and long, random ZnO NWs on the surface of the stainless steel meshes and even created hierarchical structures by combining the two types of NW. We also succeeded in coating a good seed layer and successfully grown ZnO NWs on the surface of glass fiber membranes. Our results showed that ZnO NWs had grown robustly on the seed layer, forming a spider network-like structure.

We envision a huge opportunity for fabricating anti-fouling membranes, adopting the findings in this thesis and these encouraging preliminary results. Our membranes could be used for oil/water separation where the surface wettability of ZnO NWs can be tuned to control which liquid can go through, while the excellent anti-fouling knowledge will ensure their long-term use. Another future direction is to synergy the photocatalytic activity of ZnO NWs and liquid repellency from the infiltrated polymers/lubricants to fabricate superhydrophobic photocatalytic membranes. This membrane type could be useful as surface contaminants and residuals will be removed through photocatalytic activity. However, optimization of the two properties should be studied because there is a trade-off between them where photocatalysis can also degrade hydrophobic polymers. Furthermore, as our protocols for growing ZnO NWs and fabricating liquid repellency coatings are relatively simple, it could enable scalable manufacturing of ZnO NWs-based anti-fouling surfaces/membranes to other substrates.

Conclusions and Perspectives

Summary and Conclusions

This thesis aims to develop anti-fouling nanocomposite surfaces with high stability under challenging situations. Specifically, we have developed two new capillarity-based methods for fabricating two unique types of anti-fouling surfaces: multifunctional superhydrophobic nanocomposite surfaces and lubricant depletion-resistant slippery lubricant-infused porous surfaces (SLIPS). We fabricated these nanocomposite surfaces by inducing the infiltration of polymers or lubricants into the interstices of surface-grown ZnO nanowires (NWs). Our surfaces presented several useful features: self-cleaning, anti-icing, solvent and chemical resistance, high transparency, self-healing, and anti-biofouling properties. The key findings of this thesis are: 1) a straightforward and scalable approach for fabricating repellent nanocomposite surfaces that precisely retain the original morphology of ZnO NW arrays; 2) retaining lubricant within the nanostructures is a key for producing stable SLIPS. These capillarity-based techniques present a tremendous simplification in fabricating anti-fouling nanocomposite surfaces, offering a huge opportunity for scalable manufacturing.

In Chapter 1, we summarized the pressing challenges of fouling and the attractiveness of using repellent surfaces to tackle such challenges. The fundamental concepts, preparation, and applications of repellent surfaces were highlighted. Specifically, we presented a general overview of superhydrophobic surfaces, polymer-grafted surfaces, and SLIPS, along with their mechanisms of repellency. In addition, the inherent drawbacks and critical factors leading to the repellency failure on these surfaces were discussed. We identified ZnO NW arrays-based nanocomposite surfaces as excellent nanostructured materials for repellent surfaces because of their ease of preparation, high surface roughness, and remarkable mechanical and chemical stability. Despite remarkable progress, the conventional methods for making these repellent nanocomposite surfaces involve multiple steps and are only suitable for lab-scale fabrication. We thus introduced a promising and new capillarity-based method for fabricating anti-fouling nanocomposite surfaces in a scalable fashion.

This thesis used surface-grown ZnO NW arrays as the key porous nanostructures for polymer and lubricant infiltration. Chapter 2 provided all experimental details on the growth and optimization of ZnO NW arrays by a chemical bath deposition method. In principle, this chemical bath deposition process leverages the heterogeneous growth of ZnO NW arrays on a nucleation surface (e.g., glass, silicon wafer), submerged in a bath of zinc and hydroxide ions source at a moderate temperature of 90 °C. The optimal concentrations of zinc nitrate hexahydrate and hexamethylenetetramine are 25 mM and the optimal growth time is 2h, respectively. One of the unique advantages of this method is its versatility in tuning the orientation of NWs. We controlled the orientation of ZnO NW arrays by changing the number of ZnO seed layer coatings. Our results showed that a higher number of seed layer depositions improves the verticality of NW orientation due to a larger grain size of ZnO on the nucleation surface. We also described the fabrication of random NWs with a high aspect ratio (i.e., the ratio between the length and diameter), which underwent aggregation to form bundles upon drying. All details about the preparation of a poly(dimethylsiloxane) (PDMS) elastomer through a cross-linking process (2h at 80 °C) were also described. Information about the characterization techniques, such as SEM, EDS, Raman, and water contact angle measurement and devices for sample preparation and testing (i.e., UV lamps, oxygen plasma system, thermal copper substrate) were fully provided in this chapter.

Nanocomposite films (NCFs), having vertical ZnO NW arrays, exhibit several useful properties owing to the unique morphology of vertical ZnO NWs. However, one of the critical challenges in fabricating such a NCF is retaining the original alignment of NWs throughout NCF fabrication. Conventional methods require multiple steps and are thus time-consuming and unsuitable for large-scale manufacturing, consequently constraining their widespread applicability. Chapter 3 described a new capillarity-based method for fabricating a nanocomposite surface with vertical ZnO NW arrays, leveraging leaching-enabled capillary rise infiltration (LeCaRI) of uncross-linked and mobile oligomers from a PDMS slab into the space between NWs. Several essential properties were demonstrated, including superhydrophobicity, self-cleaning, solvent resistance, anti-icing, high transparency, and anti-reflection properties. Upon infiltration of PDMS via LeCaRI, the surface of ZnO NW arrays became superhydrophobic and maintained its superhydrophobicity over one year of storage in the ambient air. When a droplet of water was brought into dynamic contact with the NCF surface, the droplet did not stick to the surface even if it was pressed onto the surface. Due to its superhydrophobic surface, PDMS/ZnO NW NCFs exhibited an excellent self-cleaning behavior by inducing roll-off of water droplets that picked up and removed the contaminants on the surface.

Furthermore, the PDMS/ZnO NWs NCFs demonstrated a superior anti-icing property to ZnO NWs and PDMS film, significantly delaying the formation of ice nuclei and reducing the growth rate of ice crystals. The ability to resist failure due to UV light ageing could be extremely useful for outdoor settings; we thus explored and demonstrated excellent stability of our PDMS/ZnO NWs NCFs against UV light. The resistance to common organic solvents was also discussed in this chapter. We believe this method could potentially be scaled up to enable the continuous fabrication of these versatile NCFs. The results shown in this chapter were published in the following paper: H. Tran, B. Venkatesh, Y. Kim, D. Lee, D. Riassetto, *Nanoscale* 2019, 11, 22099 – 22107.

Despite their great promise, superhydrophobic PDMS/ZnO NW NCFs have drawbacks that make their applications challenging under harsh conditions, such as long-term immersion under acidic media or in contact with biological species. This is a fundamental limitation of superhydrophobic surfaces because of its repellency mechanism based on a solid-liquid interface and susceptibility of the air-cushion layer. Inspired by SLIPS, Chapter 4 described a new approach to using silicone oil as the infiltrating component to create a repellent surface with a dynamic liquid-liquid interface to overcome these drawbacks. However, the lubricant layer is depleted over time, causing degradation of surface properties. The formation of wetting ridges surrounding liquid droplets on the surface of SLIPS was identified as one of the primary sources of lubricant depletion. We hypothesized that controlling pore features of NWs could be an effective way to improve the stability of the infiltrated silicone oil. One way to achieve this would be to change the orientation of NWs. Specifically, we described a capillarity-based method for producing stable SLIPS by infiltrating silicone oil into the three types of ZnO NW arrays with different orientations, including vertical, tilted, and random NW arrays. The orientation of NWs strongly affected lubricant infiltration and the stability of SLIPS properties. The strong lubricant retention ability provided by the nanoporous structure of the random NWs array suppressed the growth of a wetting ridge around a water droplet and could even resist lubricant depletion under strong external forces. The results shown in this chapter were published in the following paper: H. Tran, Y. Kim, C. Ternon, M. Langlet, D. Riassetto, D. Lee, *Advanced Materials Interfaces* 2021, 8, 2002058.

Advancing from these exciting findings, we explored the anti-biofouling property of our surfaces. We studied the early biofilm formation of the model pathogen *Pseudomonas aeruginosa* on NWs-based surfaces. Three different approaches were used to study the efficiency of NW-based surfaces in preventing biofilm formation: rolling-drop experiments, microtiter-dish formation assays, and flow cell experiments. Our results suggested that the silicone oil-infiltrated random ZnO NW samples exhibited the most promising anti-biofouling property. The remarkable prevention against bacterial adhesion of this sample could derive from the dynamic features of the infiltrated silicone oil layer, inducing liquid-liquid interfaces between this surface and the liquid environment. Such a mobile surface prevents contact points/areas between the surface and the liquid environment, which is not the case for other samples having a solid surface where the biological adhesives could make permanent interactions. Indeed, we observed a thick layer of bacterial biofilm on the silicone oil-infiltrated ZnO NW sample surface after 46h. However, this biofilm layer was loosely attached to the sample surface and could be detached easily (e.g., by vibrating, shaking, or strongly rinsing), enabling biofilm removal from the surface. Also, our results showed that after 60 min under dynamic conditions, only about 0.6% of this surface was covered by bacteria, about 2 times smaller than on the random ZnO NWs surface and 20 times smaller than on the glass surface. Although works are still in progress to confirm the efficiency of our silicone oil-infiltrated ZnO NW samples, these very encouraging results indicate the great potential of our repellent surfaces as an effective anti-biofouling surface.

Also, in this chapter, we explored the potential use of our ZnO NW materials for membrane separation applications. We described our preliminary results on the development of ZnO NWs-based membranes. There were two types of membranes (stainless steel mesh and glass fiber membrane) with two distinct pore sizes used as membrane substrates for growing ZnO NWs. Following the standard growth of ZnO NWs, we uniformly grew ZnO NW arrays on the surface of the stainless steel meshes. Besides this typical ZnO NW array, we successfully grew long and random ZnO NWs on the surface of the stainless steel meshes and even created hierarchical structures by combining the two types of NW. A hierarchical structure with two different length scales could provide a strong capillarity for wicking and retaining properties. In addition, we also succeeded in coating a good seed layer and successfully grown ZnO NWs on the surface of glass fiber membranes. Our results showed that ZnO NWs had grown robustly on the seed layer, forming a spider network-like structure. Such a structure could be highly desirable in separating emulsified oil/water mixtures where the size of the oil droplets is tiny. Thus, these results strongly suggested the success of our methods in fabricating ZnO NWs-based membranes via a scalable and straightforward approach, which holds great potential in the future.

Our membranes could be used for on-demand oil/water separation where the surface wettability of ZnO NWs can be tuned to control the penetrating liquids, while our anti-fouling knowledge will ensure their long-term use. Another exciting direction is to combine the photocatalytic activity of ZnO NWs and liquid repellency from the infiltrated polymers/lubricants to fabricate superhydrophobic photocatalytic membranes. This membrane type could be useful as surface contaminants and residuals will be removed through photocatalytic activity. However, optimization of the two properties should be studied because there is a trade-off between them where photocatalysis can also degrade hydrophobic polymers. Furthermore, the preparation of self-standing ZnO NWs-based membranes could also be an exciting direction where we could differently functionalize the two surfaces of the membrane to impart two opposite wettability, potentially resulting in functional Janus membranes.

Perspectives

Lubricant depletion induced by wetting ridges is a pressing challenge that must be overcome for the widespread use of SLIPS. A fundamental understanding of wetting ridges is a key to designing stable SLIPS. Nanostructured materials show enormous potential in retaining lubricant through high capillarity. Capillary rise infiltration lubrication is unique in infusing a thin lubricant layer on various porous structures, potentially generating a precisely structured lubricant layer.[399] Such a capillarity-based approach can easily generate a structured and thin lubricant layer that holds great promise as the future direction in fabricating stable SLIPS. Capillary-based techniques have been used extensively to make polymeric nanocomposites in which the infiltrated polymers are exclusively located in the interstitial pores.[31, 32, 34, 342, 345, 388] Thereby, these capillary-based techniques could be applied to lubricate porous structures with high roughness, enabling rapid fabrication of structured SLIPS.

Previous studies have confirmed the excellent lubricant retention of nanostructures owning to their high capillarity originating from the small length scales. However, surfaces with nanostructures still present some drawbacks. For example, it has been shown that the liquid flow within nanostructured surfaces is slower compared to that in microstructured surfaces because of the high viscous drag.[527] It is thus possible that the self-healing ability is not efficient due to the slow lubricant movement within and between nanopores. The combination of micro and nano-scale structures could be a promising solution. Therefore, hierarchical structures promise to improve lubricant retention via suppression of wetting ridge formation. For example, porous substrates can be modified to have a rough surface, followed by lubricant infiltration via capillary rise lubrication. Thereby, stable and self-healing SLIPS can be obtained.

In addition to suppressing the formation of wetting ridges, the fabrication of a slippery, rough surface also leads to opportunities to study the interaction between a liquid droplet with a rough lubricant (soft) layer. Since the morphology of structured SLIPS is similar to superhydrophobic structures, comparative studies between them are essential to better understand their underlying repellency mechanisms. It will also be essential to understand the behavior of moving liquid droplets on such a rough lubricant layer, including the dust/particle removal mechanism for self-cleaning applications or preventing adhesion in anti-biofouling applications.

Theoretical understanding of structured SLIPS needs further development. Current thermodynamic understandings of the deposition of a liquid droplet on SLIPS exclusively assume that there are only two possibilities either the droplet will float on the lubricant layer with wetting ridges or sink.[119, 206, 401, 528] However, as we highlighted, recent studies have shown that wetting ridges can be minimized or even eliminated; it is thus essential to extend those current understandings, which could enable the discoveries of new stable SLIPS.

Recent successes in making rough SLIPS with no excessive lubricant could positively impact applications such as condenser and force sensor coatings, surface-enhanced Raman spectroscopy surfaces, and water harvesting. These applications will benefit from the remarkable liquid repellency without worrying about lubricant contamination.

We used silicone oil as a lubricant rather than the fluorinated oils used by many other groups in fabricating SLIPS because silicone oil could be used as a solvent for a wide range of molecules/drugs. We imagine that surfaces made with silicone oil could act as depots and release molecules/drugs to deliver the required functionalities into surrounding environments actively. Also, previous works showed that silicone oils perform better than perfluorinated oils in preventing biofouling on medical devices. For example, small molecules could diffuse through the silicone oil layer, making it potential drug-releasing biomaterials.[404]

Our LeCaRI method only involves physical contact between the PDMS elastomer and a porous surface; it can be adopted to make patterned NCFs with localized wettability. For example, we could fabricate surfaces with wetting gradients. Such surfaces could be helpful for droplet manipulation and transportation research.

Despite significant progress in repellent surfaces, scalable manufacturing of these repellent surfaces remains a critical challenge and is vital for future development. To reduce the complexity of processing challenges, promoting the development of surfaces/materials with multiple functions is needed to realize the practical impact. Thus, the findings of this thesis on a straightforward and scalable approach for fabricating repellent nanocomposite surfaces and a concept for producing stable SLIPS are essential. These capillarity-based techniques represent a considerable simplification, making them uniquely suited for manufacturing anti-fouling nanocomposite surfaces. The fundamental understanding from this thesis can also enable others to design long-lasting liquid-repellent surfaces.

References

1. Kota, A.K., W. Choi, and A. Tuteja, Superomniphobic surfaces: Design and durability. *MRS Bulletin*, **2013**. 38(5): p. 383-390.
2. Chu, S., Y. Cui, and N. Liu, The path towards sustainable energy. *Nature Mater,* **2016**. 16(1): p. 16-22.
3. Kreder, M.J., et al., Design of anti-icing surfaces: smooth, textured or slippery? *Nature Reviews Materials*, **2016**. 1(1): p. 15003.
4. Tian, X., T. Verho, and R.H. Ras, Surface Wear. Moving superhydrophobic surfaces toward real-world applications. *Science*, **2016**. 352(6282): p. 142-3.
5. Darmanin, T. and F. Guittard, Recent advances in the potential applications of bioinspired superhydrophobic materials. *Journal of Materials Chemistry A*, **2014**. 2(39): p. 16319-16359.
6. Onda, T., et al., Super-Water-Repellent Fractal Surfaces. *Langmuir*, **1996**. 12(9): p. 2125-2127.
7. Lu, Y., et al., Repellent materials. Robust self-cleaning surfaces that function when exposed to either air or oil. *Science*, **2015**. 347(6226): p. 1132-5.
8. Wang, Z., et al., Mussel-Inspired Surface Engineering for Water-Remediation Materials. *Matter*, **2019**. 1(1): p. 115-155.
9. Liu, G., et al., Wetting-regulated gas-involving (photo)electrocatalysis: biomimetics in energy conversion. *Chemical Society Review*, **2021**. 50(18): p. 10674-10699.
10. Li, H., et al., SLIPS-LAB-A bioinspired bioanalysis system for metabolic evaluation of urinary stone disease. *Science Advances*, **2020**. 6(21): p. eaba8535.
11. Leslie, D.C., et al., A bioinspired omniphobic surface coating on medical devices prevents thrombosis and biofouling. *Nature Biotechnology*, **2014**. 32(11): p. 1134-40.
12. Norskov, J.K. and C.H. Christensen, Chemistry. Toward efficient hydrogen production at surfaces. *Science*, **2006**. 312(5778): p. 1322-3.
13. Park, K.C., et al., Condensation on slippery asymmetric bumps. *Nature*, **2016**. 531(7592): p. 78-82.
14. Wang, J., et al., Viscoelastic solid-repellent coatings for extreme water saving and global sanitation. *Nature Sustainability*, **2019**. 2(12): p. 1097-1105.
15. Polizos, G., et al., Transparent superhydrophobic surfaces using a spray coating process. *Solar Energy Materials and Solar Cells*, **2018**. 176: p. 405-410.
16. Sutha, S., et al., Transparent alumina based superhydrophobic self–cleaning coatings for solar cell cover glass applications. *Solar Energy Materials and Solar Cells,* **2017**. 165: p. 128-137.
17. Liu, J., et al., Elastic Superhydrophobic and Photocatalytic Active Films Used as Blood Repellent Dressing. *Advanced Materials*, **2020**. 32(11): p. e1908008.
18. Howell, C., et al., Designing Liquid-Infused Surfaces for Medical Applications: A Review. *Advanced Materials*, **2018**. 30(50): p. e1802724.
19. IUPAC, TOP TEN EMERGING TECHNOLOGIES IN CHEMISTRY. **2021**.
20. Dhyani, A., et al., Design and applications of surfaces that control the accretion of matter. *Science*, **2021**. 373(6552): p. eaba5010.
21. Daniel, D., et al., Origins of Extreme Liquid Repellency on Structured, Flat, and Lubricated Hydrophobic Surfaces. *Physical Review Letters*, **2018**. 120(24): p. 244503.
22. Giacomello, A., et al., Metastable wetting on superhydrophobic surfaces: continuum and atomistic views of the Cassie-Baxter-Wenzel transition. *Physical Review Letters,* **2012**. 109(22): p. 226102.

23. Lv, P., et al., Metastable states and wetting transition of submerged superhydrophobic structures. *Physical Review Letters*, **2014**. 112(19): p. 196101.
24. Prakash, S., E. Xi, and A.J. Patel, Spontaneous recovery of superhydrophobicity on nanotextured surfaces. *Proceedings of the National Academy of Sciences of the United States of America*, **2016**. 113(20): p. 5508-13.
25. Poetes, R., et al., Metastable underwater superhydrophobicity. *Physical Review Letters*, **2010**. 105(16): p. 166104.
26. Wang, Y., S.B. Darling, and J. Chen, Selectivity of Per- and Polyfluoroalkyl Substance Sensors and Sorbents in Water. *ACS Applied Materials & Interfaces*, **2021**. 13(51): p. 60789-60814.
27. Kreder, M.J., et al., Film Dynamics and Lubricant Depletion by Droplets Moving on Lubricated Surfaces. *Physical Review X*, **2018**. 8(3): p. 031053.
28. Baumli, P., et al., Flow-Induced Long-Term Stable Slippery Surfaces. *Advanced Science (Weinh)*, **2019**. 6(11): p. 1900019.
29. Gong, G., et al., A highly durable silica/polyimide superhydrophobic nanocomposite film with excellent thermal stability and abrasion-resistant performance. *Journal of Materials Chemistry A*, **2015**. 3(2): p. 713-718.
30. Yang, J., et al., Fabrication of stable, transparent and superhydrophobic nanocomposite films with polystyrene functionalized carbon nanotubes. *Applied Surface Science*, **2009**. 255(22): p. 9244-9247.
31. Hor, J.L., et al., Nanoporous Polymer-Infiltrated Nanoparticle Films with Uniform or Graded Porosity via Undersaturated Capillary Rise Infiltration. *ACS Nano*, **2017**. 11(3): p. 3229-3236.
32. Huang, Y.R., et al., Polymer nanocomposite films with extremely high nanoparticle loadings via capillary rise infiltration (CaRI). *Nanoscale*, **2015**. 7(2): p. 798-805.
33. Manohar, N., K.J. Stebe, and D. Lee, Effect of Confinement on Solvent-Driven Infiltration of the Polymer into Nanoparticle Packings. *Macromolecules*, **2020**. 53(15): p. 6740-6746.
34. Venkatesh, R.B., et al., Polymer-Infiltrated Nanoparticle Films Using Capillarity-Based Techniques: Toward Multifunctional Coatings and Membranes. *Annual Review of Chemical and Biomolecular Engineering*, **2021**. 12: p. 411-437.
35. Qiang, Y., et al., Polymer blend-filled nanoparticle films via monomer-driven infiltration of polymer and photopolymerization. *Molecular Systems Design & Engineering*, **2018**. 3(1): p. 96-102.
36. Young, T., III. An essay on the cohesion of fluids. *Philosophical Transactions of the Royal Society of London*, **1997**. 95: p. 65-87.
37. de Gennes, P.-G., F. Brochard-Wyart, and D. Quéré, Capillarity and Wetting Phenomena: Drops, Bubbles, Pearls, Waves. *Springer*, **2004**: 978-0-387-21656-0.
38. Huhtamaki, T., et al., Surface-wetting characterization using contact-angle measurements. *Nature Protocols*, **2018**. 13(7): p. 1521-1538.
39. Yong, J., et al., Superoleophobic surfaces. *Chemical Society Review*, **2017**. 46(14): p. 4168-4217.
40. Wenzel, R.N., Resistance of Solid Surfaces to Wetting by Water. *Industrial & Engineering Chemistry*, **2002**. 28(8): p. 988-994.
41. Nosonovsky, M. and B. Bhushan, Superhydrophobic surfaces and emerging applications: Non-adhesion, energy, green engineering. *Current Opinion in Colloid & Interface Science*, **2009**. 14(4): p. 270-280.
42. Cassie, A.B.D. and S. Baxter, Wettability of porous surfaces. *Transactions of the Faraday Society*, **1944**. 40: p. 546-551.
43. Carraher Jr, C.E., Introduction to Polymer Chemistry. *CRC Press*, **2017**.

44. Barthlott, W. and C. Neinhuis, Purity of the sacred lotus, or escape from contamination in biological surfaces. *Planta*, **1997**. 202(1): p. 1-8.
45. Tuteja, A., et al., Designing superoleophobic surfaces. *Science*, **2007**. 318(5856): p. 1618-22.
46. Tuteja, A., et al., Robust omniphobic surfaces. *Proceedings of the National Academy of Sciences of the United States of America*, **2008**. 105(47): p. 18200-5.
47. Ahuja, A., et al., Nanonails: a simple geometrical approach to electrically tunable superlyophobic surfaces. *Langmuir*, **2008**. 24(1): p. 9-14.
48. Liu, T.L. and C.J. Kim, Repellent surfaces. Turning a surface superrepellent even to completely wetting liquids. *Science*, **2014**. 346(6213): p. 1096-100.
49. Wong, T.S., et al., Bioinspired self-repairing slippery surfaces with pressure-stable omniphobicity. *Nature*, **2011**. 477(7365): p. 443-7.
50. Quéré, D., Wetting and Roughness. *Annual Review of Materials Research*, **2008**. 38(1): p. 71-99.
51. Bocquet, L. and E. Lauga, A smooth future*? Nature Materials*, **2011**. 10(5): p. 334-7.
52. Cheng, D.F., et al., A statically oleophilic but dynamically oleophobic smooth nonperfluorinated surface. *Angewandte Chemie International Edition*, **2012**. 51(12): p. 2956-9.
53. Wang, L. and T.J. McCarthy, Covalently Attached Liquids: Instant Omniphobic Surfaces with Unprecedented Repellency. *Angewandte Chemie International Edition*, **2016**. 128(1): p. 252-256.
54. Krumpfer, J.W. and T.J. McCarthy, Contact angle hysteresis: a different view and a trivial recipe for low hysteresis hydrophobic surfaces. *Faraday Discussion*, **2010**. 146: p. 103-11.
55. Epstein, A.K., et al., Liquid-infused structured surfaces with exceptional anti-biofouling performance. *Proceedings of the National Academy of Sciences of the United States of America*, **2012**. 109(33): p. 13182-7.
56. Langmuir, I., The mechanism of the surface phenomena of flotation. *Transactions of the Faraday Society*, **1920**. 15(June).
57. Celia, E., et al., Recent advances in designing superhydrophobic surfaces. *Journal of Colloid and Interface Science*, **2013**. 402: p. 1-18.
58. Bellanger, H., et al., Chemical and physical pathways for the preparation of superoleophobic surfaces and related wetting theories. *Chemical Review*, **2014**. 114(5): p. 2694-716.
59. Darmanin, T. and F. Guittard, Superhydrophobic and superoleophobic properties in nature. *Materials Today*, **2015**. 18(5): p. 273-285.
60. Wang, S., et al., Bioinspired Surfaces with Superwettability: New Insight on Theory, Design, and Applications. *Chemical Review*, **2015**. 115(16): p. 8230-93.
61. Liu, M., S. Wang, and L. Jiang, Nature-inspired superwettability systems. *Nature Reviews Materials*, **2017**. 2(7): p. 17036.
62. Zhang, W., et al., Robust superhydrophobicity: mechanisms and strategies. *Chemical Society Review*, **2021**. 50(6): p. 4031-4061.
63. Yu, C., et al., Nature–Inspired self–cleaning surfaces: Mechanisms, modelling, and manufacturing. *Chemical Engineering Research and Design*, **2020**. 155: p. 48-65.
64. Li, X.M., D. Reinhoudt, and M. Crego-Calama, What do we need for a superhydrophobic surface? A review on the recent progress in the preparation of superhydrophobic surfaces. *Chemical Society Review*, **2007**. 36(8): p. 1350-68.
65. Guo, Z., W. Liu, and B.L. Su, Superhydrophobic surfaces: from natural to biomimetic to functional. *Journal of Colloid and Interface Science*, **2011**. 353(2): p. 335-55.

66. Yan, Y.Y., N. Gao, and W. Barthlott, Mimicking natural superhydrophobic surfaces and grasping the wetting process: a review on recent progress in preparing superhydrophobic surfaces. *Advances in Colloid and Interface Science*, **2011**. 169(2): p. 80-105.
67. Webb, H.K., R.J. Crawford, and E.P. Ivanova, Wettability of natural superhydrophobic surfaces. *Advances in Colloid and Interface Science*, **2014**. 210: p. 58-64.
68. Feng, L., et al., Super-Hydrophobic Surfaces: From Natural to Artificial. *Advanced Materials,* **2002**. 14(24): p. 1857-1860.
69. Razavi, S.M.R., et al., Superhydrophobic Surfaces Made from Naturally Derived Hydrophobic Materials. *ACS Sustainable Chemistry & Engineering*, **2017**. 5(12): p. 11362-11370.
70. Deng, X., et al., Candle soot as a template for a transparent robust superamphiphobic coating. *Science*, **2012**. 335(6064): p. 67-70.
71. Peng, C., Z. Chen, and M.K. Tiwari, All-organic superhydrophobic coatings with mechanochemical robustness and liquid impalement resistance. *Nature Materials*, **2018**. 17(4): p. 355-360.
72. Ma, J., et al., Ultra-thin self-healing vitrimer coatings for durable hydrophobicity. *Nature Communications*, **2021**. 12(1): p. 5210.
73. Liravi, M., et al., A comprehensive review on recent advances in superhydrophobic surfaces and their applications for drag reduction. *Progress in Organic Coatings,* **2020**. 140: p. 105537.
74. Esmeryan, K.D., et al., Early stage anti-bioadhesion behavior of superhydrophobic soot based coatings towards Pseudomonas putida. *Materials & Design,* **2018**. 160: p. 395-404.
75. Thamaraiselvan, C., et al., Superhydrophobic Candle Soot as a Low Fouling Stable Coating on Water Treatment Membrane Feed Spacers. *ACS Applied Bio Materials,* **2021**. 4(5): p. 4191-4200.
76. Blossey, R., Self-cleaning surfaces--virtual realities. *Nature Materials*, **2003**. 2(5): p. 301-6.
77. Lv, J., et al., Bio-inspired strategies for anti-icing. *ACS Nano*, **2014**. 8(4): p. 3152-69.
78. Cao, L., et al., Anti-icing superhydrophobic coatings. *Langmuir,* **2009**. 25(21): p. 12444-8.
79. Li, W., Y. Zhan, and S. Yu, Applications of superhydrophobic coatings in anti-icing: Theory, mechanisms, impact factors, challenges and perspectives. *Progress in Organic Coatings*, **2021**. 152: p. 106117.
80. Ivanova, E.P., et al., Natural bactericidal surfaces: mechanical rupture of Pseudomonas aeruginosa cells by cicada wings. *Small*, **2012**. 8(16): p. 2489-94.
81. Watson, G.S., et al., A gecko skin micro/nano structure - A low adhesion, superhydrophobic, anti-wetting, self-cleaning, biocompatible, antibacterial surface. *Acta Biomaterialia*, **2015**. 21: p. 109-22.
82. Zhang, X., L. Wang, and E. Levänen, Superhydrophobic surfaces for the reduction of bacterial adhesion. *RSC Advances*, **2013**. 3(30): p. 12003-12020.
83. Tuo, Y., et al., One-step hydrothermal method to fabricate drag reduction superhydrophobic surface on aluminum foil. *Applied Surface Science,* **2018**. 446: p. 230-235.
84. Truesdell, R., et al., Drag reduction on a patterned superhydrophobic surface. *Physical Review Letters*, **2006**. 97(4): p. 044504.
85. Samaha, M.A., H.V. Tafreshi, and M. Gad-el-Hak, Influence of flow on longevity of superhydrophobic coatings. *Langmuir*, **2012**. 28(25): p. 9759-66.

86. Miljkovic, N. and E.N. Wang, Condensation heat transfer on superhydrophobic surfaces. *MRS Bulletin*, **2013**. 38(5): p. 397-406.
87. Chavan, S., et al., Heat Transfer through a Condensate Droplet on Hydrophobic and Nanostructured Superhydrophobic Surfaces. *Langmuir*, **2016**. 32(31): p. 7774-87.
88. Dietz, C., et al., Visualization of droplet departure on a superhydrophobic surface and implications to heat transfer enhancement during dropwise condensation. *Applied Physics Letters*, **2010**. 97(3): p. 033104.
89. Yu, Z., et al., Desert Beetle-Inspired Superwettable Patterned Surfaces for Water Harvesting. *Small*, **2017**. 13(36): p. 1701403.
90. Wang, X., et al., Superamphiphobic coatings with polymer-wrapped particles: enhancing water harvesting. *Journal of Materials Chemistry A*, **2019**. 7(10): p. 5426-5433.
91. Zhai, L., et al., Patterned superhydrophobic surfaces: toward a synthetic mimic of the Namib Desert beetle. *Nano Letters*, **2006**. 6(6): p. 1213-7.
92. Marto, P.J., et al., Evaluation of organic coatings for the promotion of dropwise condensation of steam. *International Journal of Heat and Mass Transfer*, **1986**. 29(8): p. 1109-1117.
93. Vemuri, S., et al., Long term testing for dropwise condensation using self-assembled monolayer coatings of n-octadecyl mercaptan. *Applied Thermal Engineering*, **2006**. 26(4): p. 421-429.
94. Rose, J.W., Dropwise condensation theory and experiment: A review. *Proceedings of the Institution of Mechanical Engineers, Part A: Journal of Power and Energy*, **2005**. 216(2): p. 115-128.
95. Kim, H.Y., H.J. Lee, and B.H. Kang, Sliding of liquid drops down an inclined solid surface. *Journal of Colloid and Interface Science*, **2002**. 247(2): p. 372-80.
96. Boreyko, J.B. and C.H. Chen, Self-propelled dropwise condensate on superhydrophobic surfaces. *Physical Review Letters*, **2009**. 103(18): p. 184501.
97. Kota, A.K., et al., *H*ygro-responsive membranes for effective oil-water separation. *Nature Communications*, **2012**. 3: p. 1025.
98. Padaki, M., et al., Membrane technology enhancement in oil–water separation. A review. *Desalination*, **2015**. 357: p. 197-207.
99. Zhu, Y., et al., Recent progress in developing advanced membranes for emulsified oil/water separation. *NPG Asia Materials*, **2014**. 6(5): p. e101-e101.
100. Wei, Y., et al., Specially Wettable Membranes for Oil–Water Separation. *Advanced Materials Interfaces*, **2018**. 5(23): p. 1800576.
101. Maximous, N., G. Nakhla, and W. Wan, Comparative assessment of hydrophobic and hydrophilic membrane fouling in wastewater applications. *Journal of Membrane Science*, **2009**. 339(1-2): p. 93-99.
102. Boussu, K., et al., Surfactant fouling of nanofiltration membranes: measurements and mechanisms. *Chemphyschem*, **2007**. 8(12): p. 1836-45.
103. Wang, K., et al., Hydrophilic surface coating on hydrophobic PTFE membrane for robust anti-oil-fouling membrane distillation. *Applied Surface Science*, **2018**. 450: p. 57-65.
104. Zarghami, S., et al., Superhydrophilic and underwater superoleophobic membranes - A review of synthesis methods. *Progress in Polymer Science*, **2019**. 98: p. 101166.
105. Liu, R., et al., Robust bio-inspired superhydrophilic and underwater superoleophobic membranes for simultaneously fast water and oil recovery. *Journal of Membrane Science*, **2021**. 623: p. 119041

106. Zhang, W., et al., Salt-induced fabrication of superhydrophilic and underwater superoleophobic PAA-g-PVDF membranes for effective separation of oil-in-water emulsions. *Angewandte Chemie International Edition*, **2014**. 53(3): p. 856-60.
107. Zhou, D.-L., et al., Fabrication of superhydrophilic and underwater superoleophobic membranes for fast and effective oil/water separation with excellent durability. *Journal of Membrane Science*, **2021**. 620: p. 118898.
108. Dong, Z., et al., 3D Printing of Superhydrophobic Objects with Bulk Nanostructure. *Advanced Materials*, **2021**. 33(45): p. e2106068.
109. Miljkovic, N., et al., Jumping-droplet-enhanced condensation on scalable superhydrophobic nanostructured surfaces. *Nano Letters*, **2013**. 13(1): p. 179-87.
110. Genzer, J. and K. Efimenko, Creating long-lived superhydrophobic polymer surfaces through mechanically assembled monolayers. *Science*, **2000**. 290(5499): p. 2130-3.
111. Meuler, A.J., et al., Examination of wettability and surface energy in fluorodecyl POSS/polymer blends. *Soft Matter*, **2011**. 7(21): p. 10122-10134.
112. Wang, L. and T.J. McCarthy, Covalently Attached Liquids: Instant Omniphobic Surfaces with Unprecedented Repellency. *Angewandte Chemie International Edition*, **2016**. 55(1): p. 244-8.
113. Wooh, S. and D. Vollmer, Silicone Brushes: Omniphobic Surfaces with Low Sliding Angles. *Angewandte Chemie International Edition*, **2016**. 55(24): p. 6822-4.
114. Zhang, L., et al., Gradient Quasi-Liquid Surface Enabled Self-Propulsion of Highly Wetting Liquids. *Advanced Functional Materials*, **2021**. 31(13): p. 2008614.
115. Zhang, L., et al., Passive Removal of Highly Wetting Liquids and Ice on Quasi-Liquid Surfaces. *ACS Applied Materials & Interfaces*, **2020**. 12(17): p. 20084-20095.
116. Singh, N., et al., Omniphobic Metal Surfaces with Low Contact Angle Hysteresis and Tilt Angles. *Langmuir*, **2018**. 34(38): p. 11405-11413.
117. Zhao, X., et al., Macroscopic Evidence of the Liquidlike Nature of Nanoscale Polydimethylsiloxane Brushes. *ACS Nano*, **2021**, 15, 8: p. 13559–13567.
118. Wooh, S., et al., Stable Hydrophobic Metal-Oxide Photocatalysts via Grafting Polydimethylsiloxane Brush. *Advanced Materials*, **2017**. 29(16): p. 1604637.
119. Smith, J.D., et al., Droplet mobility on lubricant-impregnated surfaces. *Soft Matter*, **2013**. 9(6): p. 1772-1780.
120. Peppou-Chapman, S., et al., Life and death of liquid-infused surfaces: a review on the choice, analysis and fate of the infused liquid layer. *Chemical Society Review*, **2020**. 49(11): p. 3688-3715.
121. Zhang, J., A. Wang, and S. Seeger, NepenthesPitcher Inspired Anti-Wetting Silicone Nanofilaments Coatings: Preparation, Unique Anti-Wetting and Self-Cleaning Behaviors. *Advanced Functional Materials*, **2014**. 24(8): p. 1074-1080.
122. Jing, X. and Z. Guo, Fabrication of biocompatible super stable lubricant-immobilized slippery surfaces by grafting a polydimethylsiloxane brush: excellent boiling water resistance, hot liquid repellency and long-term slippery stability. *Nanoscale*, **2019**. 11(18): p. 8870-8881.
123. Kim, P., et al., Liquid-infused nanostructured surfaces with extreme anti-ice and anti-frost performance. *ACS Nano*, **2012**. 6(8): p. 6569-77.
124. Wong, W.S.Y., et al., Capillary Balancing: Designing Frost-Resistant Lubricant-Infused Surfaces. *Nano Letters*, **2020**. 20(12): p. 8508-8515.
125. Coady, M.J., et al., Icephobic Behavior of UV-Cured Polymer Networks Incorporated into Slippery Lubricant-Infused Porous Surfaces: Improving SLIPS Durability. *ACS Applied Materials & Interfaces*, **2018**. 10(3): p. 2890-2896.
126. Amini, S., et al., Preventing mussel adhesion using lubricant-infused materials. *Science*, **2017**. 357(6352): p. 668-673.

127. Kovalenko, Y., et al., Bacterial Interactions with Immobilized Liquid Layers. *Advanced Healthcare Materials*, **2017**. 6(15): p. 1600948.

128. Doll, K., et al., Liquid-Infused Structured Titanium Surfaces: Antiadhesive Mechanism to Repel Streptococcus oralis Biofilms. *ACS Applied Materials & Interfaces,* **2019**. 11(26): p. 23026-23038.

129. Girard, H.L., et al., Lubricant-Impregnated Surfaces for Mitigating Asphaltene Deposition. *ACS Applied Materials & Interfaces,* **2020**. 12(25): p. 28750-28758.

130. Zhao, H., et al., Earthworm-Inspired Rough Polymer Coatings with Self-Replenishing Lubrication for Adaptive Friction-Reduction and Antifouling Surfaces. *Advanced Materials,* **2018**. 30(29): p. e1802141.

131. Xiang, T., et al., Slippery liquid-infused porous surface for corrosion protection with self-healing property. *Chemical Engineering Journal*, **2018**. 345: p. 147-155.

132. Zhang, J., C. Gu, and J. Tu, Robust Slippery Coating with Superior Corrosion Resistance and Anti-Icing Performance for AZ31B Mg Alloy Protection. *ACS Applied Materials & Interfaces*, **2017**. 9(12): p. 11247-11257.

133. Karkantonis, T., et al., Femtosecond laser-induced sub-micron and multi-scale topographies for durable lubricant impregnated surfaces for food packaging applications. *Surface and Coatings Technology*, **2020**. 399: p. 126166.

134. Zouaghi, S., et al., Biomimetic surface modifications of stainless steel targeting dairy fouling mitigation and bacterial adhesion. *Food and Bioproducts Processing,* **2019**. 113: p. 32-38.

135. Asawa, K., et al., Guiding light via slippery liquid-infused porous surfaces. *Applied Physics Letters,* **2021**. 118(9): p. 091602.

136. Nandyala, D., et al., Design, Fabrication, and Analysis of a Capillary Diode for Potential Application in Water-Oil Separation. *ACS Applied Materials & Interfaces,* **2020**. 12(41): p. 45950-45960.

137. Li, J., et al., Liquid film-induced critical heat flux enhancement on structured surfaces. *Science Advances*, **2021**. 7(26): p. eabg4537.

138. Ho, J.Y., et al., Dropwise condensation of low surface tension fluids on lubricant-infused surfaces: Droplet size distribution and heat transfer. *International Journal of Heat and Mass Transfer*, **2021**. 172: p. 121149.

139. Sett, S., et al., Stable Dropwise Condensation of Ethanol and Hexane on Rationally Designed Ultrascalable Nanostructured Lubricant-Infused Surfaces. *Nano Letters*, **2019**. 19(8): p. 5287-5296.

140. Ge, Q., et al., Condensation of Satellite Droplets on Lubricant-Cloaked Droplets. *ACS Applied Materials & Interfaces,* **2020**. 12(19): p. 22246-22255.

141. Rosenberg, B.J., et al., Turbulent drag reduction over air- and liquid- impregnated surfaces. *Physics of Fluids*, **2016**. 28(1): p. 015103.

142. Kant, K. and R. Pitchumani, Laminar drag reduction in microchannels with liquid infused textured surfaces. *Chemical Engineering Science*, **2021**. 230: p. 116196.

143. Lee, S.J., et al., A nature-inspired lubricant-infused surface for sustainable drag reduction. *Soft Matter,* **2019**. 15(42): p. 8459-8467.

144. Liu, J., et al., One-Step Synthesis of a Durable and Liquid-Repellent Poly(dimethylsiloxane) Coating. *Advanced Materials,* **2021**. 33(23): p. e2100237.

145. Dai, X., et al., Hydrophilic directional slippery rough surfaces for water harvesting. *Science Advances,* **2018**. 4(3): p. eaaq0919.

146. Guo, Z., et al., Hydrophilic slippery surface enabled coarsening effect for rapid water harvesting. *Cell Reports Physical Science*, **2021**. 2(4): p. 100387.

147. Feng, R., et al., A Bioinspired Slippery Surface with Stable Lubricant Impregnation for Efficient Water Harvesting. *ACS Applied Materials & Interfaces*, **2020**. 12(10): p. 12373-12381.
148. Golovin, K., et al., Designing durable icephobic surfaces. *Science Advances*, **2016**. 2(3): p. e1501496.
149. Irajizad, P., et al., Magnetic slippery extreme icephobic surfaces. *Nature Communications*, **2016**. 7: p. 13395.
150. Sunny, S., et al., Transparent antifouling material for improved operative field visibility in endoscopy. *Proceedings of the National Academy of Sciences of the United States of America*, **2016**. 113(42): p. 11676-11681.
151. Yin, J., et al., Self-cleaning and antibiofouling enamel surface by slippery liquid-infused technique. *Scientific Reports*, **2016**. 6: p. 25924.
152. Yang, S., et al., Ultrasensitive surface-enhanced Raman scattering detection in common fluids. *Proceedings of the National Academy of Sciences of the United States of America*, **2016**. 113(2): p. 268-73.
153. Lambley, H., T.M. Schutzius, and D. Poulikakos, Superhydrophobic surfaces for extreme environmental conditions. *Proceedings of the National Academy of Sciences of the United States of America*, **2020**. 117(44): p. 27188-27194.
154. Papadopoulos, P., et al., How superhydrophobicity breaks down. *Proceedings of the National Academy of Sciences of the United States of America*, **2013**. 110(9): p. 3254-8.
155. Kwon, H.M., et al., Rapid deceleration-driven wetting transition during pendant drop deposition on superhydrophobic surfaces. *Physical Review Letters*, **2011**. 106(3): p. 036102.
156. Kusumaatmaja, H., et al., The collapse transition on superhydrophobic surfaces. *EPL (Europhysics Letters)*, **2008**. 81(3): p. 36003.
157. Manukyan, G., et al., Electrical switching of wetting states on superhydrophobic surfaces: a route towards reversible Cassie-to-Wenzel transitions. *Physical Review Letters*, **2011**. 106(1): p. 014501.
158. McHale, G., et al., Analysis of droplet evaporation on a superhydrophobic surface. *Langmuir*, **2005**. 21(24): p. 11053-60.
159. He, X., et al., The Cassie-to-Wenzel wetting transition of water films on textured surfaces with different topologies. *Physics of Fluids*, **2021**. 33(11): p. 112006.
160. Patankar, N.A., Transition between superhydrophobic states on rough surfaces. *Langmuir*, **2004**. 20(17): p. 7097-102.
161. Zhu, P., et al., Well-defined porous membranes for robust omniphobic surfaces via microfluidic emulsion templating. *Nature Communications*, **2017**. 8: p. 15823.
162. Wilke, K.L., et al., Toward Condensation-Resistant Omniphobic Surfaces. *ACS Nano*, **2018**. 12(11): p. 11013-11021.
163. Domingues, E.M., et al., Biomimetic coating-free surfaces for long-term entrapment of air under wetting liquids. *Nature Communications*, **2018**. 9(1): p. 3606.
164. Panter, J.R., Y. Gizaw, and H. Kusumaatmaja, Multifaceted design optimization for superomniphobic surfaces. *Science Advances*, **2019**. 5(6): p. eaav7328.
165. Liu, X., et al., 3D Printing of Bioinspired Liquid Superrepellent Structures. *Advanced Materials*, **2018**. 30(22): p. e1800103.
166. Sun, J., et al., Robust liquid repellency by stepwise wetting resistance. *Applied Physics Reviews*, **2021**. 8(3): p. . 031403
167. Yun, G.T., et al., Springtail-inspired superomniphobic surface with extreme pressure resistance. *Science Advances*, **2018**. 4(8): p. eaat4978.

168. Baumli, P., et al., The challenge of lubricant-replenishment on lubricant-impregnated surfaces. *Advances in Colloid and Interface Science*, **2021**. 287: p. 102329.
169. Chen, X., G. Wen, and Z. Guo, What are the design principles, from the choice of lubricants and structures to the preparation method, for a stable slippery lubricant-infused porous surface?. *Materials Horizons*, **2020**, 7, 1697-1726.
170. Sett, S., et al., Lubricant-Infused Surfaces for Low-Surface-Tension Fluids: Promise versus Reality. *ACS Applied Materials & Interfaces*, **2017**. 9(41): p. 36400-36408.
171. Rykaczewski, K., et al., Dropwise condensation of low surface tension fluids on omniphobic surfaces. *Scientific Reports*, **2014**. 4: p. 4158.
172. Preston, D.J., et al., Heat Transfer Enhancement During Water and Hydrocarbon Condensation on Lubricant Infused Surfaces. *Scientific Reports*, **2018**. 8(1): p. 540.
173. Zhu, Y., et al., Slippery Liquid-Like Solid Surfaces with Promising Antibiofilm Performance under Both Static and Flow Conditions. *ACS Applied Materials & Interfaces*, **2022**. 14(5): p. 6307-6319.
174. Hourlier-Fargette, A., et al., Role of uncrosslinked chains in droplets dynamics on silicone elastomers. *Soft Matter*, **2017**. 13(19): p. 3484-3491.
175. Hourlier-Fargette, A., et al., Extraction of Silicone Uncrosslinked Chains at Air-Water-Polydimethylsiloxane Triple Lines. *Langmuir*, **2018**. 34(41): p. 12244-12250.
176. Howell, C., et al., Self-replenishing vascularized fouling-release surfaces. *ACS Applied Materials & Interfaces*, **2014**. 6(15): p. 13299-307.
177. Zhang, J., et al., Evaporation-induced transition from Nepenthes pitcher-inspired slippery surfaces to lotus leaf-inspired superoleophobic surfaces. *Langmuir*, **2014**. 30(47): p. 14292-9.
178. Kim, H.N., et al., Depletion of lubricant impregnated in a cavity of lubricant-infused surface. *Physics of Fluids*, **2021**. 33(2): p. 022005.
179. Wexler, J.S., I. Jacobi, and H.A. Stone, Shear-driven failure of liquid-infused surfaces. *Physical Review Letters*, **2015**. 114(16): p. 168301.
180. Hauer, L., et al., How Frost Forms and Grows on Lubricated Micro- and Nanostructured Surfaces. *ACS Nano*, **2021**. 15(3): p. 4658-4668.
181. Seiwert, J., et al., Drainage on a rough surface. *EPL (Europhysics Letters)*, **2011**. 94(1): p. 16002 .
182. Adera, S., et al., Depletion of Lubricant from Nanostructured Oil-Infused Surfaces by Pendant Condensate Droplets. *ACS Nano*, **2020**. 14(7): p. 8024-8035.
183. Muschi, M., et al., Drop impact dynamics on slippery liquid-infused porous surfaces: influence of oil thickness. *Soft Matter*, **2018**. 14(7): p. 1100-1107.
184. Ding, Y., et al., Ionic-Liquid-Gel Surfaces Showing Easy-Sliding and Ultradurable Features. *Advanced Materials Interfaces*, **2015**. 2(10): p. 1500177.
185. Galvan, Y., et al., Ionic-Liquid-Infused Nanostructures as Repellent Surfaces. *Langmuir*, **2018**. 34(23): p. 6894-6902.
186. Tian, X., et al., Suppressing Evaporative Loss in Slippery Liquid-Infused Porous Surfaces (SLIPS) with Self-Suspended Perfluorinated Nanoparticles. *Langmuir*, **2020**. 36(19): p. 5106-5111.
187. Howell, C., et al., Stability of Surface-Immobilized Lubricant Interfaces under Flow. *Chemistry of Materials*, **2015**. 27(5): p. 1792-1800.
188. Villegas, M., et al., Liquid-Infused Surfaces: A Review of Theory, Design, and Applications. *ACS Nano*, **2019**. 13(8): p. 8517-8536.
189. Huang, C. and Z. Guo, Fabrications and Applications of Slippery Liquid-infused Porous Surfaces Inspired from Nature: A Review. *Journal of Bionic Engineering*, **2019**. 16(5): p. 769-793.

190. Zeng, X., Z. Guo, and W. Liu, Recent advances in slippery liquid-infused surfaces with unique properties inspired by nature. *Bio-Design and Manufacturing*, **2021**. 4(3): p. 506-525.
191. Liu, B., et al., Strategies for anti-icing: low surface energy or liquid-infused? *RSC Advances*, **2016**. 6(74): p. 70251-70260.
192. Wang, G. and Z. Guo, Liquid infused surfaces with anti-icing properties. *Nanoscale*, **2019**. 11(47): p. 22615-22635.
193. Deng, R., et al., Slippery liquid-infused porous surfaces (SLIPSs): a perfect solution to both marine fouling and corrosion? *Journal of Materials Chemistry A*, **2020**. 8(16): p. 7536-7547.
194. Princen, H.M. and S.G. Mason, Shape of a fluid drop at a fluid-liquid interface. II. Theory for three-phase systems. *Journal of Colloid Science*, **1965**. 20(3): p. 246-266.
195. Carré, A., J.-C. Gastel, and M.E.R. Shanahan, Viscoelastic effects in the spreading of liquids. *Nature*, **1996**. 379(6564): p. 432-434.
196. Lester, G.R., Contact angles of liquids at deformable solid surfaces. *Journal of Colloid Science*, **1961**. 16(4): p. 315-326.
197. Shanahan, M.E.R. and A. Carre, Viscoelastic Dissipation in Wetting and Adhesion Phenomena. *Langmuir*, **2002**. 11(4): p. 1396-1402.
198. Style, R.W., et al., Elastocapillarity: Surface Tension and the Mechanics of Soft Solids. *Annual Review of Condensed Matter Physics*, **2017**. 8(1): p. 99-118.
199. Style, R.W., et al., Universal deformation of soft substrates near a contact line and the direct measurement of solid surface stresses. *Physical Review Letters*, **2013**. 110(6): p. 066103.
200. Wong, W.S.Y., et al., Super liquid repellent surfaces for anti-foaming and froth management. *Nature Communications*, **2021**. 12(1): p. 5358.
201. Sadullah, M.S., C. Semprebon, and H. Kusumaatmaja, Drop Dynamics on Liquid-Infused Surfaces: The Role of the Lubricant Ridge. *Langmuir*, **2018**. 34(27): p. 8112-8118.
202. Butt, H.-J., et al., Design principles for superamphiphobic surfaces. *Soft Matter*, **2013**. 9(2): p. 418-428.
203. Fernandez-Toledano, J.C., et al., On the cohesion of fluids and their adhesion to solids: Young's equation at the atomic scale. *Advances in Colloid and Interface Science*, **2017**. 245: p. 102-107.
204. Tas, N.R., et al., Capillarity Induced Negative Pressure of Water Plugs in Nanochannels. *Nano Letters*, **2003**. 3(11): p. 1537-1540.
205. Teisala, H., et al., Wetting over pre-existing liquid films. *Physical Review Fluids*, **2018**. 3(8): p. 084002.
206. Guo, L., G.H. Tang, and S. Kumar, Droplet Morphology and Mobility on Lubricant-Impregnated Surfaces: A Molecular Dynamics Study. *Langmuir*, **2019**. 35(49): p. 16377-16387.
207. Guo, L., G.H. Tang, and S. Kumar, Dynamic Wettability on the Lubricant-Impregnated Surface: From Nucleation to Growth and Coalescence. *ACS Applied Materials & Interfaces*, **2020**. 12(23): p. 26555-26565.
208. Schmidhalter, I., et al., Liquid film drag out in the presence of molecular forces. *Physics of Fluids*, **2013**. 25(3): p. 032105.
209. Daniel, D., et al., Oleoplaning droplets on lubricated surfaces. *Nature Physics*, **2017**. 13(10): p. 1020-1025.
210. Keiser, A., et al., Drop friction on liquid-infused materials. *Soft Matter*, **2017**. 13(39): p. 6981-6987.
211. Dai, X., et al., Slippery Wenzel State. *ACS Nano*, **2015**. 9(9): p. 9260-7.

212. Cui, J., et al., Effect of the texture geometry on the slippery behavior of liquid-infused nanoporous surfaces. *Journal of Materials Science*, **2018**. 54(3): p. 2729-2739.
213. Peppou-Chapman, S. and C. Neto, Mapping Depletion of Lubricant Films on Antibiofouling Wrinkled Slippery Surfaces. A*CS Applied Materials & Interfaces*, **2018**. 10(39): p. 33669-33677.
214. Peppou-Chapman, S. and C. Neto, Depletion of the Lubricant from Lubricant-Infused Surfaces due to an Air/Water Interface. *Langmuir*, **2021**. 37(10): p. 3025-3037.
215. Dong, Z., et al., Superoleophobic Slippery Lubricant-Infused Surfaces: Combining Two Extremes in the Same Surface. *Advanced Materials*, **2018**. 30(45): p. e1803890.
216. Bruchmann, J., et al., Patterned SLIPS for the Formation of Arrays of Biofilm Microclusters with Defined Geometries. *Advanced Healthcare Materials*, **2017**. 6(1): p. 1601082.
217. Yang, X., et al., Creation of Topological Ultraslippery Surfaces for Droplet Motion Control. *ACS Nano*, **2021**. 15(2): p. 2589-2599.
218. Kim, P., et al., Hierarchical or not? Effect of the length scale and hierarchy of the surface roughness on omniphobicity of lubricant-infused substrates. *Nano Letters*, **2013**. 13(4): p. 1793-9.
219. Zhang, P., et al., Drops Sliding on Non-SLIPS Structures. *Langmuir*, **2021**. 37, 30, 9053–9058.
220. Krishnamoorti, R. and R.A. Vaia, Polymer nanocomposites. *Journal of Polymer Science Part B: Polymer Physics*, **2007**. 45(24): p. 3252-3256.
221. Lossada, F., et al., Self-Assembled Bioinspired Nanocomposites. *Accounts in Chemical Research*, **2020**. 53(11): p. 2622-2635.
222. Guan, Q.-F., et al., Nacre-Inspired Sustainable Coatings with Remarkable Fire-Retardant and Energy-Saving Cooling Performance. *ACS Materials Letters*, **2021**. 3(2): p. 243-248.
223. Xu, Z., et al., A Transparent, Skin-Inspired Composite Film with Outstanding Tear Resistance Based on Flat Silk Cocoon. *Advanced Materials*, **2020**. 32(34): p. e2002695.
224. Zhao, C., et al., Layered nanocomposites by shear-flow-induced alignment of nanosheets. *Nature*, **2020**. 580(7802): p. 210-215.
225. Winey, K.I. and R.A. Vaia, Polymer Nanocomposites. *MRS Bulletin*, **2011**. 32(4): p. 314-322.
226. Vaia, R.A. and E.P. Giannelis, Polymer Nanocomposites: Status and Opportunities. *MRS Bulletin*, **2011**. 26(5): p. 394-401.
227. Kumar, S.K., V. Ganesan, and R.A. Riggleman, Perspective: Outstanding theoretical questions in polymer-nanoparticle hybrids. *Journal of Chemical Physics*, **2017**. 147(2): p. 020901.
228. Shen, X., Q. Zheng, and J.-K. Kim, Rational design of two-dimensional nanofillers for polymer nanocomposites toward multifunctional applications. *Progress in Materials Science*, **2021**. 115: p. 100708.
229. Misra, S. and H. Wang, Review on the growth, properties and applications of self-assembled oxide-metal vertically aligned nanocomposite thin films-current and future perspectives. *Materials Horizons*, **2021**. 8(3): p. 869-884.
230. Gong, M., L. Zhang, and P. Wan, Polymer nanocomposite meshes for flexible electronic devices. *Progress in Polymer Science*, **2020**. 107: p. 101279.
231. Wei, H., et al., Multifunctions of Polymer Nanocomposites: Environmental Remediation, Electromagnetic Interference Shielding, And Sensing Applications. *ChemNanoMat*, **2020**. 6(2): p. 174-184.
232. Pastoriza-Santos, I., et al., Plasmonic polymer nanocomposites. *Nature Reviews Materials*, **2018**. 3(10): p. 375-391.

233. Bharadwaz, A. and A.C. Jayasuriya, Recent trends in the application of widely used natural and synthetic polymer nanocomposites in bone tissue regeneration. *Materials Science and Engineering: C*. **2020**. 110: p. 110698.
234. Huang, G., et al., Multifunctional graphene-based nano-additives toward high-performance polymer nanocomposites with enhanced mechanical, thermal, flame retardancy and smoke suppressive properties. *Chemical Engineering Journal*, **2021**. 410: p. 127590 .
235. Shakeri, A., et al., *P*olyoxometalate based thin film nanocomposite forward osmosis membrane: Superhydrophilic, anti-fouling, and high water permeable. J*ournal of Colloid and Interface Science*, **2019**. 536: p. 328-338.
236. Alpatova, A., et al., Fabrication of porous polymeric nanocomposite membranes with enhanced anti-fouling properties: Effect of casting composition. *Journal of Membrane Science*, **2013**. 444: p. 449-460.
237. Lu, L., et al., Cooperative plasmonic effect of Ag and Au nanoparticles on enhancing performance of polymer solar cells. *Nano Lett*ers, **2013**. 13(1): p. 59-64.
238. Santiago, A.A.G., et al., Development of ZnO/PDMS nanocomposite with photocatalytic/hydrophobic multifunction. *Chemical Physics Letters*, **2020**. 740: p. 137051.
239. Salaluk, S., et al., Nanonetwork Composite Coating for Sensing and Corrosion Inhibition. *Advanced Materials Interfaces*, **2020**. 7(20): p. 2001073.
240. Wang, S., et al., Scalable-Manufactured Superhydrophobic Multilayer Nanocomposite Coating with Mechanochemical Robustness and High-Temperature Endurance. *ACS Applied Materials & Interfaces*, **2020**. 12(31): p. 35502-35512.
241. Janowicz, N.J., et al., Fluorine-Free Transparent Superhydrophobic Nanocomposite Coatings from Mesoporous Silica. *Langmuir*, **2020**. 36(45): p. 13426-13438.
242. Idumah, C.I., et al., Recently Emerging Nanotechnological Advancements in Polymer Nanocomposite Coatings for Anti-corrosion, Anti-fouling and Self-healing. *Surfaces and Interfaces*, **2020**. 21: p. 100734.
243. Imani, S.M., et al., Antimicrobial Nanomaterials and Coatings: Current Mechanisms and Future Perspectives to Control the Spread of Viruses Including SARS-CoV-2. *ACS Nano*, **2020**. 14(10): p. 12341-12369.
244. Yeom, B., et al., Abiotic tooth enamel. *Nature*, **2017**. 543(7643): p. 95-98.
245. Harito, C., et al., Polymer nanocomposites having a high filler content: synthesis, structures, properties, and applications. *Nanoscale*, **2019**. 11(11): p. 4653-4682.
246. Huang, W., et al., A natural impact-resistant bicontinuous composite nanoparticle coating. *Nature Materials*, **2020**. 19(11): p. 1236-1243.
247. Qi, Y., et al., Highly loaded CoO/graphene nanocomposites as lithium-ion anodes with superior reversible capacity. *Journal of Materials Chemistry A*, **2013**. 1(6): p. 2337-2342.
248. Nolte, H., C. Schilde, and A. Kwade, Production of Highly Loaded Nanocomposites by Dispersing Nanoparticles in Epoxy Resin. *Chemical Engineering & Technology*, **2010**. 33(9): p. 1447-1455.
249. Siochi, E.J. and J.S. Harrison, Structural nanocomposites for aerospace applications. *MRS Bulletin*, **2015**. 40(10): p. 829-835.
250. Pourjavadi, A., et al., Graphene oxide/poly(vinyl imidazole) nanocomposite: an effective support for preparation of highly loaded heterogeneous copper catalyst. *Applied Organometallic Chemistry*, **2015**. 29(9): p. 601-607.
251. Gopakumar, T.G., et al., Influence of clay exfoliation on the physical properties of montmorillonite/polyethylene composites. *Polymer*, **2002**. 43(20): p. 5483-5491.

252. de Jongh, P.E. and T.M. Eggenhuisen, Melt infiltration: an emerging technique for the preparation of novel functional nanostructured materials. *Advanced Materials*, **2013**. 25(46): p. 6672-90.
253. Jouault, N., et al., Well-Dispersed Fractal Aggregates as Filler in Polymer−Silica Nanocomposites: Long-Range Effects in Rheology. *Macromolecules*, **2009**. 42(6): p. 2031-2040.
254. Novak, B.M., Hybrid Nanocomposite Materials between inorganic glasses and organic polymers. *Advanced Materials*, **1993**. 5(6): p. 422-433.
255. Srivastava, S. and N.A. Kotov, Composite Layer-by-Layer (LBL) assembly with inorganic nanoparticles and nanowires. *Accounts in Chemical Research*, **2008**. 41(12): p. 1831-41.
256. Kulkarni, D.D., et al., Graphene oxide--polyelectrolyte nanomembranes. *ACS Nano*, **2010**. 4(8): p. 4667-76.
257. Pokrajac, L., et al., Nanotechnology for a Sustainable Future: Addressing Global Challenges with the International Network4Sustainable Nanotechnology. *ACS Nano*, **2021**. 15, 12: p. 18608–18623.
258. Hor, J.L., et al., Effect of Physical Nanoconfinement on the Viscosity of Unentangled Polymers during Capillary Rise Infiltration. *Macromolecules*, **2018**. 51(14): p. 5069-5078.
259. Norton, D.P., et al., ZnO: growth, doping & processing. *Materials Today*, **2004**. 7(6): p. 34-40.
260. Klingshirn, C., ZnO: material, physics and applications. *Chemphyschem*, **2007**. 8(6): p. 782-803.
261. Schmidt-Mende, L. and J.L. MacManus-Driscoll, ZnO – nanostructures, defects, and devices. *Materials Today*, **2007**. 10(5): p. 40-48.
262. Wang, Z.L., ZnO nanowire and nanobelt platform for nanotechnology. *Materials Science and Engineering: R: Reports*, **2009**. 64(3-4): p. 33-71.
263. Zhang, Q., et al., ZnO Nanostructures for Dye-Sensitized Solar Cells. *Advanced Materials*, **2009**. 21(41): p. 4087-4108.
264. Mishra, Y.K. and R. Adelung, ZnO tetrapod materials for functional applications. *Materials Today*, **2018**. 21(6): p. 631-651.
265. Tavakoli, M.M., et al., Light Management in Organic Photovoltaics Processed in Ambient Conditions Using ZnO Nanowire and Antireflection Layer with Nanocone Array. *Small*, **2019**. 15(25): p. e1900508.
266. Zhang, H., et al., A strategy for ZnO nanorod mediated multi-mode cancer treatment. *Biomaterials*, **2011**. 32(7): p. 1906-14.
267. Malakooti, M.H., et al., ZnO nanowire interfaces for high strength multifunctional composites with embedded energy harvesting. *Energy & Environmental Science*, **2016**. 9(2): p. 634-643.
268. McLaren, A., et al., Shape and size effects of ZnO nanocrystals on photocatalytic activity. *Journal of the American Chemical Society*, **2009**. 131(35): p. 12540-1.
269. Market, Z.O. Zinc Oxide Market by Process (French Process, Wet Process, American Process), Grade (Standard, Treated, USP, FCC), Application (Rubber, Ceramics, Chemicals, Agriculture, Cosmetics & Personal Care, Pharmaceuticals), *Region - Global Forecast to 2024.* [cited **2021**; Available from: https://www.marketsandmarkets.com/Market-Reports/zinc-oxide-market-116672256.html.
270. Kolodziejczak-Radzimska, A. and T. Jesionowski, Zinc Oxide-From Synthesis to Application: A Review. *Materials (Basel)*, **2014**. 7(4): p. 2833-2881.

271. Badre, C., et al., Effects of nanorod structure and conformation of fatty acid self-assembled layers on superhydrophobicity of zinc oxide surface. *Journal of Colloid and Interface Science*, **2007**. 316(2): p. 233-7.

272. Hiralal, P., et al., Nanowire-based multifunctional antireflection coatings for solar cells. *Nanoscale*, **2014**. 6(23): p. 14555-62.

273. Kumar, R., et al., Efficient ZnO-based visible-light-driven photocatalyst for antibacterial applications. *ACS Applied Materials & Interfaces*, **2014**. 6(15): p. 13138-48.

274. Fu, F., et al., Construction of cellulose based ZnO nanocomposite films with antibacterial properties through one-step coagulation. *ACS Applied Materials & Interfaces*, **2015**. 7(4): p. 2597-606.

275. Liu, Y., et al., Reversible superhydrophobic-superhydrophilic transition of ZnO nanorod/epoxy composite films. *ACS Applied Materials & Interfaces*, **2012**. 4(8): p. 3959-64.

276. Liu, C., et al., ZnO nanowire-decorated Al_2O_3 hybrids for improving the thermal conductivity of polymer composites. *Journal of Materials Chemistry C*, **2020**. 8(16): p. 5380-5388.

277. Chu, S., et al., *F*lexible Dye-Sensitized Solar Cell Based on Vertical ZnO Nanowire Arrays. *Nanoscale Research Letters*, **2011**. 6(1): p. 38.

278. Choudhary, S., et al., Rapid synthesis of ZnO nanowires and nanoplates with highly enhanced photocatalytic performance. *Applied Surface Science*, **2021**. 541: p. 148484.

279. Amara, N., et al., ZnO nanowires/YAG:Ce functional heterostructure coatings with tunable optical properties. *Journal of Alloys and Compounds*, **2020**. 842: p. 155708.

280. Chen, C.Q., et al., Size dependence of Young's modulus in ZnO nanowires. *Physical Review Letters*, **2006**. 96(7): p. 075505.

281. Gong, M., et al., Superhydrophobicity of hierarchical ZnO nanowire coatings. *Journal of Materials Chemistry A*, **2014**. 2(17): p. 6180-6184.

282. Zhong, Z., et al., Unusual Air Filters with Ultrahigh Efficiency and Antibacterial Functionality Enabled by ZnO Nanorods. *ACS Applied Materials & Interfaces*, **2015**. 7(38): p. 21538-44.

283. Bazrafshan, A.A., et al., Synthesis of ZnO-nanorod-based materials for antibacterial, antifungal activities, DNA cleavage and efficient ultrasound-assisted dyes adsorption. *Ecotoxicology and Environmental Safety*, **2017**. 142: p. 330-337.

284. Wang, W., et al., Development of novel implants with self-antibacterial performance through in-situ growth of 1D ZnO nanowire. *Colloids Surfaces B Biointerfaces*, **2016**. 141: p. 623-633.

285. Li, J., et al., Balancing Bacteria-Osteoblast Competition through Selective Physical Puncture and Biofunctionalization of ZnO/Polydopamine/Arginine-Glycine-Aspartic Acid-Cysteine Nanorods. *ACS Nano*, **2017**. 11(11): p. 11250-11263.

286. Wu, G.S., et al., Controlled synthesis of ZnO nanowires or nanotubes via sol–gel template process. *Solid State Communications*, **2005**. 134(7): p. 485-489.

287. Ha, L.P.P., et al., Visible-light-driven photocatalysis of anisotropic silver nanoparticles decorated on ZnO nanorods: Synthesis and characterizations. *Journal of Environmental Chemical Engineering*, **2021**. 9(2): p. 105103.

288. Demes, T., et al., Comprehensive study of hydrothermally grown ZnO nanowires. *Journal of Materials Science*, **2016**. 51(23): p. 10652-10661.

289. Cheng, H.-M., et al., Formation of Branched ZnO Nanowires from Solvothermal Method and Dye-Sensitized Solar Cells Applications. *The Journal of Physical Chemistry C*, **2008**. 112(42): p. 16359-16364.

290. Bui, Q.C., et al., Morphology Transition of ZnO from Thin Film to Nanowires on Silicon and its Correlated Enhanced Zinc Polarity Uniformity and Piezoelectric Responses. *ACS Applied Materials & Interfaces*, **2020**. 12(26): p. 29583-29593.
291. Manzano, C.V., L. Philippe, and A. Serrà, Recent progress in the electrochemical deposition of ZnO nanowires: synthesis approaches and applications. *Critical Reviews in Solid State and Materials Sciences*, **2021**: p. 1-34.
292. Xu, S. and Z.L. Wang, One-dimensional ZnO nanostructures: Solution growth and functional properties. *Nano Research*, **2011**. 4(11): p. 1013-1098.
293. Theerthagiri, J., et al., A review on ZnO nanostructured materials: energy, environmental and biological applications. *Nanotechnology*, **2019**. 30(39): p. 392001.
294. Zhang, Y., et al., Synthesis, Characterization, and Applications of ZnO Nanowires. *Journal of Nanomaterials*, **2012**: p. 1-22.
295. Consonni, V. and A.M. Lord, Polarity in ZnO nanowires: A critical issue for piezotronic and piezoelectric devices. *Nano Energy*, **2021**. 83: p. 105789 .
296. Weintraub, B., et al., Solution synthesis of one-dimensional ZnO nanomaterials and their applications. *Nanoscale*, **2010**. 2(9): p. 1573-87.
297. Vayssieres, L., Growth of Arrayed Nanorods and Nanowires of ZnO from Aqueous Solutions. *Advanced Materials*, **2003**. 15(5): p. 464-466.
298. Wang, X., et al., A study on the antibacterial activity of one-dimensional ZnO nanowire arrays: effects of the orientation and plane surface. *Chemical Communications (Camb),* **2007**.(42): p. 4419-21.
299. Lee, J., et al., The control of cell adhesion and viability by zinc oxide nanorods. *Biomaterials,* **2008**. 29(27): p. 3743-3749.
300. Nakade, K., et al., Adhesion and Bactericidal Properties of a Wettability-Controlled Artificial Nanostructure. *ACS Applied Nano Materials*, **2018**. 1(10): p. 5736-5741.
301. Valiei, A., et al., Hydrophilic Mechano-Bactericidal Nanopillars Require External Forces to Rapidly Kill Bacteria. *Nano Lett*ers, **2020**. 20(8): p. 5720-5727.
302. Jeong, E., et al., Quantitative evaluation of the antibacterial factors of ZnO nanorod arrays under dark conditions: Physical and chemical effects on Escherichia coli inactivation. *Science of Total Environment*, **2020**. 712: p. 136574.
303. Cai, Q., et al., Insight into Biological Effects of Zinc Oxide Nanoflowers on Bacteria: Why Morphology Matters. *ACS Applied Materials & Interfaces*, **2016**. 8(16): p. 10109-20.
304. Mardosaitė, R., A. Jurkevičiūtė, and S. Račkauskas, Superhydrophobic ZnO Nanowires: Wettability Mechanisms and Functional Applications. *Crystal Growth & Design*, **2021**. 21(8): p. 4765-4779.
305. Wang, S., et al., Hierarchical Ti3C2Tx MXene/Ni Chain/ZnO Array Hybrid Nanostructures on Cotton Fabric for Durable Self-Cleaning and Enhanced Microwave Absorption. *ACS Nano,* **2020**. 14(7): p. 8634-8645.
306. Lee, J. and K. Yong, Combining the lotus leaf effect with artificial photosynthesis: regeneration of underwater superhydrophobicity of hierarchical ZnO/Si surfaces by solar water splitting. *NPG Asia Materials*, **2015**. 7(7): p. e201-e201.
307. Wang, J., et al., Rational Design of Transparent Nanowire Architectures with Tunable Geometries for Preventing Marine Fouling. *Advanced Materials Interfaces*, **2020**. 7(17): p. 2000672.
308. Xie, Y., et al., Ultrafast physical bacterial inactivation and photocatalytic self-cleaning of ZnO nanoarrays for rapid and sustainable bactericidal applications. *Science of Total Environment*, **2020**. 738: p. 139714.
309. Yi, G.-C., C. Wang, and W.I. Park, ZnO nanorods: synthesis, characterization and applications. *Semiconductor Science and Technology*, **2005**. 20(4): p. S22-S34.

310. Greene, L.E., et al., Solution-grown zinc oxide nanowires. *Inorganic Chemistry*, **2006**. 45(19): p. 7535-43.
311. Chiou, W.-T., W.-Y. Wu, and J.-M. Ting, Growth of single crystal ZnO nanowires using sputter deposition. *Diamond and Related Materials*, **2003**. 12(10-11): p. 1841-1844.
312. Gao, P.X. and Z.L. Wang, Substrate Atomic-Termination-Induced Anisotropic Growth of ZnO Nanowires/Nanorods by the VLS Process. *The Journal of Physical Chemistry B*, **2004**. 108(23): p. 7534-7537.
313. Lee, W., M.-C. Jeong, and J.-M. Myoung, Catalyst-free growth of ZnO nanowires by metal-organic chemical vapour deposition (MOCVD) and thermal evaporation. *Acta Materialia*, **2004**. 52(13): p. 3949-3957.
314. Hassan, M., et al., Catalyst free growth of ZnO thin film nanostructures on Si substrate by thermal evaporation. *Applied Physics A*, **2021**. 127(7): p. 553.
315. Elias, J., et al., Electrochemical growth of ZnO nanowires on atomic layer deposition coated polystyrene sphere templates. *Electrochimica Acta*, **2013**. 110: p. 387-392.
316. Yoo, K., et al., Low-temperature large-area fabrication of ZnO nanowires on flexible plastic substrates by solution-processible metal-seeded hydrothermal growth. *Nano Converg*, **2020**. 7(1): p. 24.
317. Huang, Y.-C., et al., Facile, wafer-scale compatible growth of ZnO nanowires via chemical bath deposition: assessment of zinc ion contribution and other limiting factors. *Nanoscale Advances*, **2020**. 2(11): p. 5288-5295.
318. Urgessa, Z.N., et al., Synthesis of well-aligned ZnO nanorods on silicon substrate at lower temperature. *Journal of Alloys and Compounds*, **2013**. 580: p. 120-124.
319. Vayssieres, L., et al., Purpose-Built Anisotropic Metal Oxide Material: 3D Highly Oriented Microrod Array of ZnO. *The Journal of Physical Chemistry B*, **2001**. 105(17): p. 3350-3352.
320. Xu, S., et al., Optimizing and Improving the Growth Quality of ZnO Nanowire Arrays Guided by Statistical Design of Experiments. *ACS Nano*, **2009**. 3(7): p. 1803-12.
321. Xu, S., et al., Patterned growth of vertically aligned ZnO nanowire arrays on inorganic substrates at low temperature without catalyst. *Journal of the American Chemical Society*, **2008**. 130(45): p. 14958-9.
322. Wei, Y., et al., Wafer-scale high-throughput ordered growth of vertically aligned ZnO nanowire arrays. *Nano Letters*, **2010**. 10(9): p. 3414-9.
323. Ko, S.H., et al., Nanoforest of hydrothermally grown hierarchical ZnO nanowires for a high efficiency dye-sensitized solar cell. *Nano Letters*, **2011**. 11(2): p. 666-71.
324. Guillemin, S., et al., Critical Nucleation Effects on the Structural Relationship Between ZnO Seed Layer and Nanowires. *The Journal of Physical Chemistry C*, **2012**. 116(47): p. 25106-25111.
325. Song, J. and S. Lim, Effect of Seed Layer on the Growth of ZnO Nanorods. *The Journal of Physical Chemistry C*, **2006**. 111(2): p. 596-600.
326. McPeak, K.M., et al., Chemical bath deposition of ZnO nanowires at near-neutral pH conditions without hexamethylenetetramine (HMTA): understanding the role of HMTA in ZnO nanowire growth. *Langmuir*, **2011**. 27(7): p. 3672-7.
327. Strano, V., et al., Double Role of HMTA in ZnO Nanorods Grown by Chemical Bath Deposition. *The Journal of Physical Chemistry C*, **2014**. 118(48): p. 28189-28195.
328. Cossuet, T., et al., Well-ordered ZnO nanowires with controllable inclination on semipolar ZnO surfaces by chemical bath deposition. *Nanotechnology*, **2018**. 29(47): p. 475601.

329. Choy, J.H., et al., Soft Solution Route to Directionally Grown ZnO Nanorod Arrays on Si Wafer; Room-Temperature Ultraviolet Laser. *Advanced Materials*, **2003**. 15(22): p. 1911-1914.
330. Sugunan, A., et al., Zinc oxide nanowires in chemical bath on seeded substrates: Role of hexamine. *Journal of Sol-Gel Science and Technology*, **2006**. 39(1): p. 49-56.
331. Parize, R., et al., Effects of Hexamethylenetetramine on the Nucleation and Radial Growth of ZnO Nanowires by Chemical Bath Deposition. *The Journal of Physical Chemistry C*, **2016**. 120(9): p. 5242-5250.
332. Verrier, C., et al., Effects of the pH on the Formation and Doping Mechanisms of ZnO Nanowires Using Aluminum Nitrate and Ammonia. *Inorganic Chemistry*, **2017**. 56(21): p. 13111-13122.
333. Boercker, J.E., J.B. Schmidt, and E.S. Aydil, Transport Limited Growth of Zinc Oxide Nanowires. *Crystal Growth & Design*, **2009**. 9(6): p. 2783-2789.
334. Cheng, J.J., et al., Dimensional Tailoring of Hydrothermally Grown Zinc Oxide Nanowire Arrays. *Nano Letters*, **2016**. 16(1): p. 753-9.
335. Greene, L.E., et al., General route to vertical ZnO nanowire arrays using textured ZnO seeds. *Nano Letters*, **2005**. 5(7): p. 1231-6.
336. Demes, T., et al., Mechanisms involved in the hydrothermal growth of ultra-thin and high aspect ratio ZnO nanowires. *Applied Surface Science*, **2017**. 410: p. 423-431.
337. Demes, T., et al., New insights in the structural and morphological properties of sol-gel deposited ZnO multilayer films. *Journal of Physics and Chemistry of Solids*, **2016**. 95: p. 43-55.
338. Kenanakis, G., et al., Growth of c-axis oriented ZnO nanowires from aqueous solution: The decisive role of a seed layer for controlling the wires' diameter. *Journal of Crystal Growth*, **2009**. 311(23-24): p. 4799-4804.
339. Ji, L.-W., et al., Effect of seed layer on the growth of well-aligned ZnO nanowires. *Journal of Physics and Chemistry of Solids*, **2009**. 70(10): p. 1359-1362.
340. Liu, Y., K. Tai, and S.J. Dillon, Growth Kinetics and Morphological Evolution of ZnO Precipitated from Solution. *Chemistry of Materials*, **2013**. 25(15): p. 2927-2933.
341. Znaidi, L., Sol–gel-deposited ZnO thin films: A review. *Materials Science and Engineering: B*, **2010**. 174(1-3): p. 18-30.
342. Tran, H.H., et al., Multifunctional composite films with vertically aligned ZnO nanowires by leaching-enabled capillary rise infiltration. *Nanoscale*, **2019**. 11(45): p. 22099-22107.
343. Manohar, N., K.J. Stebe, and D. Lee, Solvent-Driven Infiltration of Polymer (SIP) into Nanoparticle Packings. *ACS Macro Letters*, **2017**. 6(10): p. 1104-1108.
344. Wang, H., et al., Dramatic Increase in Polymer Glass Transition Temperature under Extreme Nanoconfinement in Weakly Interacting Nanoparticle Films. *ACS Nano*, **2018** 12, 6: p. 5580–5587..
345. Hor, J.L., et al., Effects of polymer-nanoparticle interactions on the viscosity of unentangled polymers under extreme nanoconfinement during capillary rise infiltration. *Soft Matter*, **2018**. 14(13): p. 2438-2446.
346. Jiang, Y., et al., Toughening Nanoparticle Films via Polymer Infiltration and Confinement. *ACS Applied Materials & Interfaces*, **2018**. 10(50): p. 44011-44017.
347. Hoffmann, R., et al., Inverse Nanocomposites Based on Indium Tin Oxide for Display Applications: Improved Electrical Conductivity via Polymer Addition. *ACS Applied Nano Materials*, **2019**. 2, 4: p. 2273–2282.
348. Chen, W., et al., Vertically-aligned carbon nanotubes infiltrated with temperature-responsive polymers: smart nanocomposite films for self-cleaning and controlled release. *Chemical Communications (Camb)*, **2008**. (2): p. 163-5.

349. Peng, S., et al., Photocatalytically Stable Superhydrophobic and Translucent Coatings Generated from PDMS-Grafted-SiO_2/TiO_2@PDMS with Multiple Applications. *Langmuir*, **2019**. 35(7): p. 2760-2771.
350. Chan, E.P., et al., Tailoring the permselectivity of water desalination membranes via nanoparticle assembly. *Langmuir,* **2014**. 30(2): p. 611-6.
351. Barako, M.T., et al., Dense Vertically Aligned Copper Nanowire Composites as High Performance Thermal Interface Materials. *ACS Applied Materials & Interfaces,* **2017**. 9(48): p. 42067-42074.
352. Fragouli, D., et al., Dynamical formation of spatially localized arrays of aligned nanowires in plastic films with magnetic anisotropy. *ACS Nano*, **2010**. 4(4): p. 1873-8.
353. Qu, X., et al., Enhanced electrochromic performance of nanocomposite film based on Preyssler-type polyoxometalate and TiO_2 nanowires. *Inorganic Chemistry Communications*, **2018**. 98: p. 174-179.
354. Kim, M.K., D.K. Yi, and U. Paik, Tunable, flexible antireflection layer of ZnO nanowires embedded in PDMS. *Langmuir,* **2010**. 26(10): p. 7552-4.
355. Meng, X., et al., Matrix replacement route to vertically aligned nickel nanowire array/polydimethylsiloxane nanocomposite film. *Applied Physics Letters*, **2008**. 93(26): p. 263101.
356. Plass, K.E., et al., Flexible Polymer-Embedded Si Wire Arrays. *Advanced Materials,* **2009**. 21(3): p. 325-328.
357. Yuan, J., et al., Superwetting nanowire membranes for selective absorption. *Nature Nanotechnology*, **2008**. 3(6): p. 332-6.
358. Yao, Y., et al., Vertically Aligned and Interconnected SiC Nanowire Networks Leading to Significantly Enhanced Thermal Conductivity of Polymer Composites. *ACS Applied Materials & Interfaces*, **2018**. 10(11): p. 9669-9678.
359. Taylor, C.M., et al., Enhancing the photo-corrosion resistance of ZnO nanowire photocatalysts. *Journal of Hazardous Materials*, **2019**. 378: p. 120799.
360. Zhang, L., et al., A ZnO nanowire-based microfiber coupler for all-optical photodetection applications. *Nanoscale*, **2019**. 11(17): p. 8319-8326.
361. Wen, B., J.E. Sader, and J.J. Boland, Mechanical properties of ZnO nanowires. *Physical Review Letters*, **2008**. 101(17): p. 175502.
362. Wan, Q., et al., Fabrication and ethanol sensing characteristics of ZnO nanowire gas sensors. *Applied Physics Letters,* **2004**. 84(18): p. 3654-3656.
363. Gao, Y., et al., Highly transparent and UV-resistant superhydrophobic SiO_2-coated ZnO nanorod arrays. *ACS Applied Materials & Interfaces*, **2014**. 6(4): p. 2219-23.
364. Ma, S., et al., Facile synthesis of ZnO nanorod arrays and hierarchical nanostructures for photocatalysis and gas sensor applications. *Journal of Hazardous Materials,* **2011**. 192(2): p. 730-40.
365. Kuo, T.-J., et al., Growth of Ultralong ZnO Nanowires on Silicon Substrates by Vapor Transport and Their Use as Recyclable Photocatalysts. *Chemistry of Materials,* **2007**. 19(21): p. 5143-5147.
366. Chu, F.H., et al., Well-aligned ZnO nanowires with excellent field emission and photocatalytic properties. *Nanoscale*, **2012**. 4(5): p. 1471-5.
367. Boughey, F.L., et al., Vertically aligned zinc oxide nanowires electrodeposited within porous polycarbonate templates for vibrational energy harvesting. *Nanotechnology,* **2016**. 27(28): p. 28LT02.
368. Shekhar, S., P. Stokes, and S.I. Khondaker, Ultrahigh density alignment of carbon nanotube arrays by dielectrophoresis. *ACS Nano*, **2011**. 5(3): p. 1739-46.

369. Li, L., et al., Highly Aligned Molybdenum Trioxide Nanobelts for Flexible Thin-Film Transistors and Supercapacitors: Macroscopic Assembly and Anisotropic Electrical Properties. *ACS Applied Nano Materials*, **2019**. 2(3): p. 1466-1471.
370. Gong, M., J. Zhang, and S. Ren, Magnetic field-directed hybrid anisotropic nanocomposites. *Nanotechnology*, **2018**. 29(34): p. 345602.
371. Liu, Z., et al., Hydration-induced nano- to micro-scale self-recovery of the tooth enamel of the giant panda. *Acta Biomaterialia*, **2018**. 81: p. 267-277.
372. Meyvantsson, I. and D.J. Beebe, Cell culture models in microfluidic systems. *Annual Review of Analytical Chemistry,* **2008**. 1: p. 423-49.
373. Hiltunen, J., et al., Roll-to-roll fabrication of integrated PDMS-paper microfluidics for nucleic acid amplification. *Lab on Chip,* **2018**. 18(11): p. 1552-1559.
374. Regehr, K.J., et al., Biological implications of polydimethylsiloxane-based microfluidic cell culture. *Lab on Chip*, **2009**. 9(15): p. 2132-9.
375. Yang, L., et al., Effect of surface free energy on PDMS transfer in microcontact printing and its application to ToF-SIMS to probe surface energies. *Langmuir*, **2009**. 25(10): p. 5674-83.
376. Thibault, C., et al., Poly(dimethylsiloxane) contamination in microcontact printing and its influence on patterning oligonucleotides. *Langmuir*, **2007**. 23(21): p. 10706-14.
377. Halldorsson, S., et al., Advantages and challenges of microfluidic cell culture in polydimethylsiloxane devices. *Biosensors and Bioelectronics,* **2015**. 63: p. 218-231.
378. Lee, J.N., C. Park, and G.M. Whitesides, Solvent compatibility of poly(dimethylsiloxane)-based microfluidic devices. *Analytical Chemistry*, **2003**. 75(23): p. 6544-54.
379. Kim, J., M.K. Chaudhury, and M.J. Owen, Hydrophobic Recovery of Polydimethylsiloxane Elastomer Exposed to Partial Electrical Discharge. *Journal of Colloid and Interface Science*, **2000**. 226(2): p. 231-236.
380. Eddington, D.T., J.P. Puccinelli, and D.J. Beebe, Thermal aging and reduced hydrophobic recovery of polydimethylsiloxane. *Sensors and Actuators B: Chemical*, **2006**. 114(1): p. 170-172.
381. Bodas, D. and C. Khan-Malek, Hydrophilization and hydrophobic recovery of PDMS by oxygen plasma and chemical treatment—An SEM investigation. *Sensors and Actuators B: Chemical,* **2007**. 123(1): p. 368-373.
382. Berthier, E., E.W. Young, and D. Beebe, Engineers are from PDMS-land, Biologists are from Polystyrenia. *Lab on Chip,* **2012**. 12(7): p. 1224-37.
383. Jensen, K.E., et al., Wetting and phase separation in soft adhesion. *Proceedings of the National Academy of Sciences of the United States of America,* **2015**. 112(47): p. 14490-4.
384. Liu, Q. and Z. Suo, Osmocapillary phase separation. *Extreme Mechanics Letters,* **2016**. 7: p. 27-33.
385. Peaudecerf, F.J., et al., Traces of surfactants can severely limit the drag reduction of superhydrophobic surfaces. *Proceedings of the National Academy of Sciences of the United States of America*, **2017**. 114(28): p. 7254-7259.
386. Pezzulla, M., et al., Morphing of geometric composites via residual swelling. *Soft Matter*, **2015**. 11(29): p. 5812-20.
387. Kim, J.H., et al., Hydrophobically recovered and contact printed siloxane oligomers for general-purpose surface patterning. *Langmuir*, **2010**. 26(15): p. 13015-9.
388. Venkatesh, R.B., S.H. Han, and D. Lee, Patterning polymer-filled nanoparticle films via leaching-enabled capillary rise infiltration (LeCaRI). *Nanoscale Horizons*, **2019**. 4(4): p. 933-939.

389. Bae, S.C., et al., *C*hemical imaging in a surface forces apparatus: confocal raman spectroscopy of confined poly(dimethylsiloxane). *Langmuir*, **2005**. 21(13): p. 5685-8.
390. Cuscó, R., et al., Temperature dependence of Raman scattering in ZnO. *Physical Review B*, **2007**. 75(16): p. 165202.
391. Yoshikawa, H. and S. Adachi, Optical Constants of ZnO. *Japanese Journal of Applied Physics*, **1997**. 36: p. 6237-6243.
392. Raguin, D.H. and G.M. Morris, Antireflection structured surfaces for the infrared spectral region. *Applied Optics*, **1993**. 32(7): p. 1154-67.
393. Cassie, A.B.D. and S. Baxter, Wettability of porous surfaces. *Transactions of the Faraday Society*, **1944**. 40: p. 546.
394. Wen, L., Y. Tian, and L. Jiang, Bioinspired super-wettability from fundamental research to practical applications. *Angewandte Chemie International Edition*, **2015**. 54(11): p. 3387-99.
395. Li, Q. and Z. Guo, Fundamentals of icing and common strategies for designing biomimetic anti-icing surfaces. *Journal of Materials Chemistry A*, **2018**. 6(28): p. 13549-13581.
396. Mishchenko, L., et al., Design of ice-free nanostructured surfaces based on repulsion of impacting water droplets. *ACS Nano*, **2010**. 4(12): p. 7699-707.
397. Rico, V.J., et al., Hydrophobicity, Freezing Delay, and Morphology of Laser-Treated Aluminum Surfaces. *Langmuir*, **2019**. 35(19): p. 6483-6491.
398. Wang, L., et al., Robust anti-icing performance of silicon wafer with hollow micro-/nano-structured ZnO. J*ournal of Industrial and Engineering Chemistry*, **2018**. 62: p. 46-51.
399. Tran, H.H., et al., Lubricant Depletion-Resistant Slippery Liquid-Infused Porous Surfaces via Capillary Rise Lubrication of Nanowire Array. *Advanced Materials Interfaces*, **2021**. 8(7): p. 2002058.
400. Sotiri, I., et al., Tunability of liquid-infused silicone materials for biointerfaces. *Biointerphases*, **2018**. 13(6): p. 06D401.
401. Lafuma, A. and D. Quéré, Slippery pre-suffused surfaces. *EPL (Europhysics Letters)*, **2011**. 96(5): p. 56001.
402. Heydarian, S., R. Jafari, and G. Momen, Recent progress in the anti-icing performance of slippery liquid-infused surfaces. *Progress in Organic Coatings*, **2021**. 151: p. 106096.
403. Wang, P., et al., Fabrication of Slippery Lubricant-Infused Porous Surface with High Underwater Transparency for the Control of Marine Biofouling. *ACS Applied Materials & Interfaces*, **2017**. 9(1): p. 972-982.
404. Mackie, G., et al., Clinical Potential of Immobilized Liquid Interfaces: Perspectives on Biological Interactions. *Trends in Biotechnology*, **2019**. 37(3): p. 268-280.
405. Wang, Z., L. Heng, and L. Jiang, Effect of lubricant viscosity on the self-healing properties and electrically driven sliding of droplets on anisotropic slippery surfaces. *Journal of Materials Chemistry A*, **2018**. 6(8): p. 3414-3421.
406. Lee, C., H. Kim, and Y. Nam, Drop impact dynamics on oil-infused nanostructured surfaces. *Langmuir*, **2014**. 30(28): p. 8400-7.
407. Kim, J.H. and J.P. Rothstein, Droplet Impact Dynamics on Lubricant-Infused Superhydrophobic Surfaces: The Role of Viscosity Ratio. *Langmuir*, **2016**. 32(40): p. 10166-10176.
408. Liu, Y., et al., Effect of viscosity ratio on the shear-driven failure of liquid-infused surfaces. *Physical Review Fluids*, **2016**. 1(7): p. 074003 .
409. Ware, C.S., et al., Marine Antifouling Behavior of Lubricant-Infused Nanowrinkled Polymeric Surfaces. *ACS Applied Materials & Interfaces*, **2018**. 10(4): p. 4173-4182.

410. Yao, Y., et al., Theory on Capillary Filling of Polymer Melts in Nanopores. *Macromolecular Rapid Communications*, **2018**. 39(14): p. e1800087.
411. Chen, X., et al., Water Droplet Spreading and Wicking on Nanostructured Surfaces. *Langmuir*, **2017**. 33(27): p. 6701-6707.
412. Rykaczewski, K., et al., Mechanism of frost formation on lubricant-impregnated surfaces. *Langmuir*, **2013**. 29(17): p. 5230-8.
413. Olad, A., et al., Potential of slippery liquid infused porous surface coatings as flashover inhibitors on porcelain insulators in icing, contaminated, and harsh environments. *Progress in Organic Coatings*, **2021**. 151: p. 106082.
414. Tuo, Y., et al., Corrosion protection application of slippery liquid-infused porous surface based on aluminum foil. *Applied Surface Science*, **2017**. 423: p. 365-374.
415. Hao, Z., et al., Slippery liquid-infused porous surface via thermally induced phase separation for enhanced corrosion protection. *Journal of Polymer Science*, **2020**. 58(21): p. 3031-3041.
416. Qiu, R., et al., Fabrication of slippery liquid-infused porous surface based on carbon fiber with enhanced corrosion inhibition property. *Colloids and Surfaces A: Physicochemical and Engineering Aspects*, **2014**. 453: p. 132-141.
417. Wang, P., Z. Lu, and D. Zhang, Slippery liquid-infused porous surfaces fabricated on aluminum as a barrier to corrosion induced by sulfate reducing bacteria. *Corrosion Science*, **2015**. 93: p. 159-166.
418. Dinh, H.T., et al., Iron corrosion by novel anaerobic microorganisms. *Nature*, **2004**. 427(6977): p. 829-32.
419. Liu, Y., et al., Topical ferumoxytol nanoparticles disrupt biofilms and prevent tooth decay in vivo via intrinsic catalytic activity. *Nature Communications*, **2018**. 9(1): p. 2920.
420. Costerton, J.W., P.S. Stewart, and E.P. Greenberg, Bacterial biofilms: a common cause of persistent infections. *Science*, **1999**. 284(5418): p. 1318-22.
421. Selim, M.S., et al., Recent progress in marine foul-release polymeric nanocomposite coatings. *Progress in Materials Science*, **2017**. 87: p. 1-32.
422. Lee, S.W., et al., *How microbes read the map:* Effects of implant topography on bacterial adhesion and biofilm formation. *Biomaterials*, **2021**. 268: p. 120595.
423. Hall-Stoodley, L., J.W. Costerton, and P. Stoodley, Bacterial biofilms: from the natural environment to infectious diseases. *Nature Review Microbiology*, **2004**. 2(2): p. 95-108.
424. Donlan, R.M., Biofilms: microbial life on surfaces. *Emerging Infectious Diseases*, **2002**. 8(9): p. 881-90.
425. Davies, D.G., et al., The involvement of cell-to-cell signals in the development of a bacterial biofilm. *Science*, **1998**. 280(5361): p. 295-8.
426. de Beer, D., P. Stoodley, and Z. Lewandowski, Liquid flow in heterogeneous biofilms. *Biotechnology and Bioengineering*, **1994**. 44(5): p. 636-41.
427. Davies, D.G., A.M. Chakrabarty, and G.G. Geesey, Exopolysaccharide production in biofilms: substratum activation of alginate gene expression by *Pseudomonas aeruginosa*. *Applied and Environmental Microbiology*, **1993**. 59(4): p. 1181-6.
428. Costerton, J.W., et al., *M*icrobial biofilms. *Annual Review of Microbiology*, **1995**. 49: p. 711-45.
429. Tripathy, A., et al., Natural and bioinspired nanostructured bactericidal surfaces. *Advances in Colloid and Interface Science*, **2017**. 248: p. 85-104.
430. Elbourne, A., Truong, V. K., Cheeseman, S., Rajapaksha, P., Gangadoo, S., Chapman, J., & Crawford, R. J., The use of nanomaterials for the mitigation of pathogenic biofilm formation. *Methods in Microbiology*, **2019**. Elsevier.

431. Smith, K.M., et al., Infectious disease and economics: The case for considering multi-sectoral impacts. *One Health*, **2019**. 7: p. 100080.
432. Magill, S.S., et al., Multistate point-prevalence survey of health care-associated infections. *New England Journal of Medicine*, **2014**. 370(13): p. 1198-208.
433. Bjarnsholt, T., The role of bacterial biofilms in chronic infections. *APMIS*, **2013**(136): p. 1-51.
434. Brackman, G., et al., Quorum sensing inhibitors increase the susceptibility of bacterial biofilms to antibiotics in vitro and in vivo. *Antimicrob Agents Chemother*, **2011**. 55(6): p. 2655-61.
435. Shi, J., et al., Efficacy of combined vancomycin and fosfomycin against methicillin-resistant Staphylococcus aureus in biofilms in vivo. *PLoS One*, **2014**. 9(12): p. e113133.
436. Adelson, R.T. and N.D. Adappa, What is the proper role of oral antibiotics in the treatment of patients with chronic sinusitis? *Current Opinion in Otolaryngology & Head and Neck Surgery*, **2013**. 21(1): p. 61-8.
437. Albright, V., et al., Polyphosphazenes enable durable, hemocompatible, highly efficient antibacterial coatings. *Biomaterials*, **2021**. 268: p. 120586.
438. Krishnasami, Z., et al., Management of hemodialysis catheter-related bacteremia with an adjunctive antibiotic lock solution. *Kidney International*, **2002**. 61(3): p. 1136-42.
439. Chodak, G.W. and M.E. Plaut, Use of systemic antibiotics for prophylaxis in surgery: a critical review. *The Archives of Surgery*, **1977**. 112(3): p. 326-34.
440. Rehman, I.U., et al., Knowledge and Practice of Pharmacists toward Antimicrobial Stewardship in Pakistan. *Pharmacy (Basel)*, **2018**. 6(4): p. 116.
441. Li, W., et al., *Surface* Design for Antibacterial Materials: From Fundamentals to Advanced Strategies. *Advanced Science (Weinh)*, **2021**. 8(19): p. e2100368.
442. Amoretti, M., et al., Production and detection of cold antihydrogen atoms. *Nature*, **2002**. 419(6906): p. 456-9.
443. Larrañaga-Altuna, M., et al., Bactericidal surfaces: An emerging 21st-century ultra-precision manufacturing and materials puzzle. *Applied Physics Reviews*, **2021**. 8(2): p. 021303.
444. Koo, H., et al., *Targeting microbial biofilms: current and prospective therapeutic strategies. Nature Review Microbiology*, **2017**. 15(12): p. 740-755.
445. Ishantha Senevirathne, S.W.M.A., et al., Trends in Bactericidal Nanostructured Surfaces: An Analytical Perspective. *ACS Applied Bio Materials*, **2021**. 4(10): p. 7626-7642.
446. Wei, T., et al., Smart Antibacterial Surfaces with Switchable Bacteria-Killing and Bacteria-Releasing Capabilities. *ACS Applied Materials & Interfaces*, **2017**. 9(43): p. 37511-37523.
447. Hwang, G., et al., Catalytic antimicrobial robots for biofilm eradication. *Science Robotics*, **2019**. 4(29): p. eaaw2388.
448. Yan, Y., et al., Antibacterial and Biofilm-Preventive Photocatalytic Activity and Mechanisms on P/F-Modified TiO_2 Coatings. *ACS Applied Bio Materials*, **2020**. 3(9): p. 5687-5698.
449. Ramos Chagas, G., et al., Anti-bacterial and fluorescent properties of hydrophobic electrodeposited non-fluorinated polypyrenes. *Applied Surface Science*, **2018**. 452: p. 352-363.
450. Jiang, S. and Z. Cao, Ultralow-fouling, functionalizable, and hydrolyzable zwitterionic materials and their derivatives for biological applications. *Advanced Materials*, **2010**. 22(9): p. 920-32.

451. Smith, R.S., et al., Vascular catheters with a nonleaching poly-sulfobetaine surface modification reduce thrombus formation and microbial attachment. *Science Translational Medicine*, **2012**. 4(153): p. 153ra132.
452. Autumn, K., et al., Evidence for van der Waals adhesion in gecko setae. *Proceedings of the National Academy of Sciences of the United States of America*, **2002**. 99(19): p. 12252-6.
453. Hook, A.L., et al., Combinatorial discovery of polymers resistant to bacterial attachment. *Nature Biotechnology,* **2012**. 30(9): p. 868-875.
454. Park, K.D., et al., Bacterial adhesion on PEG modified polyurethane surfaces. *Biomaterials,* **1998**. 19(7-9): p. 851-859.
455. Hwang, G.B., et al., The Anti-Biofouling Properties of Superhydrophobic Surfaces are Short-Lived. *ACS Nano*, **2018**. 12(6): p. 6050-6058.
456. Banerjee, I., R.C. Pangule, and R.S. Kane, Antifouling coatings: recent developments in the design of surfaces that prevent fouling by proteins, bacteria, and marine organisms. *Advanced Materials*, **2011**. 23(6): p. 690-718.
457. Bos, R., et al., Retention of bacteria on a substratum surface with micro-patterned hydrophobicity. *FEMS Microbiology Letters*, **2000**. 189(2): p. 311-5.
458. Encinas, N., et al., Submicrometer-Sized Roughness Suppresses Bacteria Adhesion. *ACS Applied Materials & Interfaces*, **2020**. 12(19): p. 21192-21200.
459. Geyer, F., et al., How to Coat the Inside of Narrow and Long Tubes with a Super-Liquid-Repellent Layer-A Promising Candidate for Antibacterial Catheters. *Advanced Materials*, **2019**. 31(2): p. e1801324.
460. Milionis, A., et al., Water-Based Scalable Methods for Self-Cleaning Antibacterial ZnO-Nanostructured Surfaces. *Industrial & Engineering Chemistry Research,* **2020**. 59(32): p. 14323-14333.
461. Tang, Y., et al., Bioinspired photocatalytic ZnO/Au nanopillar-modified surface for enhanced antibacterial and antiadhesive property. *Chemical Engineering Journal*, **2020**. 398: p. 125575.
462. Yi, G., et al., ZnO Nanopillar Coated Surfaces with Substrate-Dependent Superbactericidal Property. *Small,* **2018**. 14(14): p. 1703159.
463. Patir, A., et al., Crystal Violet-Impregnated Slippery Surface to Prevent Bacterial Contamination of Surfaces. *ACS Applied Materials & Interfaces,* **2021**. 13(4): p. 5478-5485.
464. Chen, J., et al., An immobilized liquid interface prevents device associated bacterial infection in vivo. *Biomaterials,* **2017**. 113: p. 80-92.
465. O'Toole, G.A., *Microtiter Dish Biofilm Formation Assay. Journal of Visualized Experiments,* **2011**. 47: p. e2437.
466. Conrad, J.C., et al., Flagella and pili-mediated near-surface single-cell motility mechanisms in *P. aeruginosa. Biophysical Journal,* **2011**. 100(7): p. 1608-16.
467. Guzman-Soto, I., et al., Mimicking biofilm formation and development: Recent progress in in vitro and in vivo biofilm models. *iScience,* **2021**. 24(5): p. 102443.
468. Schwarzenbach, R.P., et al., The challenge of micropollutants in aquatic systems. *Science,* **2006**. 313(5790): p. 1072-7.
469. Elimelech, M., The global challenge for adequate and safe water. *Journal of Water Supply: Research and Technology - Aqua*, **2006**. 55(1): p. 3-10.
470. Luo, Y., et al., A review on the occurrence of micropollutants in the aquatic environment and their fate and removal during wastewater treatment. *Science of Total Environment*, **2014**. 473-474: p. 619-41.

471. Kolpin, D.W., et al., Pharmaceuticals, hormones, and other organic wastewater contaminants in U.S. streams, 1999-2000: a national reconnaissance. *Environmental Science & Technology*, **2002**. 36(6): p. 1202-11.
472. Vidic, R.D., et al., Impact of shale gas development on regional water quality. *Science*, **2013**. 340(6134): p. 1235009.
473. Pye, V.I. and R. Patrick, Ground water contamination in the United States. *Science*, **1983**. 221(4612): p. 713-8.
474. Craun, G.F., et al., Causes of outbreaks associated with drinking water in the United States from 1971 to 2006. *Clinical Microbiology Reviews*, **2010**. 23(3): p. 507-28.
475. Shannon, M.A., et al., Science and technology for water purification in the coming decades. *Nature*, **2008**. 452(7185): p. 301-10.
476. Montgomery, M.A. and M. Elimelech, *Water and sanitation in developing countries: including health in the equation. Environmental Science & Technology*, **2007**. 41(1): p. 17-24.
477. Logan, B.E. and M. Elimelech, Membrane-based processes for sustainable power generation using water. *Nature*, **2012**. 488(7411): p. 313-9.
478. Werber, J.R., C.O. Osuji, and M. Elimelech, Materials for next-generation desalination and water purification membranes. *Nature Reviews Materials*, **2016**. 1(5): p. 16018.
479. Strathmann, H., Membrane separation processes. *Journal of Membrane Science*, **1981**. 9(1-2): p. 121-189.
480. Takht Ravanchi, M., T. Kaghazchi, and A. Kargari, Application of membrane separation processes in petrochemical industry: a review. *Desalination*, **2009**. 235(1-3): p. 199-244.
481. van Voorthuizen, E., et al., Biological black water treatment combined with membrane separation. *Water Research*, **2008**. 42(16): p. 4334-40.
482. Ding, F. and M. Gao, Pore wettability for enhanced oil recovery, contaminant adsorption and oil/water separation: A review. *Advances in Colloid and Interface Science*, **2021**. 289: p. 102377.
483. Afsari, M., H.K. Shon, and L.D. Tijing, Janus membranes for membrane distillation: Recent advances and challenges. *Advances in Colloid and Interface Science*, **2021**. 289: p. 102362.
484. Khanzada, N.K., et al., Removal of organic micropollutants using advanced membrane-based water and wastewater treatment: A review. *Journal of Membrane Science*, **2020**. 598: p. 117672.
485. Ulbricht, M., Advanced functional polymer membranes. *Polymer*, **2006**. 47(7): p. 2217-2262.
486. Koros, W.J., M.R. Coleman, and D.R.B. Walker, Controlled Permeability Polymer Membranes. *Annual Review of Materials Science*, **1992**. 22(1): p. 47-89.
487. Yasuda, H. and J.T. Tsai, Pore size of microporous polymer membranes. *Journal of Applied Polymer Science*, **1974**. 18(3): p. 805-819.
488. Semenova, S.I., Polymer membranes for hydrocarbon separation and removal. *Journal of Membrane Science*, **2004**. 231(1-2): p. 189-207.
489. Kamcev, J. and B.D. Freeman, Charged Polymer Membranes for Environmental/Energy Applications. *Annual Review of Chemical and Biomolecular Engineering*, **2016**. **7**: p. 111-33.
490. Zhang, F., et al., Nanowire-haired inorganic membranes with superhydrophilicity and underwater ultralow adhesive superoleophobicity for high-efficiency oil/water separation. *Advanced Materials*, **2013**. 25(30): p. 4192-8.
491. Abdollahzadeh Sharghi, E., B. Bonakdarpour, and M. Pakzadeh, Treatment of hypersaline produced water employing a moderately halophilic bacterial consortium in

a membrane bioreactor: effect of salt concentration on organic removal performance, mixed liquor characteristics and membrane fouling. *Bioresource Technology,* **2014**. 164: p. 203-13.

492. Wang, Y., et al., An integrated strategy for achieving oil-in-water separation, removal, and anti-oil/dye/bacteria-fouling. *Chemical Engineering Journal*, **2021**. 413: p. 127493.
493. Zhu, X., H.-E. Loo, and R. Bai, A novel membrane showing both hydrophilic and oleophobic surface properties and its non-fouling performances for potential water treatment applications. *Journal of Membrane Science*, **2013**. 436: p. 47-56.
494. Ding, Y., et al., Superhydrophilic carbonaceous-silver nanofibrous membrane for complex oil/water separation and removal of heavy metal ions, organic dyes and bacteria. *Journal of Membrane Science,* **2020**. 614: p. 118491.
495. Zhijun, R., et al., Effects of a low-strength magnetic field on the characteristics of activated sludge for membrane fouling mitigation. *RSC Advances,* **2019**. 9(16): p. 9180-9186.
496. Yu, L., et al., Effects of solids retention time on the performance and microbial community structures in membrane bioreactors treating synthetic oil refinery wastewater. *Chemical Engineering Journal*, **2018**. 344: p. 462-468.
497. Chen, Y.-R., et al., Hydrophobic alumina hollow fiber membranes for sucrose concentration by vacuum membrane distillation. *Journal of Membrane Science,* **2018**. 555: p. 250-257.
498. Xue, Z., M. Liu, and L. Jiang, Recent developments in polymeric superoleophobic surfaces. *Journal of Polymer Science Part B: Polymer Physics,* **2012**. 50(17): p. 1209-1224.
499. Kota, A.K., et al., Hierarchically structured superoleophobic surfaces with ultralow contact angle hysteresis. *Advanced Materials*, **2012**. 24(43): p. 5838-43.
500. Wang, H., et al., Hydrophobic Silica Nanorod Arrays Vertically Grown on Melamine Foams for Oil/Water Separation. *ACS Applied Nano Materials*, **2020**. 3(2): p. 1479-1488.
501. Huang, A., et al., Fabrication of zinc oxide nanostructure coated membranes for efficient oil/water separation. *Journal of Membrane Science,* **2018**. 566: p. 249-257.
502. Li, Q., et al., High-Flux Oil/Water Separation with Interfacial Capillary Effect in Switchable Superwetting $Cu(OH)_2$@ZIF-8 Nanowire Membranes. *ACS Applied Materials & Interfaces,* **2018**. 10(46): p. 40265-40273.
503. Berger, T.E., et al., Photocatalytic degradation of organic dye via atomic layer deposited TiO_2 on ceramic membranes in single-pass flow-through operation. *Journal of Membrane Science,* **2020**. 604: p. 118015.
504. Zhou, C., et al., Superhydrophilic and underwater superoleophobic titania nanowires surface for oil repellency and oil/water separation. *Chemical Engineering Journal,* **2016**. 301: p. 249-256.
505. Liu, J., et al., A Robust $Cu(OH)_2$ Nanoneedles Mesh with Tunable Wettability for Nonaqueous Multiphase Liquid Separation. *Small,* **2017**. 13(4): p. 1600499.
506. Yin, X., et al., Preparation of durable, self-cleaning and photocatalytic superhydrophobic Ni_3S_2 coating on 304 stainless steel surface against contaminations. *Journal of Materials Science*, **2021**. 56(11): p. 6719-6731.
507. Hang, T., et al., TiO_2 nanowire-templated hierarchical nanowire network as water-repelling coating. *Royal Society Open Science,* **2017**. 4(12): p. 171431.
508. Xiong, S., et al., Atomic-layer-deposition-enabled nonwoven membranes with hierarchical ZnO nanostructures for switchable water/oil separations. *Journal of Membrane Science,* **2015**. 493: p. 478-485.

509. Wang, T., et al., Superhydrophobic ceramic hollow fiber membrane planted by ZnO nanorod-array for high-salinity water desalination. *Journal of the Taiwan Institute of Chemical Engineers*, **2019**. 105: p. 17-27.
510. Raturi, P., K. Yadav, and J.P. Singh, ZnO-Nanowires-Coated Smart Surface Mesh with Reversible Wettability for Efficient On-Demand Oil/Water Separation. *ACS Applied Materials & Interfaces*, **2017**. 9(7): p. 6007-6013.
511. Huang, A., et al., Nanoarchitectured design of porous ZnO@copper membranes enabled by atomic-layer-deposition for oil/water separation. *Journal of Membrane Science*, **2019**. 582: p. 120-131.
512. Pan, T.D., et al., Buoyancy Assisted Janus Membrane Preparation by ZnO Interfacial Deposition for Water Pollution Treatment and Self-cleaning. *Advanced Materials Interfaces*, **2019**. 6(21): p. 1901130.
513. Le Pivert, M., et al., Smart ZnO decorated optimized engineering materials for water purification under natural sunlight. *Construction and Building Materials*, **2020**. 257: p. 119592.
514. Pan, T., et al., *A* Sm-doped Egeria-densa-like ZnO nanowires@PVDF nanofiber membrane for high-efficiency water clean. *Science of Total Environment*, **2020**. 737: p. 139818.
515. Hsu, M.H. and C.J. Chang, Ag-doped ZnO nanorods coated metal wire meshes as hierarchical photocatalysts with high visible-light driven photoactivity and photostability. *Journal of Hazardous Materials*, **2014**. 278: p. 444-53.
516. Jung, S. and K. Yong, Fabrication of CuO-ZnO nanowires on a stainless steel mesh for highly efficient photocatalytic applications. *Chemical Communications (Camb)*, **2011**. 47(9): p. 2643-5.
517. Song, Z., et al., TiO_2 nanofiltration membranes prepared by molecular layer deposition for water purification. *Journal of Membrane Science*, **2016**. 510: p. 72-78.
518. Cheng, Q., et al., Facile fabrication of superhydrophilic membranes consisted of fibrous tunicate cellulose nanocrystals for highly efficient oil/water separation. *Journal of Membrane Science*, **2017**. 525: p. 1-8.
519. Zhang, M., et al., Amphipathic Pentiptycene-Based Water-Resistant Cu-MOF for Efficient Oil/Water Separation. *Inorganic Chemistry*, **2019**. 58(9): p. 5384-5387.
520. Vu, T.T., et al., Stainless steel wire mesh-supported ZnO for the catalytic photodegradation of methylene blue under ultraviolet irradiation. *Journal of Hazardous Materials*, **2013**. 246-247: p. 126-34.
521. Nasser, J., K. Steinke, and H. Sodano, ZnO Nanostructured Interphase for Multifunctional and Lightweight Glass Fiber Reinforced Composite Materials under Various Loading Conditions. *ACS Applied Nano Materials*, **2020**. 3(2): p. 1363-1372.
522. Wang, M., et al., ZnO Nanorod Array Modified PVDF Membrane with Superhydrophobic Surface for Vacuum Membrane Distillation Application. *ACS Applied Materials & Interfaces*, **2018**. 10(16): p. 13452-13461.
523. Rogé, V., et al., Tuneable Functionalization of Glass Fibre Membranes with ZnO/SnO_2 Heterostructures for Photocatalytic Water Treatment: Effect of SnO_2 Coverage Rate on the Photocatalytic Degradation of Organics. *Catalysts*, **2020**. 10(7): p. 733.
524. Huang, X., et al., Type-II ZnO nanorod-SnO_2 nanoparticle heterostructures: characterization of structural, optical and photocatalytic properties. *Nanoscale*, **2013**. 5(9): p. 3828-33.
525. Zhang, W., et al., Superwetting Porous Materials for Wastewater Treatment: from Immiscible Oil/Water Mixture to Emulsion Separation. *Advanced Materials Interfaces*, **2017**. 4(10): p. 1600029.

526. Zheng, W., et al., Advanced Materials with Special Wettability toward Intelligent Oily Wastewater Remediation. *ACS Applied Materials & Interfaces*, **2021**. 13(1): p. 67-87.
527. Ishino, C., et al., Wicking within forests of micropillars. *Europhysics Letters (EPL)*, **2007**. 79(5): p. 56005.
528. Gunjan, M.R., A. Kumar, and R. Raj, Cloaked Droplets on Lubricant-Infused Surfaces: Union of Constant Mean Curvature Interfaces Dictated by Thin-Film Tension. *Langmuir*, **2021**. 37(22): p. 6601-6612.

Publications

1. **Hong-Huy Tran**, R Bharath Venkatesh, Youngjin Kim, Daeyeon Lee*, David Riassetto* "Multifunctional Composite Films with Vertically Aligned ZnO Nanowires by Leaching-enabled Capillary Rise Infiltration", *Nanoscale* (2019) 11, 22099–22107.
2. **Hong-Huy Tran**, Youngjin Kim, Céline Ternon, Michel Langlet, David Riassetto*, Daeyeon Lee* "Lubricant Depletion-Resistant Slippery Liquid-Infused Porous Surfaces via Capillary Rise Lubrication of Nanowire Array", *Advanced Materials Interfaces* (2021), 8, 2002058.
3. R. Bharath Venkatesh, Neha Manohar, Yiwei Qiang, Haonan Wang, **Hong-Huy Tran**, Baekmin Q. Kim, Anastasia Neuman, Tian Ren, Zahra Fakhraai, Robert A. Riggleman, Kathleen J. Stebe, Kevin Turner, Daeyeon Lee* "Polymer-Infiltrated Nanoparticle Films using Capillarity-based Techniques: towards Multifunctional Coatings and Membranes", *Annual Review of Chemical and Biomolecular Engineering* (2021), 12:411-437.
4. **Hong-Huy Tran**, Daeyeon Lee*, David Riassetto* “Wetting Ridges on Slippery Liquid Infused Porous Surfaces”, (**To be submitted**).
5. Youngjin Kim, **Hong-Huy Tran**, F. Morisot, Céline Ternon, Michel Langlet, David Riassetto* “Combined Nano/Micro-Rough Structure Consisting of Double Zinc Oxide Nanowire Networks for Robust Superhydrophobicity and Multifunctionality", (**To be Submitted**).